EXCHANGES BETWEEN HEMISPHERES AND GYRES: A DIRECT APPROACH TO THE MEAN CIRCULATION OF THE EQUATORIAL PACIFIC

by

Susan E. Wijffels

B. Sc. Hons. Oceanography and Meteorology, Flinders University of South Australia, 1986

submitted in partial fulfillment of the requirements for the degree of

DOCTOR OF PHILOSOPHY

at the

MASSACHUSETTS INSTITUTE OF TECHNOLOGY

and the

WOODS HOLE OCEANOGRAPHIC INSTITUTION

September 1993

Signature of Author_____

Joint Program in Oceanography,
Massachusetts Institute of Technology/Woods Hole
Oceanographic Institution

Certified by_____

John M. Toole
Associate Scientist
Thesis Supervisor

Accepted by_____

Lawrence J. Pratt,
Chair, Joint Committee in Physical Oceanography
Massachusetts Institute of Technology/Woods Hole
Oceanographic Institution

EXCHANGES BETWEEN HEMISPHERES AND GYRES: A DIRECT APPROACH TO THE MEAN CIRCULATION OF THE EQUATORIAL PACIFIC

by
Susan Elizabeth Wijffels

submitted in partial fulfillment of the requirements for the degree of
Doctor of Philosophy to the Massachusetts Institute of Technology
and the Woods Hole Oceanographic Institution Joint Program in
Physical Oceanography.
September11, 1993.

Abstract

An extensive set of new high-quality hydrographic data is assembled in order to determine the mean circulation in the equatorial Pacific, and thus the pathways for cross-equatorial and cross-gyre exchange. Making up the core of the data set are two onetime transpacific zonal sections nominally at 10°N and 14°S. Supplementing these are repeat surveys of the equatorial currents along the 165°E meridian with direct shear measurements, and repeat surveys of the western boundary current at 8°N including direct velocity measurements. The repeat survey data are crucial for obtaining a good estimate of the mean conditions in the face of strong annual and interannual variability of the near-equatorial flow field. A comparison with historical XBT and hydrographic data shows that the interior thermocline transports in the one-time sections are fortuitously representative of the mean conditions.

A detailed study of the water mass distribution along the sections is the basis for choosing reference levels for the thermal wind shear in an initial guess circulation field. Using an inverse model, the initial guess circulation is adjusted such that volume, heat and salt are conserved in a set of subthermocline layers ($\sigma_\Theta > 26.7$). Cross-isopycnal diffusion and advection are explicitly accounted for in the inverse model, and the diapycnal diffusivity is constrained to be positive, though its value is allowed to vary with depth and location. Net mass conservation constraints are applied to the enclosed volumes of the North Pacific and eastern Pacific, and essentially require that the Ekman divergence be equal to the geostrophic convergence. The Ekman fluxes as estimated from wind-stress climatologies are an important element of the mass budget, and yet are subject to large uncertainties. The model is therefore given the freedom to determine the Ekman fluxes within the range of error of the wind-stresses.

The circulation of the coldest waters ($\Theta < 1.2$°C) is dominated by the northward flow of Lower Circumpolar Water (LCPW) in a system of narrow western boundary currents. A net transport of 12.1 Sv of LCPW flows across 14°S, 9.6 Sv of which flows into the North Pacific across 10°N. The bulk of the LCPW flux across the equator appears to occur in the denser part of the western boundary current which follows topography directly across the equator. Dissipation in the boundary layer can thus modify the potential vorticity of the fluid and allow it to cross the equator. The circulation of the upper part of the LCPW is dominated by a strong westward jet at the equator which is supplied both by upwelling from below and the recirculation of modified LCPW from the North Pacific.

At mid-depth ($4.0 > \Theta > 1.2$°C) high silica and low oxygen concentrations mark the North

Pacific Deep Water (NPDW) which is present in both the North and South Pacific Oceans. Across both 10°N and 14°S, a net of 11 Sv of NPDW flows southward, returning the northward mass flux associated with the LCPW. In contrast to the LCPW, narrow western boundary currents are not present in this layer, and it is not clear how the deep water flows across the equator. Strong zonal jets on and about the equator may be important in allowing mass to cross the equator by increasing the time available for the cross-equatorial diffusion of potential vorticity to act on a fluid parcel.

At intermediate depths equatorward advection is suggested by the presence of intermediate water salinity minima formed in the subpolar latitudes: Antarctic Intermediate Water dominates the 4 to 8°C classes south of the equator, while North Pacific Intermediate Water occupies this range north of the equator. Determination of the mean circulation of the intermediate waters is, however, confounded by the large eddies that dominate the geostrophic transport stream function along the onetime zonal sections.

The equatorial thermocline is occupied by waters of subtropical origin: the shallow salinity minimum waters and saline Central Water from both the North and South Pacific Ocean. The equator marks the location of a front between northern and southern subtropical gyre waters, except in the lower thermocline where water from the South Pacific subtropical gyre penetrates to about 4°N to feed the Northern Subsurface Countercurrent at 165°E. All of the equatorward flowing thermocline waters are entrained in the eastward equatorial currents which in turn feed the upwelling system in the eastern Pacific. The upwelled waters largely supply the South Equatorial Current in the eastern Pacific, accounting for its large transport compared to that predicted by Sverdrup dynamics. Northward flow across the equator of the upwelled waters in the thermocline or surface layer in the western Pacific is necessary to supply the Ekman flux into the North Pacific.

The analysis indicates that the Pacific Ocean does not convert a large amount of abyssal water to thermocline water, as required by several theories of the global thermohaline circulation. In contrast to the Atlantic Ocean, the thermocline circulation in the Pacific appears decoupled from the abyssal overturning, with little upwelling of abyssal waters occurring in either the North Pacific or the equatorial Pacific. The leakage of Pacific water into the Indian Ocean is deduced to be essentially zero, though an error analysis allows a range of 0-8 x $10^6 m^3 s^{-1}$.

Thesis Supervisor: John M. Toole, Associate Scientist
Woods Hole Oceanographic Institution

Acknowledgments

Dr. Harry Bryden, who acted as my advisor during most of my years working on this thesis, inspired my interest in many aspects of oceanography: from global heat and freshwater fluxes to the equatorial circulation. His encouragement, patience and good advice were essential to my scientific development, as well as my happiness during my years in the Joint Program.

Dr. John Toole, as first a committee member and then advisor, has been a great source of moral and intellectual support throughout. His generosity, patience and calmness kept me on an even keel during the last hectic year of this project.

I thank the rest of my thesis Committee, Drs. Melinda Hall, Joseph Pedlosky and Paola Rizzoli for both their time, understanding and encouragement. Their perspectives and careful criticisms aided in the development and clarification of this work. In addition, I thank Ray Schmitt for being my Thesis Chairman, and for his moral support.

This analysis was made possible by the data contributions of many: John Toole, Harry Bryden and Esther Brady were essential in the collection and processing of the MW893 data set, which was supported in its entirety by the National Science Foundation grant OCE87-6910; Stan Hayes, Bruce Taft, Dave Behringer and Doug Wilson provided access to the TEW data; John Toole made possible the use of the USPRC repeat survey data and Eric Firing, the processed ADCP data along 8°N; Yves Gouriou and John Toole provided their mean fields at 165°E; Billy Kessler generously gave access to his XBT and CTD data archive, as well as his extensive software collection; Mike McPhaden sent us the data from the 0°, 165°E mooring; Steve Worley at NCAR provided speedy access to various surface flux data sets over the Internet. I had many stimulating conversations with Billy Kessler, Greg Johnson, Paul Robbins, Kurt Polzin, Terry Joyce, Xin Huang, Ray Schmitt, Zhengyu Liu, Rebecca Schudlich and Bo Qui. As a student, I was supported by the 1986 Caltex Graduate Women Scholarship, and a NASA Scholarship in Global Change Research.

I thank all my friends, office and house-mates in Woods Hole and Cambridge for their support and encouragement, and for the fun and silliness they added to life. Joe Adelstein has been the source of much energy, encouragement and laughter, keeping me smiling despite facing what seemed impossible goals. Finally, I thank my parents, sisters and friends in Australia, for their enduring love and support.

Table of Contents

List of Figures

Chapter 1

Introduction

Evidence for cross-equatorial exchange in the property fields has been recognized for many years and yet is poorly understood, from both the observational and theoretical points of view. A primary reason lies in the difficulty in quantifying cross-equatorial flow: at the equator, the diagnostic tool relied upon heavily by oceanographers, the geostrophic balance, no longer holds. In addition, the surface equatorial circulation is highly variable and many realizations of the flow are necessary in order to determine a statistically significant mean field to which steady state balances may be safely applied.

In the study to follow, the issue cross-equatorial exchange in the Pacific ocean will be explored by attempting to directly measure the mean circulation field, and thus identify the pathways of cross-equatorial flow. First, we explore the theoretical issues associated with flow across the equator and then review the evidence for such flow in the Pacific Ocean.

1.1 Dynamical Considerations

As pointed out by Killworth (1991), how fluid crosses the equator has long perplexed oceanographers and meteorologists. Linear inviscid theory, so useful in accounting for flow in the subtropics breaks down at the equator due to the change in sign of the Coriolis parameter. In a region of the ocean away from sources and sinks of momentum and buoyancy, Ertel's potential vorticity is conserved along streamlines, and is well approximated by its vertical component:

$$-g\,(\zeta + f)\,\frac{\partial \rho}{\partial z} \tag{1}$$

where g is the gravitational potential, f the Coriolis parameter, ρ the *in situ* density, z the vertical co-ordinate and ζ the vertical component of the relative vorticity. As a water parcel approaches the equator, the decrease in $|f|$ must be compensated in either a change in the stratification or an increase in the size of the relative vorticity. Since $\partial\rho/\partial z$ is constrained to be positive for stability, relative vorticity must play an essential role in any inviscid theory of flow across the equator. Otherwise, the conservation of potential vorticity requires strong

forcing or dissipation to allow flow to cross the equator.

Inspired by the observations of western boundary currents crossing the equator in both the atmosphere and ocean, most studies of cross-equatorial flow analyze the problem of a boundary jet approaching the equator. Anderson (1976) demonstrates that in the linear inviscid case, no steady solution exists. In the inviscid case, a free jet approaching the equator behaves much the same as one in the subtropics. Anderson and Moore (1979) find that as the jet travels northwards, say, its thickness decreases and velocity intensifies as both stretching and relative vorticity compensate for the decrease in $|f|$. At some latitude, separation from the boundary occurs and the boundary current enters the interior as a free zonal jet. The distance of penetration into the opposite hemisphere is dependent on the initial configuration which sets the potential vorticity of the jet. In general, then, inertial effects can allow fluid to cross the equator in a boundary current. Special cases can be found where equatorial blocking occurs. Nof (1990) demonstrates that when the jet is bounded by an offshore front, it can never cross the equator, and instead detaches from the boundary as an equatorial jet.

Where non-linear effects are precluded, friction becomes essential for cross-equatorial flow. Kawase (1987) examined the basin-wide set up in an active bottom layer model due to a single localized fluid source in the northern hemisphere. His system was linear and contained two kinds of damping: horizontal viscosity and a damping term in the continuity equation. The latter both detrains fluid from the layer and acts to damp pressure anomalies. In the cases examined by Kawase, the injected fluid flows along the characteristics of Kelvin waves: an equatorward western boundary current forms, which then detaches at the equator and flows eastward to feed poleward boundary flow in both hemispheres. The size of the pressure damping term determines the nature of the steady flow by controlling the effect of Rossby waves. For high damping the equatorial and poleward flows are narrow and jet-like, while for low damping Rossby waves have extended the flow perturbation into the interior to form the Stommel-Arons (1960) solution. In the latter case the western boundary current extends southwards across the equator to feed the interior flow in the southern hemisphere. Anderson (1976) drove a linear boundary current across the equator by placing a localized source and sink region on either side, suggesting that the distribution of the fluid sources and sinks determines whether the boundary current will cross the equator. Interior cross-equatorial flow did not occur in either Anderson's or Kawase's study.

Using a higher resolution and fully non-linear numerical model, Kawase *et al.* (1992) examined in detail the dynamics of the boundary current's approach to the equator. Their calculation demonstrated that, in the steady limit, the boundary current flows directly across the equator, balancing planetary vorticity changes with lateral dissipation. Though an eastward equatorial jet is initially set up as in Kawase (1987), it is not steady under the weaker frictional regime in the Kawase *et al.* (1992) model, and the equatorially trapped flow eventually disappears.

Killworth (1991) sheds light on the problem of interior cross-equatorial flow, by examining the geostrophic adjustment of a front near the equator. For an zonally infinite ocean, he demonstrates that fluid can only cross a distance of at most two Rossby deformation radii and still preserve its potential vorticity. In the case where meridional boundaries exist, the western boundary current provides a mechanism for modifying the potential vorticity of the fluid, and becomes the dominant pathway for cross-equatorial flow, once the basin wide front has come close to adjustment. Hence steady *interior* cross-equatorial flow does not seem likely, and both Killworth's (1991) and Kawase *et al.*'s (1992) studies point to the western boundary current as the dominant pathway significant steady cross-equatorial flow.

An alternative mechanism was put forward by Joyce (1988). He demonstrates that a modified Sverdrup relation governs the meridional velocity at the equator. At any point, both pressure and stress torques can drive flow across the equator. In the upper ocean wind-stress curl is responsible for flow across the equator. This pathway proves important in the observed circulation.

1.2 Observational Background

Studies of water properties suggest that cross-equatorial exchange does occur in the Pacific, possibly at all depths. In the following the evidence is discussed for the upper, intermediate and deep water masses, following the historical separation of studies of different parts of the water column.

1.2.1Upper-waters

The upper waters of the tropical Pacific contain a shallow, energetic and complex set of predominantly zonal currents, which vary substantially both spatially and temporally (Wyrtki, 1967; Wyrtki and Kilonsky, 1982). A schematic of the mean upper ocean currents as they

would appear in an equatorial cross-section is presented for reference along with their abbreviations to be used in the thesis (Figure 1.1).

Tsuchiya (1968) used property distributions derived from historical data to deduce the source waters of these currents. Both the North Equatorial Current (NEC) and South Equatorial Current (SEC) are manifestations of the equatorward boundary of the large Pacific subtropical gyres, and they derive much of their water from the gyre interiors, and so carry predominantly subtropical water masses. Upon arriving at the western boundary of the Pacific Ocean the westward NEC and SEC bifurcate, with part of the flow returning poleward in the beginnings of the western boundary currents (East Australia Current in the southern hemisphere and the Kuroshio in the northern hemisphere), and part turning equatorward to eventually feed the eastward equatorial currents: the North Equatorial Countercurrent (NECC); Equatorial Under Current (EUC) and sub-surface counter-currents. Tsuchiya (1968) and Reid (1965) conclude that the NECC is partially fed by water from the southern hemisphere based on high values of oxygen and low values of phosphate observed in the current in the far west. Similarly, in the far west the EUC is also deduced to be fed by southern hemisphere waters evidenced by a high salinity and oxygen signature that can be traced across the breadth of the Pacific in the core of the current (Tsuchiya, 1968; Lukas, 1986). Using recent high-resolution data sets from the western tropical Pacific, Lindstrom *et al.* (1987) and Toole *et al.* (1988) also attributed some southern origins to waters of the NECC and EUC.

As the EUC flows eastward, it rises along the sloping thermocline, bringing an admixture of cool waters from both northern and southern hemisphere close to the surface (Bryden and Brady, 1985). What becomes of this water at the terminus of the EUC at the eastern boundary was examined by Lukas (1986). He described a complex circulation with part of the EUC waters recirculating into the SEC (westward) and part flowing south from the equator to supply the Peru-Chile Undercurrent (PCUC), which continues southward along the South American coast, beneath the zone of active coastal upwelling.

Fine (1985) and Fine *et al.* (1987) describe the distribution of bomb-produced tritium in the upper Pacific and deduce cross-equatorial fluxes. Atmospheric thermonuclear bomb tests in the 1960's, enriched high latitude surface waters in the northern hemisphere with tritium. These waters have subsequently appeared in mid-thermocline layers of the subtropical gyre of the North Pacific and a tritium maximum is seen spreading across the equator along den-

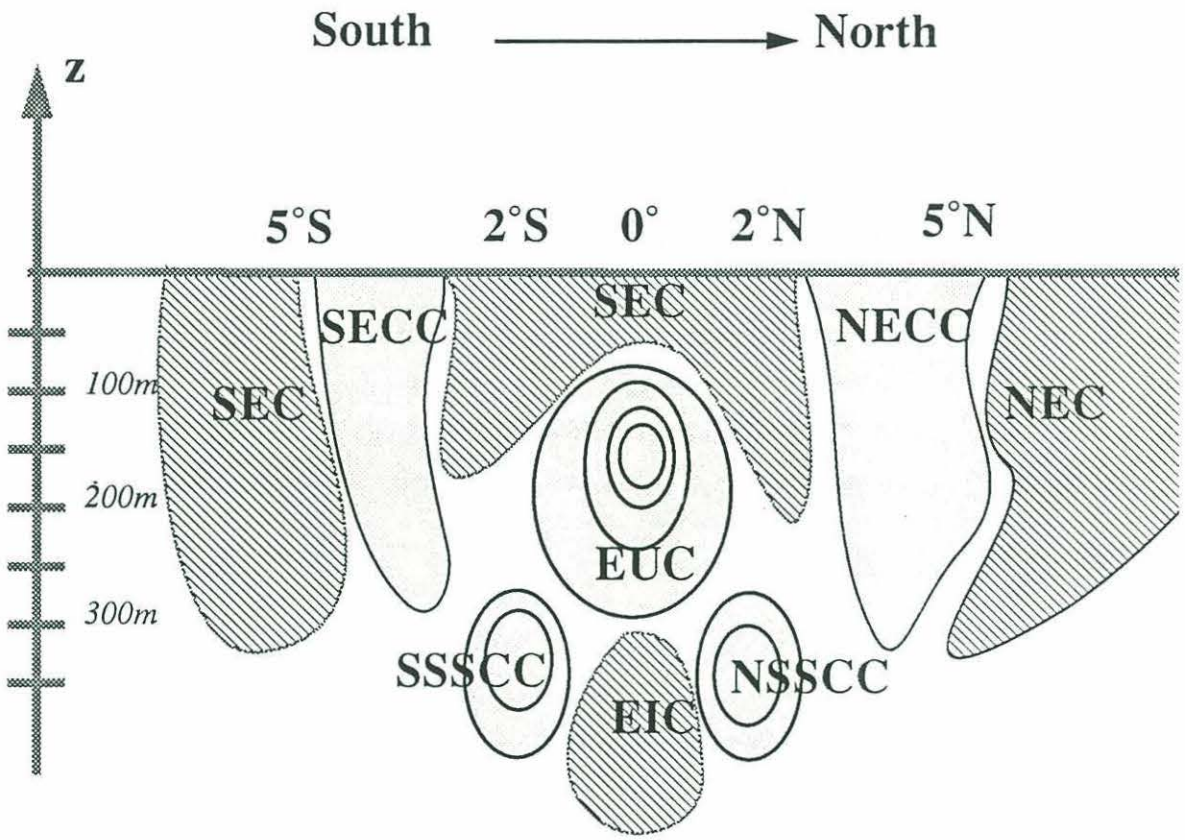

Figure 1.1 Schematic of spatial relation between the major upper ocean equatorial currents. Abbreviations stand for: SEC = South Equatorial Current; SECC = South Equatorial Counter Current; NECC = North Equatorial Counter Current; EUC = Equatorial Under Current; SSSCC and NSSCC = Southern and Northern Subsurface Counter Currents; EIC = Equatorial Intermediate Current. All flow is eastward except where hatched.

sity surfaces at the level of the EUC. As Fine *et al.* (1987) discuss, the cores of the major equatorial currents are tagged by anomalies of tritium indicating their source waters. For example, the NECC and EUC have high tritium signatures suggesting rapid communication with the high latitude North Pacific surface waters via the ventilated layers in the subtropical gyre. Hence these currents contain a mixture of waters of both hemispheres. The SEC is low in tritium, suggesting that it is fed by tritium poor southern hemisphere surface waters. As noted by Fine and co-workers, quantifying the mixing and advection rates using the tritium fields remains problematic due to the unknown rate of tritium input into the oceanic surface, which is strongly time-dependent.

The property fields suggest direct cross-equatorial exchange of thermocline waters in boundary current: northward flow along the northern coast of Papua New Guinea; and southward flow along the eastern oceanic boundary (Tsuchiya, 1968). Mixing across the equator is suggested by the continuous change in properties of the water masses flowing in the EUC and NECC, though it is difficult to distinguish this from the effects of vertical mixing and horizontal entrainment. The intriguing tritium distributions provide further insight to the processes at work. Though analyses of the property fields indicate the direction of fluxes, they have not easily lead to estimates of the sizes of the cross-equatorial exchange.

1.2.2 Intermediate Waters

The dominant features in the Pacific intermediate waters are two tongues of fresh water which lie below the warm salty tropical waters in the thermocline. In the South Pacific, the low salinity tongue originates from the subduction of fresh waters in high latitudes (40°S - 60°S), and their advection into the deep layers of the wind-driven subtropical gyre. The core of the tongue penetrates to approximately 900m beneath the bowl of the South Pacific thermocline. Unlike its southern counterpart, the fresh tongue of North Pacific Intermediate Water cannot be traced to surface formation and its source is still controversial. Talley (1991) argues that dense outflows from the Okhotsk Sea can account for the salinity minimum. Being significantly fresher and less dense than the South Pacific fresh intermediate tongue, the northern feature only reaches depths of 600m in mid-latitudes and then rises towards the equator, shoaling to 200m at 10°N.

There are strong property contrasts between the north and south Pacific intermediate waters. The North Pacific intermediate water is rich in nutrients (phosphate, silicate and alkalinity) and poor in oxygen. In comparison, in the South Pacific, the intermediate water

is high in oxygen, and relatively low in nutrients. In the water mass below the fresh tongues (North Pacific Deep Water), distributions as described by Reid (1965) suggest a southward flow of intermediate water across the equator in the basin interior accounting for a tongue of high phosphate water with a core at 2000m which protrudes southward across the equator. In the horizontal plane, property distributions suggest northward flow along the northern coastline of Papua New Guinea (PNG) and southward flow along the Pacific's eastern boundary. Reid (1986), in a circulation scheme for the South Pacific based upon properties and geostrophic shear fields, found North Pacific influence at all deep levels below the fresh mid-level tongue, and inferred inflow from the north along the coast of the Americas. It is not clear whether tracers, such as phosphate and oxygen can be truly passive below the highly biologically productive areas along the equator and in the eastern Pacific. In contrast to the nutrients, salinity is horizontally nearly homogeneous in the intermediate waters between 10°N and 10°S.

As for the upper waters, property distributions indicate that cross-equatorial exchange occurs at intermediate levels in the Pacific Ocean and that flow is mainly from north to south. However, these ideas have been difficult to test and quantify.

1.2.3 Deep Waters

Cross-equatorial flow is a key component of existing ideas about the abyssal circulation in the Pacific ocean. No deep water is observed to form in the North Pacific, and so the existence of the cold water masses below the locally formed intermediate waters can only be accounted for by a flux of Lower Circumpolar Water (LCPW) from the Southern Ocean. North Pacific Deep Water (NPDW) has a salinity between the very fresh overlying North Pacific Intermediate Water (NPIW) and the deep water source in the south, the LCPW. Hence one can infer a balance in the north between the advection of salty LCPW and mixing of fresh water from the overlying intermediate waters.

In accord with the theory of Stommel and Arons (1960), deep western boundary currents of modified LCPW have been identified in both the south and north Pacific as summarized by Warren (1981). In the South Pacific the deep western boundary currents are tagged by distinct property anomalies identifying the source waters of the flow (fresh and coldest for the Antarctic Bottom Water (AABW) and saline and next coldest for NADW). Though deep western boundary currents are evident in the deep shear fields in the North Pacific, no clear property anomalies are discernible. Zonal property gradients in the deep North Pacific

basins are consistent with waters of most recent southern origin entering as western boundary currents. The calculations of Taft *et al.* (1991) and Johnson and Toole (1993), have demonstrated that the 10°N and 14°S hydrographic data have allowed consistent estimates of the northward flow of modified LCPW in the deep western boundary currents of the Pacific basins.

1.3 The Pacific-Indian Throughflow.

The possibility of significant flow of Pacific water through the Indonesian Archipelago adds a further dimension to the question of cross-equatorial exchange. Since the passages are north of the equator and the North Pacific nearly closed off, any net transfer of water to the Indian Ocean must be supplied by a net northward cross-equatorial flow, originating in the Southern Ocean.

Evidence for a Pacific-Indian throughflow (hereafter called the Throughflow) has been summarized by Gordon (1986). As he notes, estimates range from 2 to 18 Sv. Based on the dynamic height gradient between the Pacific and Indian Ocean Wyrtki (1987) argues that the Throughflow must be largely confined to the upper 200-300m. Gordon (1986) argues the Throughflow is an essential part of the global thermohaline circulation providing a pathway for warm North Pacific thermocline waters to replenish the surface waters of the North Atlantic removed in the formation of North Atlantic Deep Water (NADW). A more recent demonstration of the importance of the Throughflow for the global circulation can be found in Godfrey (1989). He applies Sverdrup dynamics to the world ocean (driven by climatological winds) and explicitly accounts for the circulation around islands. In this way the dynamic height field maintained by the Sverdrup dynamics is calculated in a consistent manner from basin to basin. By disallowing a Throughflow, Godfrey found that the total dynamic height of the Indian Ocean dropped an amount equivalent to cooling the upper 500m by 6°C. Furthermore the model dynamic heights and observed relative dynamic heights cease to agree within the estimated errors, upon the closure of the Indonesian passages. Godfrey's estimate of the Throughflow is 16.4 Sv.

Fine (1985) calculated the size of the Throughflow using a tritium budget for the Indian Ocean. High tritium concentrations observed in the tropical Indian Ocean can only be accounted for by inflow of tritium rich North Pacific thermocline waters through the Indonesian Seas. Fine's estimates range between 2.0 and 13.4 Sv of Throughflow. In summary,

the existence of the Throughflow is corroborated by a variety of independent methods, though its size is still controversial, and more importantly, how it is supplied.

The implications of a large Throughflow for the heat and salt budgets of the Pacific Ocean may be substantial. Talley (1984) summarized all estimates of meridional heat transport in the Pacific Ocean, both direct and indirect. Indirect methods based upon estimating air-sea fluxes can contain large biases, which when integrated over the vast areas of the Pacific ocean, become larger than the heat fluxes themselves. It is not possible to determine even the sign of the heat flux across the equator using these methods. The direct estimates of heat flux in the South Pacific (all of which neglect the Throughflow) appear much smaller than those predicted by the air-sea fluxes. Talley estimates that the divergence of heat due to a warm Throughflow and cold return flow (via the ACC) can be as large as 0.5 PW northward, large enough to allow agreement between the direct and indirect methods in the South Pacific. Joyce (1988) estimated the meridional heat flux across the equator based on simplified dynamics which relate meridional velocity to wind stress and dynamic height gradients. His cross-equatorial heat flux ranges between 0.5 - 1.1 PW northward, while the range for the indirect estimates is 0.2 to 1.4 PW southward. In this case, taking the Throughflow into account only increases the discrepancy.

1.4 Approach and Major Findings

Before we can approach the topic of cross-equatorial exchange we first need to determine the mean circulation in the Equatorial Pacific. This is made possible by the recent acquisition of two coast to coast, top to bottom hydrographic sections at roughly $\pm 10^{\circ}$ in the tropical Pacific. These sections 'box in' the equatorial boundary layer, and the Indonesian passages through which the Throughflow is deduced to occur. Supplementing these surveys, are multiple meridional sections at 165°E and 150°W. Altogether three oceanic volumes are enclosed. At 150°W, the meridional sections are confined to the upper 1000m and are only used to analyze the thermocline flow. An inverse calculation that explicitly allows for cross-isopycnal exchange in a physically consistent manner is used to find circulation that conserves both volume and buoyancy.

The structure of the thesis reflects the strategy of breaking the problem into parts that can be independently studied: each section is described separately, and the flow across it determined, either from direct measurements where available or based upon the water mass dis-

tribution. The data are then synthesized into a mass budget for the Equatorial Pacific using the inverse model.

It will be shown that cross-equatorial flow occurs at all depths:

- near the ocean floor, LCPW flows directly across the equator in the deepest part of a deep western boundary current, while the upper part of the boundary currents in the North Pacific are fed by upwelled and recirculated waters from the North Pacific.

- the northward flux of dense LCPW from Antarctica returns below the thermocline as NPDW that is associated with a broad mid-depth silica maxima observed in both the North and South Pacific Ocean. The flow at mid-depth is not in a narrow western intensified current, and is instead a broad interior flow to the south.

- in the thermocline, southern hemisphere waters penetrate to about 5°N, but are eventually entrained into the eastward flowing equatorial currents which terminate in the upwelling system in the eastern Pacific. These eastward currents deliver their cargo of subtropical waters to the mixed layer where it is transformed to surface water. Most of the newly formed equatorial surface water first flows south in the eastern Pacific, then west in the SEC before leaving the equatorial region. A surface clockwise gyre is deduced at the equator with southward flow in the east and northward flow in the west. This gyre appears to be wind-driven.

the Throughflow is deduced to be of modest size (0-8 Sv = 1x $10^6 m^3 s^{-1}$) and must be supplied by thermocline waters from the southern hemisphere. The major pathway for the cross-equatorial flow that supplies the Throughflow must be accomplished via the entrainment of SEC waters into the equatorial upwelling system and their conversion to surface waters in the eastern Pacific. This surface water eventually crosses the equator in the wind-driven northward flow in the western Pacific, joins the northward Ekman drift and eventually is subducted into the North Pacific subtropical gyre. Below the surface, the Throughflow water is advected westward in the NEC and upon reaching the western boundary flows south in the Mindanao Current which feeds the Throughflow. This pathway is consistent with the conservation of potential vorticity since flow across the equator only occurs in the directly wind-driven surface layer. The pathway also accounts for the tracer characteristics of the Throughflow, which are predominantly of the North Pacific subtropical gyre.

Chapter 2

Observations along 10°N

2.1 Introduction

Calculations of the Sverdrup flow based on observed winds show that the boundary between the subtropical and equatorial circulation in the North Pacific occurs near the latitude of 10°N (Landsteiner, *et al.*, 1990). The flow across 10°N is a therefore a useful indicator of the exchange between the northern subtropical and the equatorial ocean.

Two data sets are utilized to study the flow across 10°N: a one-time survey that spans the breadth of the basin and a series of repeat surveys of the western boundary current at 8°N. The latter are shown to be essential to our goal of analyzing the mean flow. The variability along the western boundary is large and the boundary flow measured in the one-time transpacific section was not characteristic of the mean.

In this chapter, the data along 10°N are presented and the location of the major water masses described. The geostrophic flow across the section is also calculated. In the western boundary current, direct velocity measurements aid in determining the mean transport. Across the rest of the section we rely on the property distributions to guide in choosing reference levels, mainly following the analysis of the bottom and deep waters by Johnson and Toole (1993).

2.2 A Transpacific Hydrographic Section at 10°N

2.2.1Data

A transpacific section was made along a nominal latitude 9.5°N in the months of February through May, 1989 from on board the RV *Moana Wave* (EPIC Voyageurs, 1991). The section begins at 8°N at the coast of Mindanao in the Philippines and extends out to 130°E at this latitude before angling northeast to reach the nominal latitude of 9.5°N at 145°E. From here the ship steamed east to Costa Rica taking 221 full depth CTD/O_2 casts with nutrient samples. The station spacing was 90km over the gently sloping abyssal plains and was decreased to as little as 10km over sharply changing topography and near boundaries (Figure 2.1). The cruise was broken into four legs, and here we only use the data taken on three:

designated MW89-3, 4 and 6 for the ship name, the year and the leg number respectively. The transpacific section was interrupted for 9 days for a Hawaii Ocean Time Series station, which took nine days and constitutes the missing leg: MW89-5. These data are not considered here. The total transpacific section consisting of legs 3, 4 and 6 will be hereafter referred to as the MW893 data set.

A ship-mounted ADCP recorded ship-relative currents in the upper 300m or so of the water column for the entirety of the cruise (see data report). Except near the western boundary at 8°N, the ship was steaming into westward flow for most of the cruise, indicating that the data were taken in the NEC, north of the thermocline ridge that separates the NEC from the NECC. As measured by the ship's anemometer, the wind was fairly steady during the cruise, blowing westsouthwest at about 8m/s. These conditions are normal for the time of year of the cruise, which was during the time of maximum strength of the Trade Winds.

At each station, CTD salinity, temperature, pressure and dissolved oxygen were continuously recorded, and bottle samples taken at various depths in order to calibrate the CTD data. The data and its processing are described in the data report by the EPIC Voyageurs, (1991). Bottle/CTD salinity and oxygen differences are better than ±0.005 p.s.u. and 0.06 ml/l respectively. CTD temperature and pressure have accuracies of ±0.005°C and ±3db respectively. In addition the following nutrients were measured from the bottle samples: phosphate, nitrate/nitrite and silica to better than 1%. Both chlorofluorocarbon and helium isotopes and tritium measurements were also made at a subset of the stations. These data will not be discussed here.

2.2.2 Water Mass Distribution

The density structure and distribution of the water masses along MW893 will be described, starting in the mixed layer and working down.

Surface and Thermocline Waters

Characteristic of the low-latitude Pacific, the upper 500m can be divided into 3 regions: a layer of low temperature and salinity gradients extending from the surface to as much as 100m which we loosely call the surface layer; a sharp thermocline where temperature changes from 28°C to around 12°C in a vertical interval of order 100m; and a region of lower stratification below(Figure 2.2).

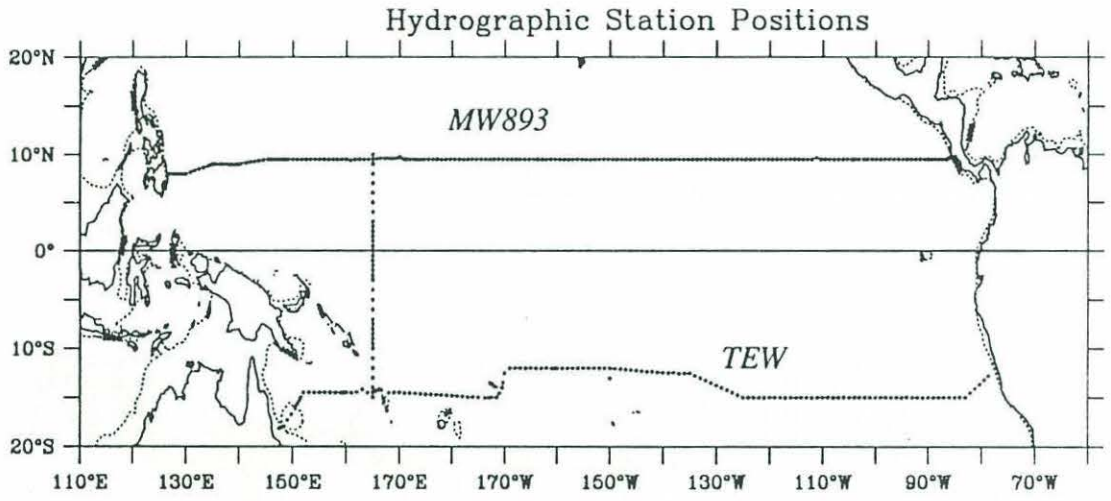

Figure 2.1 Station positions for the hydrographic sections used in the analysis. At 165°E the station positions are for the repeat cruises.

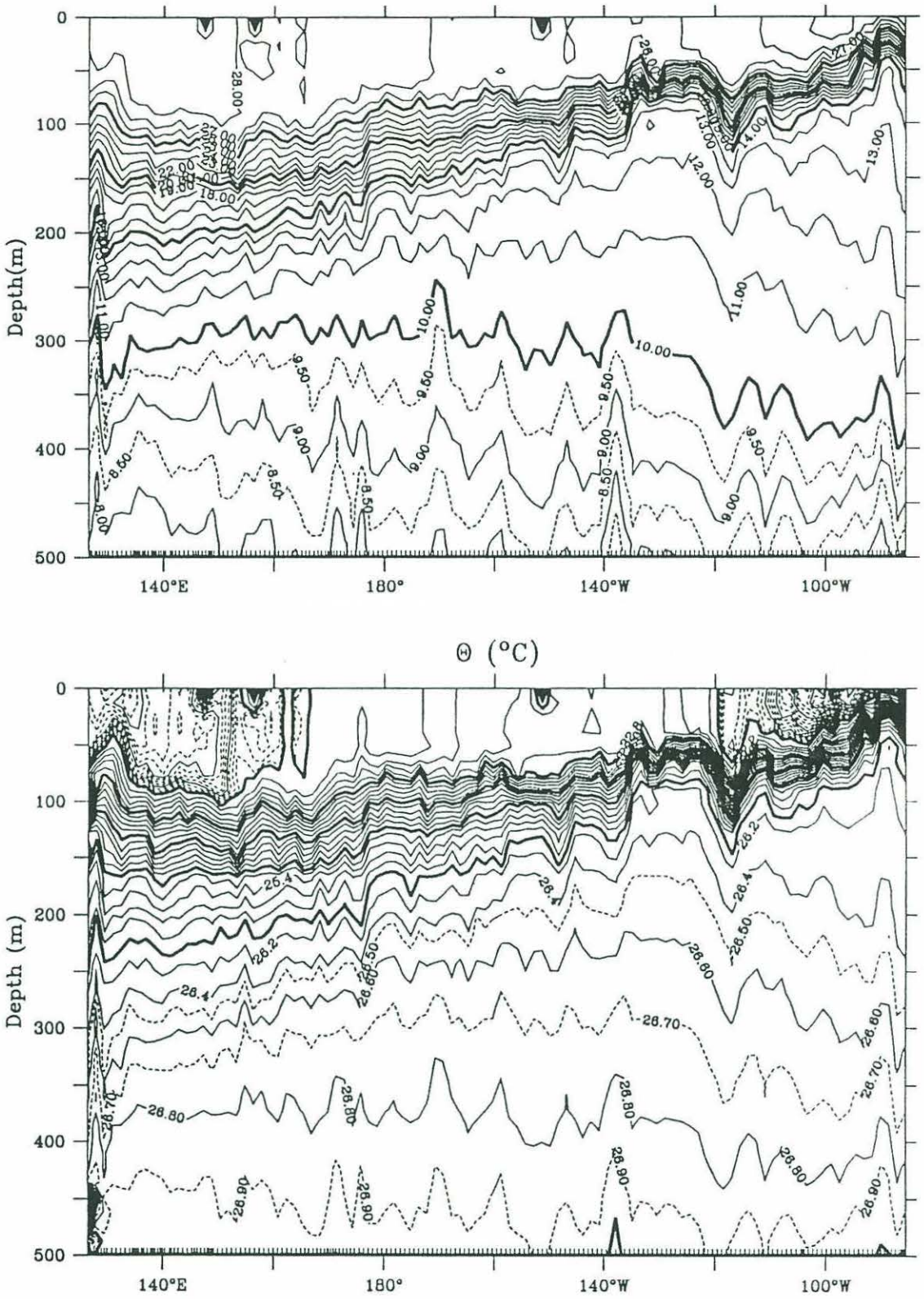

Figure 2.2 Properties along 9.5°N in the upper 600m: (a) potential temperature; (b) potential density. Opposite page: (c) salinity and (d) dissolved oxygen concentration

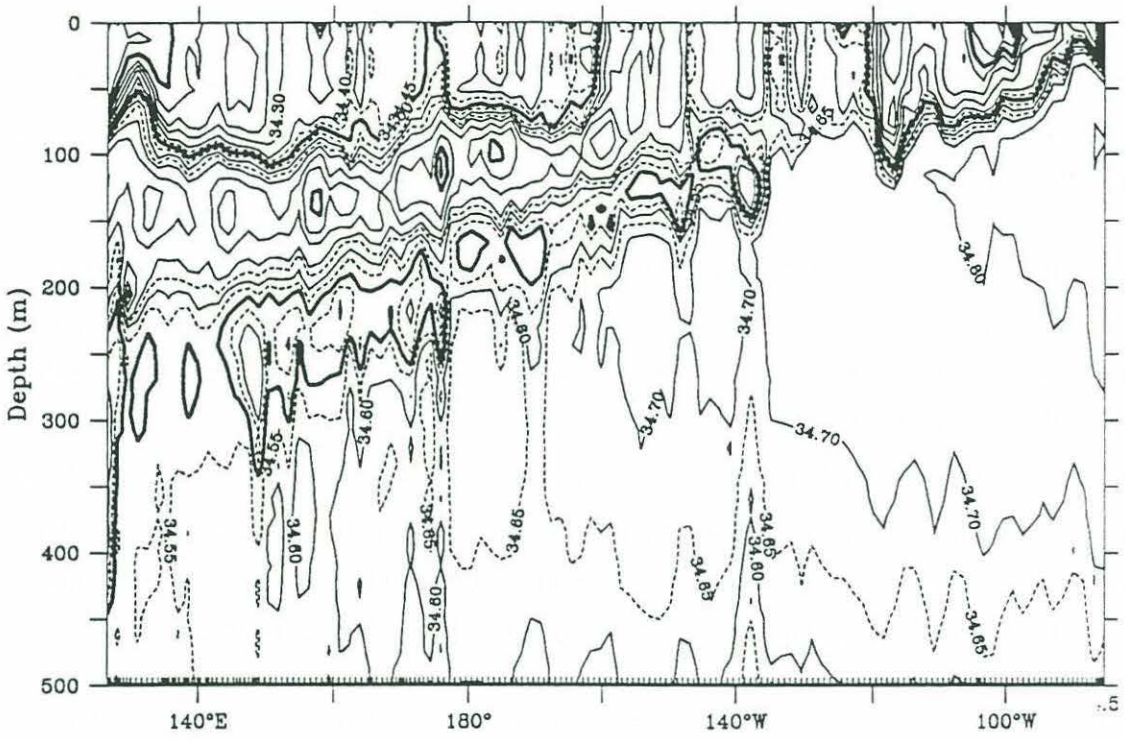

S (p.s.u)

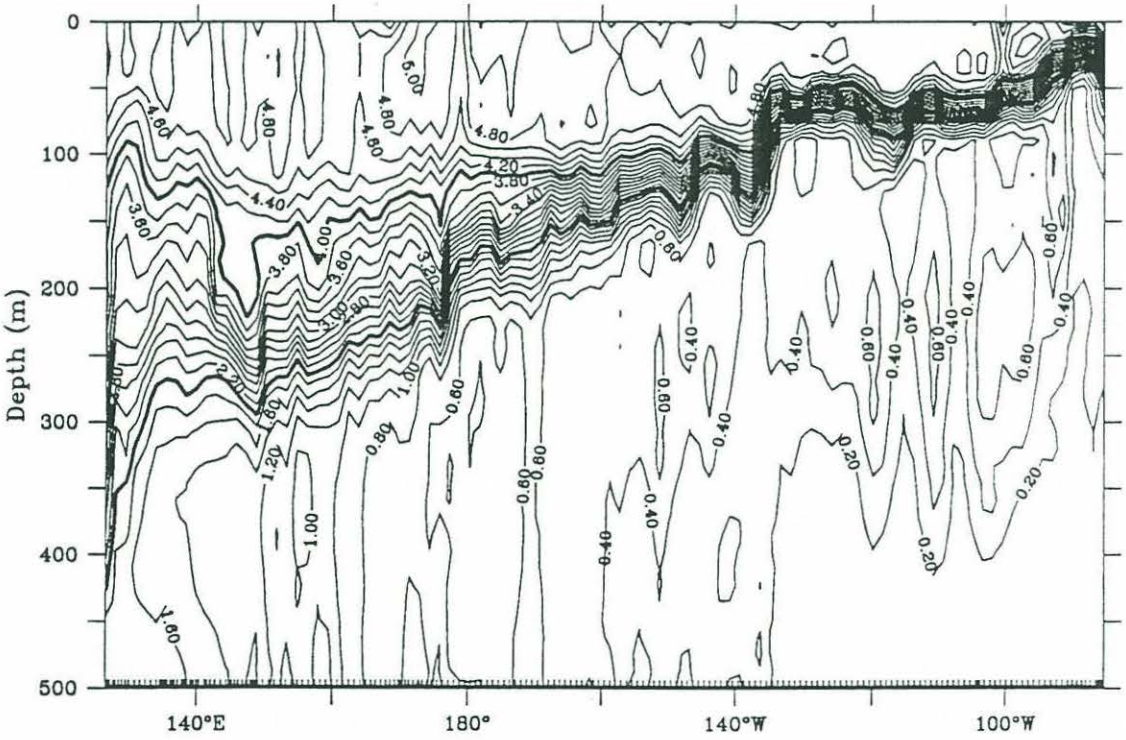

Oxygen(ml/l)

The surface layer deepens westward, its base determined by the top of the thermocline. Along most of the section salinity in the mixed layer is lower than in the thermocline, forming a cap of fresh warm water. Around 150°W in the central part of the basin, however, the near surface salinity does not contrast with that in the thermocline, though temperature and oxygen values indicate that a distinct surface layer is still present.

Isopycnals between $23.0 < \sigma_\Theta < 26.2$ are tightly bunched within a few hundred meters below the surface layer and form the shallow thermocline. The thermocline tilts down to the west and thickens from 50m at the eastern end of the section to 200m along the Philippines. Well below the thermocline at about 500m, isopycnals do not feature a broad scale tilt, and lie fairly flat. In between, at $26.2 < \sigma_\Theta < 26.9$, density surfaces start at the base of the thermocline in the western part of the section and rise with it towards the east. These surfaces then peel away from the base of the thermocline to deepen again towards the eastern boundary, with the lighter surfaces peeling away last going eastwards.

Superimposed upon the large-scale tilt of the isotherms are large eddy-like disturbances that are generally coherent with depth below the thermocline and sometimes have signatures within the thermocline. The characteristic amplitudes of these eddy displacements are 50m and 100m in the 10°C and 5°C isotherm respectively.

Salinity in the thermocline forms a series of vertically stacked maxima and minima. Though the mixed layer in the west is relatively fresh (< 34.55 psu), it overlies the saltiest water along the section. North Pacific Tropical Water (NPTW) or Central Water forms a salinity maximum in the upper thermocline between 20 and 25°C. The NPTW is only present in part of the section, between the Philippines coast and about 150°W where it terminates in the surface layer. Within the NPTW layer, lateral salinity maxima appear in several patches through out the upper thermocline and are associated with the eddy structures mentioned above. Oxygen concentrations in the salinity maximum are high ~ 4.0 ml/l, though of course those in the surface layer are higher still.

Below the Tropical Water salinity maximum, in the lower part of the thermocline is a salinity minimum which moves to higher temperatures going eastward, and terminates at the surface at 140°W, just east of where the Tropical Water terminates. In contrast to the Tropical Water, the salinity minimum is associated with a very strong gradient in oxygen, which follows it to warmer isotherms eastward across the section. Tsuchiya (1968) mapped salin-

ity, oxygen and acceleration potential on selected potential density surfaces between 20°N and 20°S in the tropical Pacific. He identifies the salinity minimum below the Tropical Water as originating from the north eastern Pacific at the surface. This fresh cold water is then carried to the western low-latitudes by the California Current, and then the NEC in its circuit around the edge of the North Pacific subtropical gyre. For brevity, this shallow salinity minimum water shall be referred to as California Current Water (CCW).

East of 150°W, the thermocline is very thin, shallow, and has a different structure than in the western half of the section. There are no maxima or minima in either salinity or temperature in the eastern thermocline, and no evidence of either Tropical Water or CCW. Instead, the thermocline contains a mixture of the local surface waters which are high in oxygen and very low in salinity, and the subthermocline water, which is very low in oxygen and high in salinity. Hence the thermocline is not only an interval of very strong temperature gradients but also very large oxygen gradients.

The subthermocline water mass in the east forms a secondary salinity maximum across the section. Occupying the 14°C to 8°C range, the salinity maximum extends westward to undercut the CCW in the west. When plotted upon potential temperature surfaces, it is apparent that the salinity maximum water and the CCW occupy the same temperature classes, only at different longitudes. Where both coexist in the central part of the section, the CCW is in the warmer classes and the salinity maxima waters are in the colder classes. Though both water masses share the same temperature classes, they are quite distinct in that the CCW is within the thermocline and is flowing to the south from a high-latitude source, while the salinity maximum water is not in the thermocline. In fact, the eastern salinity maximum coincides with those isotherms that have peeled away from the thermocline and are deepening towards the east. Hence the salinity maximum water is associated with northward geostrophic shear. Though this water mass has not been named as far as the author knows, for brevity it shall be referred to as Eastern Equatorial Water (EEW) in this study.

Intermediate Water

At about 8°C, salinity becomes more horizontally uniform on temperature surfaces than above, though there exists a general tendency for salinity to increase eastwards throughout the intermediate and deep waters. Centered about the 6°C isotherm and 750m is a deep salinity minimum. In the minimum, salinities are fall below 34.53 near the western bound-

ary and in isolated patches out to 140°W (Figure 2.3). East of 140°W, the minimum moves to colder temperatures, from 6°C to 5°C near the coast of South America.

The oxygen distribution in the intermediate waters contrasts with that of salinity. Very low oxygen concentrations in the eastern longitudes associated with the EEW penetrate westward in the warmer classes above the salinity minimum, while higher oxygen values are found along the western boundary in the colder classes below the minimum and extend eastward along temperature surfaces. There is no oxygen extremum that corresponds to the salinity minimum. Tsuchiya (1968), Reid(1965) and Talley (1991) identify the intermediate salinity minimum in the North Pacific as originating from the north western subpolar gyre. Named by Reid (1965), North Pacific Intermediate Water (NPIW), the salinity minimum is seen in his sections spreading southward towards the equator from the north western North Pacific, with an associated oxygen minimum and nutrient maximum. Nitrate and phosphate along the 10°N section show a vertical maximum at about 6°C, further identifying the salinity minimum waters as NPIW. In the west, along the boundary, however, phosphate concentrations decrease in the minimum, and oxygen concentrations increase. Tsuchiya (1991) argues that this low phosphate, high oxygen intermediate water in the western equatorial Pacific is modified Antarctic Intermediate Water (AAIW) that flows across the equator, and then travels northward as far as 45°S along the western boundary. The AAIW signature in the MW893 data support Tsuchiya's hypothesis. Whether the flow is actually to the north will be examined below.

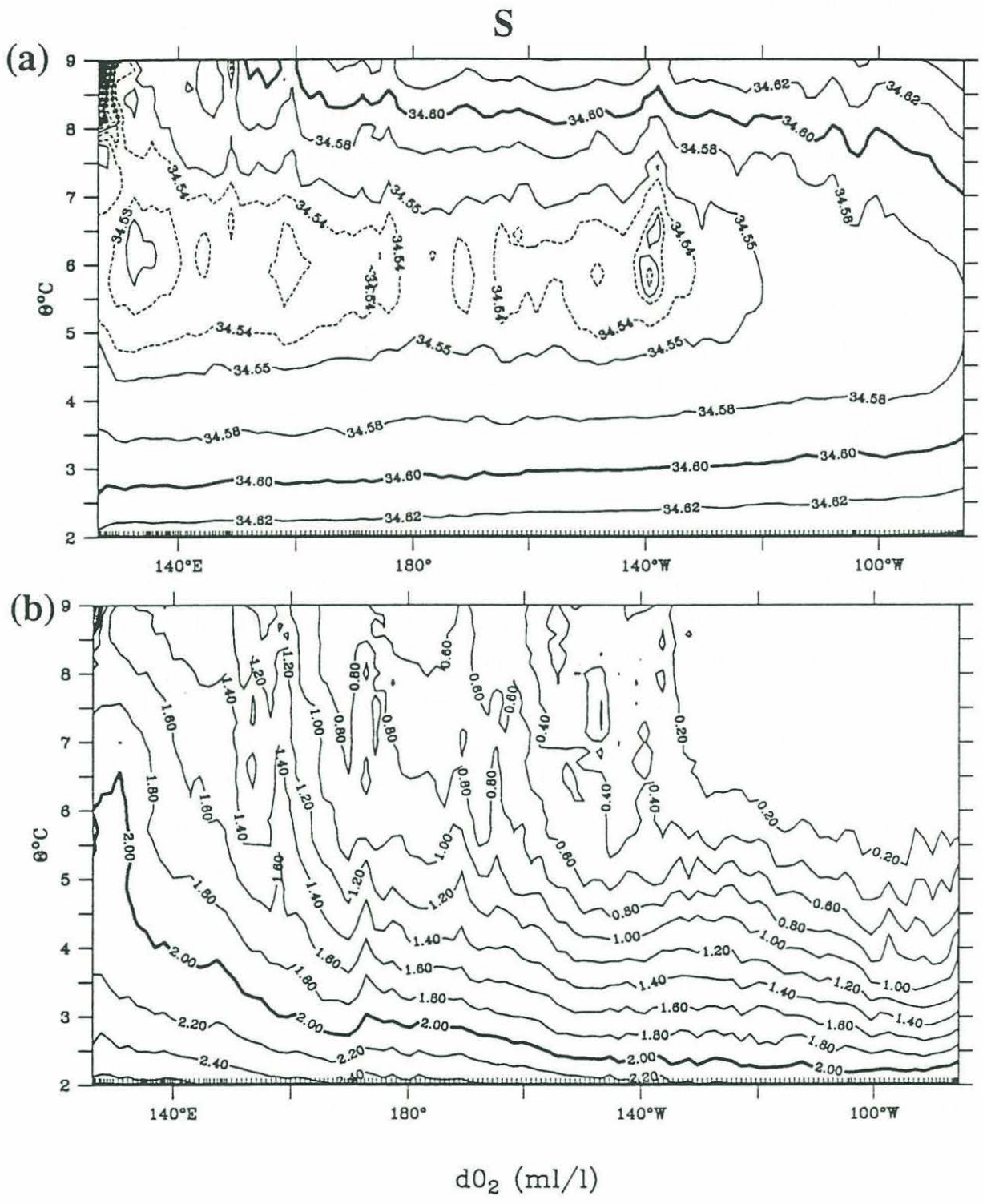

Figure 2.3 Properties on potential temperature surfaces in the intermediate waters along the 9.5°N section: (a) salinity and (b) oxygen.

Deep and Bottom Water

Surface waters in the high latitude North Pacific are very fresh and the associated halocline prevents winter-time convection from penetrating to any great depth (Warren, 1983). As a result the deep North Pacific is not ventilated locally as occurs in the North Atlantic and Southern Oceans. The densest waters in the North Pacific come from the south via the South Pacific.

A system of deep western boundary currents transport dense Lower Circumpolar Water (LCPW) to the North Pacific (Warren, 1981; Johnson and Toole, 1993). LCPW is a mixture of modified Antarctic Bottom Water (AABW) formed in the Weddell Sea and North Atlantic Deep Water (NADW) formed in the northern North Atlantic. Characteristics of the LCPW in the equatorial Pacific are relatively high oxygen and low silica concentrations and high salinity.

Above the LCPW is a water mass of large volume which occupies most of the North Pacific (Worthington, 1981): North Pacific Deep Water (NPDW). Thought to be the oldest deep water in the world's ocean, NPDW is the end-product of the slow warming and freshening of the inflowing LCPW in the vast North Pacific Ocean. The characteristics of NPDW consonant with the notion of its great age are: high dissolved silica concentrations acquired from long contact with sediments in the North East Pacific, and high concentrations of phosphate and nitrate with low oxygen concentrations due to oxidation of organic particulate matter in the water column. It is still not known whether the low oxygen and high nutrient layer in the deep South Pacific is formed *in situ* as assumed by Warren (1973) or is the result of advection from the north (Reid, 1973).Indications that the NPDW may penetrate across the equator can be found in the GEOSECS transects where a plume of high silica, nitrate and phosphate, and low oxygen water is found in the South Pacific at potential temperatures of 2°C. Circulation studies of the South Pacific generally confirm Reid's speculation, in that a net flow of deep water appears to flow southward across South Pacific sections (Wunsch, *et al*, 1982; McDonald, 1993).

Along 10°N, the isotherms below 1.3°C plunge into the bottom along the Marshall Islands in the Central Pacific Basin and along the Caroline Islands in the East Marianna Basin (Figure 2.4), associated with two separate deep western boundary currents (Johnson and Toole, 1993, hereafter JT). Over the East Pacific Rise the coldest isotherms also fall into the bot-

tom representing southward flow below a shallower reference layer.

JT chose the boundary between the LCPW and the NPDW to be the 1.2°C isotherm and the top of the NPDW at 2.0°C, defining the water mass boundaries. They estimated a net northward flow of $9.6 \times 10^9 kgs^{-1}$ of LCPW across the 10°N section, which compares well with transport estimates of deep western boundary currents in the South Pacific: $12.2 \times 10^9 kgs^{-1}$ at 14°S by Taft *et al.* (1991) and $20.0 \times 10^9 kgs^{-1}$ at 28°S and 43°S (Warren, 1973). These estimates are consonant with the Stommel-Arons dynamical model in which the deep-western boundary current is losing fluid to a poleward interior flow in the subtropics, as demonstrated by Johnson (1990).

Along the 10°N section the 'purest' NPDW properties are found in the east associated with a silica maximum centered at 1.5°C and 120°W. Deep water oxygen concentrations decrease and salinity increases eastward as is found in the NPIW layer. Part of the LCPW flowing northward in the deep western boundary current recirculates south along the East Pacific Rise below the water of highest silica. JT calculated that only 0.6 to $2.6 \times 10^9 kgs^{-1}$ of NPDW exits the North Pacific across 10°N.

Between the East Pacific Rise and the eastern Pacific boundary are a series of isolated or nearly isolated basins. Two are sampled by the transpacific data: the Guatemala Basin at 10°N and the Peru Basin at 14°S. Both are marked by low stratification, high salinity and low oxygen values on θ surfaces, when compared to the deep water in the central ventilated basins. These properties suggest that the waters of these basins are the result of slow warming by either downward heat diffusion or geothermal conduction.

Deep Circulation in the Philippines Basin

At depth in the Philippines Basin, oxygen levels increase to the bottom, as does salinity. Temperature surfaces are fairly level, indicative of weak geostrophic shear. The deep properties in the Philippines basin are almost homogeneous below 3700db, and contrast with those in neighboring West Carolina Basin, which vary linearly with depth. Uehara and Taira (1990) found a similar contrast. The high oxygen levels in the deep Philippines Basin are deduced to be sustained by the inflow of cold, saline bottom water along 10°N, at the Yap-Marianna Junction. According to the numerical model results of Kubota and Ono (1992),

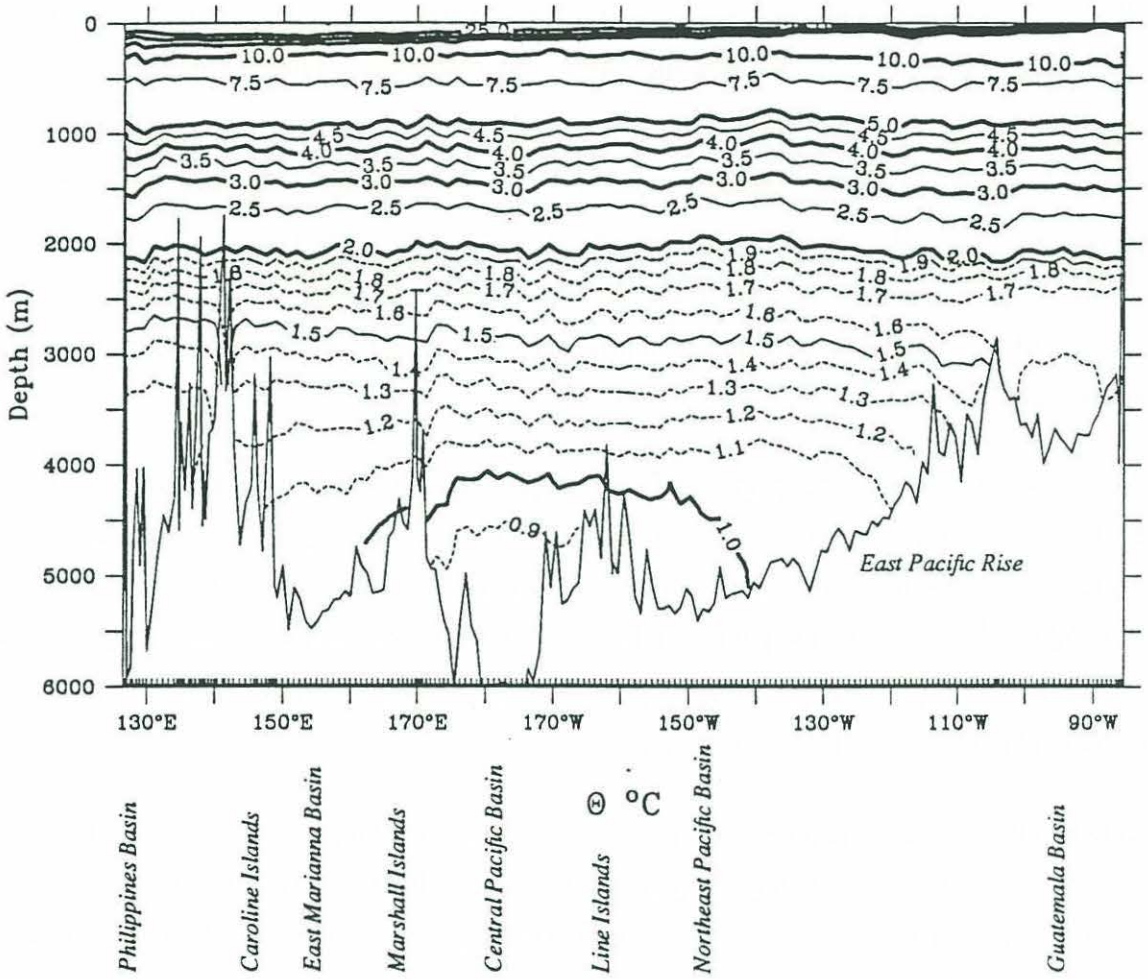

Figure 2.4 Properties in full depth along the 10°N MW893 section: (a) potential temperature; (b) salinity and (c) oxygen.

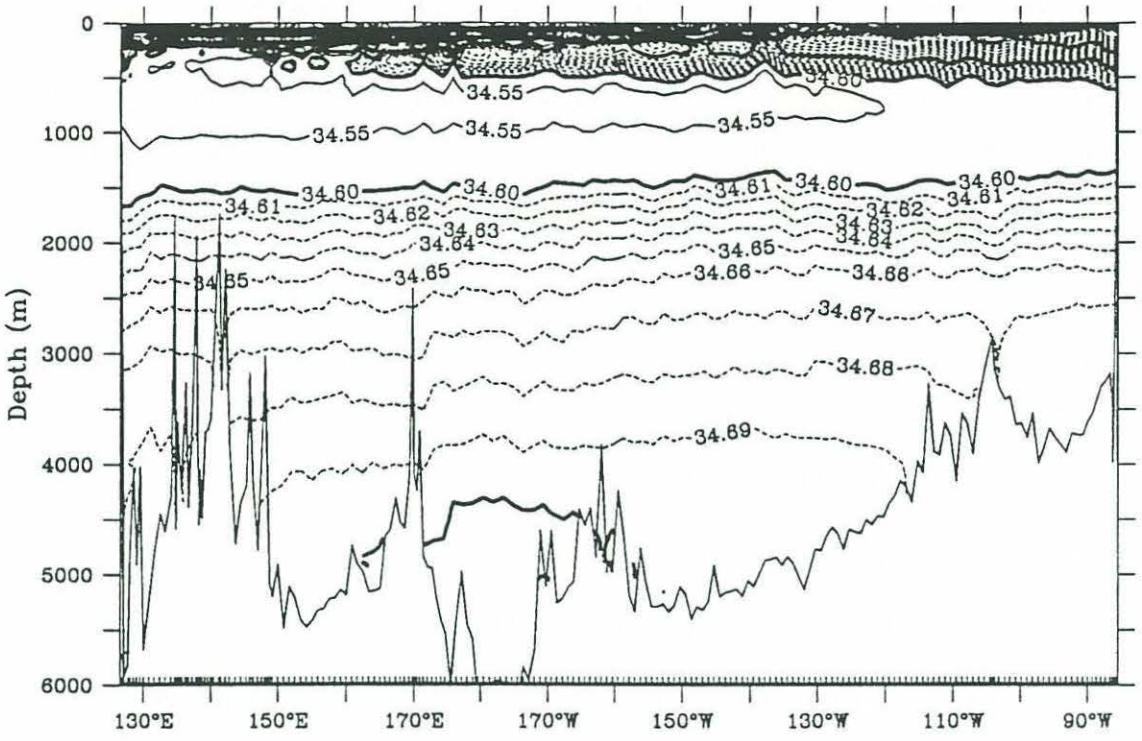
Depth (m)
0
1000
2000
3000
4000
5000
6000
130°E
150°E
170°E
170°W
150°W
130°W
110°W
90°W
34.55
34.60
34.61
34.62
34.63
34.64
34.65
34.66
34.67
34.68
34.69

S (p.s.u)

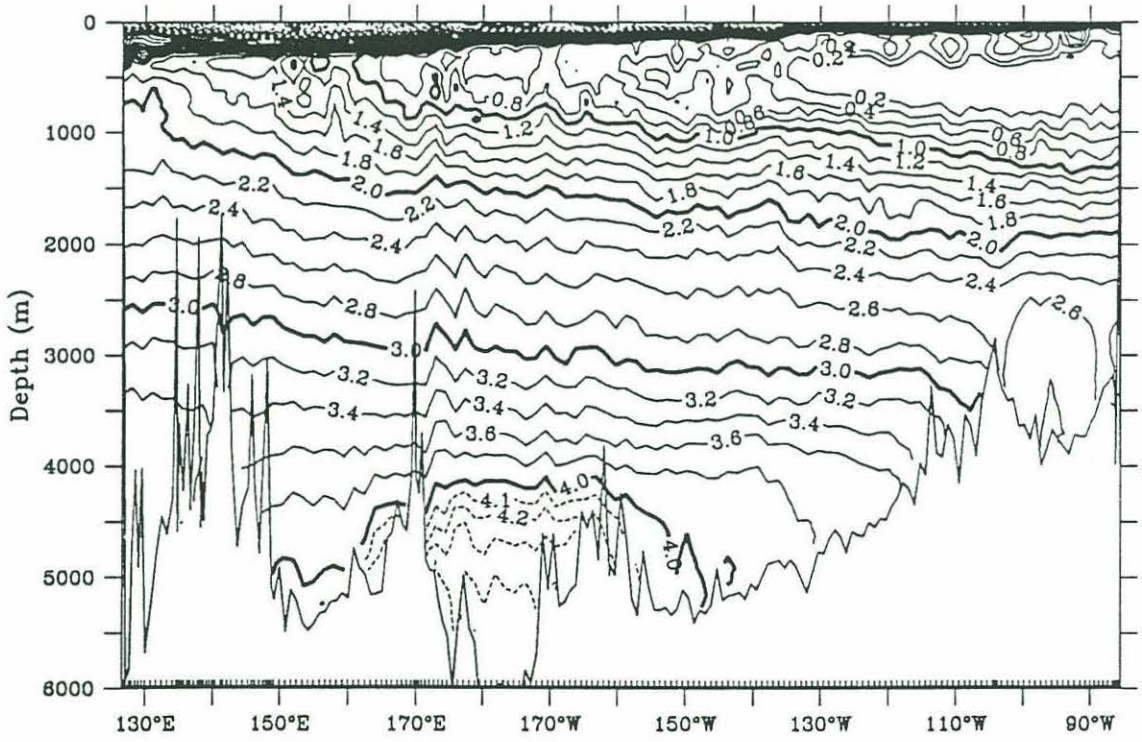
Depth (m)
0
1000
2000
3000
4000
5000
6000
130°E
150°E
170°E
170°W
150°W
130°W
110°W
90°W

dO_2 (ml/l)

the abyssal inflow forms a boundary current along the northern and western edges of the basin. A weak, broad western boundary current along the Philippines shelf slope sustains the deep water mass. According to these studies, the southern part of the Philippines Basin sampled by MW893 is relatively quiet and is at the farthermost point downstream from the inflow.

2.4.3 Reference Levels

Along the 10°N section the zero velocity surfaces that Johnson and Toole (1993) chose based upon their interpretation of the property fields are:

- θ=1.3°C (~3200 db) in the Philippines Basin
- θ=1.3°C (~3200 db) in the East Marianna Basin
- θ=1.4°C (~3000 db) in the Central Pacific Basin
- θ=1.65°C (~2500db) in the North Pacific Basin over the East Pacific Rise

These zero velocity surfaces are adopted here, though with some modification. In the Central Pacific Basin a reference level of 3000db results in the coldest bottom water moving southwards at depths below 5500db, counter to the sense of the source of LCPW. The shear associated with the deep western boundary current in the Central Pacific Basin is located on the western side of the basin with a width of about 600km banked up against the flank of the Marshall Islands. East of there the density surfaces flatten out, and then gently curve downwards towards the east. In order to have the coldest waters along the section moving north the zero velocity surface in the eastern part of the Central Pacific Basin was set to be the bottom.

Over the silica maximum water in the North East Pacific Basin, the reference level is raised another 700db to 1800db which is approximately the boundary between the intermediate and deep water as defined by JT. The effect of elevating the reference level here is to produce a greater southward flux of silica rich NPDW.

The transport derived from these reference levels will be discussed when the mass budget for the entire equatorial region is considered.

2.4.4 Summary

A transpacific section along 10°N has been presented. Water masses of subtropical origin occupy the thermocline: salty NPCW overlies fresher CCW. Below the thermocline, is a water mass associated with a salinity maximum and oxygen minimum, which we have dubbed Eastern Equatorial Water. Since EEW is not of subtropical or subpolar origin, it is likely formed *in situ* by mixing with salty southern hemisphere waters. Below the EEW and above the LCPW, water masses of northern origin dominate: NPIW and NPDW. One exception is the tracer signal of AAIW along the coast of the Philippines.

2.5 The Transport of the Mindanao Current from Repeat Surveys

2.5.5 Introduction

The Mindanao Current is a narrow boundary current that flows southwards along the coast of Philippines. Originating at the bifurcation of the North Equatorial Current at about 13°N (Nitani,1972) the Mindanao Current (hereafter, MC) is a pathway for waters from the North Pacific subtropical gyre to enter the equatorial circulation. Sverdrup calculations (Landesteiner, *et al.,* 1990) indicate that the MC closes the barotropic streamlines in a clockwise wind-driven gyre in which the NEC and NECC are the northern and southern limbs respectively. Thus the MC is a crucial element of the mass budget of the low-latitude Pacific.

The primary aim here is to determine the best possible estimate of the mean state and transport of the MC to aide in our analysis of the equatorial mass budget. Past observations have shown the MC to be highly variable in both structure and transport, making it difficult to establish a mean transport estimate. Toole *et al* (1990) observed a two fold change in the transport of the Mindanao Current at 8°N in a six month time interval, while similar changes have been observed on time scales of a few days (Cannon, 1970). In addition, the transport of the MC changes considerably in the north-south direction. Lukas et al (1991) observed that the transport above 300m increased from 13 SV at 10°N to 26 SV at 7°N.

2.5.6 Background

Water mass analyses indicate that the MC carries waters from the North Pacific subtropical thermocline (Nitani, 1972). The water mass signatures of the MC continue southward into the Celebes Sea suggesting that the MC is supplying the Pacific-Indian Throughflow (Lukas, *et al.* 1991, Piola and Gordon, 1983; Ffield and Gordon, 1992). Bingham (1993) deduces that the lower reaches of the MC carry NPIW into the Celebes Sea. At deeper depths, Tsuchiya (1991) associates higher oxygen and phosphate levels against the coast as an indicator of AAIW influence spreading northward, having crossed the equator to the south. The variability of the geostrophic velocity field has made it difficult to observe the mean flow (if any) that may be responsible for this tracer distribution.

Offshore of the MC, a northward counter flow in the thermocline is often observed and is referred to as the Mindanao Eddy. Nitani (1972) suggested that the eddy recirculates 15SV through the MC above 1200db. In the observations taken during the WEPOCS survey

(Lukas, *et al.* 1991), northward flow was also present offshore of the MC. However, Toole *et al.* (1991) did not observe a significant return flow in two surveys at 8°N: they found that the surface dynamic height (0/1000db) fell almost monotonically offshore at 8°N.

2.5.7 The Data

As part of the US/PRC-TOGA program, 7 surveys were made of the Mindanao Current near 8°N (Cook *et al.* 1990 and Lake *et al.* 1991). Five of the surveys extended out to 140°E (PRC 3,4,5,7,6 and 8), while one (PRC 7) ends at 130°E. PRC2 sampled the MC at 10°N, and extended out to 130°E. In addition, the one-time MW893 10°N section crosses the MC at 8°N, providing a eighth survey of the boundary current.

Between the Philippines coast and 130°E, the station positions of the US/PRC-TOGA surveys and the once-time section coincide (Figure 2.5). East of the 130°E, the station spacing in the US/PRC-TOGA grid widens to 2.5°, while the MW893 section traverses toward 10°N and maintains high resolution. The depths of the casts in deep water varied from section to section, though most were to at least 2000m, and many to reached to 4000m.

Averaging method

A mean section of the MC is constructed from the surveys that crossed the current at 8°N: PRC 3-8 and the MW893. The data taken at 10° along PRC 2 are left out since the WEPOCS survey suggested a strong meridional changes in transport. East of 130°E, the change in latitude of the MW893 data was ignored.

Several different averaging techniques were explored, involving both horizontal and vertical extrapolation. Horizontal extrapolation in the presence of strong isopycnal slopes proved to be problematic, and was therefore avoided by simply averaging the stations that fell on the repeat PRC survey grid. This, however, results in the exclusion of most of the closely spaced stations on the MW893 section offshore of 130°E.

It is becoming more apparent that averaging hydrographic data on pressure surfaces is also problematic (Gouriou and Toole, 1993). This is particularly true at low latitudes where the thin thermocline undergoes vertical excursions due to the internal wave field and eddies. Averaging such a field on pressure surfaces results in 'smearing' the thermocline properties in the vertical. To best preserve the structure of the MC, the data are vertically interpolated

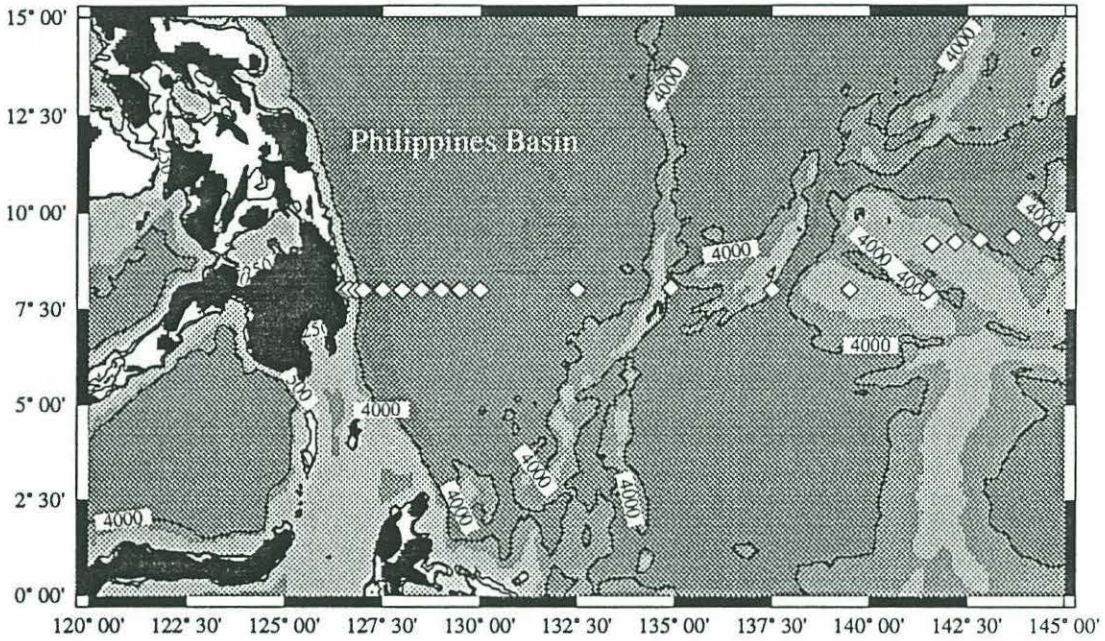

Figure 2.5 Positions of the hydrographic stations in the Philippines Sea for both the one-time transpacific section, MW893 (east of 141.5°E) and the repeat USPRC/ TOGA survey.

onto a set of potential density surfaces before averaging. Hence an average pressure, salinity and potential temperature are found for each density surface. The averaged properties were then interpolated back to a 10db uniform pressure series.

Close to the surface, potential density averaging is complicated by the occasional outcropping of density surfaces. We chose to find a mixed layer depth at each cast using the criteria of the first depth at which the density differed from that at the surface by $0.01 kgm^{-3}$. At each grid station, the mixed layer depth, temperature and salinity were averaged over all casts to find a mean. The density surfaces between that of the average mixed layer and the first density surface present on all cruises were simply averaged for the subset of cruises for which they were below the mixed layer. We point out that the mean density field obtained from such an average is technique dependent.

2.5.8 Mean Water Mass Structure

The MC is apparent in the mean density section (Figure 2.6) as the downward displacement of isopycnals toward the coast. Distinct cores of the high salinity North Pacific Central Water and the low salinity NPIW hug the shelf and slope, indicating a direct link with the North Pacific subtropical gyre. Associated with both salinity cores are elevated concentrations of dissolved oxygen, indicating more recent ventilation than the offshore waters (Figure 2.7). Bingham and Lukas (1993) describe the offshore edge of the MC as a water mass discontinuity between the equatorial and subtropical waters introduced by the MC. The salinity minima of the EIW is not present in the MC: instead, a single strong salinity minimum of NPIW is present at ~9°C (near σ_Θ =26.8). South and west of the MC, EIW dominates these temperatures, indicating that the NPIW salinity minima is short lived at these latitudes. Further downstream the NPIW salinity minimum is observed to be eroded by strong vertical mixing in the Celebes Sea (Bingham and Lukas, 1993).

Below the thermocline, there is no indication in the mean property fields of a narrow boundary current. Between 500 and 1500db, mean isotherms slope upwards towards the west from the coast out to 130°E, evidence for northward geostrophic shear below the MC. Associated with this slope are elevated oxygen levels (Figure 2.7), which extend out to about 130°E. Lower salinity levels near the coast only reach θ = 5.0°C, and unlike the oxygen signature are confined close to the shelf slope.

The elevated oxygen levels in the lower intermediate water near the coast agree with the

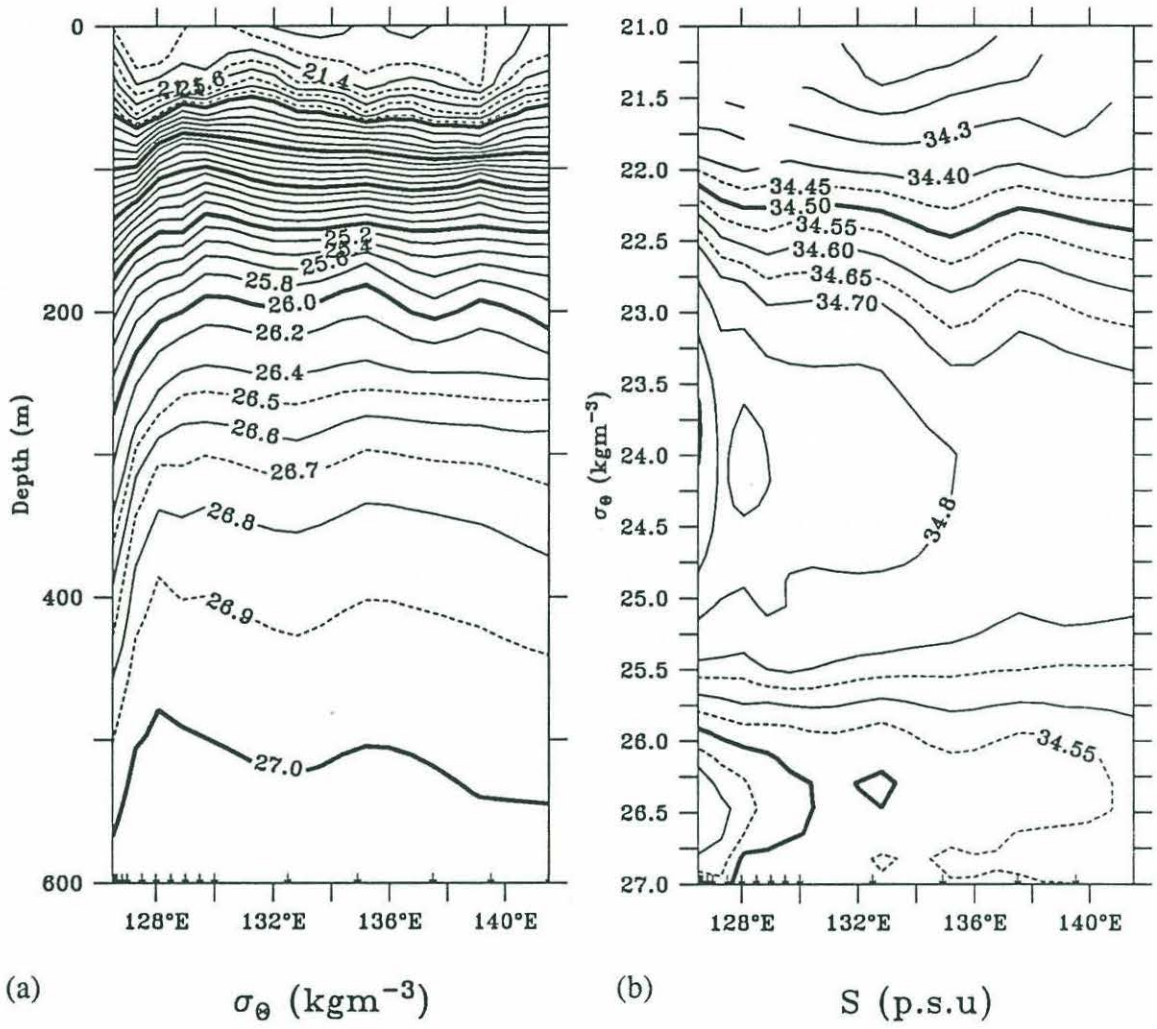

Figure 2.6 Mean hydrographic section at 8°N: (a) potential density versus depth; (b) salinity versus potential density.

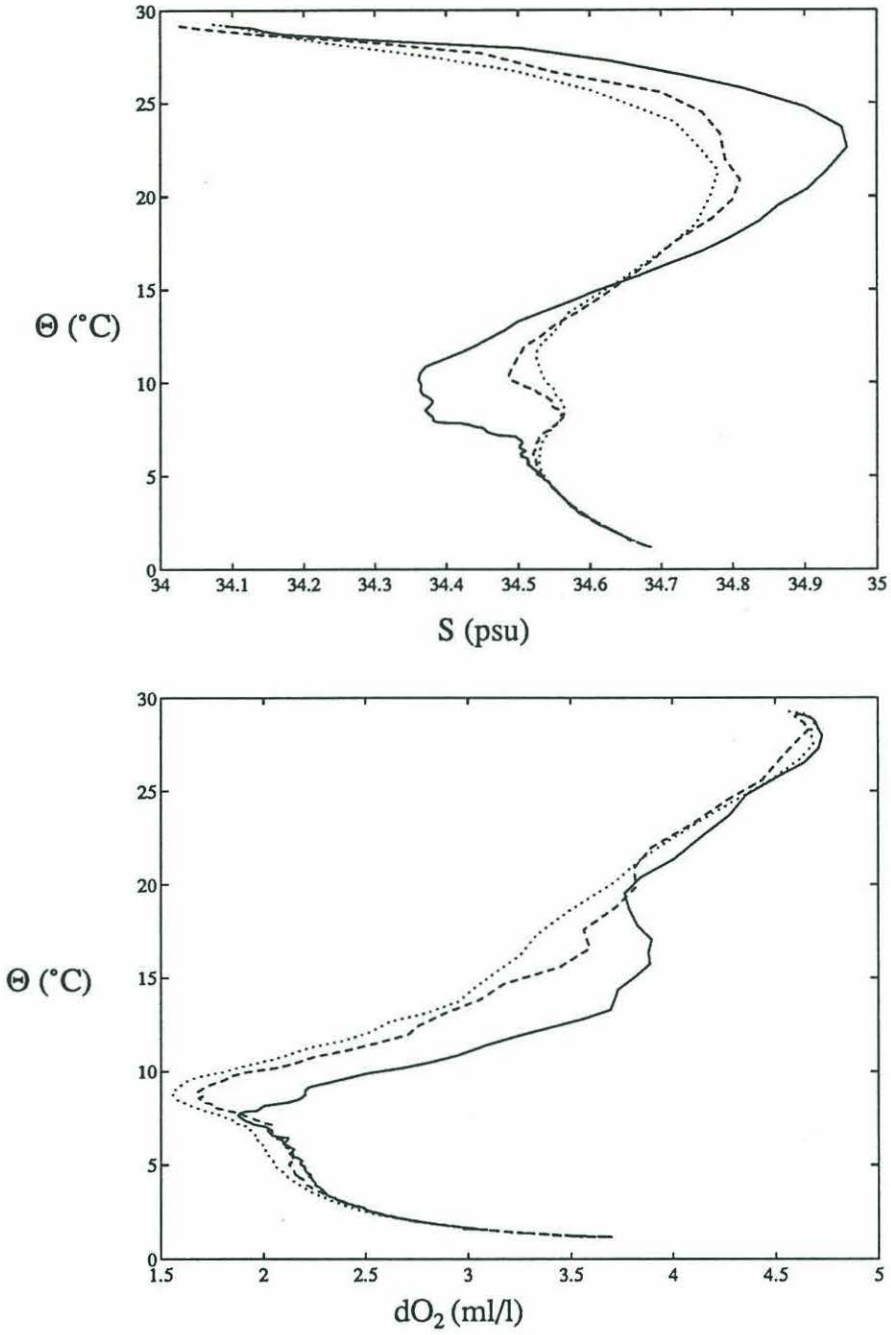

Figure 2.7 Properties in the mean Mindanao Current section: (a) salinity against potential temperature; (b) dissolved oxygen against potential temperature. The solid line is in the core Mindanao Current at 2000db over the shelf slope, the dashed line is at 130°E and the dotted at 135°E.

large-scale oxygen distribution on the isopycnal at σ_1=1032 kgm^{-3} shown by Reid and Mantyla (1978). High oxygen concentrations at the densities of the AAIW, penetrate into the North Pacific along the western boundary.

2.5.9 Mean Velocity Structure

Direct absolute velocity measurements were made during most of the repeat US/PRC-TOGA surveys by a shipmounted acoustic Doppler current profiler (ADCP) (Bahr *et al.* 1989). A mean ADCP velocity field, averaged on pressure surfaces and on a 0.2° grid in the horizontal was kindly provided by Eric Firing (Figure 2.8a). The ADCP is range limited and only penetrates to a maximum depth of 400m.

In the ADCP mean velocity field, the Mindanao Current appears as strong southward flow against the continental slope, with speeds linearly increasing towards the coast to reach over 0.8ms^{-1} on the shelf. The current is broadest at the surface and becomes narrower with depth.There is weak counter flow offshore with a subsurface maxima of 0.1ms^{-1}. Past the counter flow out to 140°E (not shown), the mean currents are weak (~0.05ms^{-1}) and disorganized. The mean velocity field is relatively smooth, and the eddy-like flow reversals typically seen geostrophic synoptic sections are absent.

A striking feature of the velocity field is that the inshore portion (west of 127° 30'E) of the MC is very steady. The standard deviation of the meridional velocity is smallest in the current core and attains a maxima offshore in the upper part of the recirculation (Figure 2.8b). The geostrophic velocity, on the other hand shows maximum variability along the shelf break, and may be attributed to large internal tide amplitudes (Firing and Toole, 1991).

The mean density section was used to find geostrophic velocities relative to 3000db or the bottom if shallower (Figure 2.8c). Over the shelf slope, the shear in the bottom triangles was initially taken from the neighboring offshore station pair. This is equivalent to horizontally extrapolating the slope of the density surfaces into the boundary. In comparison to the ADCP mean field, the geostrophic velocity has an offshore maximum, resulting from the application of a zero bottom velocity to the shallow station pairs over the continental slope. To correct for this, the mean ADCP velocity between 200 and 350m depth was used to reference the geostrophic velocity field over the shelf and slope, where the velocity differences were large (Table 2.1). Offshore, the ADCP-geostrophic differences were typically less

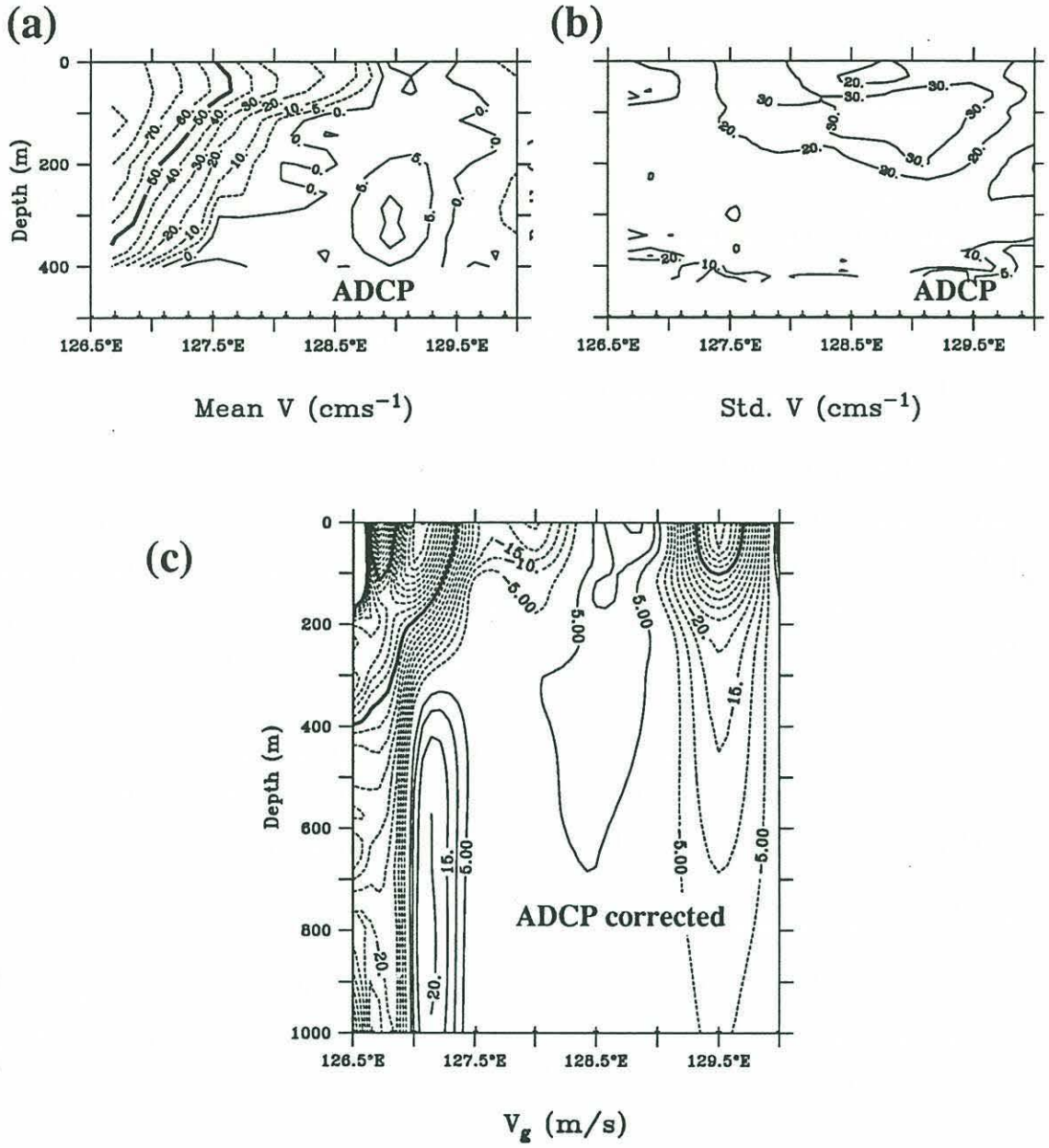

Figure 2.8 Velocity sections of the Mindanao Current at 8°N between Mindanao and 130°E: (a) ADCP velocity averaged on a 0.2° grid; (b) standard deviation of the ADCP velocity; (c) ADCP corrected geostrophic field.

Longitude	126.62°E	126.75°E	126.92°E	127.23°E
Depth	1171-1444m	1444.-2624m	2624-5152m	5152-4315m
Correction (cm/s)	-40	-21	+9	-5

Table 2.1 ADCP correction velocities applied to the geostrophic velocities in the station pairs in the Mindanao Current

than 0.05ms^{-1}. In the bottom triangles of the ADCP-corrected station pairs, the velocity was linearly reduced to zero at the bottom.

The similarity between the ADCP and geostrophic velocity sections is encouraging and supports the assumption that the mean current is in geostrophic balance. A detailed comparison of profiles (not shown) revealed that the geostrophic shear below 100m agreed well with the ADCP mean. Even the weak offshore recirculation is present in the geostrophic field, where no ADCP corrections have been made. Further offshore, between 130°E and 140°E, the surface geostrophic flow is northward, counter to the MC(Figure 2.9). Below the MC, the is shear reversal associated with the upward slope of the mean density surfaces (Figure 2.6). Even with the southward velocity corrections dictated by the ADCP measurements, a northward flow of up to 0.2ms^{-1} is observed below and offshore of the MC.

2.5.10 Transport of the Mindanao Current

Transports were found in a set of density layers for the mean fields: both the ADCP corrected and uncorrected. To assess the variability, geostrophic transports were also found for each of the survey cruises. The density layers were chosen such that layer 1 contained the thermocline flow, layer 2 the intermediate water, and layer 3 the water between 1000m and $\Theta = 2°C$. The deep circulation in the Philippines Basin is weak as discussed in section 2.2.2. For the individual survey data, the reference level was chosen to be 3000db or the bottom if shallower. Shear from offshore stations was extrapolated into the slope bottom triangles as described above.

The mean transport of the MC in the thermocline, found by integrating the ADCP velocity vertically to 400m and horizontally to 140°E, is 26.6x10^{9}kgs^{-1}. The corrected mean geo-

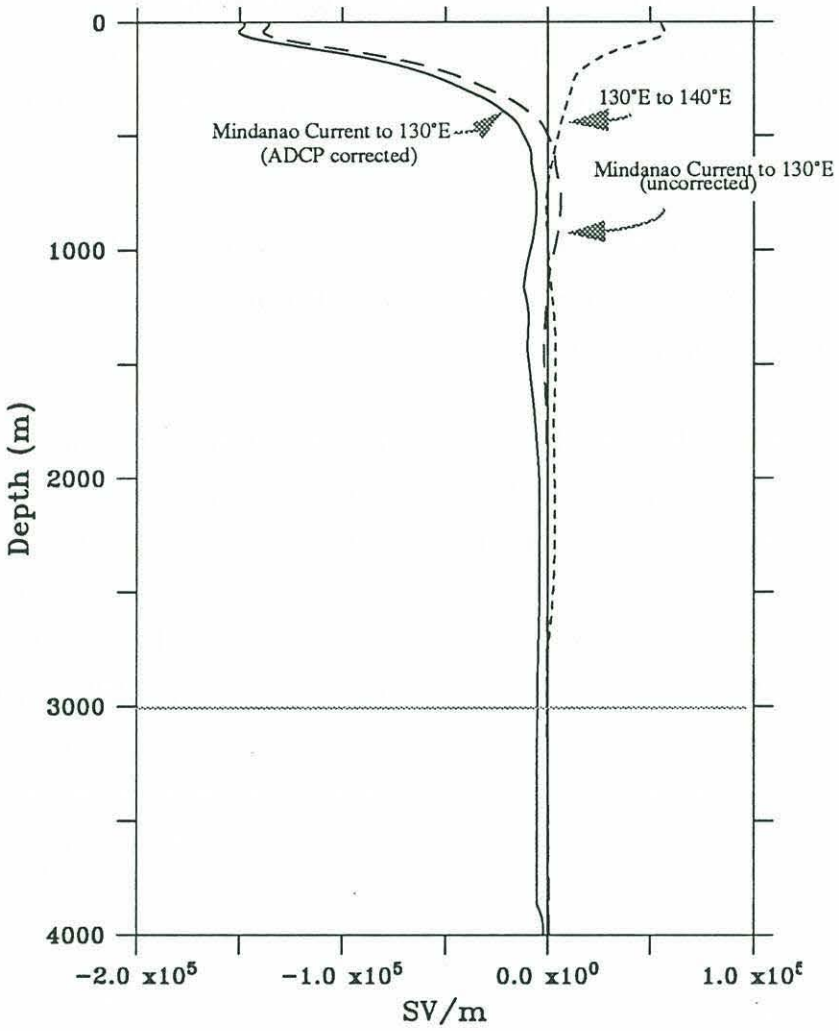

Figure 2.9 Full depth profile of the geostrophic transport relative to 3000db in the Mindanao Current, and further offshore, at 8°N. Adjustments to the ADCP mean results in an increase in southward transports at all depths.

strophic field transports a similar amount (Table 2.2). The uncorrected geostrophic field has a smaller transport due to the lower velocities over the shelf and slope. The remarkably stable flow over the shelf and slope indicated by the ADCP measurements suggests that geostrophic transports relative to the bottom will always underestimate the velocity there. Hence, the 5 SV low bias in the uncorrected mean geostrophic transport may also apply to the synoptic estimates.

The range of the synoptic geostrophic transport estimates of the MC is large: from 35 to 7 $x10^9 kgs^{-1}$ with a standard deviation of $12x10^9 kgs^{-1}$. This is consonant with previous survey results. Relative to the mean, the variability increases with depth.

For most of the surveys, the upper layer transport stream function is similar to the mean section: nearly flat to within 200km of the coast before the sharp southward drop associated with the slope-trapped current (Figure 2.10). The two surveys made in the spring of 1989 feature a different structure: the MW893 section has a strong warm core eddy offshore of the MC, while the PRC6 cruise, one month later, shows northward flow along the coast. Salinity data show that a warm core eddy containing high salinity NPCW occurs in both sections and is responsible for the transport stream-function anomalies. Similar eddies are

	1 $\sigma_\Theta < 27.0$ **0-520m**	**2** $27.0 < \sigma_\Theta < 27.35$ **520-1010m**	**3** $27.35 < \sigma_\Theta$; $\sigma_1 < 36.89$ **1010-2000m**
mean ADCP	-26.6		
mean corrected geo.	**-24.6**	**-2.8**	**-5.9**
mean uncorrected geo.	-18.2	2.6	2.9
PRC2 (at 10°N, to 130°E)	-19.5	2.1	4.6
PRC3	-34.6	-6.2	-10.1
PRC4	-26.9	-0.9	1.9
PRC5	-11.9	3.0	-3.3
MW893	-14.6	-3.7	-8.8
PRC6	-6.5	6.6	7.2
PRC7 (only to 130°E)	-31.6	-4.5	-1.6
PRC8	-34.8	-1.7	1.5
MEAN (std. error)	**-23.0 (4.4)**	**-1.1 (1.7)**	**-1.9 (2.3)**

Table 2.2 Transport estimates for the Mindanao Current at 8°N out to 140°E in density layers. Estimates from the survey data are relative to 3000db. PRC 2 at 10°N was not used to find the mean and standard deviation of the estimates.

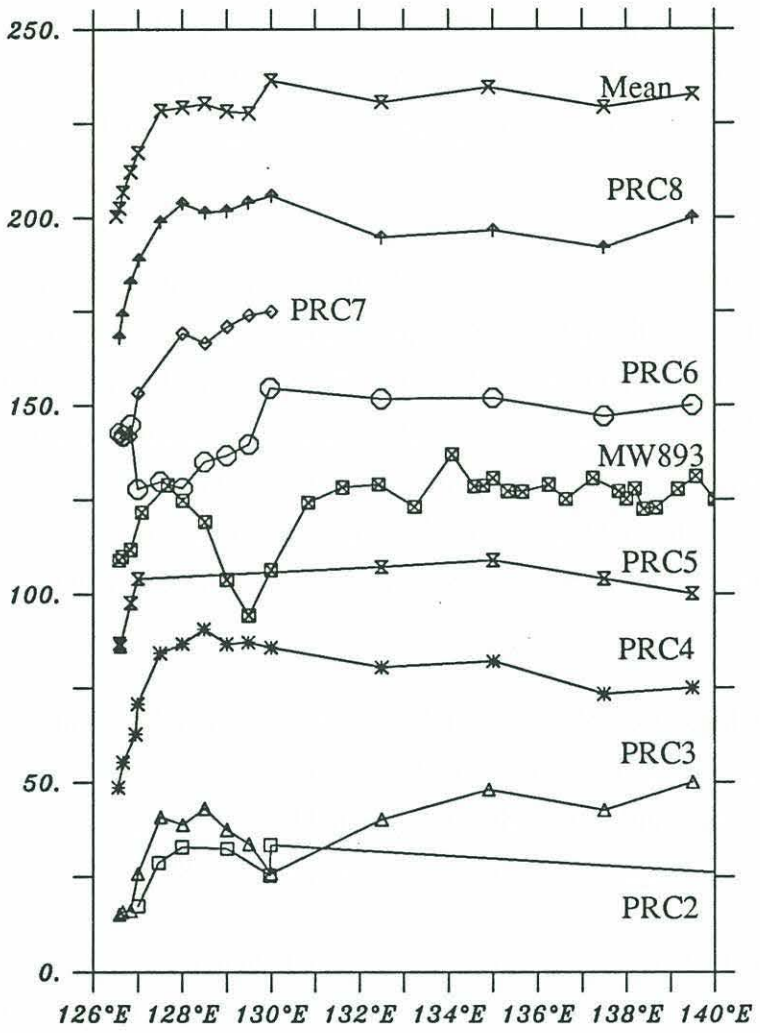

Figure 2.10 Geostrophic transport stream functions for the upper layer in the Mindanao Current along 8°N. The geostrophic transport was integrated westwards from the easternmost station pair, usually at 140°. Each survey is offset by $25 \times 10^9 kgs^{-1}$.

observed further east along the 10°N MW893 section.

In the intermediate water (layer 2), the transport stream-function shows flow oscillations that increase in amplitude towards the coast (Figure 2.10). These oscillations do not have a fixed spatial pattern and so cancel out in the mean section, resulting in a weak pattern of flow, with little net transport. Hence the offshore northward flow below the MC does not transport much water. We note that the individual survey data do not show a tendency for predominantly northward flow along the coast as suggested by the oxygen field.

2.5.11 Discussion

It is surprising that the survey data do not feature a strong expression of the Mindanao Eddy. Circulation studies of the region based upon historical data include a depression in dynamic height centered at 7°N and 130°E. Nitani (1972) suggests that 15SV may be recirculating in the eddy. Masumoto and Yamagata (1991) use a numerical model to examine the evolution of the thermocline circulation under the seasonal wind forcing. They find that instead of a tight recirculation, a broad dome like structure develops due to Ekman pumping by the local wind-stress curl. The Mindanao Dome, as they refer to it, extends out to 140°E and is strongest in the spring.

There is some indication of a dome in PRC 4, 5, 6 and 8: a broad northward recirculation in the thermocline offshore of the MC. However, in the mean section, this flow is weak. A tight recirculating Mindanao Eddy, as suggested by Nitani (1972), does not appear to be a persistent feature of the flow during the survey period at 8°N.

Though poorly resolved, the phase of the seasonal change in the survey data is opposite to that predicted by Masumoto and Yamagata (1991), and observed by Wyrtki (1961): i.e. the survey data suggest a transport maximum in the summer, instead of late winter (Figure 2.12). If plotted as an interannual variation the transport variability curve is smoother. Over the four survey years, the MC transport is a minimum at the end of odd years, suggestive of a biannual variation with an amplitude of $10x10^{9}kgs^{-1}$. Lukas (1988) used the sea level difference across the MC at 7.5°N to infer transport changes between 1976-1985. A biannual fluctuation dominated, with an amplitude for the upper 150m of 10SV. The oscillation follows a saw tooth shape: strengthening in odd years, flat or weak increases in even years and then a sharp decrease in the early part of the odd years. The survey data transport changes match the phase and strength of the biannual sea level fluctuation observed by

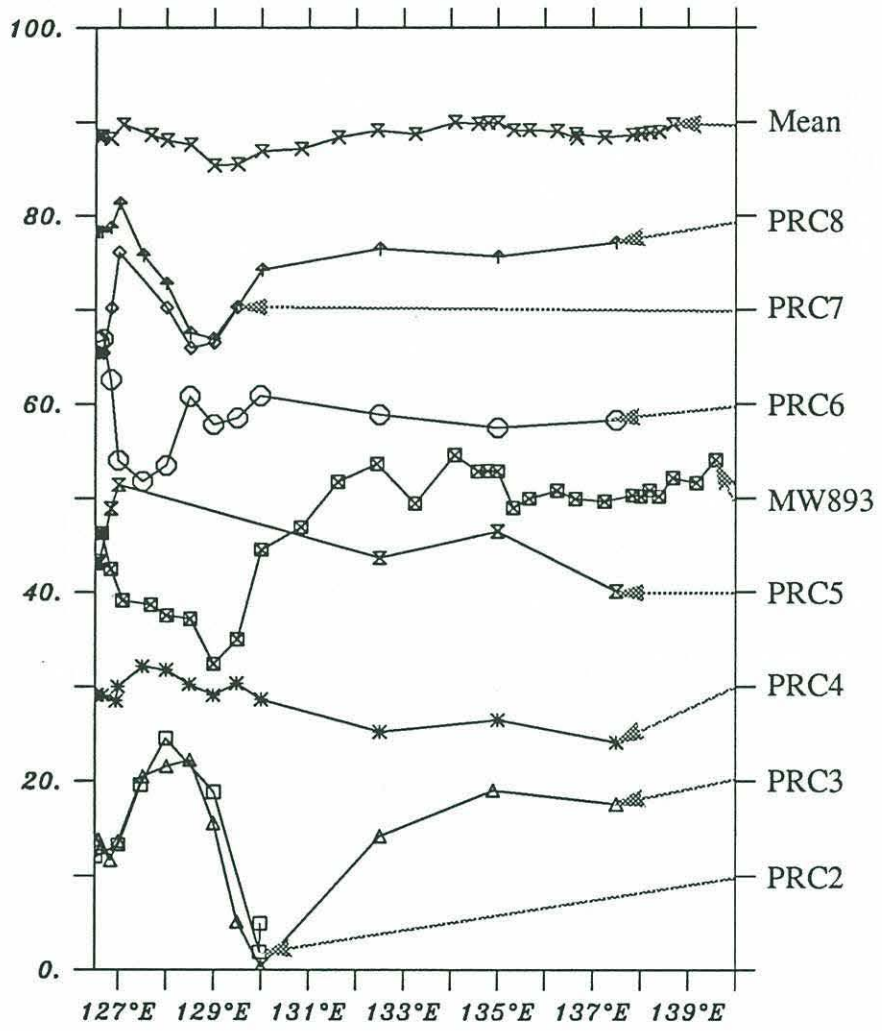

Figure 2.11 Geostrophic transport stream functions for layer 2 in the Mindanao Current along 8°N. The geostrophic transport was integrated westwards from the easternmost station pair, usually at 140°. Each survey is offset by $10 \times 10^9 kgs^{-1}$.

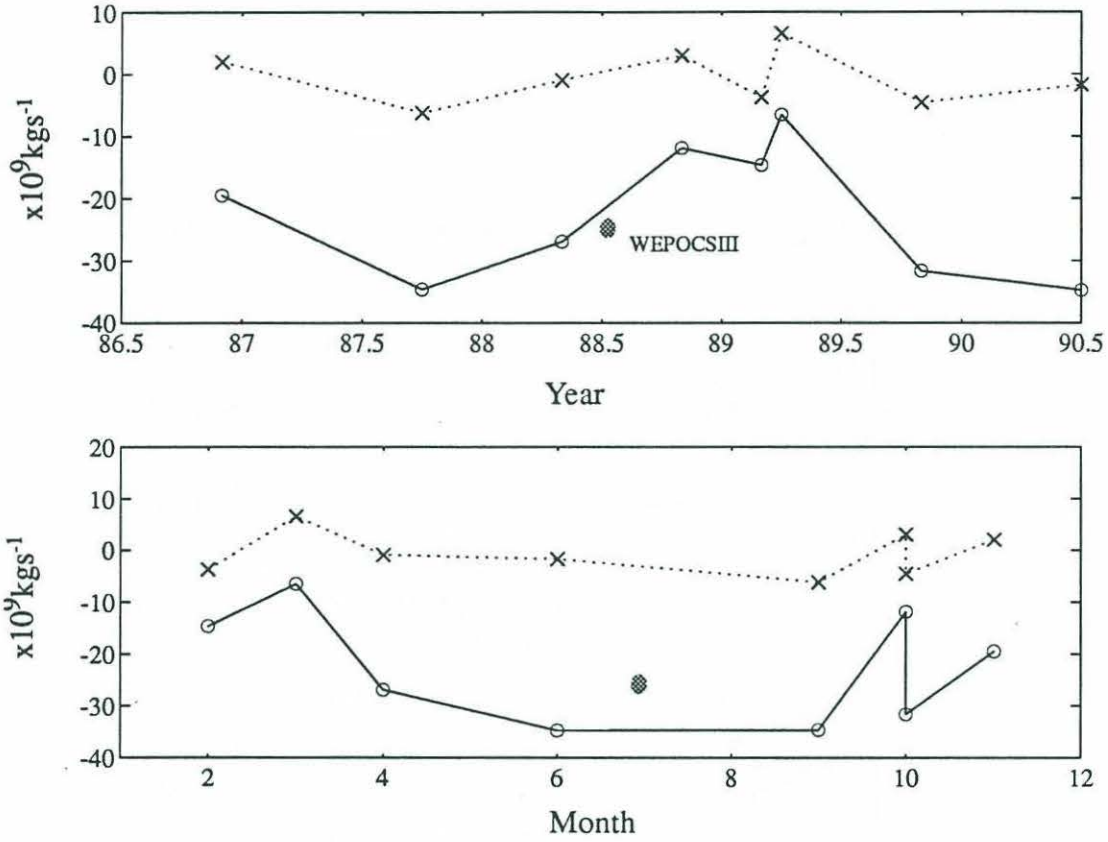

Figure 2.12 Transport variability of the Mindanao Current at 8°N: (a) transport as interannual change (b) transport as a seasonal curve. The solid line is for layer 1 and the dashed for layer 2 as defined in Table 2.2

Lukas, though this may only be fortuitous given the short period covered by the survey data.

Masumoto and Yamagata (1991) noted that fluctuations in their model MC were controlled by changes in the windstress curl west of the dateline. Consonant with this idea, Qui and Joyce (1992) demonstrated that the transport of the NEC and NECC is governed by a local Sverdrup balance, and that remotely forced Rossby waves propagating from the east are attenuated by the thermocline slope in the NEC. Hence, the fluctuations in the MC are likely driven by interannual changes of the wind stress over the western Pacific.

The mean transport of the MC predicted by a local Sverdrup balance varies between 30 and 40SV, depending which wind data set is used (Landesteiner *et al.* 1990). The top to bottom transport estimate from the survey data is 31.8SV, in good agreement with the FSU and University of Hawaii wind climatologies. The FNOC winds predict a transport of over 40SV, which is outside of the range indicated by the survey data.

Given the range of cruise-to-cruise variation, it is remarkable that the mean survey transport agrees closely with that observed during the WEPOCs III survey in July 1988 (Lukas, *et al.* 1991). At 8°N, they estimate the MC carried 26SV (22SV) in the ADCP (geostrophic) velocity field, identical to our results for the mean. Furthermore, the WEPOCS estimates fall nicely on the biennial fluctuation curve suggested by the survey data. The conclusion by Lukas *et al.* (1991) that the WEPOCSIII survey was made during a time of 'normal' conditions is supported by the PRC/TOGA survey data.

Reid and Mantyla (1978) demonstrate the northward spreading of high oxygen AAIW along the western boundary of the North Pacific. A map of geopotential anomaly at 1000db relative to 3500db features a northward flowing streamline below the MC, which they claim explains the high oxygen influence. In the survey data high oxygen levels are also found in a broad region along the Mindanao coast. However, the large variability found in the transport stream function below the thermocline makes it difficult to be certain of the sign of the mean flow: a narrow permanent boundary current under the MC was not observed. It is possible that the northward spreading of the high oxygen influence is partly achieved by the eddy field.

2.5.12 Conclusions

Four years of semiannual surveys of the Mindanao Current at 8°N were made as part of the USPRC/TOGA Cooperative Research Program between 1986 and 1990. Over the Mindanao shelf and slope, ADCP measurements indicate very stable speeds in the MC of around 70±10cm/s, which are underestimated by the geostrophic field referenced to the bottom. If the geostrophic field is referenced to the mean ADCP field at 200m, good agreement is obtained between the geostrophic and ADCP fields in both the velocity structure and transport of the MC. These results support the notion that the mean MC is in geostrophic balance.

At 8°N, the mean southward transport of the MC above $\sigma_\Theta < 27.0$ is 24.6 $x10^9 kgs^{-1}$ based on a mean geostrophic field reference to direct velocity measurements. The survey data do not feature a strong Mindanao Eddy as a permanent feature. A Mindanao Dome is present in some of the surveys, but is a weak feature in the mean section constructed from the survey data. Below the Mindanao Current the flow is also towards the south, though a reversal of the geostrophic shear in the intermediate water results in an offshore northward flow. Whether this feature is permanent is unknown, as the large variability observed in the synoptic surveys makes the direction and net transport of the mean flow there uncertain.

Chapter 3

Observations along 14°S

3.1 A transpacific section along 14°S

A transpacific section at nominally 14°S was made in 1987 by the two NOAA vessels, *Researcher* and the *Oceanographer*. The western half of the section was completed by the Pacific Marine Environmental Laboratory (PMEL) on the RV *Oceanographer* and covers the distance from Papeete (150°W) to Townsville, Australia (147°E). The eastern part of the section from 150°W to Peru was collected by the Atlantic Oceanographic and Meteorological Laboratory (AOML). The data were collected under the Transport of Equatorial Waters (TEW) program. Cruise legs are indicated by the program name, leg number, year and ship, in order.

3.1.1Data

TEW2_87OC: The western leg (June - August, 1987)

Between Papeete and Townsville, 109 CTD stations were made aboard the NOAA ship *Oceanographer* which make up the TEW2_87OC data set (Magnum *et al.*, 1991). After arriving in Townsville additional casts were made along a section of the Solomon Sea and a cross-equatorial section at 165°E on TEW3_87OC between ± 5° (see below).

The average station spacing for TEW2_87OC was 80km, with smaller spacing over steep topography. At each station, CTD pressure, temperature, conductivity and oxygen were measured to full depth. Water bottle samples were collected on each cast for calibration which is detailed in Magnum *et al.* (1991). The rms difference between the processed CTD data and bottle samples was 0.0017 psu for salinity and 0.075ml/l for oxygen. Nutrient, freon and helium samples were also collected on the TEW2_87OC cruise but are not considered here.

TEW_87RE: The eastern leg (June -July 1987)

A total of 161 CTD casts were made between Papeete and Peru aboard the NOAA ship *Researcher*. The average station spacing is 106km, decreasing to 24km over steep topogra-

phy. Due to restrictions on the number of bottle samples per cast, two casts were made per station - a shallow cast with the bottles tripped in the upper waters (typically 0-1000m) and a full depth cast with the bottles tripped in deep waters. After calibration, CTD salinity and the bottle salinity differed with a standard deviation of 0.002psu (Doug Wilson, personal communication).

CTD oxygen was also measured along the section, but at this writing is not yet calibrated. Twelve bottle oxygen values were measured at each cast, and were made available by Doug Wilson (AMOL). Two oxygen titration methods were employed: the automated Carpenter Method (automated photometric end-point titration); and the Winkler Titration. A comparison of the two methods showed considerable scatter between the methods and nearby casts. Differences in the deep water ($\geq$ 3000m) of 2ml/l are common with no obvious correspondence to titration method. As reported, the data were not suitable for plotting. By examining each cast and comparing it to its neighbors, an edited subset of the bottle oxygen data was formed and merged with the calibrated CTD oxygen data from the western leg to produce a contoured section of oxygen. The edited data set is still very noisy, only allowing features on the very largest of scales to be discernible.

Merging data from the two TEW sections

Of the total of 161 casts taken in the eastern section, only the 73 full depth casts are utilized. The data from the two sections were merged into one complete transpacific section with a top to bottom resolution of 10db for salinity, temperature and pressure. An overlap cast from the eastern leg at the section join at 150°W is left out, as are the 5 casts made in a meridional section across the Coral Sea from 14.5°S to the tip of the Louisiade Archipelago. In addition, 9 casts made in the Samoan Passage and 5 repeat casts along the western half of the section are left out. Hence of the total of 109 casts made in the western section 80 are employed here, resulting in a net total of 153 stations making up the 15°S TEW section.

Figure 2.1 shows the station positions of the composite section used in this study. Starting at the coast of Australia at 17°S, the section cuts diagonally to the center of the Coral Sea. It then continues at a latitude of roughly 15°S to 170°W near the Solomon Islands. The section then traverses north to roughly 12°S and remains at this latitude out to 134°W, after which it angles south over the East Pacific Rise to again rejoin 15°S at 125°W along which casts are taken to within 100km of the Peruvian coast. At this point the cruise track moves

northward to meet the coast of Peru at 13°S. These meridional changes along the section need to be kept in mind when interpreting the water properties in the data.

A comparison of the overlapping casts showed good agreement between the CTD calibration between the two data sets (see Appendix A).

3.1.2 Water Mass Distribution Along TEW

Thermocline Waters

In comparison to 10°N, the thermocline in the TEW data is considerably thicker and deeper, resembling more closely the typical thermocline structure of a subtropical gyre. At temperatures above 8°C, isotherms deepen to the west indicating equatorward geostrophic flow (Figure 3.1). As at 10°N, isotherms between 13°C and 10°C peel away from the thermocline such that their east-west slope is reduced. Near the coast of Peru these isotherms deepen in what appears to be an eddy.

The surface layer has an average depth of 60m along the TEW section, is deepest in the west and shoals in mid-section to less the 40m at about 160°W. Salinity in the surface layer varies considerably. In the west salinities values dip below 35.0, while at 120°W surface salinities reach 36.4. The high salinities in the surface layer intrude into the thermocline and extend towards the west, undercutting the fresh surface layer there. Where connected to the surface at 120°W, the high salinity water in the thermocline has high values of oxygen. Isopycnals associated with the salinity maxima outcrop along the section, and the subsurface plume of high salinity penetrating westward is suggestive of recent subduction. Levitus' (1982) Figure 86 shows that the $\sigma_\theta = 24.5$ isopycnal surface outcrops in the southern hemisphere winter near where the high surfaces salinities are found along the TEW section. Along this isopycnal, a belt of high salinity flows towards the northwest away from its formation area and has been subducted into the thermocline. This saline water mass, formed by evaporation and subduction during the wintertime, is comparable to the Tropical Water found along 10°N. Here it shall be referred to as South Pacific Tropical Water (SPTW).

West of the outcrop region of the SPTW, oxygen in the thermocline changes considerably across the section, and indicates that several different water masses may be present. Along the coast of Peru, below the thermocline, extremely low oxygen levels exist, which extend westward below the SPTC. Strong oxygen gradients in the lower thermocline result. At

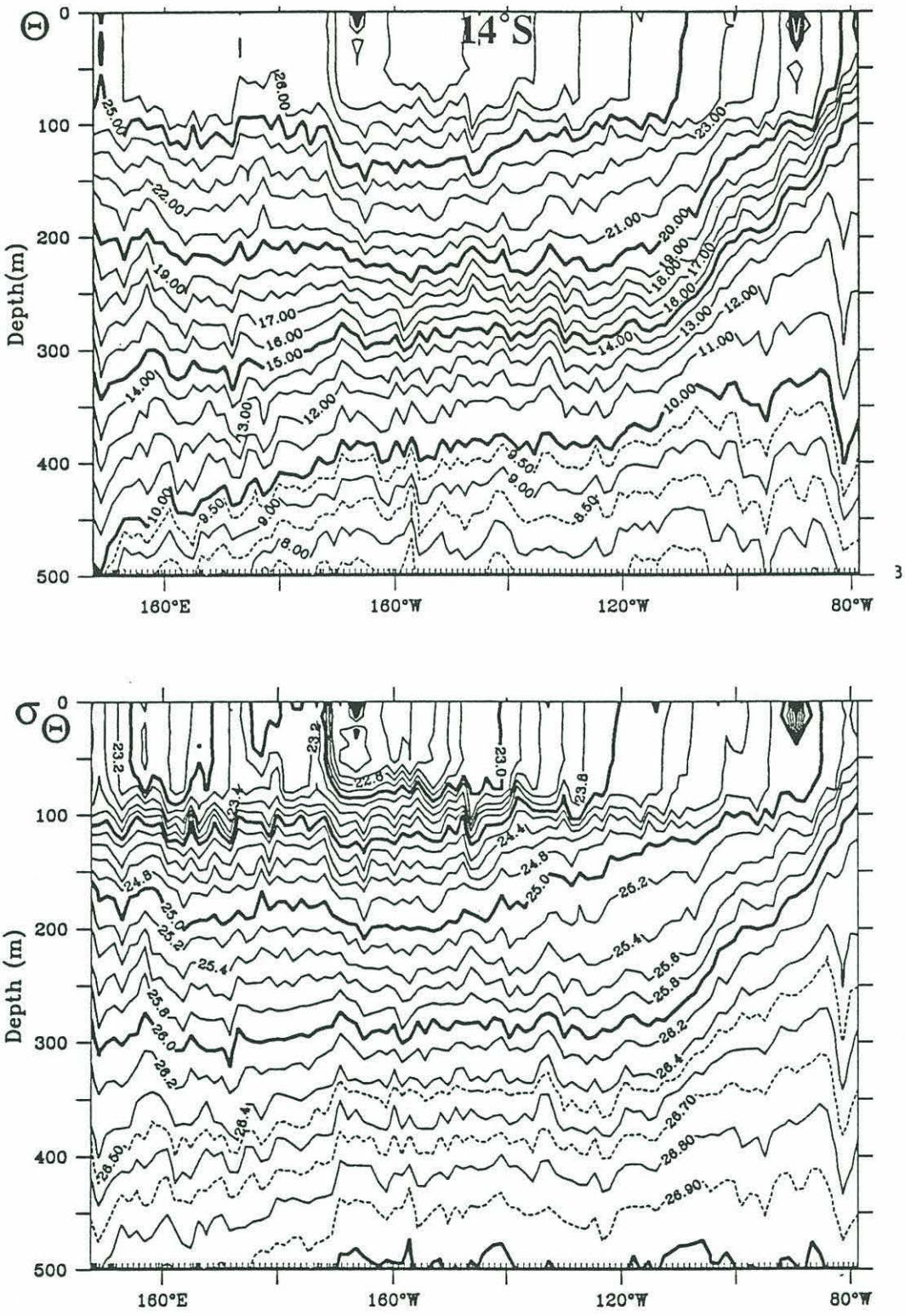

Figure 3.1 Properties along 14°S in the upper 600m: (a) potential temperature (°C); (b) potential density (kgm^{-3}). Opposite page: (b) salinity and (c) dissolved oxygen concentration (ml^{-1}). The difference in character of the oxygen plot west of 150°W is due to the switch from CTD data along the western half of TEW to the bottle data of the eastern half.

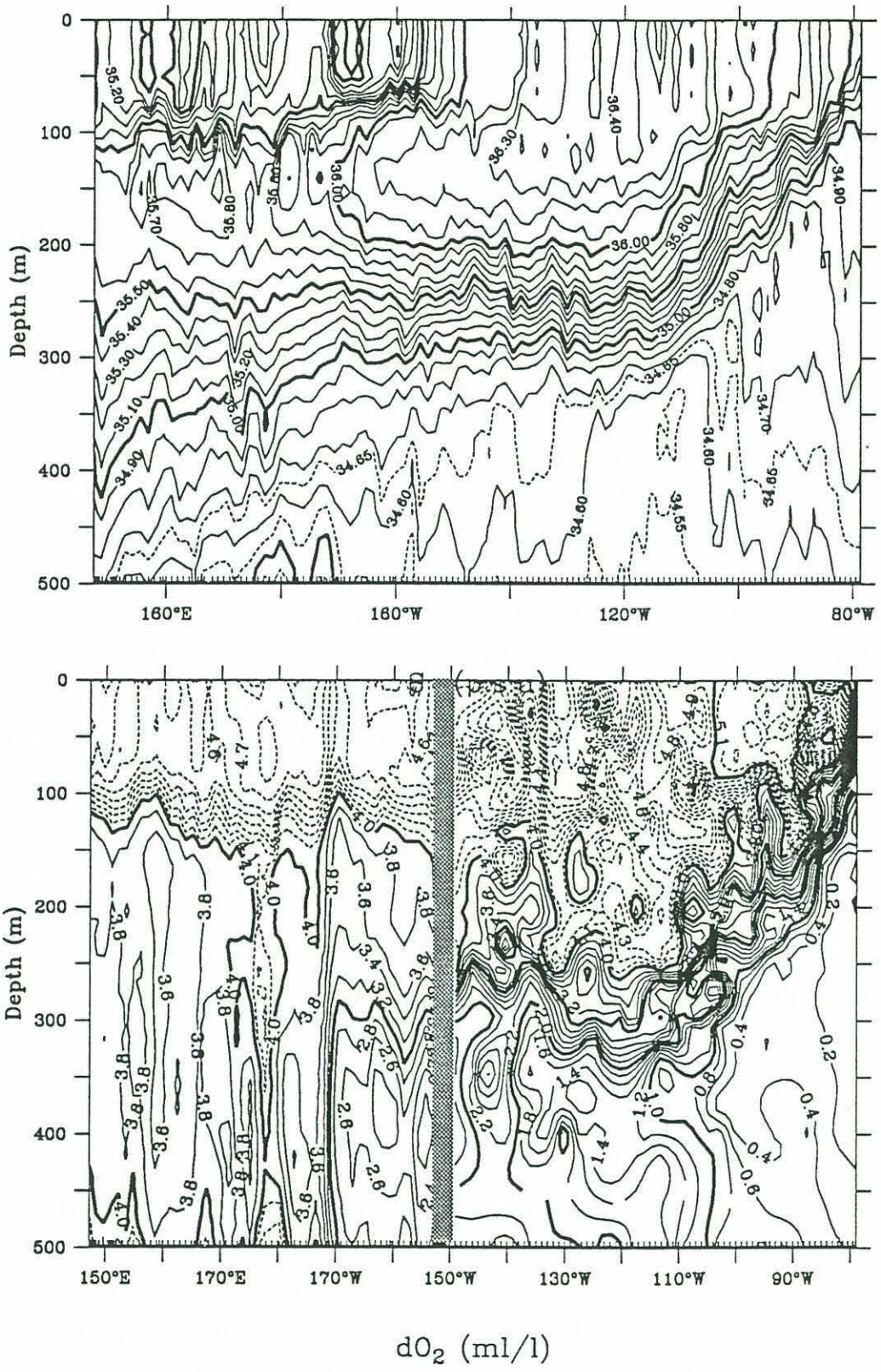
Depth (m)
0
100
200
300
400
500
160°E
160°W
120°W
80°W
150°E
170°E
170°W
150°W
130°W
110°W
90°W

dO_2 (ml/l)

170°W, the cruise track dips due south from 12°S to 15°S, and then continues westward at this latitude into the Coral Sea. The data show that a strong meridional oxygen gradient exists between 12°S and 15°S with oxygen values increasing to the south over this latitude range by 0.8ml/l between 300m and 1000m. At the same time, the salinity in the thermocline decreases.

The strong gradient or 'front' in oxygen between 10°S and 20°S can be seen in the GEOSECS Pacific Atlas (Plates 11) at 170°W and 110°W, suggesting the front may be basin-wide. Levitus'(1982) plots of zonally averaged oxygen concentrations for each ocean basin suggest that a front in oxygen at these latitudes are common for all oceans, lying below the highly saline and recently ventilated Tropical Waters. This feature appears to be the boundary between waters of Equatorial origin which are low in oxygen, and waters of high-latitude origin, typical Tropical Water and Intermediate water, which have high oxygen concentrations.

Along the TEW section, west of the 170°W, waters of both equatorial and southern origin are positioned adjacent to each other in the thermocline. Of southern origin is Western South Pacific Central Water (WSPCW) thought to have formed in the Tasman Sea along the subtropical convergence and to have reached the western Pacific by a circuit around the subtropical gyre (Tomczak and Hao, 1989). WSPCW has a high oxygen/low salinity signature through out the thermocline and is found over the West Fiji Basin and in the Coral Sea (see section 3.2) along the TEW section. Surrounding the WSPCW is Pacific Equatorial Water (PEW) which has lower oxygen and higher salinity. The origin of PEW is not made clear by Tomczak and Hao (1989), though they suggest if forms in the Equatorial currents via mixing, possibly of waters from both hemispheres.

Intermediate Waters

In contrast to 10°N, there is no salinity minimum *within* the thermocline (Θ >10°C) along the TEW section. Below the thermocline, two distinct salinity minima do occur. The dominant minimum is due to Antarctic Intermediate Water (AAIW) formed at the subantarctic front (McCartney, 1982). This water mass is seen spreading north below the thermoclines in nearly all the world's oceans (the North Pacific and North Indian Oceans being the exceptions). Along the TEW section the core of the AAIW is at a temperature of 5.5°C, though its longitudinal extent is limited along the section. High oxygen values and the low-

est salinities indicate that AAIW is only found west of about 180°(Figure 3.2). Between the coast of Australia and Fiji (178°E) two cores of AAIW are apparent: one north of Fiji with the lowest salinities along the section (< 34.4psu) and high oxygen concentrations (4.2mll^{-1}); a second, saltier core of AAIW occurs in the Coral Sea and is associated with a boundary current to be discussed in section 3.2. The AAIW core flows around the outer edge of the South Pacific subtropical gyre, and reaches its northernmost extent in the western Pacific, where it is seen to split into a northward and southward branch to flow around New Caledonia (see Reid (1965) Figure 24). Hence the western location of the 'purest' AAIW along TEW is consistent with Reid's observations.

Despite the limit in the AAIW distribution, a vertical salinity minimum persists eastward across the entire TEW section. Along the northward traverse of the cruise track at 170°W, there is a rapid increase in salinity and a decrease in oxygen. East of the traverse, oxygen decreases gradually to the east to very low values along the coast of Peru. Details in the oxygen distribution in the eastern half of the section are not available due to the scatter in the bottle oxygens there. East of 170°W salinity in the minimum is fairly uniform (34.52psu) until close to the Peruvian Coast. Oxygen concentrations as well as the θ-S relation for the AAIW and the salinity minimum water in the east suggest that two types of intermediate water exist. The eastern type is more closely related to that found at these temperatures along the 10°N section than the AAIW. Hence the low oxygen intermediate water along the eastern part of the TEW section may come from the north, and be part of the subthermocline water mass formed along the equator: EEW.

A second salinity minimum is present in the TEW data at about 11°C between 125°W and 110°W. Though very weakly expressed in the TEW data, this minimum is well known and has been documented by Reid (1973). A direct analogue to the CCW along 10°N, this feature is due to the equatorward advection of fresh, high-latitude water around the eastern edge of the subtropical gyre. The minimum in the South Pacific does not penetrate as far equatorward as the northern hemisphere version, and its signature along the TEW section is weak.

Deep and Bottom Waters

On the TEW section, a deep western boundary current is located over the Tonga Trench (Figure 3.3), associated with the sharp rise of isotherms to the west. As found further south,

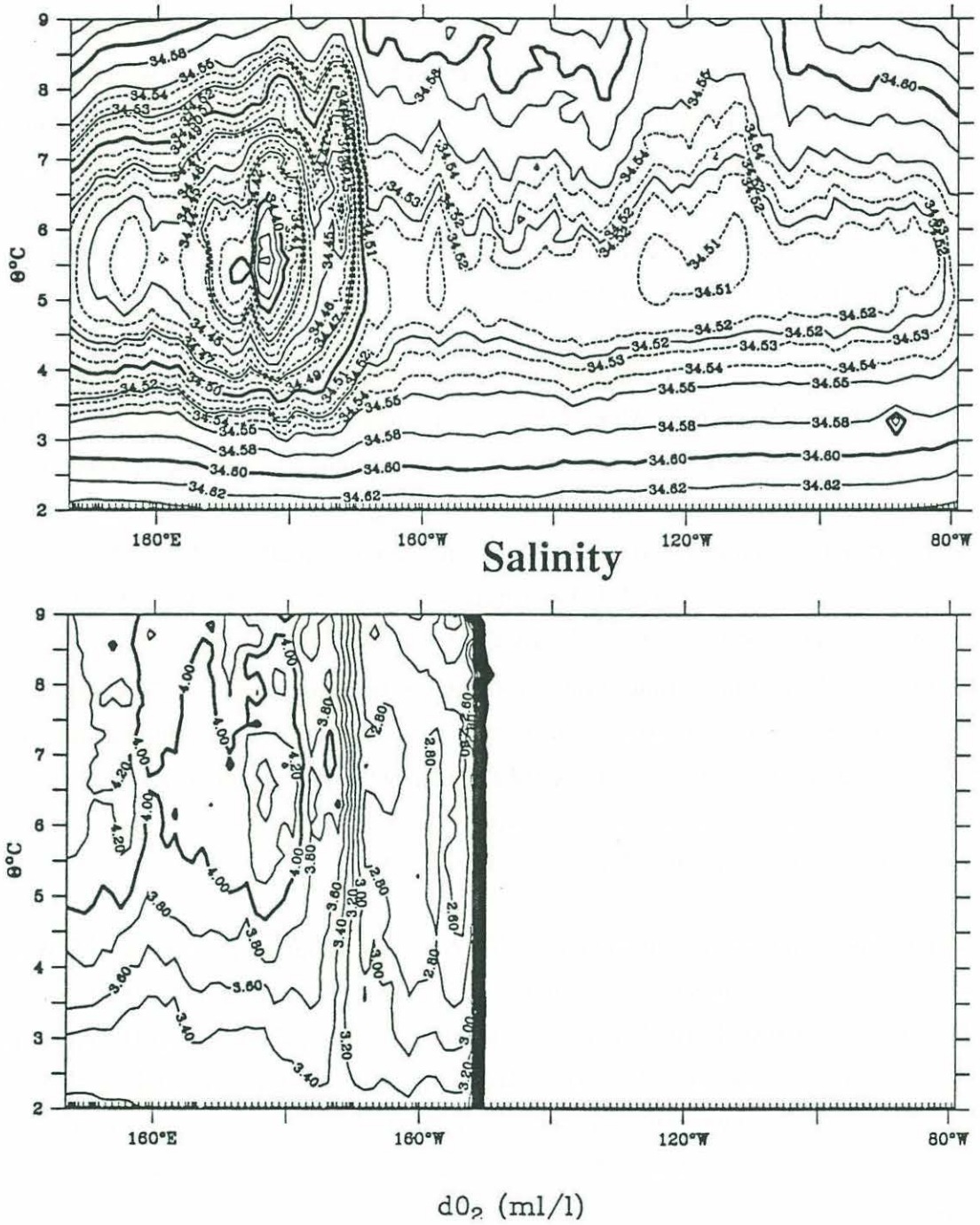

Figure 3.2 Properties on intermediate potential temperature surfaces along 14°S: (a)salinity and (b) dissolved oxygen concentrations. CTD oxygen was only available for the western half of TEW.

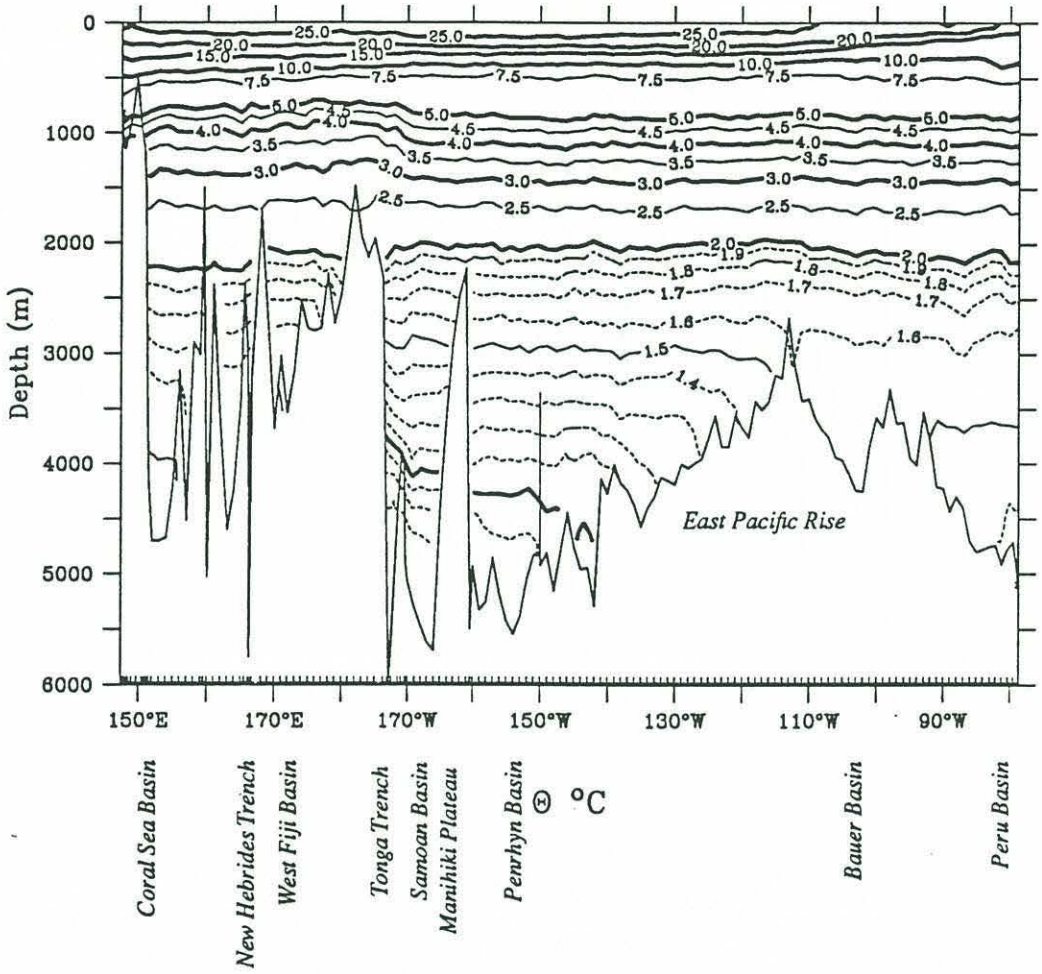

Figure 3.3 Properties along the TEW transpacific section at roughly 14°S (a) potential temperature; (b) salinity and (c) oxygen. The oxygen data east of 150°W is from water sample analyses only and not continuous CTD/02 data as in the east.

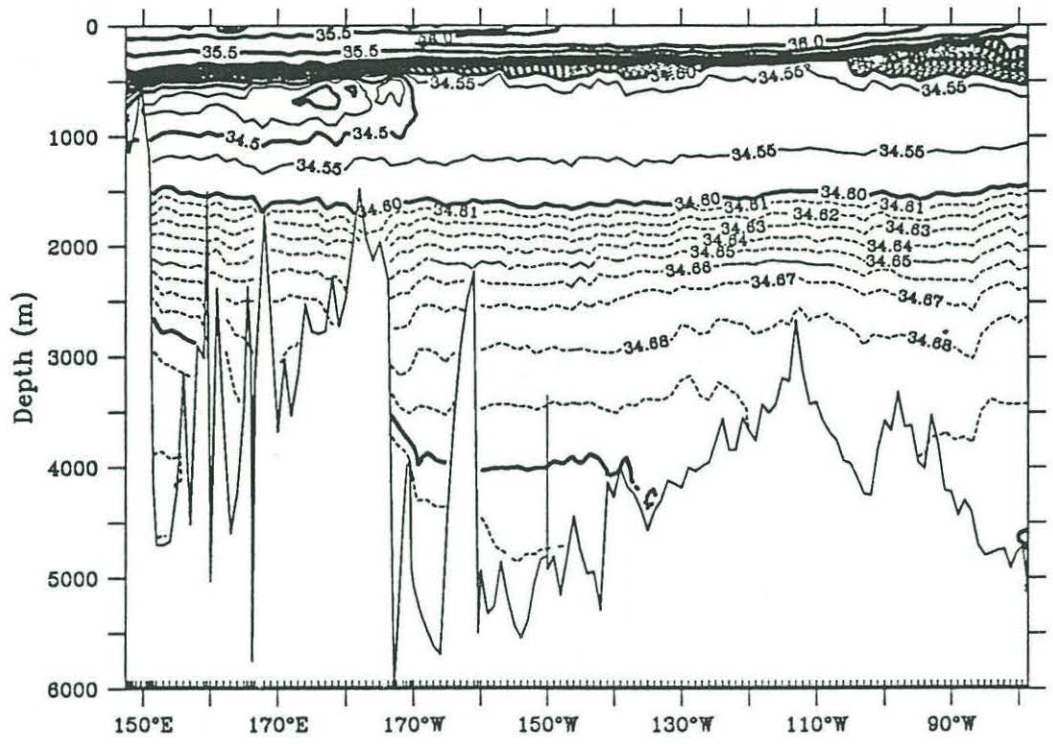
Depth (m)
0
1000
2000
3000
4000
5000
6000
150°E
170°E
170°W
150°W
130°W
110°W
90°W
35.5
35.0
34.55
34.5
34.60
34.61
34.62
34.63
34.64
34.65
34.66
34.67
34.68

S (p.s.u)

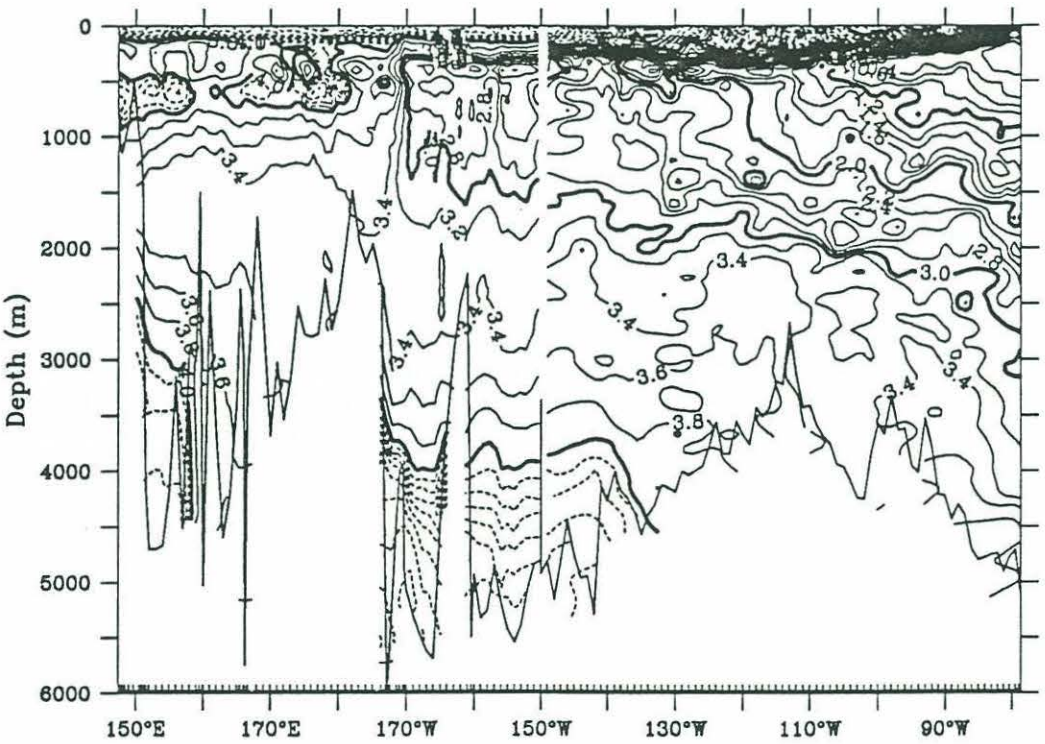
Depth (m)
0
1000
2000
3000
4000
5000
6000
150°E
170°E
170°W
150°W
130°W
110°W
90°W
3.4
3.6
3.8
3.0
2.8
2.4
2.0

dO_2 (ml/l)

the deep western boundary current still exhibits two vertically stacked water mass cores: a saltier and lower silicate NADW core overlying colder, fresher and high silica AABW (Taft *et al.*, 1991).

High oxygen values are found in the deep water of the Coral Sea, though the coldest temperatures are only 1.5°C. This temperature is believed to be controlled by the 2800m sill depth connecting the Coral Sea to Tasman Sea to the south (Wyrtki, 1967).The isolation of the Coral Sea Basin from the deep Central Pacific Basin is indicated by a distinct θ-S offset below 3°C. This basin is ventilated from the south via the Tasman Sea and not the Central Pacific Basin.

In the west, sandwiched between the high oxygen AAIW and LCPW is an oxygen minimum, centered near 1700m. Eastward of 170°W, the AAIW maximum is no longer present, and a single oxygen minimum exists, concentrated below the thermocline in the EEW. Based on the nutrient data along 28°S (Warren, 1973) and the figures in Taft *et al.* (1991), a silica maxima is associated with the low oxygen concentration at mid-depth, marking the presence of NPDW.

3.1.3 Choosing the reference levels along 14°S

Along the TEW section the lack of nutrient data make it more difficult to establish the water mass boundaries, than along 10°N. Starting in the west, 3000m is used as the reference level in the Coral Sea Basins and over the New Hebrides Trench, coincident with the top of the high oxygen concentrations in the Coral Sea Basin.

Low oxygen values and the θ-S relation in the West Fiji Basin indicate connectedness with the deep North Pacific, and isolation from the basins to the west. Geostrophic shear in this basin is weak in the deep water, and so a bottom reference level is chosen.

Over the Tonga Trench and Samoan Basins, the top of the LCPW as defined by JT is used as a reference level: 1.2°C isotherm, here approximated with the 3500db pressure level. This is also close to the reference level used by Taft *et al.* (1991) of 1.22°C. The 3500db surface was used as a reference level across the remainder of the TEW section: over the Penrhyn Basin and the East Pacific Rise.

3.1.4 Overview of Water Masses Along 10°N and 14°S

Saline Tropical Water formed in both hemispheres is found in the respective upper thermoclines of the two sections and is presumably flowing towards the equator. The two sections exhibit shallow salinity minima which have high latitude sources, and reach the low-latitudes by flowing around the eastern edge of the subtropical gyre. The southern minimum is much weaker and less extensive than that due to CCW in the north.

Common to both sections is a low oxygen, high salinity water mass in the 12-8°C temperature range which occupies an increasingly large area towards the east. This water mass is referred to here as Eastern Equatorial Water, and is deduced to form along the equator, possibly by lateral mixing in the strong zonal flows found in these temperature classes: the SubSurface Counter Currents and Equatorial Under Current. EEW includes the 13°C Thermostad waters found in the lower part of the Equatorial Current (Tsuchiya, 1981). Lukas (1986) documented the termination of the Equatorial Undercurrent and concluded that the bulk of the Thermostad water flows to the south of the Galapagos Islands and to the coast of Peru to form the Peruvian Coastal Undercurrent (PCUC) under the coastal upwelling zone there. Some of the Thermostad waters also recirculate to the north into the NEC.

The water masses that must contribute to the formation of EEW are the lower thermocline waters: the salinity minimum waters and denser Tropical Waters. The very low oxygen concentrations must come about by consumption below the extremely productive upwelling zone in the eastern equatorial Pacific and along the equator, and by a long residence time in the gyre.

In the intermediate water layers, AAIW extends northwards across 14°S (possibly in several core currents), and its signature penetrates across the equator to appear along the western boundary at 10°N. According to Tsuchiya (1991), AAIW then flows north to about 40°N in the deep Kuroshio. Along 10°N, the North Pacific subpolar water mass, NPIW flows southwards across the 10°N.

At depth, bottom water from the Southern Ocean flows northwards in a system of deep-western boundary currents, while above, at mid-depth, NPDW, formed in the northern Pacific, extends into the South Pacific ocean.

3.2 The Low Latitude Western Boundary Current in the Coral Sea

3.2.1Introduction

The low latitude western boundary currents play an important role in the mass budget of the equatorial current system. Though the subject of increasing attention, these equatorward flowing boundary currents are presently poorly described and understood. This is especially true of the South Pacific low-latitude boundary current in the Coral Sea.

The Coral Sea can be loosely defined as the body of water between the northeastern coast of Australia and the series of islands and archipelagos stretching between the Solomon Islands and New Caledonia (Figure 3.4). At depth it is divided into of a series of basins, the deepest parts being in the large Coral Sea basin and the Solomon and New Hebrides Trenches.

The analysis below utilizes a new set of hydrographic stations in the Coral Sea which were taken at the end of the TEW transpacific section near 14°S. The cruise track crosses an equatorward low-latitude boundary current twice in a traverse of the Gulf of Papua. Tracer properties and water mass characteristics in the new data are described and the net mass flux of the boundary current determined from the observations using an inverse technique. An overview of previous studies in the region is initially presented in order to provide some context for the analysis to follow.

3.2.2 Historical Overview

Water Masses

In a series of papers in the early 60's, Wyrtki(1960, 1961 and 1962) first described the hydrographic climatology and circulation of the Coral Sea and the waters to the south in the Tasman Sea. Using ship drift data, he showed that the currents in the surface layer are highly seasonal and correlate with the annual change in wind regime. From April through December steady south-east Trade Winds blow across the Coral Sea, while during December to March, the Australian Monsoon brings lighter and more variable north-westerlies. Wyrtki also characterizes the Coral Sea as an area of convergence in the upper layer, specifically during the Trade Wind Regime when the surface currents are flowing toward the Australian and Papuan coasts due to the Ekman drift.

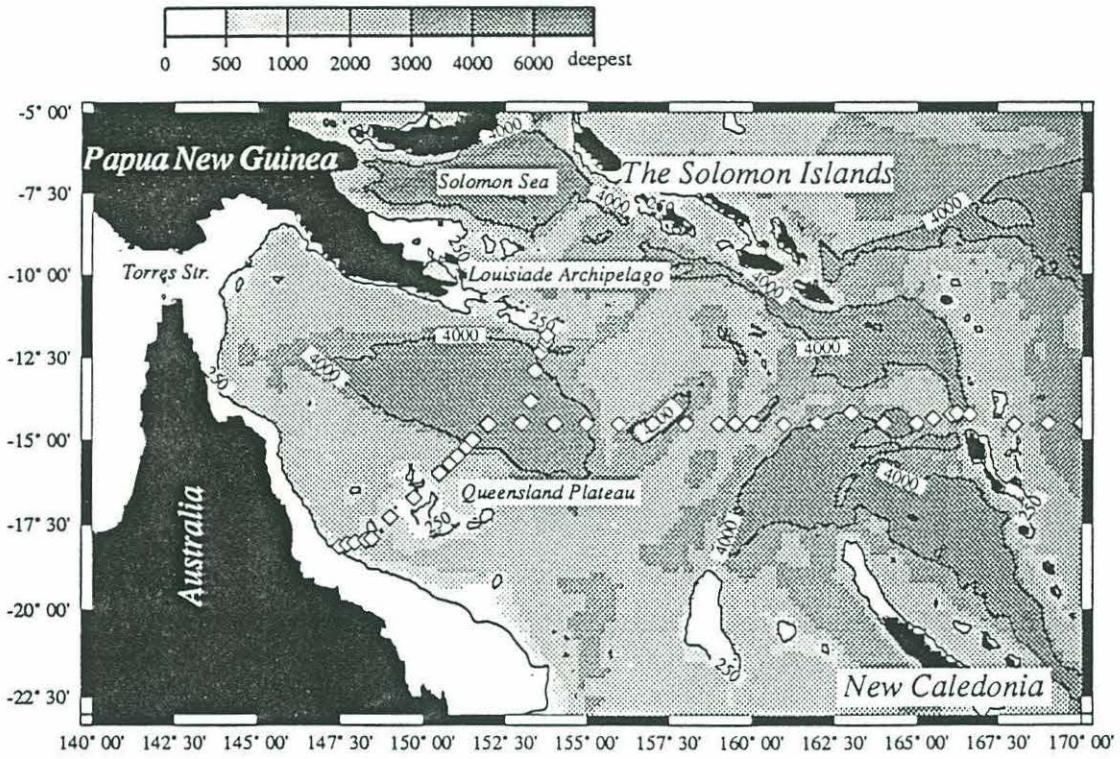

Figure 3.4 Topography of the Coral Sea. The positions of the TEW cruise track is indicated by the white diamonds. The two contoured depths are 250m and 4000m.

The major water masses found in the region and their movement are shown in Figure 3.5, taken from Wyrtki (1962). Subtropical Lower Water (STLW) is characterized by a salinity maxima below the relatively fresh mixed layer.There are two versions of STLW which form a front in the eastern Coral Sea, and are distinguished by oxygen content and salinity. This point was refined later in work by Tomczak and Hao (1989).

Associated with and below the Subtropical Lower Water (STLW) is an oxygen minimum which Wyrtki suggested is formed by *in situ* consumption through oxidation of organic detritus falling from the mixed layer. This low oxygen influence is indicated as originating from to the north and east of the Coral Sea i.e. the central and eastern equatorial Pacific. Antarctic Intermediate Water (AAIW) is characterized by an oxygen maxima and salinity minima found at 700 - 800m depth in the Coral Sea, and originates along the Subpolar Front at high southern latitudes.

At around 3000db is an oxygen minima which Wyrtki (1962) attributes to a North Pacific origin, and must be NPDW. This layer overlies bottom water which is high in both salinity and oxygen. The bottom water in the Coral Sea basin is ventilated by waters of Antarctic origin via the Tasman Sea. The sill linking the Tasman and Coral Seas has a maximum depth of 2800m. Wyrtki's (1961) water mass analysis shows that the sill controls the deep water characteristics of the Coral Seas and those linked to it to the north. This is despite the fact that deeper passages allow for communication between the Coral Sea basin, Solomon Sea and Trench with the Central Pacific Basin to the north.

Rochford (1968) analyzed water masses in detail along the $\sigma_\theta = 26.0\ kgm^{-3}$ density surface, which is in the lower thermocline in the Coral Sea at an average depth of 300m. In agreement with Wyrtki(1962), he found that the waters at this level are a mixture of northern and eastern equatorial waters (with low oxygen) and south Pacific waters formed along the tropical and subtropical convergence zones (with high oxygen).

Tomczak and Hao (1989) (TH89) further illustrated the presence of two thermocline water masses in the eastern Coral Sea. They defined two water masses in terms of θ-S curves, and showed that most of their hydrographic casts from the Coral Sea fell on either one or the other of these curves. A sharp zonal front divides the two types of thermocline water as suggested earlier by Wyrtki (1962). TH89 referred to the water mass of eastern equatorial origin as Pacific Equatorial Water (PEW) which is distinguished from its neighbor by higher

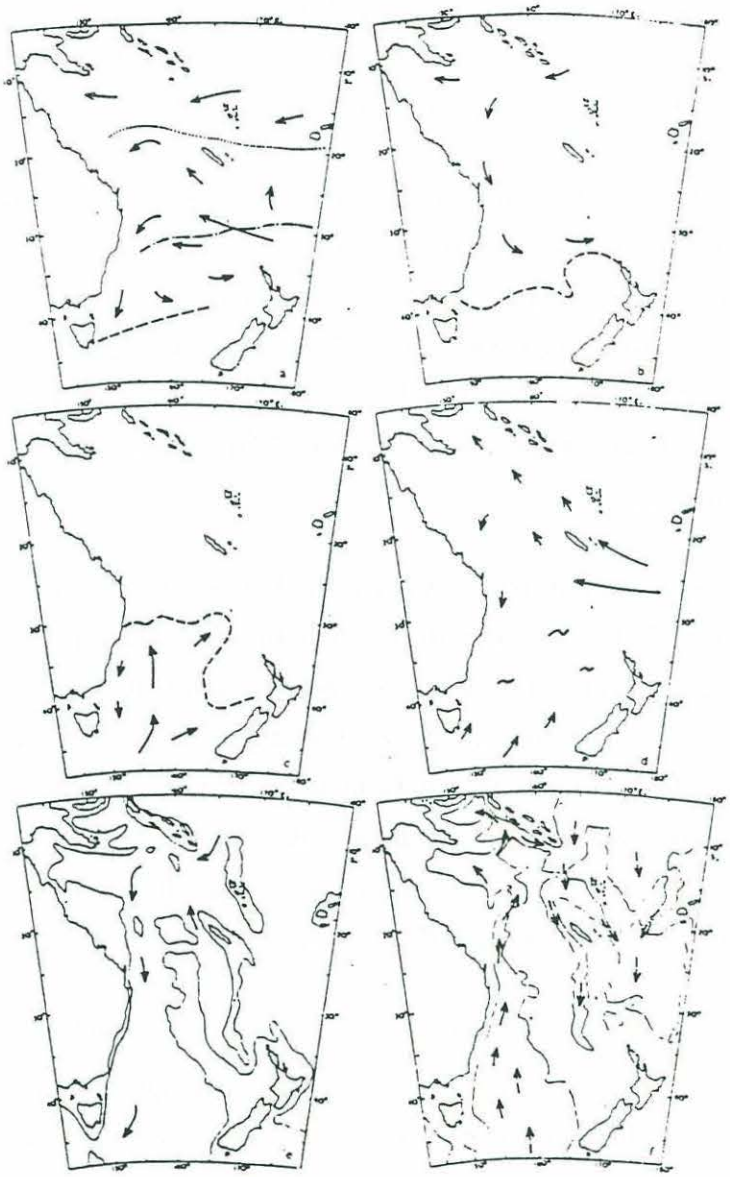

Fig. 17.—The spreading of the different water masses, as derived from the distribution of properties in their core layers. (*a*) Subtropical Lower Water, salinity maximum. . . . . Boundary between northern and southern component; ·—·—· Tropical Convergence; – – – – Subtropical Convergence. (*b*) Upper oxygen minimum. (*c*) Subantarctic Intermediate Water, oxygen maximum. – – – – Northern boundary. (*d*) Antarctic Intermediate Water, salinity minimum and oxygen maximum. (*e*) Deep oxygen minimum. The thin line gives the 2000-m depth contour. (*f*) Deep Water ⟶ Bottom Water ⟶. The thin line gives the 3000-m depth contour.

Figure 3.5 Taken from Wyrtki (1962), showing the circulation of the subsurface water masses based on a sparse set of hydrographic data.

salinities in both the upper thermocline and AAIW layer. Western South Pacific Central Water (WSPCW) is formed in the Tasman Sea and has lower salinity than PEW in the thermocline and in the AAIW (indicative of its more direct route to the Coral Sea from the south). In contrast to the core layer methodologies used by Rochford and Wyrtki, in which the water masses are predominantly vertically stacked, TH89 suggest that PEW and WSPCW occupy the entire thermocline (and considerably far below it) and are simply advected into the Coral Sea laterally with their θ-S relationships intact. We will be using the TH89 method to identify the distribution of the two thermocline water masses in the Coral Sea, and so will adopt their nomenclature: PEW for the northern water type and WSPCW for the southern water type.

Geostrophic Circulation

Water mass analyses give one an idea of the expected direction of flow based upon their origins in the Pacific basin. There also exist several studies which have determined the geostrophic flow fields in the Coral Sea region in an attempt to quantify the circulation.

Scully-Power (1973) employed a grid of hydrographic stations throughout the entire Coral Sea and analyzed the geostrophic flow relative to 1500db. The large scale features of the thermocline flow are: an inflow from the east between New Caledonia and the Solomon Islands, which is the South Equatorial Current (SEC). The SEC is the northern arm of the huge South Pacific subtropical gyre and extends across the entire basin. Impinging upon the Australian land mass, this westward flow bifurcates at about 20°S, with some streamlines directed southward to form the East Australian Current (EAC). Most of the westward directed streamlines turn northward and form a clockwise gyre in the western Coral Sea, with some outflow to the Solomon Sea. Scully-Power suggests that the flow exiting equatorward from the Coral Sea, eventually feeds the Equatorial Undercurrent. He also notes that the far northwestern Coral Sea showed considerable variability and that no regular pattern in dynamic height could be discerned there.

Employing inverse methods, Fiadeiro and Veronis (1982) determined a mass-conserving circulation for a large box that contained most of the Coral and Tasman Seas. They also found the clockwise gyre in the thermocline of the Coral Sea, with a net transport of $25 \times 10^6 m^3 s^{-1}$. Since their data set contained casts that penetrated to the bottom, flow directions in the deeper layers were also found. Of interest to the present analysis is an anticlock-

wise gyre found in the deep oxygen minimum layer. A comparison of the flow field determined by Fiadeiro and Veronis (1982) shows that Wyrtki's early analyses are consonant with a mass-conserving geostrophic flow field.

Andrews and Clegg (1989, hereafter AC89) have carried out the most recent analysis of the circulation in the Coral Sea. Using a comprehensive set of synoptic CTD measurements, AC89 derived a mass budget for the region as shown in (Figure 3.6)[1]. The data used consisted of CTD lines that criss-cross the Coral Sea and form several closed boxes. AC89 minimized abyssal velocities and conserved top to bottom transport in each closed box. Mass conservation in density layers as used by Fiadeiro and Veronis (1982) was rejected for reasons not stated.

The AC89 study reveals several new features of the flow not seen before. In the upper 1000m, the South Equatorial Current flows into the Coral Sea from the east, mostly from between Vanuatu and the Solomon Islands. Of 24Sv of inflow, 10Sv exits north directly into the Solomon Sea, and the remaining part flows westward. This flow impinges upon the north-east Australian coast and bifurcates at 18°S, with 4Sv flowing north as a narrow western boundary undercurrent into the Gulf of Papua and 6 SV exiting south, presumably to contribute to the East Australia Current.The boundary undercurrent entering the Gulf of Papua returns along the southern coast of Papua New Guinea as another narrow boundary current which flows around the tip of the Louisiade Archipelago and into the Solomon Sea. This circulation pattern agrees with the qualitative sense of flows described in earlier works.

The important features of the AC89 circulation scheme that will be compared with that derived here, are: a barotropic recirculation at the mouth of the Gulf of Papua; the fact that the undercurrent circulating around the Gulf of Papua is seen at all continental shelf crossings except one, where they assume it has moved offshore into deeper water.

The thermocline flow described by these studies is consistent with the large scale Sverdrup flow as found by Godfrey (1989). He shows that the SEC impinges upon the Australian coast bifurcates at about 18°S, forming a 20Sv equatorward boundary flow. Of this boundary current, 10Sv recirculates in the Coral Sea and 10Sv rounds the eastern tip of the Lou-

1. In Andrews and Clegg (1989) Figures 7 and 8 are mislabelled, and the figures should be swapped.

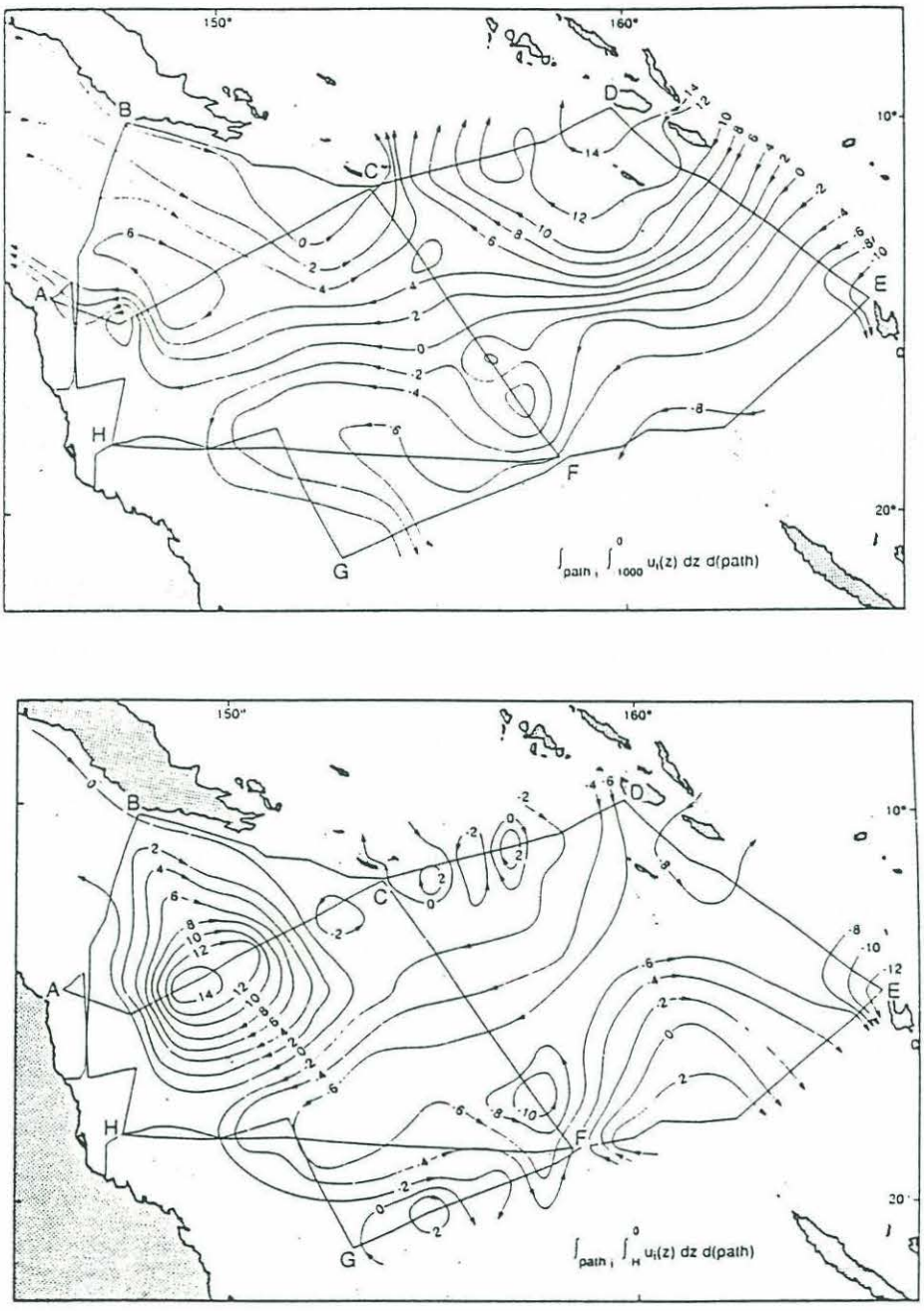

Figure 3.6 Contours of volume transport from Andrews and Clegg (1989). Contour interval is 2Sv. (a) upper 1000m and (b) total water column.

isiade Archipelago and flows along the northern coast of Papua New Guinea (PNG) to flow through the Vitiaz Strait. In the Sverdrup model this streamline contributes to the Throughflow via the Indonesian archipelago.

Lindstrom *et al.* (1987) and Tsuchiya *et al.* (1989) have speculated that the boundary currents in the Coral Sea feed the flow through Vitiaz Strait that was first observed during the WEPOCS studies. Tsuchiya *et al.* (1989) find that part of the flow through Vitiaz Strait is retroflected east to contribute to the Equatorial Undercurrent, and part must either exit the Pacific in the Throughflow or flow across the equator into the North Pacific.

The boundary currents in the Coral Sea are clearly important in the basin-wide mass balance. The high resolution data set utilized below may provide the best measurements of these boundary currents to date.

3.2.3 The Data

The data are from the Transport of Equatorial Water (TEW2) cruise made aboard *Oceanographer* in July 1987, and described by Magnum, *et al* (1987). The last 20 stations taken on TEW2 form a section across the mouth of the Gulf of Papua from the tip of the Louisiade Archipelago to Townsville at about 18°S on the north eastern coast of Australia (Figure 3.7). As this is the western end of a transpacific crossing at nominally 14°S, the station order is from 90 in the middle of the Coral Sea, heading north through to station 94 at the continental shelf break of Papua New Guinea. The ship then steamed south to resume the section from mid-basin onto Townsville, across the Queensland Plateau, so that 30 hours passed between taking the two mid-basin casts, 89 and 96.The original 2db CTD/O_2 data was interpolated onto 10db pressure intervals after applying 5db boxcar filter.

Two aspects of the data set make it novel among studies in the Coral Sea: each CTD/O_2 cast is to full depth; and the station spacing across the very narrow continental slope regions is small (~ 15km) giving good resolution of the boundary currents. In comparison, all previous data sets had coarse spacing and not all stations were to full depth. This is due to the trade-off made in those studies of resolution against large spacial coverage in a small amount of time.

3.2.4 Property Distributions

A mixed layer of about 100m is present across the section, which becomes slightly shal-

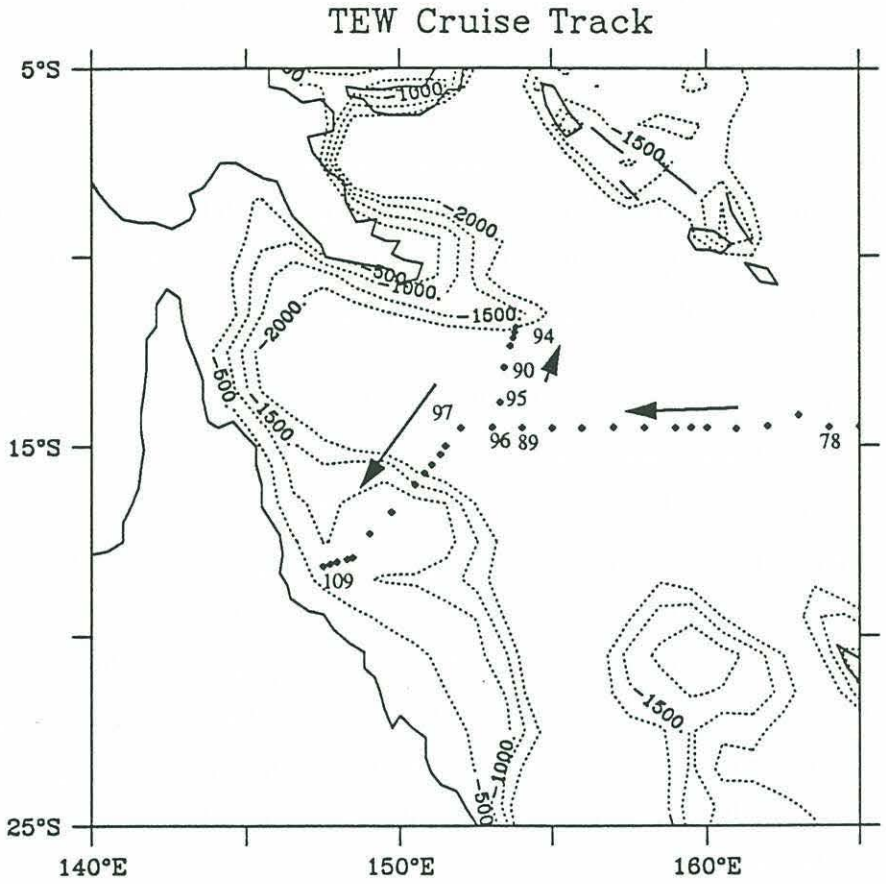

Figure 3.7 Position of the stations taken in the Coral Sea during the TEW Transpacific Cruise.

lower, fresher and warmer towards PNG (Figure 3.8). At the base of the mixed layer there is a sharp transition to a high salinity, low oxygen layer, which is embedded in the upper thermocline. This is the STLW described by Wyrtki. At a depth of between 600 and 100m, and centered at $\sigma_\Theta = 27.2$, is a salinity minimum layer which is the AAIW, with its related oxygen maxima just above.

A second oxygen minimum exists between 1500 and 2000m with an extrema at $\Theta = 2.5°C$ and S = 34.6. This layer is believed to be influenced by North Pacific Deep Water (Wyrtki, 1962). Oxygen and salinity both increase below this depth to the floor of the Coral Sea basin indicating the influence of Lower Circumpolar Water.

In order to detect the presence of two water masses in the sense that TH89 define them, salinity and oxygen anomalies were calculated on σ_Θ surfaces and are shown in (Figure 3.9). Here, anomalies are defined with respect to a section mean profile in σ_Θ co-ordinates. As was found by TH89, two distinct thermocline water masses appear, divided by a front 600km offshore from the coast of Australia. The front is located over the Queensland Plateau continental slope. North of the front, the upper thermocline is relatively salty and the lower thermocline is fresh ($\Delta S = 0.02$ psu). This northern water mass is also distinguished by a lower oxygen content, and corresponds to PEW as described by TH89. South of the front, water of opposite anomaly in both salinity and oxygen dominates, and fits the description of WSPCW.

3.2.5 Geostrophic Circulation Relative to the Bottom

Geostrophic velocities were initially calculated relative to the bottom. Over the continental slopes are several large bottom triangles. To extrapolate the velocity to the bottom of the deepest cast, the shear from the neighboring deeper station pair was used. For station pair 102-103, over the Queensland Plateau, this technique resulted in unreasonable velocities and velocity was simply linearly extrapolated to the bottom.

Flowing northwest across the section along the coast of Australia and in the Queensland Trough is an undercurrent which has two cores at about 450m and maximum velocities of15 cms^{-1} (Figure 3.10). The northward velocity cores occur at the same station pairs as the high oxygen cores in the AAIW.

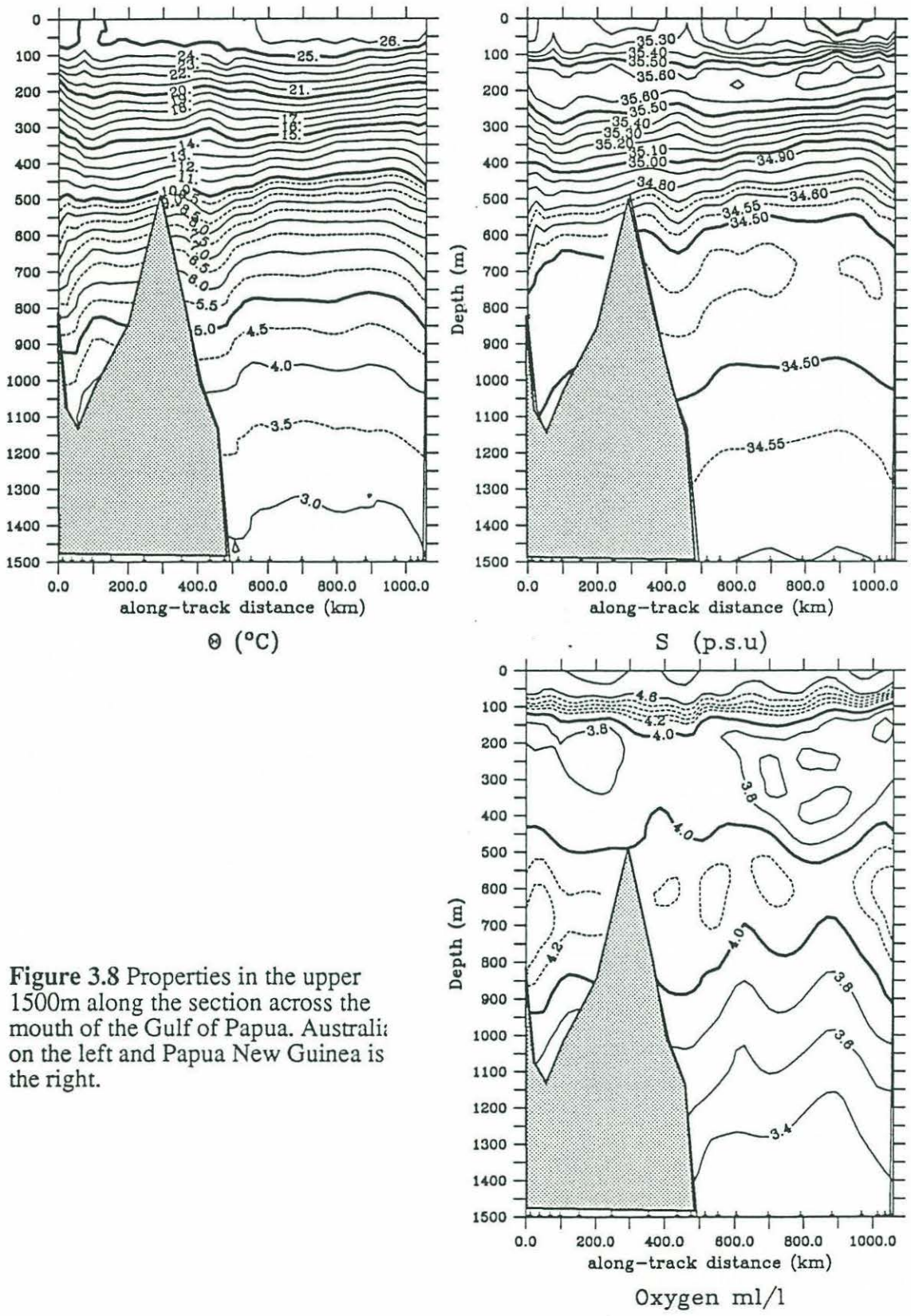

Figure 3.8 Properties in the upper 1500m along the section across the mouth of the Gulf of Papua. Australia on the left and Papua New Guinea is the right.

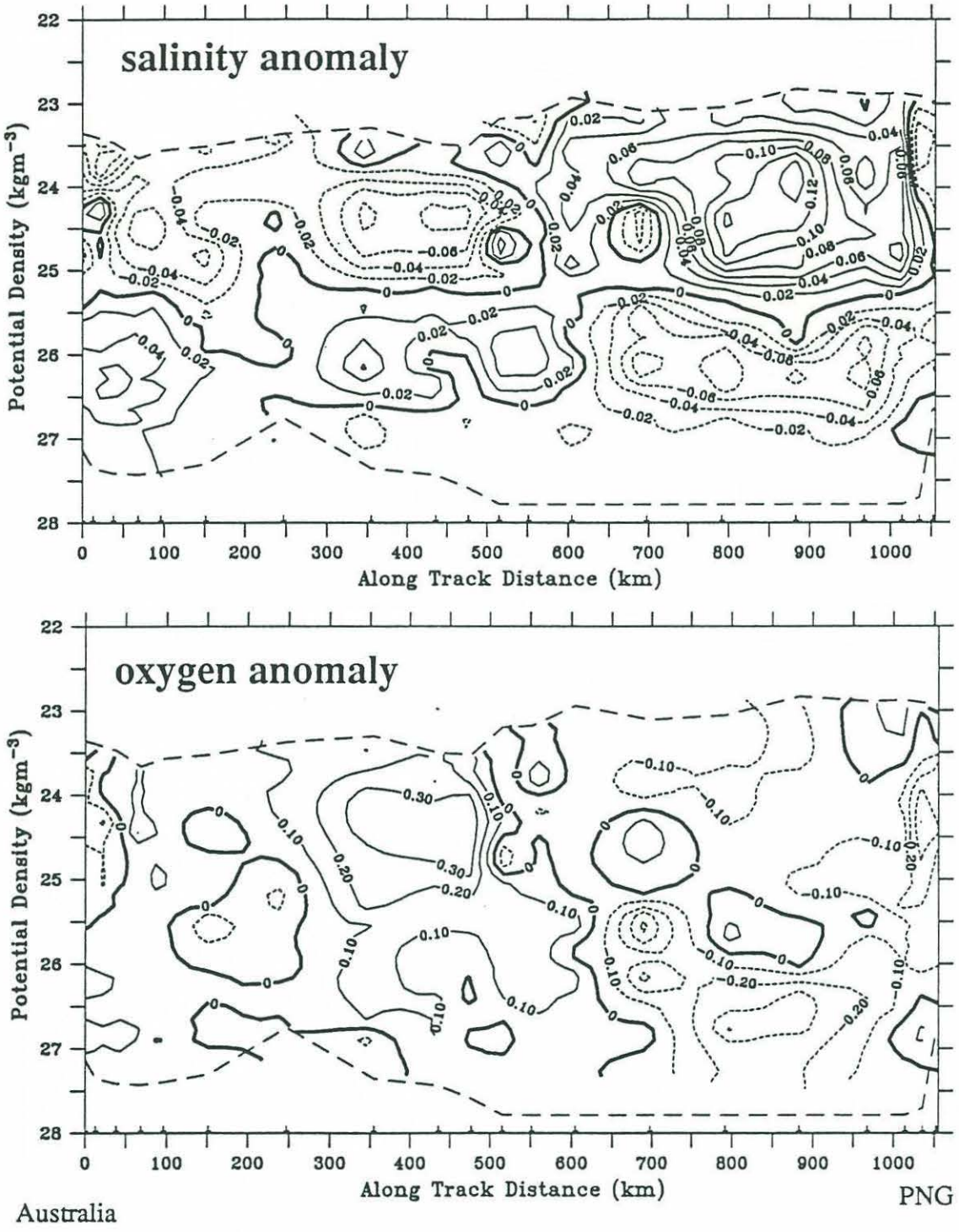

Figure 3.9 Salinity (top) and oxygen (bottom) anomalies on potential density surfaces plotted in potential density co-ordinates. Anomalies are defined relative to a section.

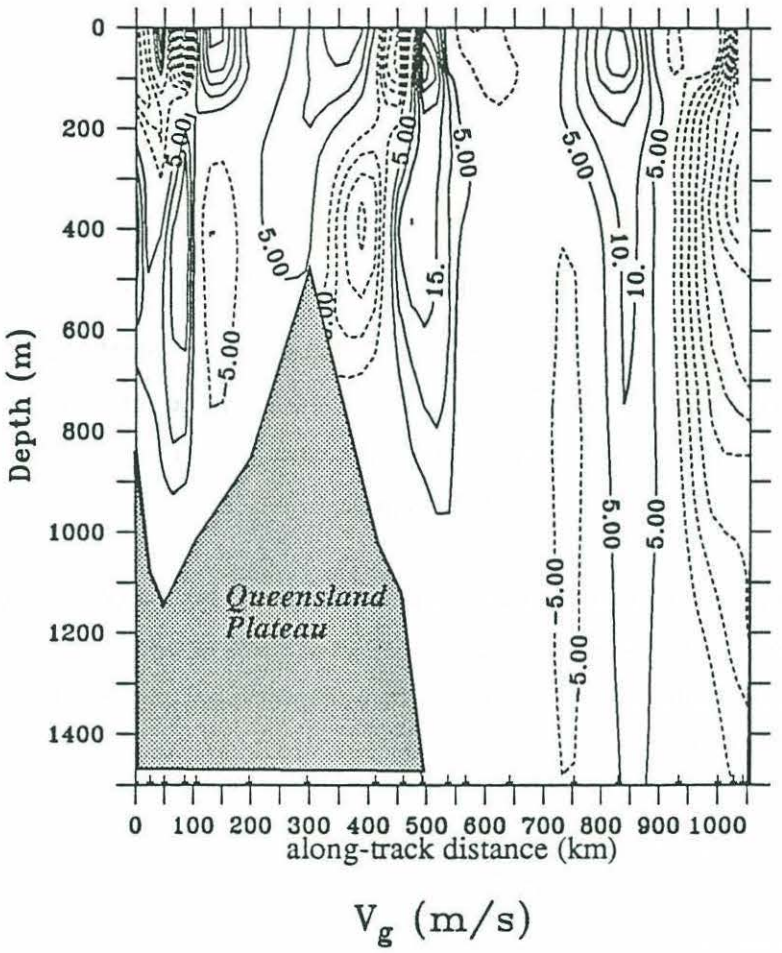

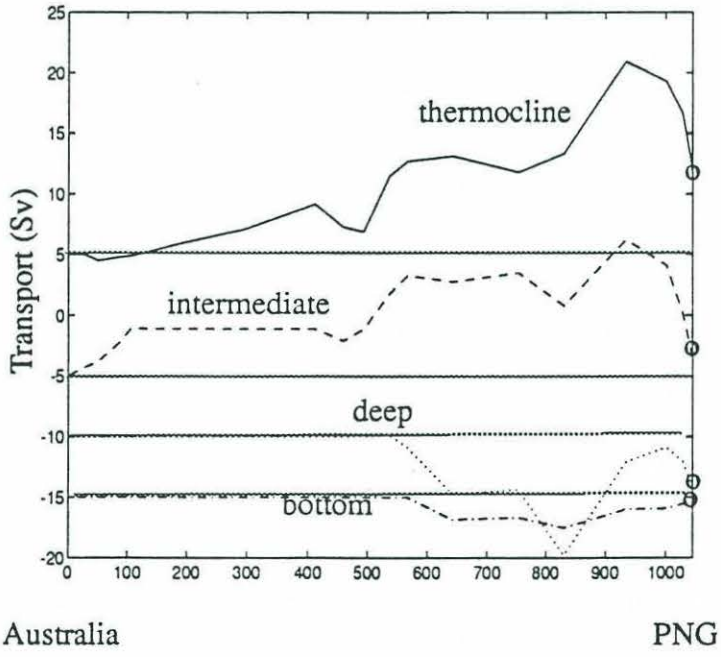

Figure 3.17 (a) Geostrophic velocity relative to the bottom in the Coral Sea. (b) Geostrophic transport stream function in density layers, integrated from the coast of Australia. Each layer is offset by 5Sv.

Layer	Definition	~Θ Equivalent
thermocline	$\sigma_\Theta < 26.5$	$\Theta > 12.5°C$
intermediate	$26.5 < \sigma_\Theta$; $\sigma_2 < 36.5$	$12.5 > \Theta > 3.9°C$
deep	$36.5 < \sigma_2 < 37.0$;	$3.9 > \Theta > 1.8°C$
bottom	$37.0 < \sigma_2$	$\Theta < 1.8°C$

Table 3.3 Definitions of isopycnal layers used in the analysis.

On the east flank of the Queensland Plateau, an anticlockwise eddy-like feature is located above the shelf slope. The northwestward (offshore) arm of this eddy is more intense in both its velocity and oxygen signature, and, as will be seen below plays a significant role in the mass budget across the section.

Along the PNG shelf slope is a swift ($80cms^{-1}$) coastally-trapped current which is surface intensified close to the coast, and an undercurrent offshore. Further offshore from PNG is a surface intensified feature, which transports low oxygen and higher salinity thermocline PEW into the Gulf of Papua.

Four isopycnal layers were chosen to represent the major water masses described previously, and are defined in Table 3.3. The terms 'inflow' and 'outflow' in the following discussion refer to currents entering or leaving the Gulf of Papua respectively. The transport was also calculated for groups of stations pairs that reflect the main boundary current locations (Table 3.4).

Layer	**Qld. Plateau**	**Qld. Slope**	**Basin**	**PNG Slope**	**NET**
station pairs	109-105	105-97	97-95,90-91	91-94	all
thermocline	1.0	7.1	7.8	-10.4	5.6
intermediate	3.9	3.9	3.4	-11.3	0.0
deep	0.	-4.7	2.6	-2.2	-4.2
bottom	0.	-1.8	0.9	0.4	-0.5
NET	4.9	4.4	14.8	-23.4	0.8

Table 3.4 Geostrophic transport into the Gulf of Papua relative to the bottom. Positive values are into the Gulf of Papua.

Relative to the bottom, there is a broad thermocline inflow of 16Sv across the section, 10Sv of which flows out of the gulf along the coast of PNG (Figure 3.10b). The two current cores associated with the oxygen maxima in the Queensland Trough and slope dominate the intermediate water stream function and transport 11.2 Sv into the basin. Nearly all of the inflow leaves in the boundary current along the coast of PNG. In the deep and bottom layers an anticyclonic gyre is found, which is in the opposite sense to the cyclonic flow above.

3.2.6 Mass Budget

The Louisiade Archipelago consists of barrier reefs and shallow lagoons which are generally less than 30m deep. Similarly, Torres Strait is shallow and choked with reefs (Pickard, *et al.*, 1977). In a steady state, then, we would expect that net transport into in the Gulf of Papua should be small.

The net geostrophic transport relative to the bottom across the section is only 0.8Sv. The Ekman transport across the section is 0.2SV out of the Gulf based on the observed station ship winds as reported in Magnum *et al.* (1989). The cruise was carried out during the season of strong steady southeast trades which had typical speeds of $8ms^{-1}$. However, these steady winds were perpendicular to the cruise track, and make little contribution to the cross-track mass flux.

Despite the fact that the net mass flux is essentially zero across the section, there are substantial imbalances in the isopycnal layers. In a steady state these imbalances imply a production of dense water in the Gulf of Papua which is unlikely. Alternatively, the flow may not be steady and the net thermocline inflow of 6Sv may be balanced by storage changes in the Gulf of Papua. If the thermocline retains it shape and simply depresses, then the observed inflow is equivalent to a deepening of order $1.0 \times 10^{-5} ms^{-1}$ or 1.0 m/day. It is likely that large-scale long-waves can deepen the thermocline over the entire Gulf of Papua at this rate. Scully-Powell(1973) noted strong time variability of the North-western Coral Sea, and Toole *et al* (1990) reported similar vertical velocities off the coast of the Philippines at a similar latitude.

Despite the possibility that the circulation measured by the data set is not steady, it is still instructive to derive a circulation that conserves volume.

Inverse Solution

We use a least-squares box model inversion to adjust the circulation so that mass is conserved in density layers. The formalism has been laid out in numerous papers (e.g. Wunsch, 1978; Roemmich, 1979; Fiadeiro and Veronis, 1982) and will not be repeated here.

A set of bottom velocities are found that adjusts the circulation such that mass is conserved in the four density layers to within 1Sv. The problem has 4 constraints and 19 unknowns (the station pair bottom velocities), and was solved by a damped-least squares solution which minimized the bottom velocities. Adding more isopycnal layers did not change the character of the solution much, nor did changing the initial guess reference level as long as it was below 2500 db. The latter result is simply an indication of the weak shears below this level.

The largest adjustments occur over shallow topography, with velocities of over $5cms^{-1}$ being added over the Queensland Plateau at depths of around 1000m (Figure 3.11). In the Coral Sea basin, abyssal velocities remain small ($1cms^{-1}$). The corrected velocity field has intensified the deep anticlockwise circulation around the Coral Sea basin, and weakened the upper layer clockwise flow. The excess transport in the thermocline layer has been removed by a southward flow over the Queensland Plateau, which also reduces the intermediate water transport over the Plateau.

Layer	Qld. Trough	Qld. Plateau	Basin	PNG Slope	NET
station pairs	109-105	105-97	97-95,90-91	91-94	all
thermocline	0.9	2.0	7.8	-9.6	0.9
intermediate	3.9	2.1	3.2	-10.1	-0.9
deep	0.	-2.7	1.8	0.7	-0.2
bottom	0.	-2.0	-0.4	2.6	0.2
NET	4.8	-0.5	12.2	-16.4	0.1

Table 3.5 Geostrophic transport into the Gulf of Papua in the mass-conserving circulation. Positive values are into the Gulf of Papua.

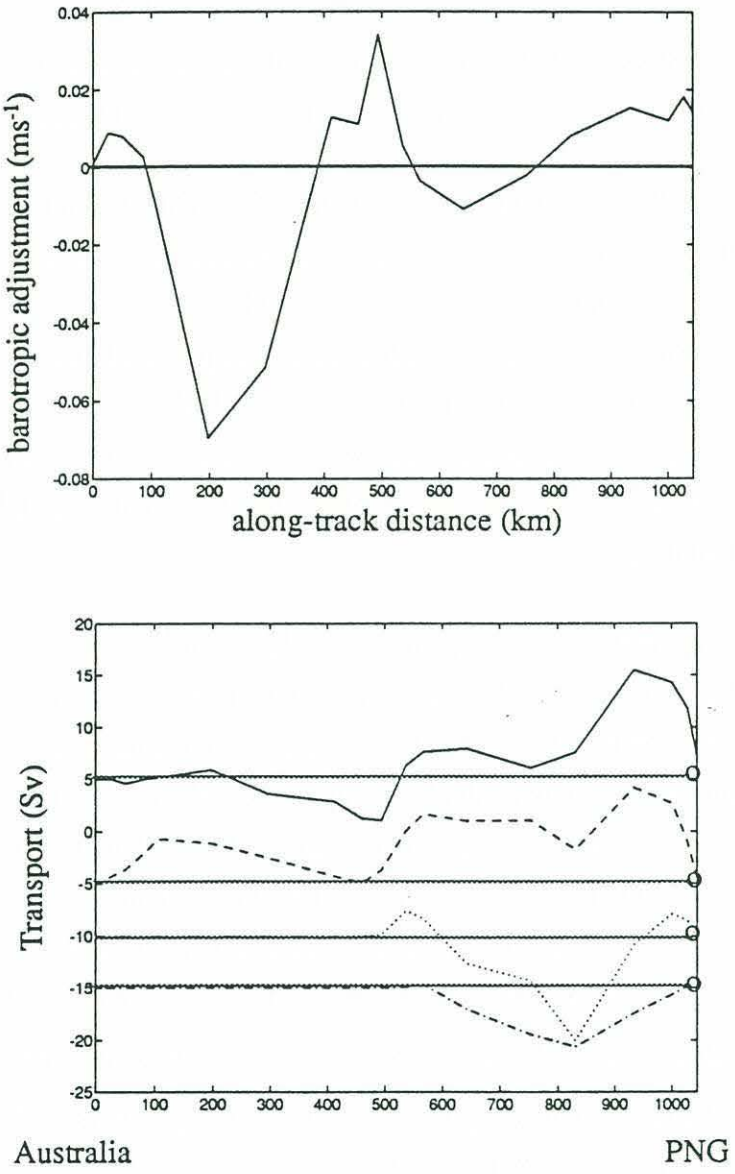

Figure 3.11 (a) Barotropic adjustment to the bottom relative circulation derived from the inverse calculation; (b) transport stream-function for the mass-conserving solution.

3.2.7 Results and Discussion

The equatorward undercurrent in the Queensland Trough has been previously observed by Church and Boland (1983) in each of nine sections taken over a two year period. This suggests that it is a permanent feature of the circulation. Church and Boland (1983) also observed a double core structure in the velocity field, similar to that seen in Figure 3.10. In a broader survey Church (1987) also observed the undercurrent to at least 14°S.

The strong equatorward flow along the offshore slope of the Queensland Trough has not been mentioned in previous studies and may therefore be a transient feature. Along with the undercurrent in the Trough, though, this current is needed to balance the transport of 20Sv of intermediate and thermocline water out of the Gulf of Papua south of PNG. The top to bottom circulation forms an cyclonic cell of between 16 and 24Sv, depending whether one takes the mass-conserving or bottom-relative flow. This cyclonic circulation is remarkably similar to the flow described by Fiadeiro and Veronis (1982) and that required by Godfrey's (1989) Sverdrup calculation.

It is not clear whether the mass-conserving circulation is any more meaningful than the bottom-relative circulation given the likelihood of aliasing by transients during the survey. We are lucky in that we can compare the circulation from the TEW data with a study based on more than just one survey. In a new study, Ridgway and Godfrey (1993) used historical XBT, hydrographic and ship-drift data to construct a circulation that conserves mass in deep density layers in a large box that contains most of the Tasman Sea. As part of this study, they calculate the flow across 15°S between Australia and 170°E. Along the Queensland coast they find a net thermocline flow ($\sigma_\Theta < 26.5$) of 7.2Sv northward, and an intermediate water flux ($26.5 < \sigma_\Theta < 27.0$) of 6.7 Sv northwards. These transports agree well with the estimated 8.0 and 7.8Sv flowing northward over the Queensland Trough and Plateau in the bottom relative circulation found here.

Andrews and Clegg (1989) indicate that the upper water circulating around the Gulf of Papua enters the Coral Sea north of 15°S, between the Solomon Islands and the New Hebrides (Figure 3.6), which implies that this water is from the equatorial Pacific and must be PEW. Our analysis show that the thermocline inflow offshore of the Queensland Trough consists of both PEW and WSPCW from further south. The PEW circulates northward in the anticyclonic gyre and is confined to the northern half of the Gulf of Papua, while the

WSPCW circulates southward over the Queensland Plateau and Trough.

3.2.8 Conclusions

Measurements of the flow across an hydrographic section in the western Coral Sea have been presented. A system of boundary currents which penetrate to below 1000m were found, which carry waters of southern origin (WSPCW and AAIW) into the Gulf of Papua (). Along the coast of Australia, the boundary current has two arms: an undercurrent in the Queensland Trough which carries about 5 Sv northward; and a boundary current along the Queensland Plateau slope of between 10 and 15 Sv. The second outer arm of the boundary current along the Queensland plateau has not been described previously. These two eastward currents supply a westward coastally-trapped current located along the southern coast of PNG of 25SV, and an outflow of thermocline water over the Queensland Trough. The water in the boundary flows are marked by high oxygen cores in the Antarctic Intermediate Water, indicating connectedness at this depth. Hence the lower part of the currents along the Queensland coast flow directly around the Gulf of Papua and out south of PNG.

In the upper layers, a more complex flow is suggested by the water properties. Extending the work of Tomczak and Hao (1989), two distinct water masses occupy the thermocline in the Western Coral Sea, and are separated by a sharp front. Both PEW and WSPCW flow across the section in mid-basin, one circulating to the north in the anticyclonic gyre in the Gulf of Papua, while the other flowing out over the Queensland Trough and Plateau.

The observations described here support the ideas put forward by Scully-Powell (1973) and Lindstrom *et al* (1987) that the boundary currents in the Coral Sea may provide a path for waters of the South Pacific, specifically AAIW to cross the equator, via the undercurrent in the Vitiaz Strait. How much of the flow in the PNG boundary current flows into the Coral Sea remains to be estimated from the remaining part of TEW2 data.

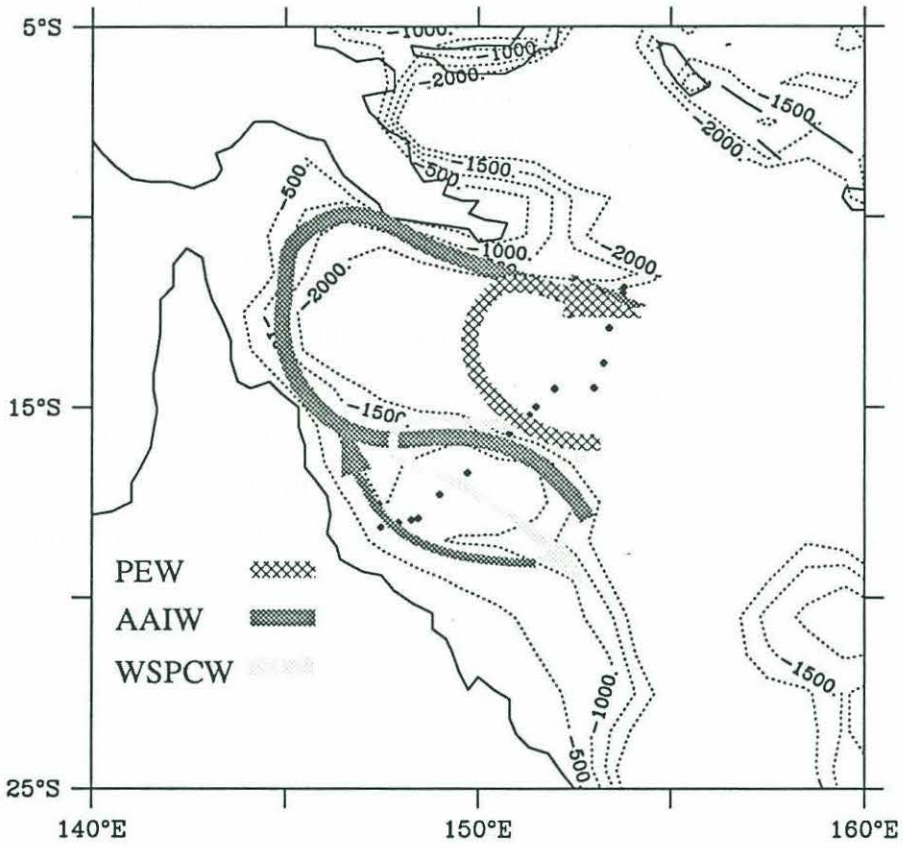

Figure 3.12 Schematic of flow in the Coral Sea of major upper and intermediate water masses. The AAIW is a subsurface water mass.

Chapter 4

A Mean Section at 165°E from Repeat Survey Data

4.1 Introduction

In this section, we attempt to construct a mean section at the 165°E meridian, and deduce the velocity field there. Due to several recent observational programs, the number of repeat cruises is impressive: 23. An more comprehensive study of the upper 1000m of the data and their mean has been carried out by Gouriou and Toole (1993), and the description here shall be brief.

4.2 Data

In recent years the western Pacific has been the location of several intense and long-term observation programs: SURTROPAC (SURveillance TRans-Oceanique du Pacifique), described in Delcroix *et al* (1987); PROPAC (PROductions Plagique dans le PACifique); TEW (Trans-Equatorial Waters) Leg 3 data (Magnum, *et al.*, 1991); and the USPRC-TOGA program (Cook, *et al.*, 1991). These data span the time period during-which the one-time zonal sections were made. In total, 23 cruises are available to construct a mean section at 165°E (Table 4.1). The upper 500m within 5° of the equator is sampled by all cruises, and the data coverage within 10° of the equator is good to 2000db. South of 10°S and deeper than 2000db, the observation density falls off rapidly (Figure 4.1).

Over most of the section, the station positions on the cruises were the same: every degree poleward of 3°; every half a degree equatorward of 3°. South of 7°S, the US-PRC/TOGA cruises angled to the west to 10°S, 162°E along the Solomon Island chain.The SURTRO-PAC cruises continued south to New Caledonia, and only a subset of these of station positions were chosen for the mean section, starting at 9°N and ending at 14°S. In this way the mean section station grid lies between the two synoptic sections.

All casts within 3° of longitude and 0.2° of latitude of a given position on the mean grid were averaged together. In order to preserve the water mass structure, averaging was carried out on potential density surfaces, using the same method as in section. As noted previously, it is difficult to uniquely define a mean stratification in the upper thermocline which is affected by excursions of the mixed layer depth. On a few stations the mixed layer depth

Cruise	Months	Year
SURTROPAC 1	Jan.	1984
SURTROPAC 2	Aug.	
SURTROPAC 3	Jan.	1985
SURTROPAC 4	Jul.	
SURTROPAC 5	Jan.	1986
US/PRC 1 *	Feb.	
SURTROPAC 6	Jun.	
US/PRC 2 *	Dec.	
SURTROPAC 7	Jan.	1987
JENEX	Feb.	
SURTROPAC 8	Jul.	
TEW 3	Jul.	
PROPAC 1	Sep.	
US/PRC 3 *	Oct.	
SURTROPAC 9	Jan.	1988
PROPAC 2	Mar.	
US/PRC 4 *	May	
SURTROPAC 10	Jun.	
PROPAC 3	Sep	
US/PRC 5 *	Nov.	
MW893 *	Feb.	1989
US/PRC 6 *	May	
US/PRC 7 *	Nov.	1990
US/PRC 8 *	Jun.	

Table 4.1 Month and year of the cruises that contribute to the mean sections at 165°E and 8°N. All the cruises except the MW893 occupied the 165°E section, while only the surveys starred occupied the 8°N section

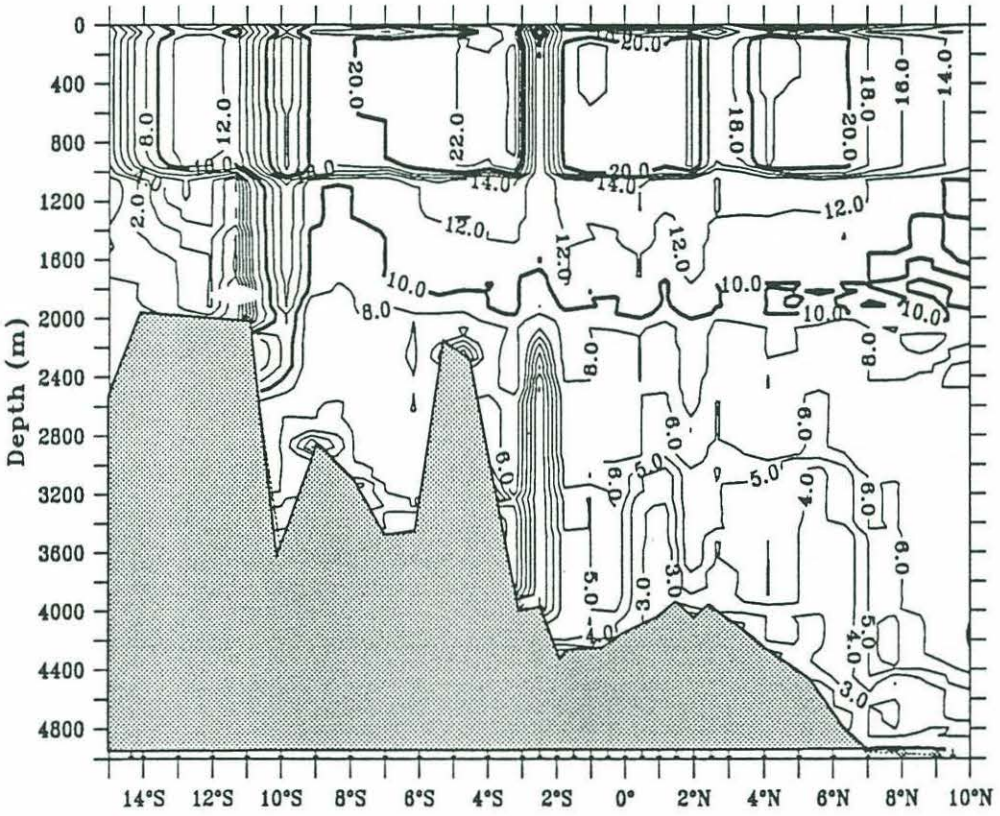

Figure 4.1 Density of hydrographic observations along 165°E. Contour interval is 2. except below 5, where it changes to 1.

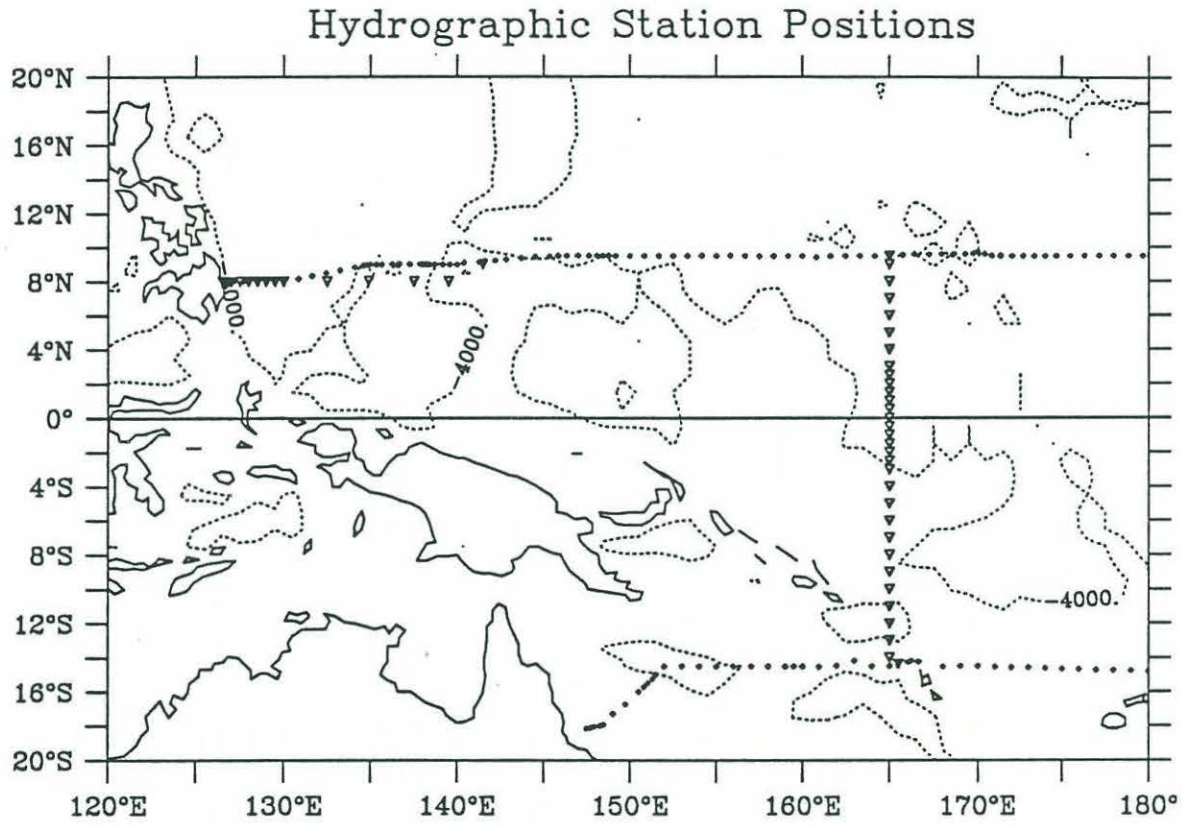

Figure 4.2 Positions of the stations chosen for constructing the mean hydrographic transect at 165°E

penetrated to great depth (~200m, σ_Θ = 23.0), though in general it remained above σ_Θ= 22.5.

4.3 Mean Sections and Water Masses

Along the mean section the mixed layer density is dominated by salinity, with temperature remaining fairly uniform both horizontally and vertically to 80m. Two pools of light, fresh water reside on either side of the equator, resulting in much shallower mixed layer depths than indicated by temperature. These fresh pools have been referred to as the barrier layer since they must be eroded away before the cool water in the thermocline can be drawn into the mixed layer. On the equator, the mean salinity is higher, as is the density. This is a result of several upwelling events sampled in the synoptic sections.

The water masses in the thermocline reflect the equatorward convergence of waters having subtropical origin. Dominating the thermocline in the southern hemisphere is the high salinity tongue of SPTW centered at σ_Θ = 24.5. At lighter densities, and lower salinities, a core of North Pacific Tropical Water extends toward the equator from the north. Below the NPTW, the shallow salinity minimum evident along the MW893 section is also seen to extend equatorward (referred to here as CCW). At the equator, a sharp salinity gradient exists, which intensifies in the lower thermocline. As noted by Gouriou and Toole (1993) the sharpest horizontal gradient shifts to 3°N below the Equatorial Undercurrent.

While the salinity distribution suggests a meridional circulation, dissolved oxygen concentrations in the thermocline reveal the effects zonal advection. The eastward EUC, NECC and the SSCCs are associated with oxygen maxima on isopycnal surfaces (Figure 4.4). Westward currents (SEC and EIC) have lower values. Higher oxygen values in the NECC compared to the SEC suggest that the near equatorial portion of the SEC does not have its source in recently ventilated subtropical gyre water. This low oxygen SEC water is PEW identified by Tomczak and Hao (1989).

Below the thermocline, a salinity minimum extends across the equator (Figure 4.5). When examined on Θ surfaces, however, two individual cores associated with the AAIW and NPIW are apparent, the former centered at 5.5°C in the south and the latter at 6.0°C in the north (Figure 4.6). The two intermediate waters are distinguishable by their oxygen content: NPIW has extremely low oxygen concentrations, while AAIW is enriched. Oxygen

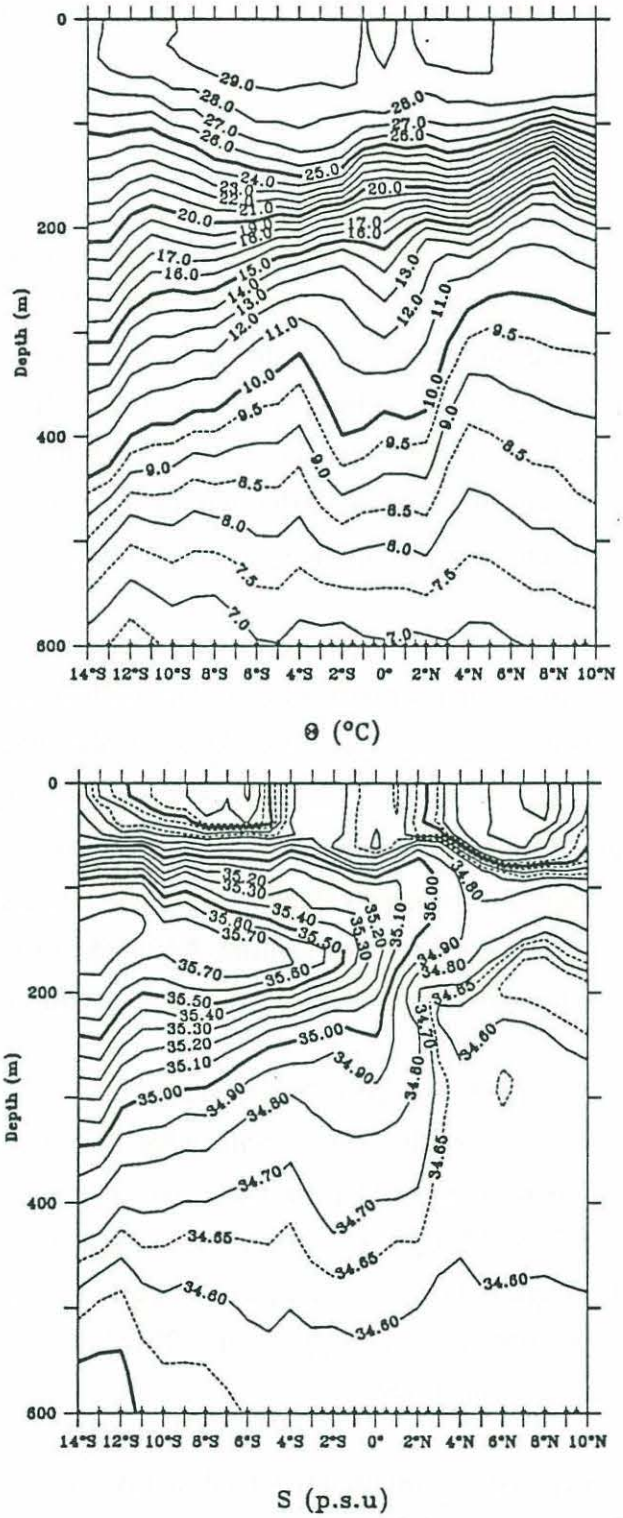

Figure 4.3 Properties along 165°E: (a) mean potential temperature; (b) mean salinity; (c) mean potential density; (d) dissolved oxygen concentrations for US/PRC-TOGA 3.

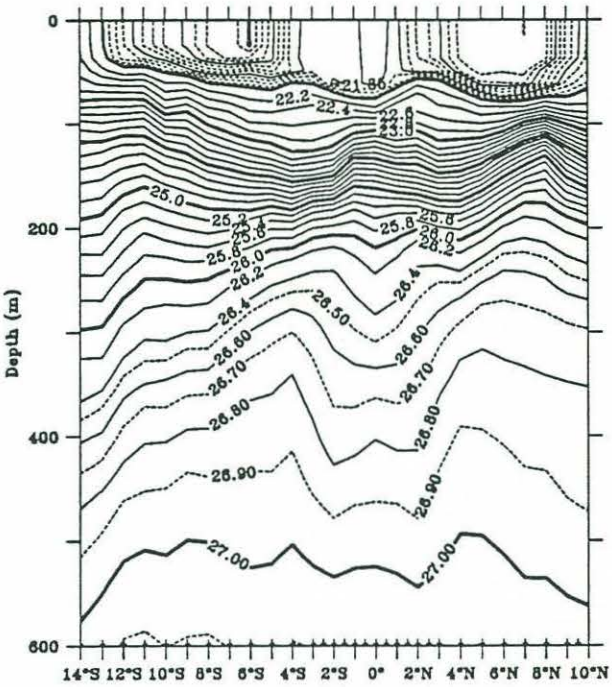

σ_θ (kgm^{-3})

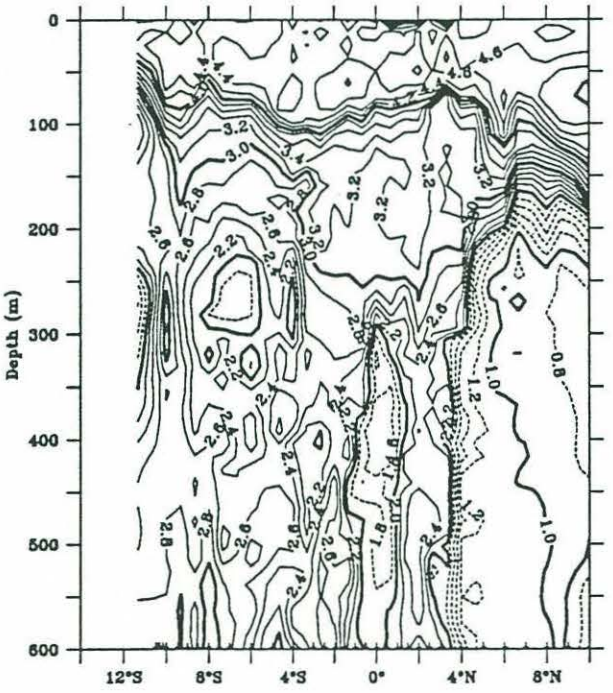

dO_2 (ml/l)

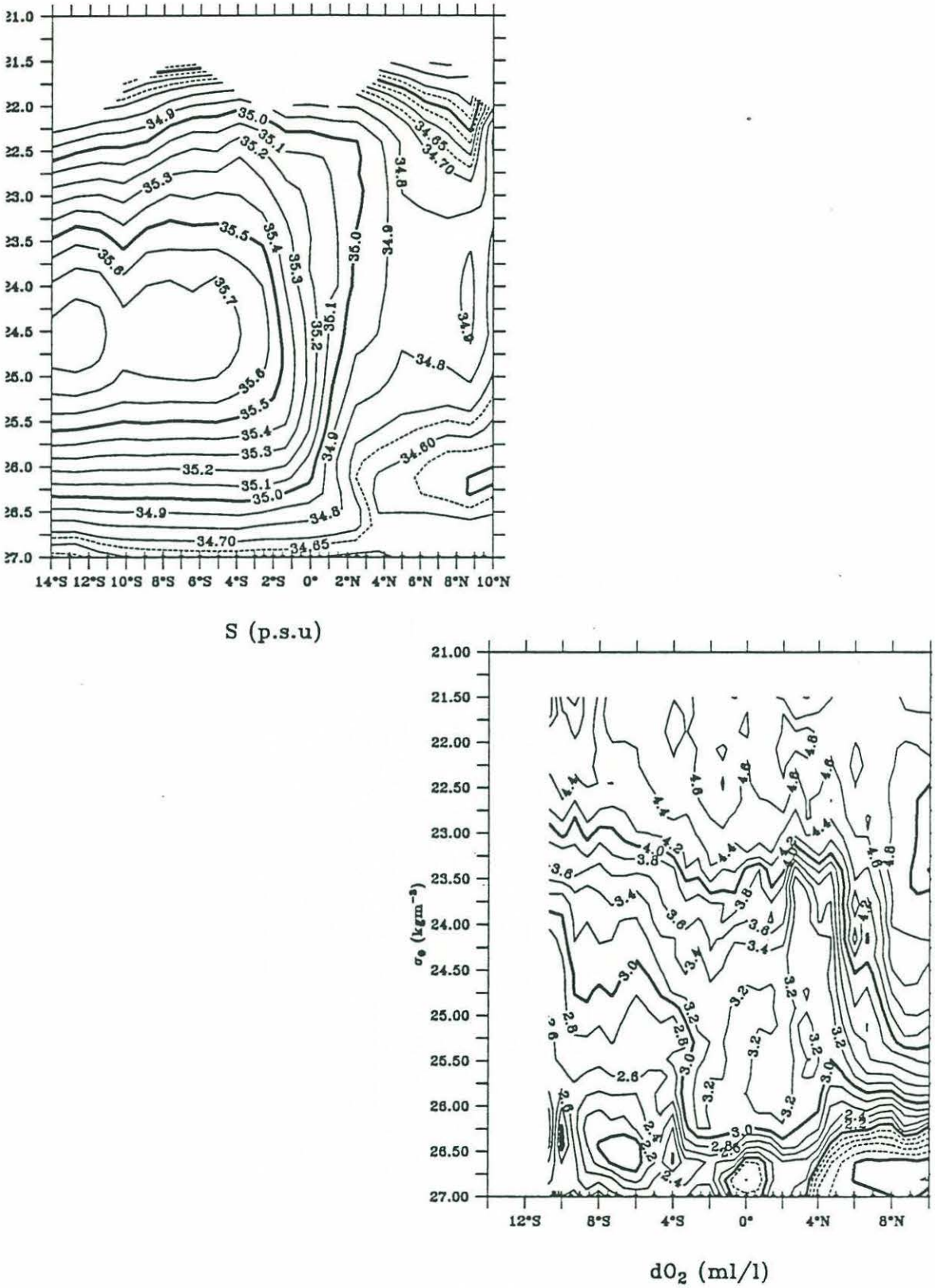

Figure 4.4 Properties on σ_Θ surfaces along 165°E: (a) mean salinity; (b) dissolved oxygen for US/PRC-TOGA 3

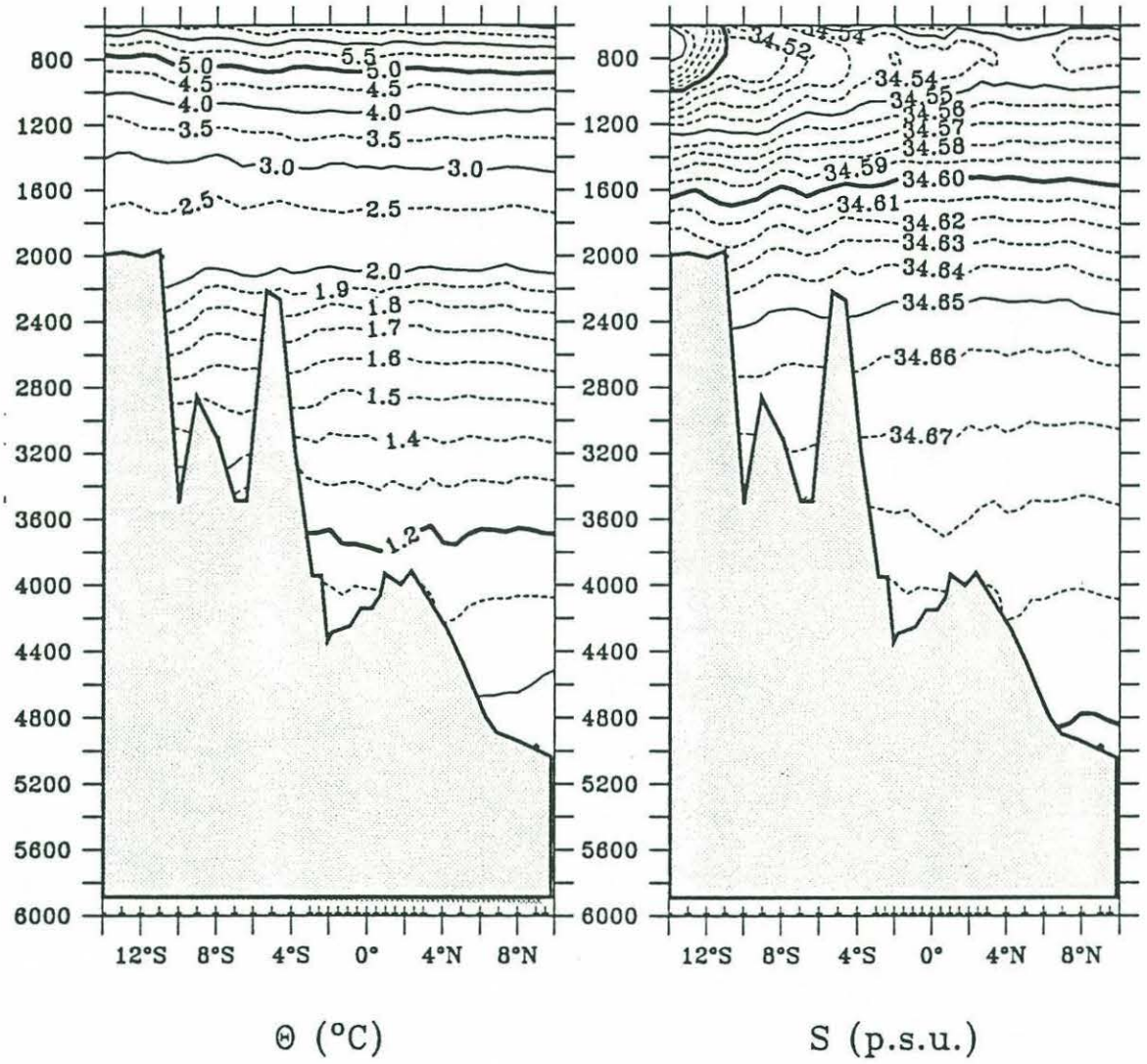

Figure 4.5 Mean potential temperature and salinity below 600m along 165°E. The bottom shown is actually the deepest observation depth.

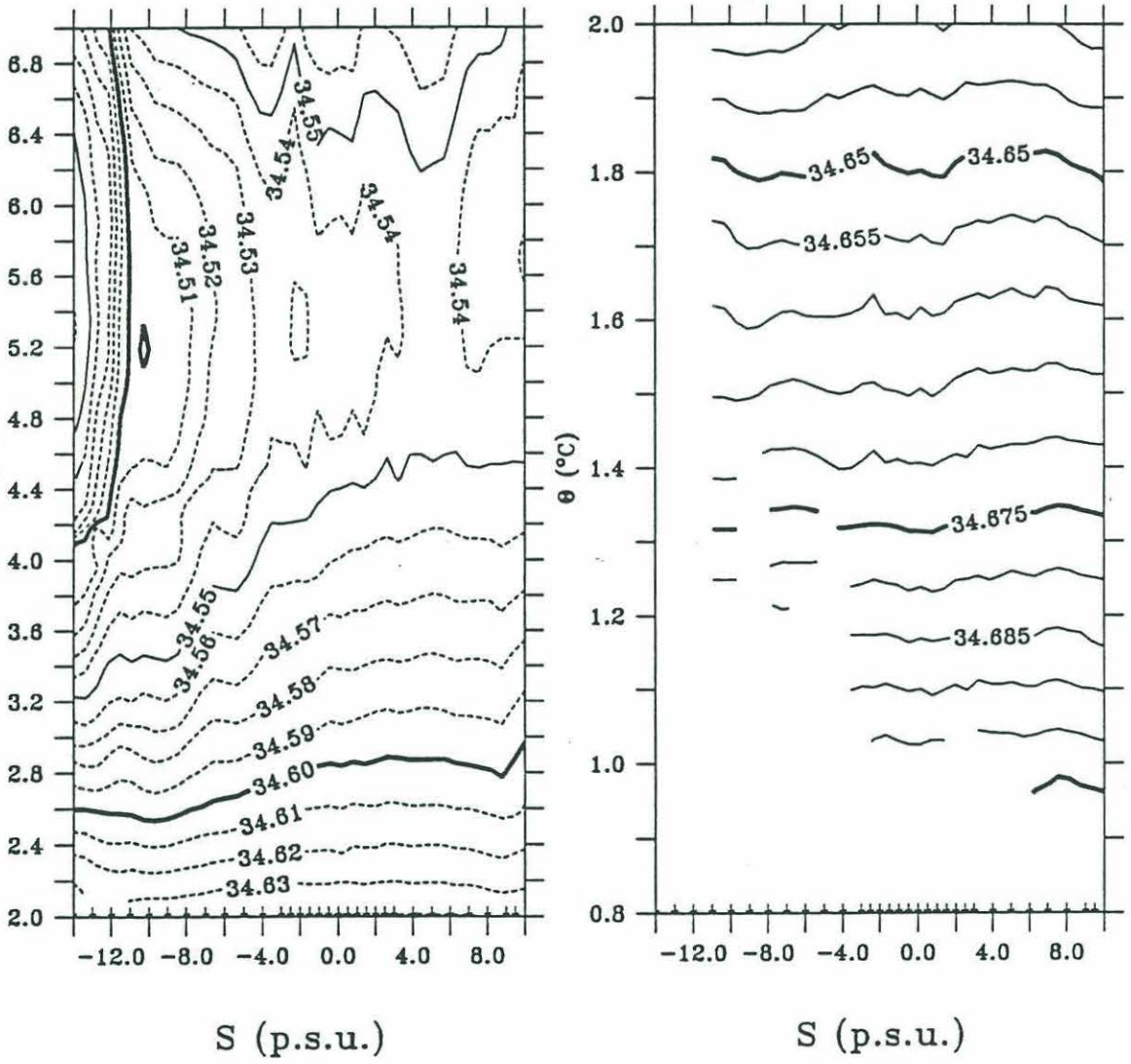

Figure 4.6 Salinity on potential temperature surfaces at 165°E: (a)in the intermediate water (7-2°C); (b) in the deep and bottom water (2-0.8°C).

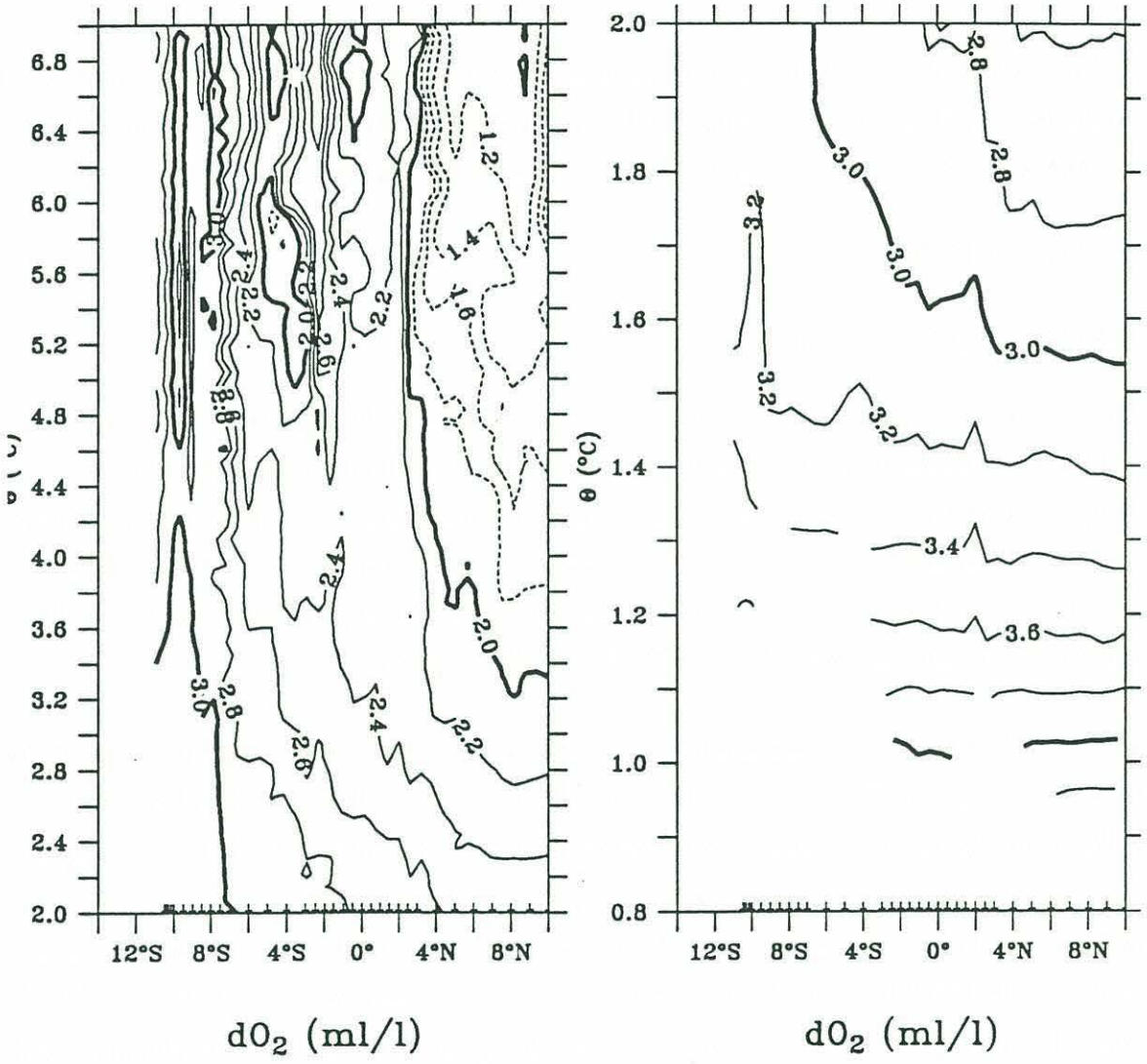

Figure 4.7 Dissolved oxygen concentrations on potential temperature surfaces along 165°E: (a) intermediate water; (b) deep and bottom water.

concentrations (here we use the PRC 3 cruise, the others being similar) suggest that NPIW penetrates to about 4°N where a sharp gradient is encountered. Both the salinity and oxygen values suggest that the water between 4°S and 4°N is a mixture of the two intermediate waters.

Below the intermediate water salinity minima, oxygen and salinity both increase with depth to the bottom. The highest salinities and lowest temperatures along 165°E occur at 9°N in the deepest part of the Melanesian Basin sampled by the section.

4.4 Velocity Field

4.4.1Velocity off the Equator

Synoptic geostrophic and direct current measurements near the equator rarely agree. Internal tides and other ageostrophic noise can obliterate the dynamic height signal due to geostrophic currents (Hayes, 1982). The upper ocean density structure is also highly variable, and confounds attempts to calculate the velocity structure. However, where long-term averages have been constructed, geostrophy and equatorial geostrophy appears to model the observed currents very well (Lukas and Firing, 1983; Hayes, 1982).

Erickson (1982) discusses the needed accuracy in the CTD data when applying geostrophy close to the equator. The small size of the Coriolis parameter amplifies the effects of small salinity offsets between casts. These offsets will appear as a linear shear in the velocity profile. One limiting factor for applying geostrophy close to the equator, then, is the expected accuracy of the salinity measurements. The intercalibration of the various data sets that went into the mean section removed salinity offsets in the deep water greater than ± 0.001, which is close to the instrument noise level. A salinity offset of 0.001 psu results in an additional shear of 21, 7, 4.2 and 3 cm /1000db at 0.25,0.75,1.25 and 1.75 ° respectively. These offsets are significant for deep flows and so we choose to apply geostrophy to only 1.75°. Equatorward of this latitude along 165°E the geostrophic velocity profiles do display unrealistically large deep shear. Between ± 3° dynamic height was spatially smoothed with a simple triangular filter.

4.4.1Velocity on the Equator

About the equator, the equatorial geostrophic relation has been shown to apply (Hayes, 1982; Firing, 1987):

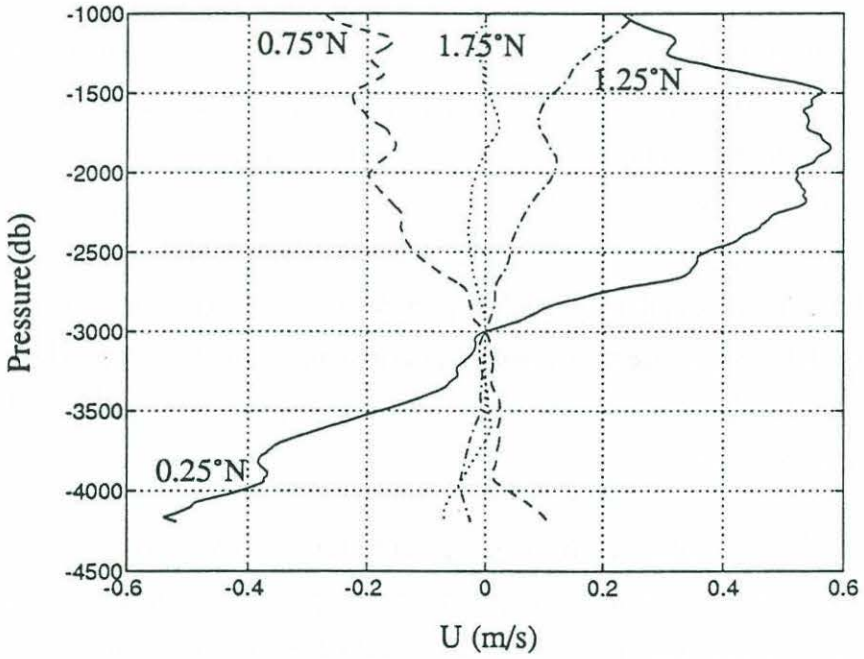

Figure 4.8 Profiles using geostrophy on near-equatorial station pairs demonstrating the unrealistic shears that arise in the deep water when geostrophy is applied close to the equator;

Several different methods have been used to find the second derivative of dynamic height at the equator, and it is not clear which method is best. Here we opted for that method which produces a profile that is most consistent with previous direct observations of the deep mean velocity profile on the equator.

The most common application of (1) has been to find the second derivative of the dynamic height field using a least-squares fit to a quadratic around the equator. Johnson and Toole (1993) applied this method to a mean 165°E section and found a deep westward flow at the equator. Repeating their calculation, a similar flow is found (Figure 4.9). However, when the fitting latitude range is changed the deep velocity profile changes character substantially. A striking feature of the equatorial shear profile fit over ± 1° are the oscillations between 1000 and 2500m. These are the equatorial deep jets, first observed by Luyten and Swallow (1976) in the Indian Ocean. Deep jets have been documented across the entire Pacific basin (see Ponte, 1988). Probably the most comprehensive observations of the deep jets were made at 159°W during the Line Islands Profiling Project (LIPP). There, the jets were observed at a similar depth range and amplitude as seen in Figure 4.9. When the fitting range is expanded, the signature of the deep jets is lost and a strong eastward shear begins to dominate the profile. This eastward shear results in unrealistic thermocline velocities for any deep reference surface.

An examination of the specific volume anomaly structure across the equator reveals that below the thermocline, a quadratic description is not appropriate. Typically, specific volume on a pressure surface features two off equatorial peaks (troughs) and an equatorial trough (peak) at the maxima in westward (eastward) shear. The best representation of this structure is a quartic polynomial (Figure 4.10). The velocity profile based on a quartic fit to ± 1.5° is reasonable: it captures the correct sign and amplitude of the Equatorial Intermediate Current with a deep reference level. This profile also agrees best with direct observations made during the LIPP experiment at 159°W (Figure 4.11). The westward shear superimposed upon the jets in both profiles is similar. It is worth pointing out, however, that the large scale vertical shear superimposed on the jets was not stationary, and slowly changed sign during the course of the LIPP observations. Though the deep jets, with vertical wavelengths of order 300m, have been shown to be in geostrophic balance (Erik-

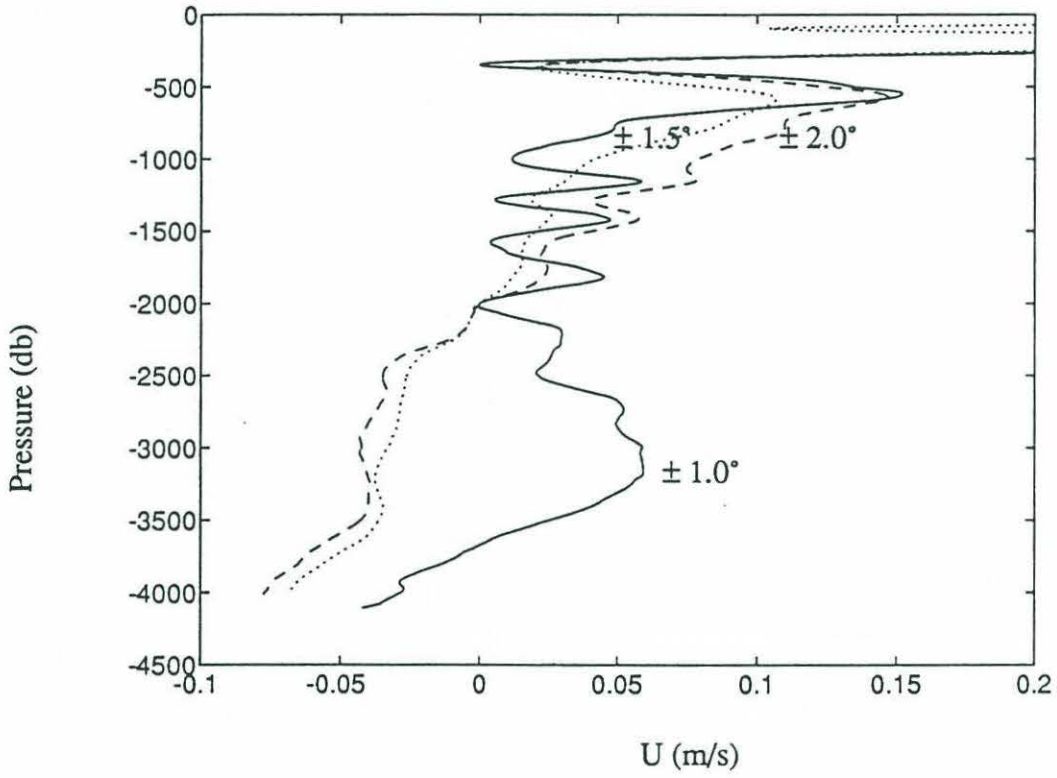

Figure 4.9 Geostrophic shear profiles on the equator below the thermocline. Profiles were found using equatorial geostrophy based on a quadratic fit for different latitude ranges.

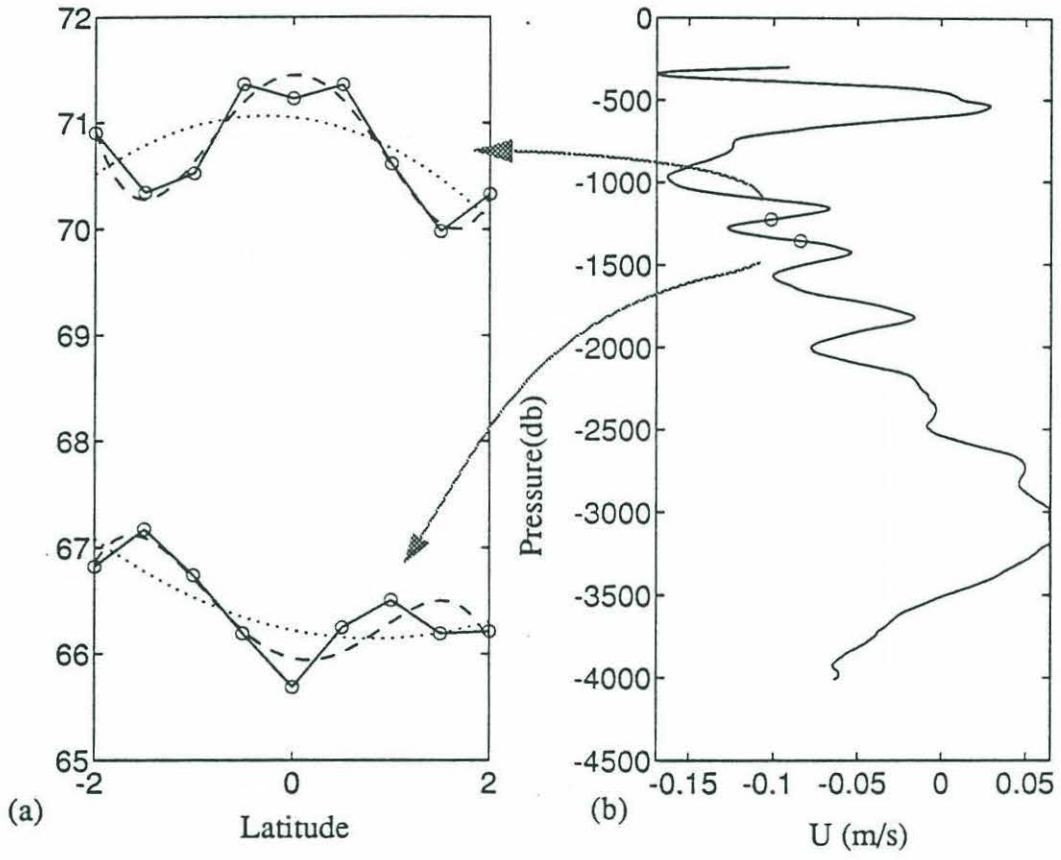

Figure 4.10 (a) Specific volume anomaly at two depths in the deep jets. The circles are the data. The least squares fit to a quadratic (dotted) and a quartic (dashed) are shown. (b) Deep velocity curve resulting from a curvature estimator based on the quartic fit. The circles are at the depths shown in (a)

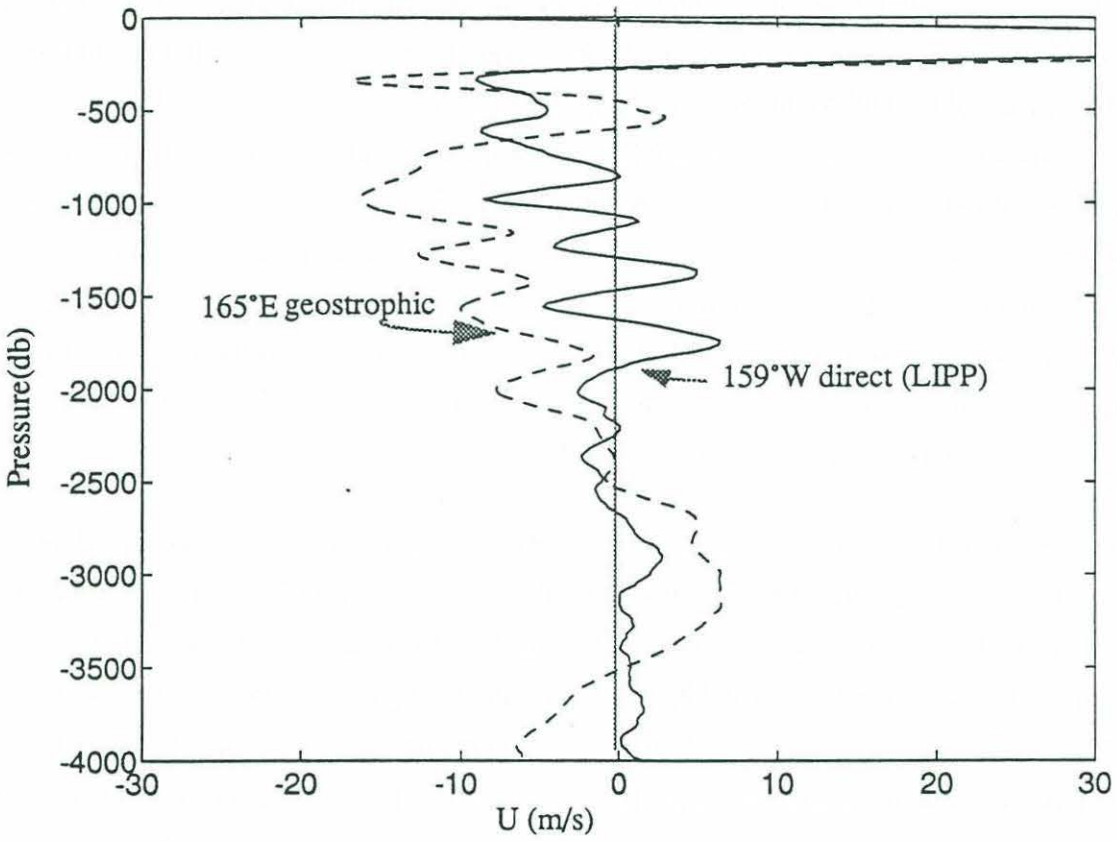

Figure 4.11 Zonal velocity at 0°, 165°E: solid line is the directly measured 15 month mean from the LIPP experiment; dashed line is the geostrophic estimate at 165°E.

son,1982; Muench, Kunze and Firing, 1993), the larger vertical scale shear may not be. It is unclear which of the deep shear profiles in Figure 4.9 is more representative of the mean circulation. Because of its good representation of the EIC and the deep jets we shall use the profile based on the ± 1.5° quartic fit.

The difficulty in determining the velocity at the equator applies equally to the upper ocean. Fortunately direct velocity measurements are available for the upper 600m. GT employed profiling current meter and shipmounted ADCP measurements from the USPRC-TOGA and SURTROPAC surveys to construct a mean velocity field. The profiling current meters only measure shear and so the mean velocity field was referenced to 600m. Their mean section included 6 additional SURTROPAC surveys and is therefore a more reliable average than the full depth section found here. A comparison of the GT mean profile at the equator with mooring measurements confirms their assumption that 600m is a good reference level on the equator. A long-term current meter mooring has been maintained at 0°, 165°E since the beginning of 1986 (McCarty and McPhaden, 1993). The mean velocity profile in the upper 300m measured by the mooring agrees very well with the direct shear measurements of GT, except in the mixed layer (Figure 4.12).

The comparison with the geostrophic shear using the mean density section derived here is less satisfactory. As was found for the deeper flow, the geostrophic shear on the equator is sensitive to the latitude range over which (2) is applied. Contrary to the deep measurements, a more realistic profile is obtained by expanding the fitting latitude range. The quartic fit over ± 1.5° which does well at depth, appears to overestimate the shear of the EUC (Figure 4.12). A ±1.5° quadratic fit does better, but the agreement is still not good. GT found excellent agreement in their comparison of geostrophic and directly observed velocity, suggesting the difference seen in Figure 4.12 is partly due to actual differences in the mean density fields. Recall that the GT average includes upper ocean data from several more cruises.

4.4.2 Features of the Velocity Field

The geostrophic velocity in the upper 600m features the usual 'cast' of equatorial currents: the Equatorial Undercurrent centered at 200m, the subsurface countercurrents (SSCC, NSCC) and the Equatorial Intermediate Current (EIC). To the north and south are the North Equatorial Counter Current and the South Equatorial Current respectively (Figure 4.13). As found by GT, the geostrophic and directly measured fields are similar.

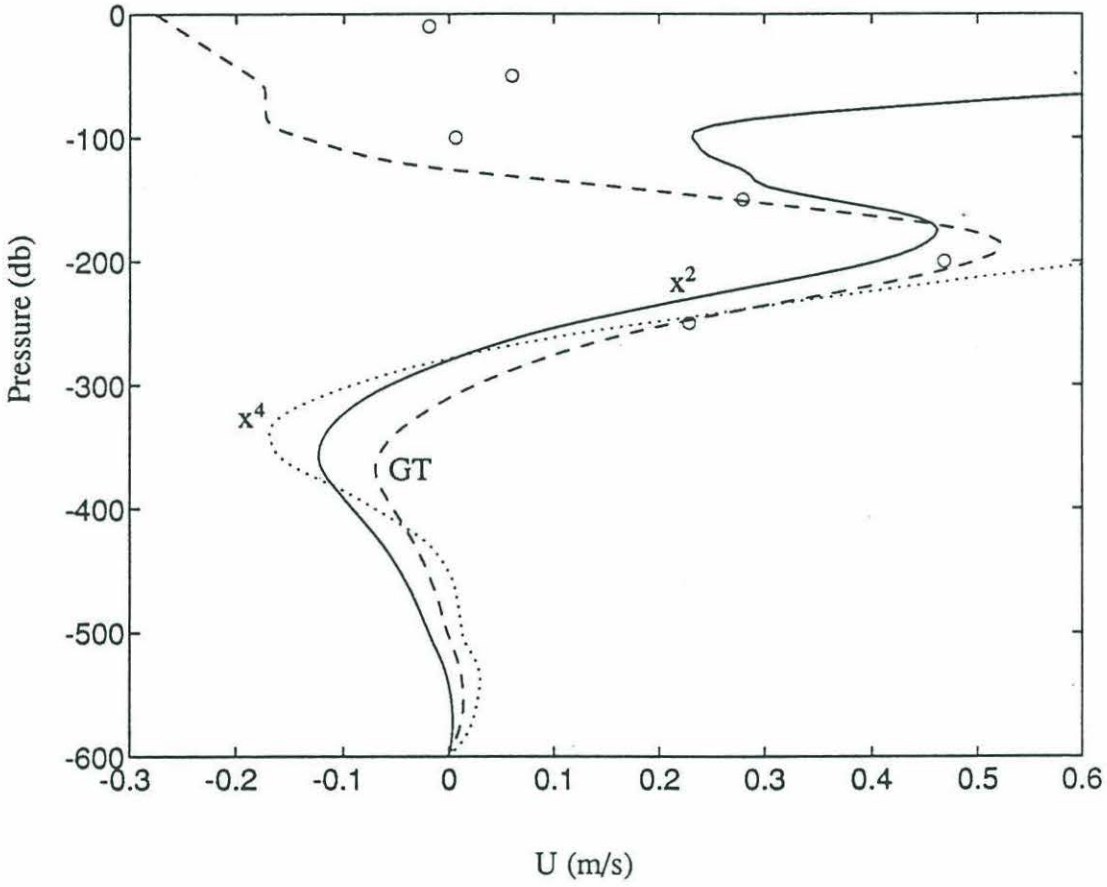

Figure 4.12 Zonal velocity at 0°, 165°E. The dashed line is the directly measured mean shear w.r.t. 600m found by GT averaged over ± 1.0°; the circles are the estimates based on 5.5 years of mooring measurements from McCarty and McPhaden (1993). Two profiles based on dynamic height curvature fits at the equator between ± 1.5° are shown: solid line is for a quadratic fit and the dotted is for a quartic fit referenced to 600db.

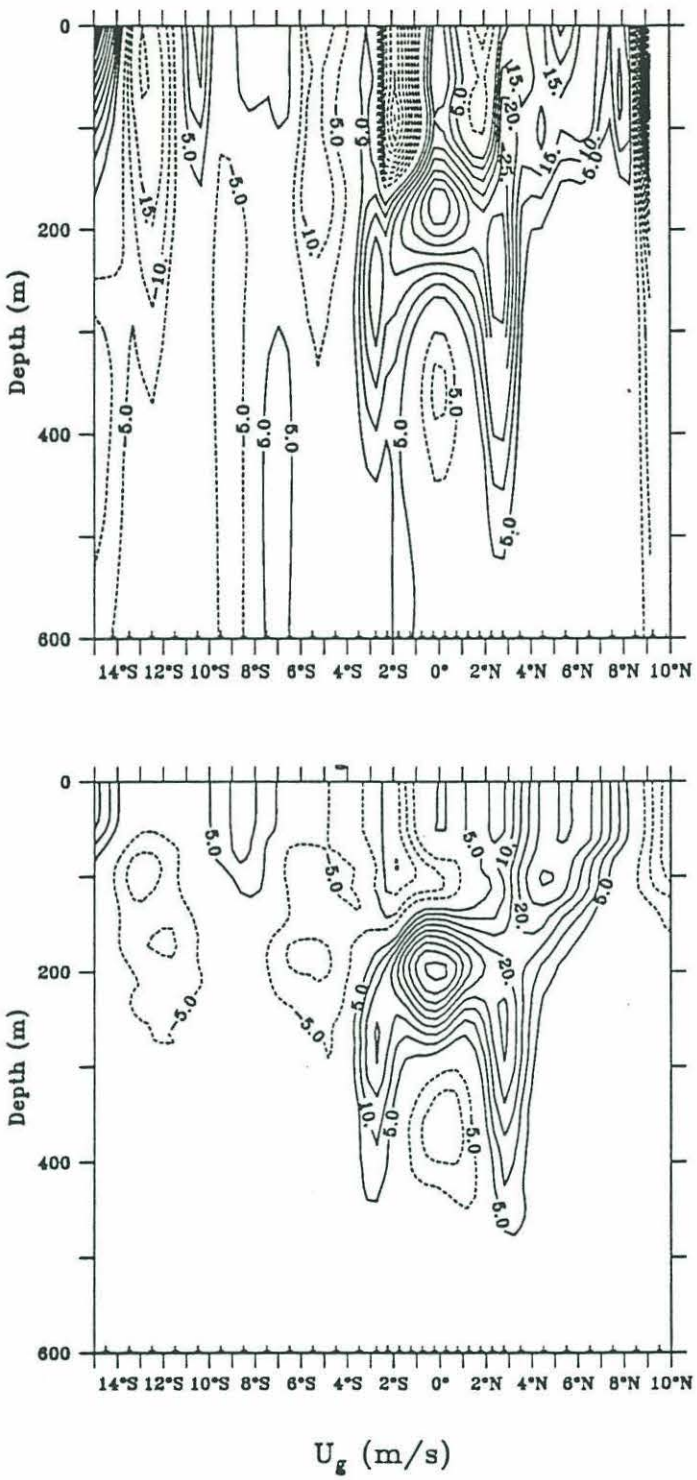

Figure 4.13 Zonal velocity along 165°E (a) geostrophic relative to 2500db (b) direct estimates relative to 600db from Gouriou and Toole (1993).

Less is known of the deep equatorial velocity field. Firing (1987) observed a complex mean current structure in the mean LIPP data along 159°W. Surprisingly, many of the features found at 159°W, are also observed in the geostrophic velocity field at 165°E (Figure 4.14). Two counterflows are observed on either side of the Equatorial Intermediate Current (EIC) which Firing(1987) named the Intermediate Countercurrents (SICC, NICC). Between these on the equator are the deep jets. South of the SICC, below the SSCC is a subsurface westward flow named the South Equatorial Intermediate Current (SEIC). The observation of these currents in the mean 165°E further supports Firing's conjectures that these features are part of the mean circulation and have long zonal scales.

4.4.3 Geostrophic transports

The final velocity field used to calculate geostrophic transports across 165°E is as follows. Off the equator, the velocity is based on the geostrophic shear, while on the equator a quartic fit to ± 1.5° was used to find the deep shear between 600m and the sea floor. Between latitudes ±2° and depths 0 and 600m, the directly measured mean shear profiles were adopted. All profiles are referenced to 2500db across the entire section, except on the equator where a 600db level is used.

The decision to use the geostrophic and not directly measured shear off the equator is based on the fact that the profiling current meter (PCM) has a sensitivity threshold of 2.5cms^{-1}, and so must underestimate the velocity in regions of low speed, such as in the broader parts of the SEC and NECC. The comparison between the direct and geostrophic transports suggest that this is the case, with the PCM underestimating the net transport of the SEC by 3 Sv.

The transports of the major currents resulting from the shear configuration described above agree well with the previous calculations along 165°E (Table 4.2). The mean estimates of Delcroix *et al.* (1992) are for the period of 1984-1986, which is free of an El Niño and is considered a 'normal' time. During the 1987 El Niño, the transports across 165°E changed dramatically. For instance the transport of the EUC varied between 0 and 47Sv, and the NECC between 58 and 7Sv. In the face of these changes, the good agreement between the eight year average presented here and the 'normal' period of Delcroix *et al.* (1992) gives confidence that the data are not badly aliased by the interannual variability.

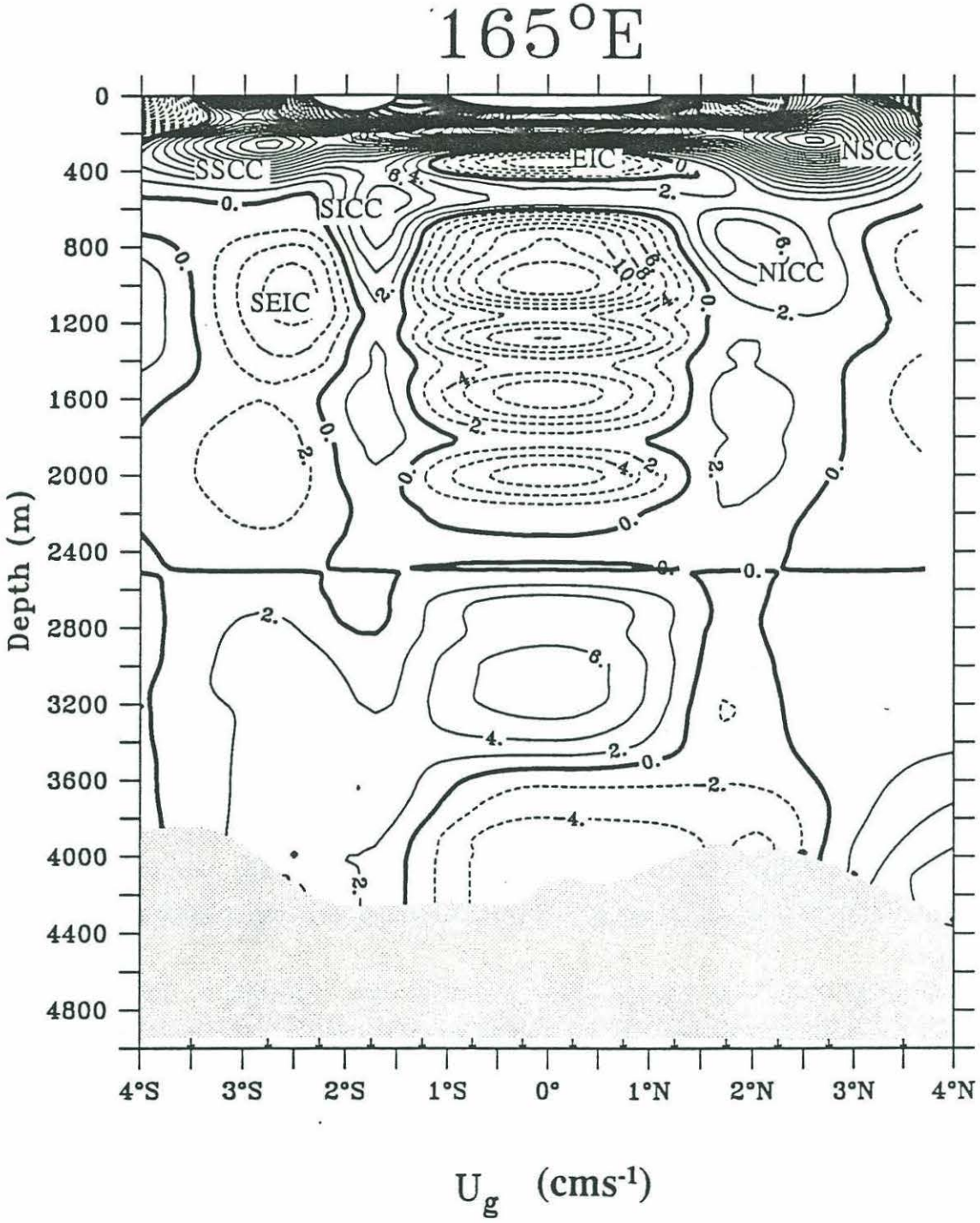

Figure 4.14 Zonal geostrophic velocity along 165°E referenced to 2500db.

Current	This study	Gouriou & Toole	Delcroix et al, 1992
SEC*	-22.7	-37.7	-46.7
SECC*	6.3	3.6	6.8
SSSCC	7.3	6.5	6.8
EUC	16.1	17.3	16.1
EIC	-4.4	-4.9	-4.1
NSSCC	9.4	11.4	12.9
NECC	19.1	19.6	20.9

Table 4.2 Transport of the zonal currents across 165°E above 600db. Both Gouriou and Toole (1993) and Delcroix *et al.* (1992) show transports wrt 600db, while the transports in this study are wrt varying reference levels as described in the text. The asterisk denote current transports integrated over latitudinal bounds that were smaller than in the other two studies.

4.5 Summary and Conclusions

An average section along 165°E based on eight years of cruise data provides a reasonable realization of the mean velocity and property fields. In the deep ocean, a sensible velocity field could be obtained using geostrophy to within 1.75° of the equator, and the equatorial geostrophic relation on the equator. The comparison with the directly measured deep zonal velocity structure at 159°W show similar features providing confidence that the mean 165°E section may be representative. In the upper ocean, direct velocity measurements at 165°E show a favorable comparison with the geostrophic field, and the transport estimates compare well with other studies along the same meridian.

Chapter 5

The Mass Budget for the Equatorial Volume

5.1 Introduction

Having estimated the circulation across the sections that bound the equatorial Pacific, the mean mass budget is now assembled. The transpacific zonal sections at 10°N and 14°S allow us to investigate the meridional exchange across the equator, while the north-south section at 165°E provides information about the east-west flow. The set of average and synoptic sections brought together for this study divides the Pacific Ocean into three nearly-enclosed volumes: the North Pacific poleward of 10°N; the eastern Pacific between 10°N, 14°S and east of 165°E; and the western equatorial Pacific west of 165°E. For the rest of the analysis these volumes will be referred to as the North Pacific basin, the eastern volume and the western volume respectively. The stations used to enclose these volumes are shown in Figure 5.1.

In the western volume, the mass budget is dominated by the poleward inflow of waters from the western boundary currents. This volume can also communicate with the Indian Ocean via the Indonesian Seas. The ocean volume east of 165°E houses the equatorial Cold Tongue in which large quantities of thermocline water of both hemispheres is exposed to the atmosphere via equatorial upwelling and warmed.

The following questions will be explored: Can the flow pathways suggested by the tracer fields be directly observed? Which elements of the circulation are important in cross-gyre and cross-equatorial exchange? Is there a large flux of mass into the Indian Ocean? Before we can address these issues a sensible mass budget of the equatorial region must first be established. First the question of whether the data are representative of the mean conditions is explored. Demonstrating that this is so justifies the use of the conservation statements pertaining to steady circulations. A circulation is will then be found that conserves mass, heat and salt, allowing us to investigate the major flow pathways.

5.2 Variability in the Equatorial Pacific: is the data representative?

In general, the equatorial Pacific is more studied for its variability than the mean state. Besides featuring an energetic seasonal cycle, the circulation is strongly modified during

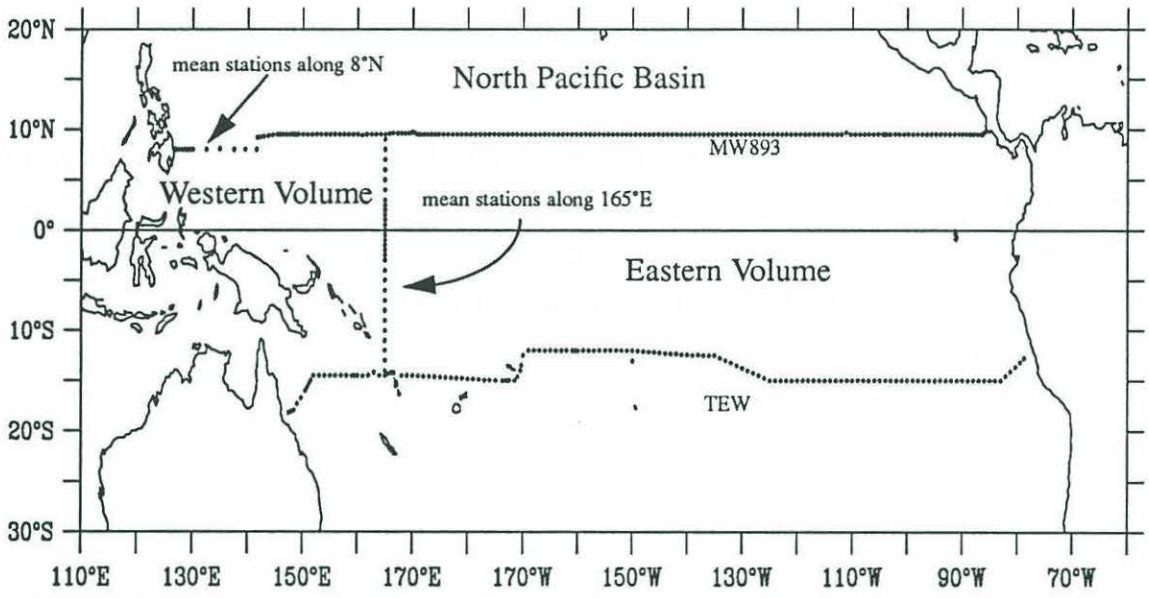

Figure 5.1 Composite full depth CTD data set used to divide the Pacific into several enclosed volumes.

the El Niño phenomena which occurs roughly every 5 to 7 years and persists for about 18 months (Rasmussen and Carpentar, 1982). Over most of the equatorial Pacific, the interannual fluctuations account for more than 80% of the low-frequency variance in the thermocline depth (Kessler, 1986, figure 3.5). A primary concern is therefore whether the data utilized here are representative of the mean conditions.

In the Coral Sea we have argued that the TEW data are similar to Ridgway's analysis of the mean flow based on the historical data archives. At 8°N and 165°E multiple survey data were available to better define the mean flow. The most suspect parts of the present data set are therefore the interior transports along the synoptic transpacific sections.

The only way to test the representativeness of the one-time data is to compare it with climatological data. Fortunately, the historical XBT archives contain enough casts to provide a robust estimate of the mean dynamic height differences across the sections in the upper 400m, where nearly all of the thermocline transport occurs. Many fewer casts penetrate below this level, and the statistical stability of the mean estimates degrade quickly with depth. We therefore focus on the upper 400m, which has the greatest impact on the warm water budget.

The approach taken is to examine the dynamic height difference between stations at the endpoints of the transpacific sections, from which an estimate of the section average geostrophic shear on pressure surfaces can be found.

Along 10°N, the full mass budget analysis will employ a composite section made up of the averaged stations along 8°N from the coast of Mindanao to 141.5°E, and the MW893 stations between 141.5°E to the coast of Costa Rica which were taken at 9.5°N. The 'patch' station at 141.5°E carries a significant amount of westward transport, indicative of the northward traverse from the northern edge of the NECC at 8°N into the southern portion of the NEC at 9.5°N. The strong westward flow of the NEC is clearly seen in the ADCP measurements at and east of 141.5°E along the MW893 cruise track. The end points for the MW893 section to be used in comparison with the historical data are therefore at 8°N, 141.5°E and 9.5°N, 274.25°E (at the coast of Costa Rica).

Along 14°S, we choose the end points to be where the TEW section crosses 165°E and the eastern end of the section, the coast of Peru. Between the Australian coast and 170°E, we

can compare the transport by TEW with Ridgway and Godfrey's (1993) analysis of historical data. This comparison is deferred until later; here interior parts of the onetime sections are checked.

Two data bases were searched: the NODC historical CTD archive for the Pacific, and the XBT/MBT archive assembled and screened by Kessler (1986). The data archives were searched for casts that are within 1.5° in latitude, and 5° in longitude of the section end points. The bin dimensions reflect the long zonal and short meridional scales of the equatorial dynamic height field. Dynamic height was calculated from each cast after the data had been interpolated to 10db intervals. A salinity profile was assigned to the MBT and XBT casts using a mean θ-S relation at each end point. The θ-S relation was based on a hand picked selection of high quality casts made in each bin. These data were usually taken in the last decade. For the rest of this section, where we refer to transport, we mean the geostrophic transport with respect to and above 400db.

A mean transport estimate was found, along with its 95% confidence interval using a bootstrap method (Efron and Gong, 1983). The transport between the end points was found 500 times, where each estimate is based on the average dynamic height profiles found from a random sample of 100 casts from each bin. The 500 estimates of the mean provide the probability density function for the mean. The transport between the actual end point casts from the synoptic sections are shown for comparison (Table 7.3).

An impression of the variability of the flow is gained from the time series plot of the surface dynamic height (Figure 5.2). Larger dynamic height is seen in the west at both sections. Along 10°N, though, the east-west difference is smaller and much more variable than at 14°S. Despite the scatter in dynamic height at the end points at 10°N, the large number of casts results in a very stable mean transport estimate of 8.5 ± 1.3 Sv to the south. This does not imply that the flow is close to steady. On the contrary, as suggested by Figure 5.2, it is not. The seasonal cycle is responsible for transport changes of 4Sv, half the mean signal. However, a fitted seasonal cycle only accounts for at most 20% of the dynamic height variance at each end point, in agreement with Kessler's (1986) analysis. The bulk of the variance appears to be due to interannual fluctuations, which produce transport anomalies (wrt the mean annual cycle) of over 15Sv at 10°N (Figure 5.3).

At 14°S, the historical data a indicate mean of 22.9 ± 0.7 Sv. Both the amplitude of the sea-

Section	10°N		14°S	
HISTORICAL DATA				
	east	west	east	west
number of casts	430	146	338	210
average position				
Latitude	9.37°N	7.98°N	12.8°S	14.5°S
Longitude	274.13°E	138.66°E	280.5°E	164.7°E
mean transport	-8.5 ± 1.3		23.0 ± 0.7	
amplitude of annual cycle	4.0		1.7	
seasonal transport at time of synoptic data	-10.8 (Feb. - May)		22.9 (June - Aug.)	
interannual anomaly min, max	-10., 15		-4.2,5.1	
SYNOPTIC DATA				
position				
Latitude	9.8°N	8.0°N	12.7°S	14.5°S
Longitude	274.1°E	141.5°E	281.3°E	165°E
transport	-10.4		22.3	

Table 7.3 Estimates of the mean geostrophic transport above and relative to 400m, from both historical data archives and the synoptic CTD data set. The errors on the mean historical estimates are for the 95% confidence interval based on a bootstrapped distribution (see text). An annual cycle was found by least squares fit to a sinusoid for dynamic height estimates at each pressure surface. The amplitude of the fitted seasonal cycle is shown, along with a prediction for the time of year the synoptic data were taken. After removing the seasonal cycle, data were averaged over 12 month periods that overlapped by 6 months to produce an interannual series of dynamic height anomaly. Where both an eastern and western estimate were available, a transport was found. The maximum and minimum of these transport anomalies are shown.

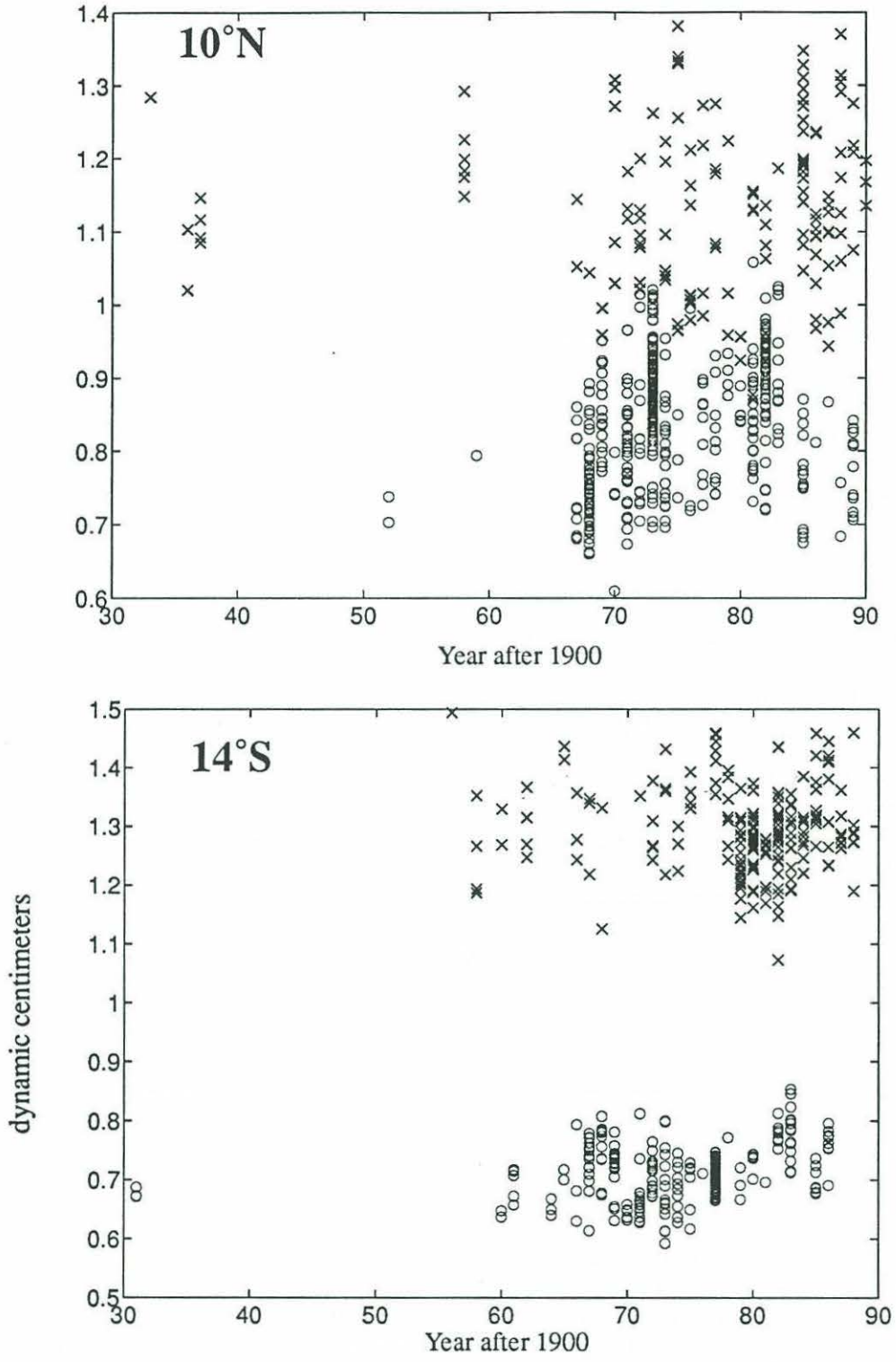

Figure 5.2 Dynamic height at the surface with respect to 400db as a function of time for all of the casts from the historical archives. Crosses are for the western endpoint and circles for the east.

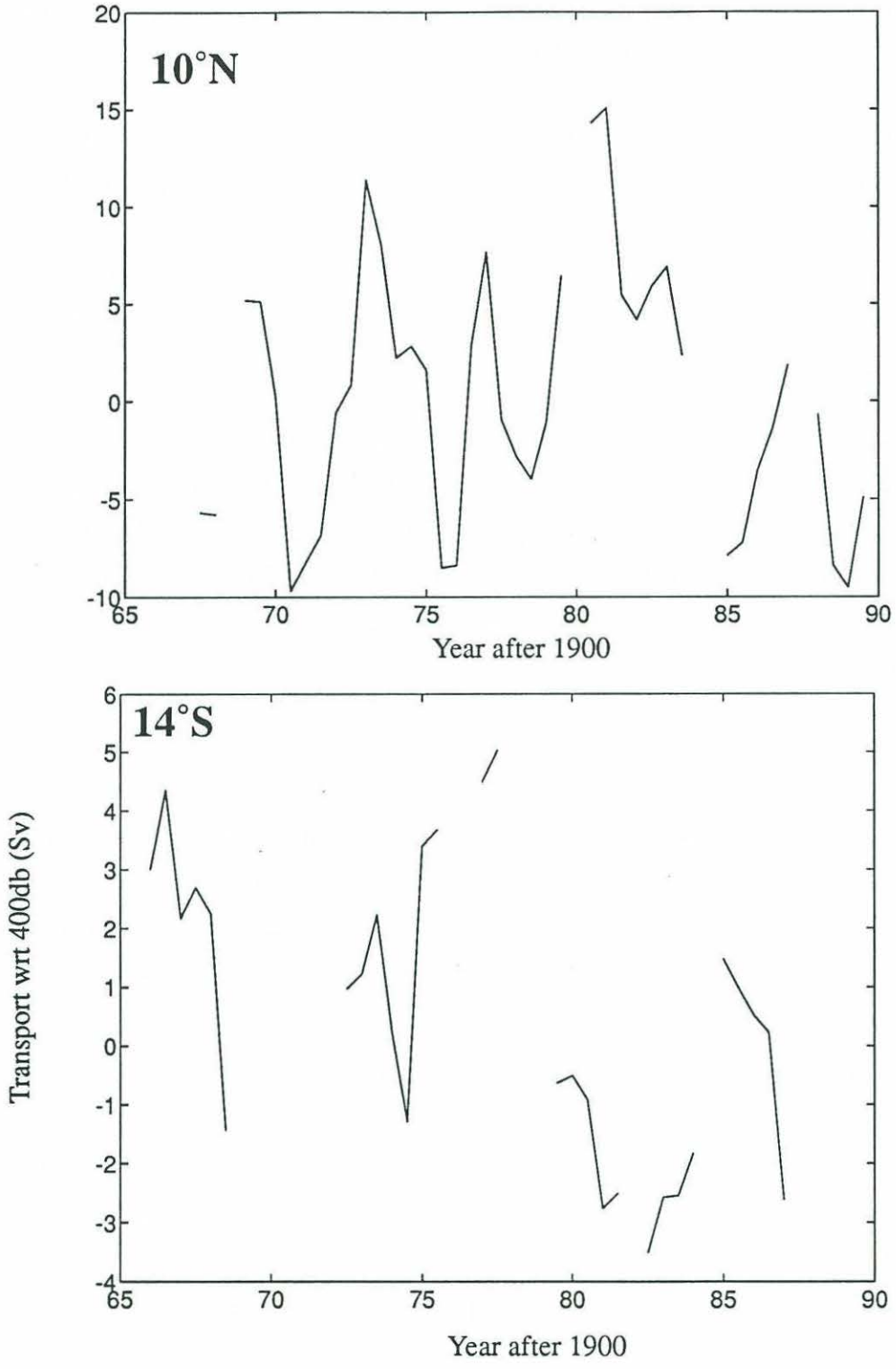

Figure 5.3 Time series of the anomaly in transport in the upper 400db. The anomaly is defined with respect to the mean annual cycle, and is found from averages over 12 month bins.

sonal cycle and the interannual extrema are smaller than at 10°N, though still large enough to cause variations of up to 25% in the mean.

Comparison of the transports between the synoptic data endpoints and the historical estimates show surprisingly good agreement. At 10°N, the synoptic transport is only 2 Sv larger than the climatological mean, and is in excellent agreement with its predicted seasonal transport. Given the interannual variability at 10°N, this can only be due to exceptionally good luck. Along 14°S, where the transport is steadier, the synoptic data also agree very well with the climatological mean.

In summary, interannual changes in transport are larger than seasonal changes, especially along 10°N where even the direction of the transport can be altered. Despite this the interior thermocline shear captured in the synoptic sections along 10°N and 14°S both show good agreement with the historical mean based on 30 years of data. This provides the justification for the following analysis in which we use the synoptic data to construct the mean annual circulation for the equatorial Pacific.

TEW west of 165 °E

Recently, Ridgway and Godfrey (1993) analyzed historical hydrographic and XBT data to deduce the mean flow in the Coral and Tasman Seas. Their analysis conserves mass in subsurface density layers in the Tasman Sea. At 15°S, close to the latitude of TEW in the Coral Sea, they find a northward geostrophic flux of 7.2 $x10^9 kgs^{-1}$ above $\sigma_\Theta = 26.5$ along the Queensland coast with an offshore return flow of 8.1 Sv west of 170°E, resulting in a small *net southward* transport of about 1 Sv of thermocline water. For comparison, the TEW data show a net transport of 0.4Sv northwards between the coast of Australia and 170°E in same density range, in good agreement. Ridgway finds that the largest net poleward transport of water in the Coral Sea occurs largely as intermediate water, with northward transport of 7.7 Sv for $26.5 < \sigma_\Theta < 27.5$, which agrees well with the value of 7.3 Sv out to 170°E along TEW relative to 3000db. Hence the TEW data appear in remarkably good agreement with the mean, as derived from the historical data base.

5.3 A First Look at the Total Mass Budget

Here we examine the basic issue of mass conservation in the ocean volumes defined by the

data. We have confidence that the thermocline transports, at least, are fairly representative of the steady state. The variability of the transports at depth remains an issue. Along 8°N and 165°E, large variations are indicated in the deep and intermediate water layers both between surveys and along any given section due to the eddy field. As will be seen below this remains a large source of uncertainty. The second source of uncertainty comes from the large range in estimates of the wind-stress in the equatorial Pacific. This has a profound impact on the present work, since the Ekman flow is one of the dominant mechanisms exporting mass from the region.

Before proceeding we first define the set of isopycnal layers chosen for the analysis: a total of 19 layers are chosen, about half of which are in the thermocline (Table 5.7)

5.3.1 Ekman Fluxes

Besides the small outflow to the Arctic Seas through the Bering Strait (Coachman and Aagaard, 1988), the North Pacific north of 10°N is a closed basin. The net flow across 10°N must be roughly zero, ignoring any meridional transport west of the Philippines, and so a balance between the net geostrophic and Ekman transports across the section is expected. The same applies for the enclosed volume east of 165°E. A balance between the Ekman and geostrophic convergence may not be expected in the western volume or for the flow across 14°S, as the leakage through the Indonesian Seas come into play.

Meridional Ekman fluxes

As the equator is approached the Ekman component of the meridional Sverdrup flow becomes increasingly important. According to the Ekman balance the Ekman flux increases inversely with the Coriolis parameter:

$$M_E^x = -\frac{\tau^y}{f} \qquad M_E^y = \frac{\tau^x}{f} \tag{1}$$

Over the tropical Pacific, the prevailing winds are the quasi-steady easterly Trades, which drive a divergence of mass away from the equator.

Despite its simplicity, the Ekman balance has predicted the wind-driven flux across both 10°N in the Atlantic and Pacific Oceans to within the observational error of roughly 15%(Chereskin and Roemmich, 1991; Appendix C). We have good confidence, then that

Density surfaces	No.	Description
	1	surface most layer containing predominantly the mixed layer
$\sigma_\theta = 23.0$		
	2	
23.5		
	3	
24.0		thermocline layers containing the highly saline Tropical Waters in both
	4	hemispheres
24.5		
	5	
25.0		
	6	
25.5		
	7	
26.2		
	8	13°C Thermostad
26.70		
	9	shallow salinity minimums in both hemispheres
26.90		
	10	NPIW at 10°N. Upper AAIW at 14°S
$\sigma_2 = 36.50$ (1000m)	11	AAIW core at 14°S
36.75		
	12	
36.855		θ=2.1°C: top of NPDW
	13	
36.95		
	14	silica maxima along 10°N
$\sigma_4 = 45.81$		
	15	
45.85		θ=1.21°C: boundary between NPDW and LCPW
	16	
45.88		
	17	
45.91		Lower Circumpolar Water
	18	
45.93		
	19	

NPDW

LCPW

Table 5.7
Definition and description of the density layers used in the analysis.

Latitude	Width (km)	Θ_{Ek}	S_{Ek}	M_{Ek} (10^9kgs^{-1})		
				HR	FSU	Harrison
9°N	16 297	27.8	34.478	43.3	37.4	32.6
13°S	14 909	26.7	35.797	-28.4	-26.3	-23.3

Table 5.8 Mean annual Ekman mass flux across the study zonal sections. The transport weighted mean temperature and salinity are also listed.

the balance is robust and that the mean annual wind-stress can be used to determine this important element of the circulation.

The difficulty in calculating the mean annual Ekman fluxes lies more with determining the wind-stress. Several climatologies have been constructed using surface ship observations, daily surface pressure analyses, cloud motions and more recently, the wind fields from the routine global weather prediction systems. The range of variation in the surface stress fields amongst the climatologies is great, and can be attributed, not only to the different data bases used, but also to how the drag coefficient was chosen. The physics of the air-sea boundary layer is not well understood, and it is difficult to find a single parameterization of the momentum transfer that works well under all conditions.

Here, three global wind-stress climatologies are presented which span the range of Ekman flux estimates. The aim is to demonstrate the possible variations, not give a comprehensive survey of all available products. The Hellerman and Rosenstien (1983) windstress climatology is probably the most well known among oceanographers, and is widely used to force models. A second climatology can be constructed from 18 years of wind analyses from the Florida State University (Goldenburg and O'Brien, 1981). The FSU analyses provide monthly fields of pseudo-stress (u,v)*|u|. These were multiplied by a drag coefficient of 1.2×10^{-3} before averaging. Finally, the estimates of the meridional Ekman transports reported by Harrison (1989) are also examined.

The net meridional Ekman mass flux across the two transpacific zonal section was found from the zonal integration of (1). Ignoring the small changes in latitude of the sections, the mean annual Ekman mass flux across 9.5°N and 14°S are shown in Table 5.8

The larger Ekman mass flux across 10°N is due to the larger basin width and stronger zonal

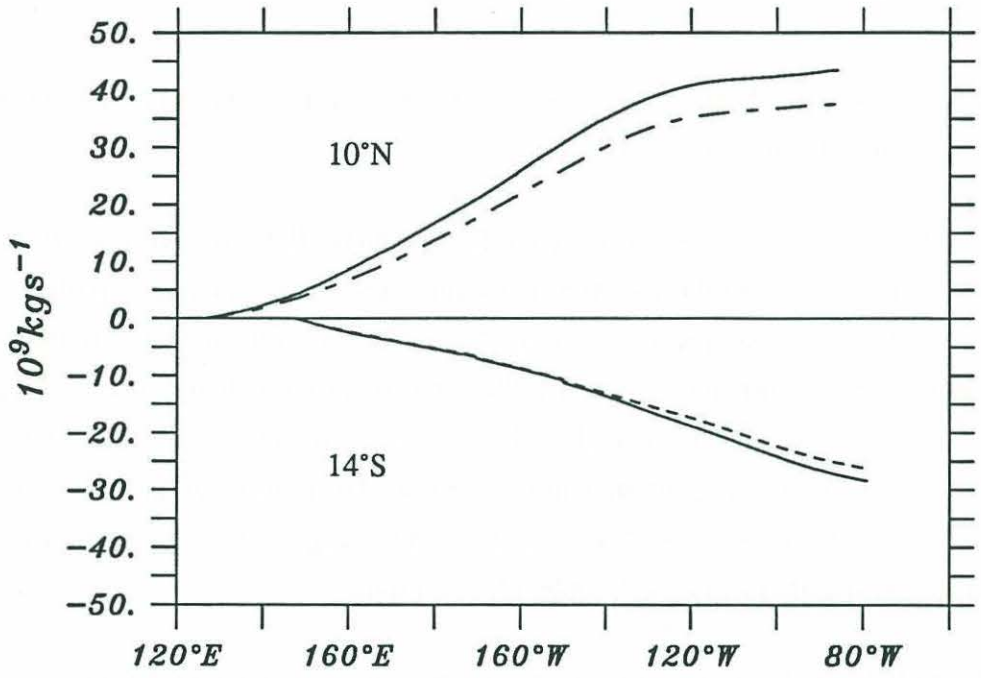

Figure 5.4 Cumulative Ekman mass flux across the study sections: 10°N and 14°S. The solid line is calculated from the Hellerman and Rosenstien winds while the dashed lines are for the FSU winds.

winds. Along both sections, the zonal component of the wind stress is single signed, and is fairly constant giving rise to an almost linear increase in the cumulative Ekman mass flux integrated across the section (Figure 5.4).

Associated with the Ekman mass transport are fluxes of salt and heat. To calculate these, some assumptions about the depth penetration of the Ekman velocity must be made. Wijffels *et al.* (1993) (Appendix C here) found that the bulk of the Ekman flux along the 10°N section resides above the shallowest depth at which $\partial\rho/\partial\sigma_\Theta$ 0.01kgm^{-3}. An Ekman temperature and salinity was found from each CTD station pair, assuming a linear velocity profile above this depth to the surface. Wind stress was projected onto the positions mid-way between station pairs using a cubic-spline interpolation. Hence the Ekman heat and salt fluxes are:

$$H_E = \int \frac{\tau}{f} c_p \Theta_E dx \qquad (2)$$

$$S_E = \int \frac{\tau}{f} s_E 0.001 dx$$

Because the Ekman mass fluxes are unidirectional, a useful way to consider the associated heat and salt transport is a transport weighted mean Ekman temperature and salinity, as shown in Table 5.8. The Ekman flux across 10°N is warmer by 1°C and fresher by 1.2 p.s.u. than across 14°S, reflecting the more poleward position of the TEW section, as well as the higher surface salinities found in the South Pacific. As a result, the northward Ekman flux is removing very light water, while heavier density classes are being advected southwards.

Zonal Wind-driven Transports

The meridional Ekman balance (1) can also be used to find the zonal Ekman mass flux across meridional sections, though it is only valid off the equator. The meridional wind-stress is weak in the western and central equatorial Pacific and drives only small zonal transports across the sections. However, at the equator the Ekman balance is no longer valid, and another means of determining the wind-driven flux is needed.

Along the equator the steady state zonal momentum balance is, for $v \equiv 0$:

$$u \cdot \nabla u + \frac{\partial P}{\partial x} + \left(A \frac{\partial u}{\partial z}\right)_z = 0 \tag{3}$$

Here, a turbulent stress term has been added to parameterize the effects of wind-driven turbulence. Assuming that the stress is zero at the base of the mixed layer at depth z=ML, neglect of the non-linear term, and integration to the surface results in:

$$A \frac{\partial u}{\partial z}\Big|_{z=0} = - \int_{-H_{ML}}^{0} \frac{\partial P}{\partial x} dz + \tau_o^x \tag{4}$$

Hence the shear in the upper layer is determined by the residual between the depth-integrated zonal pressure gradient and the surface windstress.

In the analysis to follow, we will be utilizing data from 165°E as well as 150°W to further subdivide the eastern volume, and so will require estimates of the wind-driven flow at both longitudes. Bryden and Brady (1985, hereafter, BB) used (4) to find a wind-driven velocity correction to the geostrophic flow across 150°W. Observing that the zonal pressure gradient accounted for 81% of the surface windstress, BB calculated a value for A from the shear implied by a direct measurement of the surface velocity, and the geostrophic velocity at the base of the mixed layer. For a mixed layer depth of 75m, they deduced A to be $16.6 \times 10^{-4} m^2 s^{-1}$. From the Hellerman and Rosenstein (1983) climatology, the annual windstress at 0°, 150°W is 0.072 Pa. Taking BB's mixed layer depth of 75m, then the wind-driven velocity difference is 64cm/s. Such a velocity gives an wind-driven transport of 3.6 Sv if distributed between ± 1°.

A second estimate of the wind-driven flow at 150°W comes from the difference between the geostrophic and directly measured shear. Lukas and Firing (1984) compared the geostrophic and directly measured shear field at 150°W averaged over a 16 month period starting in February 1979. In their difference field, a westward surface jet occupies the upper 65m between ± 2°. Maximum velocities in the jet are around 15cm/s, with an average of about 7cm/s, much smaller than the BB formula would give. A rough estimate of the transport of this jet is 2.0Sv. Thus, these two estimates of the wind-driven flux across 150°W suggests that is small (< 5Sv) though its exact value is uncertain.

Longitude	τ_x (Pa)	M_E (10^9kgs^{-1})
155°W (± 2°)	-0.072	-2.0
(total)		-1.6

Table 5.9 Wind stress and wind-driven zonal mass flux across 150°W. The total is the sum of the transport of the westward equatorial jet of Lukas and Firing (1984) and the off-equatorial flux due to the normal Ekman balance.

At 165°E, the zonal wind-stress on the equator is even weaker than at 150°W, with an annual mean on the equator of only 0.025 Pa westward (based on HR). The direct shear measurements of Gouriou and Toole (1993) do not feature a westward jet on the equator (Figure 4.13). The surface flow about the equator is asymmetrical with weak eastward flow to the north and strong westward flow to the south. On the equator the surface velocity is weak, in agreement with the mean flow estimates from the mooring time series (Figure 4.12). As discussed in Chapter 4, determining the geostrophic shear in the upper 100m is difficult due to the large variations in the density field. Hence we do not feel confident enough of the geostrophic shear to attempt a comparison like that of Lukas and Firing (1984). We will bypass the need for an independent estimate of the wind-driven flux at the equator, by using the directly measured shear within 2° of the equator along the 165°E section.

5.3.2 Geostrophic convergence in the equatorial volume

In Table 7.3 the net transport across the 3 sections in broad water mass classes can be compared. This "first guess" circulation, based on the reference levels outlined in the previous chapters, features a meridional overturning that is characteristic of the Pacific basin: a northward flux of roughly 10 Sv of LCPW which returns southward largely below the thermocline. This overturning has been documented at nearly all zonal Pacific sections (e.g. Wunsch *et al.*, 1983; Roemmich and McCallister, 1989). At 14°S, there is more water of LCPW densities flowing north than returning in the intermediate and deep layers, while at 10°S there is more intermediate and deep water moving south than LCPW flowing north. There is also a substantial convergence of LCPW between 10°N and 14°S in this initial guess flow field.

It is interesting to note that the thermocline and Ekman transports across the meridional sec-

tions balance within the range of Ekman estimates (Table 5.10). This has also been observed in the Atlantic (Roemmich, 1983). However, in contrast with the Atlantic in which there is a net northward cross-equatorial flux of warm water of about 10 Sv, the Pacific appears to have a more symmetrical circulation, where enough thermocline water flows equatorward geostrophically in each hemisphere to supply the respective returning poleward Ekman flux.

The net geostrophic transports across the zonal sections are larger in both cases than the estimates of the Ekman fluxes. This is acceptable at 14°S due to the possibility of leakage into the Indian Ocean. Across 10°N, the large imbalance violates the assumption of continuity: adjustments to the reference level scheme thus are necessary.

The mass convergences in the eastern and western volume also suggest that the circulation needs to be adjusted. In the eastern volume there is a much larger net geostrophic mass convergence than Ekman divergence (Table 5.11). Much of the excess convergence occurs in the deep water. In the western box, a 10Sv divergence in the deep water is compensated by a convergence in the intermediate water, implying large downward cross-isopycnal fluxes.

Water Mass	θ bounds	Model Layers	10°N	14°S	165°E
Geostrophic Transport					
Thermocline	> 11.3°C	1-8	-39.3	26.9	13.6
Int. Water	11.3 > Θ > 2.1	9-12	-9.3	-2.1	-16.9
Deep Water	2.1 > Θ > 1.2	13-15	-6.2	-4.8	2.2
Bottom Water	Θ < 1.2	16-19	7.1	15.3	-6.1
Net Geostrophic			-47.7	34.4	-7.2
Ekman Transport					
Hellerman and Rosenstien			43.4	-28.4	-1.0
FSU			37.4	-26.3	-
Harrison			32.6	-23.1	-

Table 5.10 Geostrophic transport ($10^9 kgs^{-1}$)across the transpacific sections in broad water mass classes. The Ekman transports for three climatologies are also shown. At 165°E, direct shear measurements are used within ± 2°, and are assumed to include the directly wind-driven shear there.

Water Mass	θ bounds	Model Layers	Eastern	Western
Geostrophic Convergence				
Thermocline	> 11.3°C	1-8	60.5	6.1
Int. Water	11.3 > Θ > 2.1	9-12	-4.5	11.9
Deep Water	2.1 > Θ > 1.2	13-15	12.0	-11.6
Bottom Water	Θ < 1.2	16-19	7.4	0.8
Net Geostrophic			75.5	7.2
Ekman Convergence				
Hellerman and Rosenstien			-58.2	-13.6
FSU			-52.6	-11.1
Harrison			-46.3	-9.8

Table 5.11 Mass convergence in the equatorial Pacific volumes for different components of the flow, in the unadjusted circulation.

It is unlikely that these features are real. Before we can analyze the circulation, we must first ensure that it is 'sensible': i.e. that volume, heat and salt are conserved through out the enclosed volumes, as required for a steady state system.

5.4 The Inverse Model

5.4.1 Introduction

It is difficult to construct in an *ad hoc* way a circulation scheme that obeys what we know to be true of the real ocean i.e. that mass, heat and salt are conserved away from sources and sinks in the subsurface ocean. The initial guess field described above does not conserve volume in the North Pacific basin or in the eastern Pacific.Furthermore, it demands improbably large cross-isopycnal fluxes in the deep ocean. It is more likely that the first guess reference surfaces for the thermal wind shear are not quite correct.

Here, a least-squares inverse model is used to find a circulation scheme which does conserve such properties as volume, heat and salt. The model is one of a family of optimization schemes used in recent years to examine the circulation across hydrographic sections (e.g. Wunsch *et al.*, 1983; Roemmich and Wunsch, 1985; Rintoul, 1991). In the following sections the model construction is explained and compared with the more commonly used solution form in inverse box models: the 'minimum length' solution. The solution form used here is slightly modified to accommodate inequalities as constraints.

5.4.2 Model Formulation

The following starting assumptions are made:

- the flow is steady and the data set assembled is a good representation of the mean state of the ocean
- the flow is geostrophic below the mixed layer
- the Ekman balance holds in the surface layer

The circulation will be constrained as follows:

- mass, salt and heat (i.e. $C = \rho$; $C = \rho S * 1e\text{-}3$; $C = \rho c_p \theta$, respectively) are conserved in density layers deeper than the leakage out of the Indonesian Passages. It is generally believed that the Throughflow occurs predominantly in the upper 200m of the water column (Wyrtki, 1987). Therefore the solution is constrained so that little of the subthermocline waters participate in the Throughflow.
- there is zero net salt convergence between 10°N and the Bering Straits, and the flux

out of Bering Strait is specified

- there is zero net salt convergence in the eastern box

The implementation of these constraints are outlined below.

Conservation Statements for Density Layers

In the deep Equatorial Pacific, salinity and temperature changes along density surfaces are small, and the surfaces nearly horizontal. Potential density surfaces are then a close approximation to the neutral surfaces along which a fluid parcel can flow adiabatically. Here locally referenced potential density surfaces are used in lieu of neutral surfaces.

Consider a layer of water bounded laterally by hydrographic sections and land masses, and vertically by potential density surfaces referenced to a nearby pressure surface. The expression for mass conservation for such a layer is:

$$\iint \rho u dx dz + \iint \rho \omega dx dy|_{z_t}^{z_b} = 0 \tag{5}$$

where **x** is the along track co-ordinate, **u** is the cross-track velocity (positive *into* the volume), ρ the water density, ω the cross-isopycnal velocity (positive upwards) and z_b, z_t the lower and upper interfaces of the layer. Conservation of a tracer 'C', such as heat or salinity is written as:

$$\iint C u dx dx + \iint C \omega dx dy|_{z_t}^{z_b} + \iint K \frac{\partial C}{\partial z} dx dy|_{z_t}^{z_b} = 0 \tag{6}$$

Horizontal and vertical advective convergences of the property are balanced by diffusion across the isopycnal surfaces. Here K is the vertical diffusivity. Epipycnal diffusion is assumed to be negligible.

Cross-isopycnal fluxes in (5) and (6) are assumed to be due to mechanical mixing by turbulence that is fueled by the internal wave field or some other sources of vertical shear. Other processes that may contribute to ω are caballing and salt-fingering which come about from the combined effect of horizontal mixing and the non-linearity of the equation of state for seawater, as discussed by McDougall (1984). These effects are assumed to be negligible

in this study. Estimates of the contributions to ω due to these processes require values of the horizontal cross-track gradients of temperature and salinity on neutral surfaces, which are difficult to calculate and not available from the data set in hand. If these processes are important, then we might expect that the model will not be able to account for the property distributions.

Discretization

Applying the constraints (5) and (6) to the two volumes of water bounded by the MW893, TEW and 165°E sections, zonal integrals are discretized as a sum of the transports between hydrographic station pairs. The total geostrophic velocity is split into a part relative to an initial reference level (that is known) and a barotropic adjustment that is unknown i.e $\mathbf{u} = \mathbf{u}_g + \mathbf{b}$. Mass conservation in the density layer *ib* is then written:

$$\sum_{ix=1}^{nx} A^{\rho}_{ib,ix} b_{ix} + a_{ib}\omega_{ib}\rho\Big|_{top}^{bottom} = \sum_{ix=1}^{nx} T^{\rho}_{ib,ix} \qquad (7)$$

where:

$A^{\rho}_{ib,ix} = \int\int_{(ib,ix)} \rho dxdz$ i.e. the area integral of density for the ib^{th} density layer and ix^{th} station pair; $T^{\rho}_{ib,ix} = \int\int_{(ib,ix)} \rho u_g dxdz$ i.e. the area integral of the initial guess geostrophic mass flux between the station pair for that density layer; a_{ib} is the horizontal surface area of the density surface respectively, and ω_{ib} the average isopycnal velocity across it. The tracer constraints can be written similarly, but with expressions for the vertical divergence of the diffusive terms added.

Following Hogg (1987), the tracer conserving statements are replaced by an equation for the *tracer anomaly*. This is necessary since the variations in salinity, for example, are a small percentage of the total salt content, and so constraining total salt in each layer is almost equivalent to constraining mass. However, conservation of the salinity anomaly may be quite independent of the conservation of mass. Arguments for using anomaly equations to maximize the independent data in the constraints are discussed in McDougall (1991).

A layer averaged tracer concentration is defined as:

$$\langle C \rangle = \frac{\iint C dx dz}{\iint dx dz} \tag{8}$$

Multiplying the mass conservation statement (5) by <C> and subtracting it from the property equation results in:

$$\sum_{ix=1}^{nx} (A^{C}_{ix,ib} - \langle C \rangle_{ib} A^{\rho}_{ix,ib})\, b_{ix} + \omega_{is} a_{is} (C_{is} - \langle C \rangle_{ib}) \Big|_{is=ib}^{is=ib+1} + K_{is} \frac{\partial C}{\partial z}_{is} \Big|_{is=ib}^{is=ib+1}$$

$$= \sum_{ix=1}^{nx} [T^{C}_{ix,ib} - \langle C \rangle_{ib} T^{\rho}_{ix,ib}] \tag{9}$$

For the ocean volume bounded by the data, information is only available around the edges and not within. Hence $\frac{\partial C}{\partial z}$ is not known everywhere. The assumption is made that the average of $\frac{\partial C}{\partial z}$ around the edges is a good approximation of its value throughout the volume on any given density level. Justification is based upon the observation that below the equatorial thermocline properties in the intermediate and deep water layers are fairly homogeneous within 10° of the equator, as suggested by the GEOSECS Atlas. One can then think of mixing density, salt and heat against a single vertical profile that is representative of the average conditions in each volume. The same approach is taken for the property values at the interfaces. Hence we neglect horizontal inhomogeneities in ω, $\frac{\partial C}{\partial z}$, and C.

At each isopycnal interface, vertical gradients are calculated by a least squares fit over a 50m interval centered around the interface at each hydrographic station. These values are then averaged over all casts that bound the volume to find the mean value for that interface. Similarly, the mean values of potential temperature and salinity at the bounding surfaces are found for each volume. The mean values at the interfaces are not the same as the average value <C> for any given layer. Representative profiles of the tracers and their gradients are calculated for each volume separately.

Continuity, heat and salt conservation is applied below the thermocline, layers 9-19. The layers above are left unconstrained because the water masses are no longer common between the two sections. Also, in the eastern Pacific, layers above this level outcrop and lose fluid to the mixed layer, while in the western Pacific, fluid at these depths can exit via the Throughflow.

Total Salt Conservation

The atmosphere cannot flux significant amounts of salt, and so salt must be conserved in closed ocean volumes. Between 10°N and the Bering Strait there should be no net convergence of salt by the mean circulation. Through Bering Strait $0.8(\pm 0.1)x10^6 m^3 s^{-1}$ of water at 32.5 psu flows from the North Pacific into the Arctic Ocean (Coachman and Aagaard, 1988). The associated salt flux of 26.7 ($\pm$ 3.3) x $10^6 kgs^{-1}$ out of the Pacific via the Bering Strait must be compensated for by an identical salt flux across 10°N. This is added as a constraint to the circulation. Similarly, the net salt convergence in the eastern box is required to be zero: the sum of the salt input by the geostrophic flow must balance the salt divergence due to the Ekman flows.

These constraints replace the constraint on no net mass convergence in bounded ocean volumes typically applied in box inversions of hydrographic data. Conserving salt instead of mass allows for the explicit treatment and calculation of the net mass convergences due to the surface fluxes of freshwater (Wijffels, *et al.*, 1992).

Isolated Deep Basins

A further set of constraints is added to the system. In Chapter 3 it was observed that along 14°S the deep θ-S relation west of Vanuatu is distinct from that to the east. It was concluded that the deep waters in the Coral Sea and New Caledonia Trough do not communicate directly to the north and west with the North Pacific, but are ventilated from the far south via the Tasman Sea. Formulating this observation into a constraint for the inverse model, no net flow is allowed through layers below 2000db along the TEW section (12 through 19) west of Vanuatu.

The West Fiji basin east of Vanuatu, is also assumed to be removed from the major pathway of LCPW transport into the North Pacific, and no net inflow is allowed into this basin. As

discussed in Chapter 2, the Philippines is also considered a 'dead' end for the bottom water flow basin below 3500db, and so the net transport below this depth is required to be zero.

5.4.3 Optimization Function

We aim to find a set of adjustments to the initial guess circulation, so that the constraints are satisfied. The number of unknowns far exceeds the number of constraints. In an under-determined system there are an infinity of solutions. An optimization technique is therefore employed to choose the *best* solution. What defines the optimal solution is outlined below.

The constraint equations can be written in matrix form as follows:

$$[A]\begin{bmatrix}\underset{\sim}{K}\\ \underset{\sim}{\omega}\\ \underset{\sim}{b}\end{bmatrix} = \underset{\sim}{T} \tag{10}$$

where $\underset{\sim}{K}$, $\underset{\sim}{\omega}$, $\underset{\sim}{b}$ are vectors of the unknowns, **A** the constraint matrix and **T** the r.h.s of the constraint equations. The initial guess for the barotropic velocities are $\mathbf{b}_o = 0$ at the reference surface. The cross-isopycnal terms are also started at zero. A cost function is formulated which is a measure of the difference between the solution and the initial guess, and how well the constraints are satisfied:

$$L = \varepsilon^2\left[\sum_{ix}(b-b_o)^2_{ix} + \sum_{ib}(\omega-\omega_o)^2_{ib} + \sum_{ib}(K-K_o)^2_{ib}\right] + \sum_{ic}(\text{residual of the icth constraint})^2$$

$$= \varepsilon^2 x^T x + e^T e \tag{11}$$

The single vector **x** denotes the adjustments made to the initial guess, and the vector **e** denotes the constraint imbalances:

$$e = (T - Ax) \tag{12}$$

The relative importance of the size of the adjustments compared to the size of the residuals in the cost function L, is controlled by the parameter ε, which must be chosen *a priori*.

L(x) is minimized with respect to **x** yielding the equation that the optimal **x** must satisfy:

$$\frac{\partial L}{\partial x} = 0 \Rightarrow \qquad [A^T A + \varepsilon^2 I]\, x = A^T T \tag{13}$$

Singular Value Decomposition

The solution can be found in terms of the singular value decomposition (SVD) of A. Decomposing A in the usual way:

$$A = U \Lambda V^T \tag{14}$$

then U is a matrix whose columns span the column space of A, and V is a matrix whose first NC^{th} columns span the row space of A, where NC is the number of constraint equations (and rows of A). The diagonal of Λ contains the eigenvalues, λ associated with the eigenvectors in the columns of V. The SVD can be thought of as an EOF of the row space of A. Vectors that span the row space of A are rearranged by the singular value decomposition into the array V such that the vector containing the greatest amount of variance of the row space is the first column vector of V and has the largest eigenvalue, located in the first row of the diagonal matrix Λ. The vector that captures the smallest amount of variance of the row space of A is in the NC^{th} row of V, with the smallest eigenvalue in the last row of Λ.

Using the SVD, the solution to (13) can be written:

$$x = \sum_i \underset{\sim}{v}_i \left(\frac{\lambda_i}{\lambda_i^2 + \varepsilon^2} \right) (\underset{\sim}{u}_i \cdot T) \tag{15}$$

For comparison the 'minimum length' solution to the original problem (10) is:

$$x = \sum_i \underset{\sim}{v}_i \left(\frac{1}{\lambda_i} \right) (\underset{\sim}{u}_i \cdot T) \tag{16}$$

In both cases, the adjustment vector **x**, is a linear combination of vectors that span the row space of A, denoted as the $\mathbf{v}_i$. Each vector is weighted by a projection of the residuals onto the eigenvectors of the column space of A, and by a factor involving the eigenvalues. The rank of the minimum length solution is the number of eigenvectors used in the sum in (16). As the rank is increased the variance of the solution increases since each additional eigenvector is multiplied by the inverse of its eigenvalue. Hence the high rank eigenvalues add

increasingly greater variance to the solution. At full rank, the constraints are satisfied perfectly. In practical applications, however, the full rank solution is never utilized since requiring the constraints to be perfectly satisfied is not reasonable. Uncertainties are to be expected in the constraints: observational errors exist in the data; and the assumptions on which the constraints are based do not account for all the processes at work in the ocean. To account for such errors, the rank of the system is usually chosen to be less than the full rank.

Choosing ε in the 'damped least squares' solution (15) is analogous to choosing rank in (16). If $\varepsilon = 0$, (15) reverts back to the 'minimum length' solution (16). For ε small, the result is to damp the high eigen-vectors, limiting the size of the solution. The cost of limiting the solution size is that the constraints are not perfectly satisfied. The larger ε, the smaller the solution size and the larger are the residuals in the constraints. This trade-off, explicit in (11) determines the effective rank of the 'damped least squares' solution.

5.4.4 Weighting the Constraints

If the constraints are multiplied by a set of weights, the contribution of each constraint to the residual **e**, and hence the cost function L, will be modified. The most obvious need for weighting lies with the natural units of the system. Unweighted heat residuals are in units of 10^{15}W, mass residuals in 10^{9}kg/s and so forth. A normalization is at least required to compensate for the units.

The second use of constraint (or row) weighting is to give relative importance to constraints that one has the most confidence in. An error variance is assigned to each constraint: σ_{ic}^2 and a weight matrix is defined as:

$$W = \begin{bmatrix} 1/\sigma_1 & 0 & 0 & 0 \\ 0 & 1/\sigma_2 & 0 & 0 \\ 0 & 0 & 1/\sigma_3 & 0 \\ 0 & 0 & 0 & \ldots \end{bmatrix} \qquad (17)$$

The system solved is now:

$$[WA]x = [W\hat{T}] \tag{18}$$

where each constraint is divided by the standard deviation of it's error distribution. Therefore constraints with large expected errors are down-weighted in the cost function.

5.4.5 A priori errors

Layer continuity constraints

It is not obvious how to choose the uncertainty to apply to the mass balance in each layer. Roemmich (1983) choose an *ad hoc* value of 3 SV. Here, we choose to base the uncertainty on the observed eddy variability in the synoptic sections. Typically, the basin wide fluxes are associated with small spatially persistent velocities that are superimposed on an energetic eddy field. For example, along 10°N the eddy variation in layer 11 is of order 3SV while the estimated net mass flux is close to zero (Figure 5.5). For layers with a smaller area or deep depth the eddy variability is smaller. The uncertainty in the continuity equations was therefore assigned as the standard deviation of the station pair transports for each volume in each layer:

$$\sigma^{\rho}_{ib} = std|_{ix}(T^{\rho}_{ib,ix}) \tag{19}$$

Throughout most of the water column, the uncertainty is close to or less than $1x10^9 kgs^{-1}$, except in the thicker intermediate water layers and thin thermocline layers (Figure 5.5). In the deep isolated basins west of Vanuatu, errors are also assigned to each isopycnal layer using (19).

Errors in the buoyancy constraints

The variance of the mass conservation errors $\sigma^{r}_{ib,}$ is used to estimate the errors for the salt and heat anomaly equations. Uncertainty in the mass balance for a density layer produces uncertainty in the advective convergence of heat and salt in that layer. Vertical property gradients are generally larger than horizontal gradients and an unresolved mass flux of size σ^{r}_{ib} passing through the layer will result in a maximum property convergence of:

$$\sigma^{C}_{ib} = (\sigma^{\rho}_{ib}/\rho)\,(C_{ib+1} - C_{ib}) \tag{20}$$

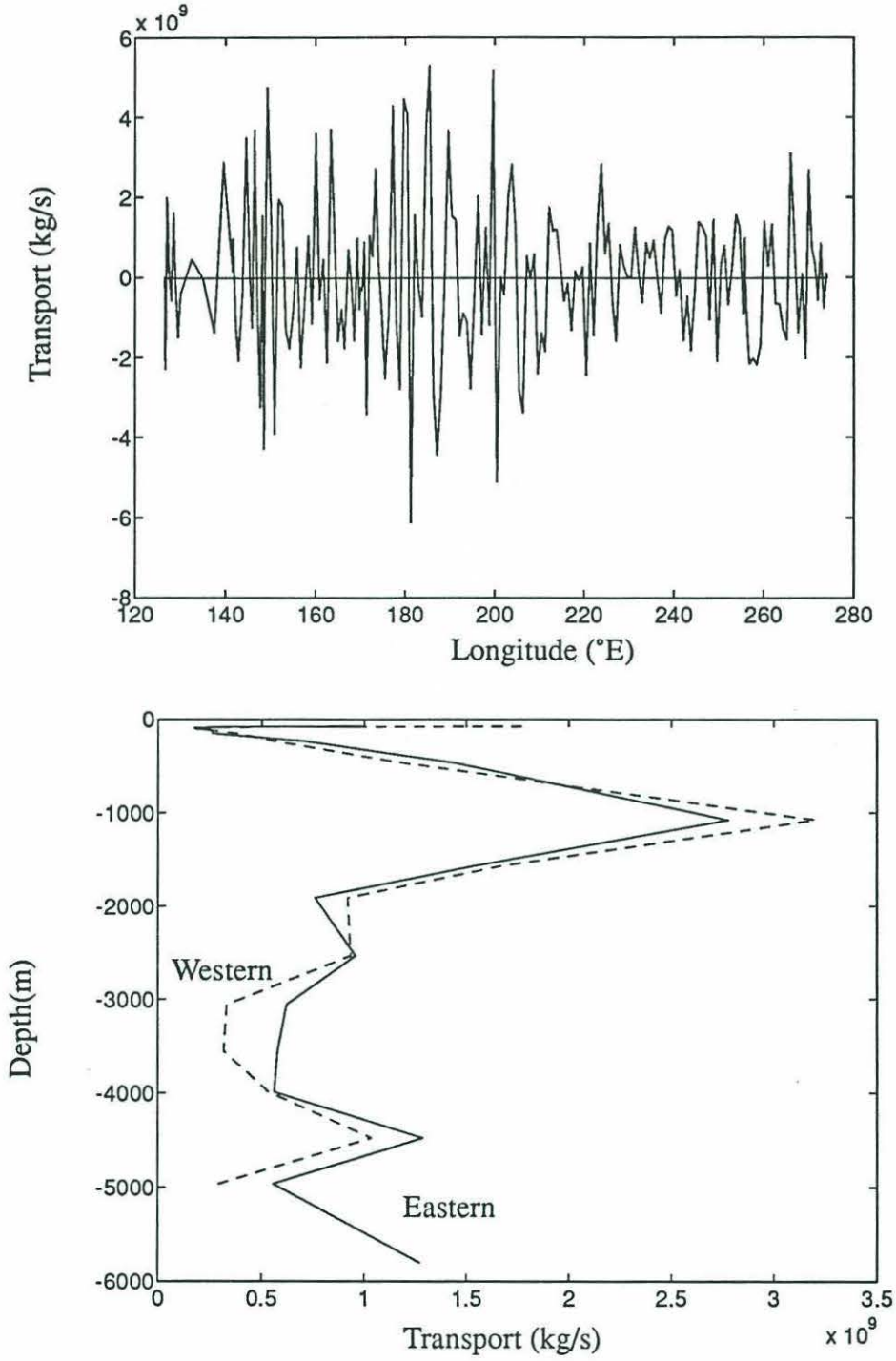

Figure 5.5 (a) Transport in station pairs in layer 11 across 10°N. The mean is superimposed. The large fluctuations show the size of the eddy variability along the section. The standard deviation of the station pair transport is used to assign uncertainties to the layer continuity constraints, shown in (b).

where σ^{ρ}_{ib}/ρ is the error in the cross-isopycnal volume flux for that layer.

Errors in total salt constraints

For the conservation of salt constraint in the North Pacific, we start with the error in the measured volume flux through Bering Strait of 0.1 SV, which translates to an uncertainty in the salt flux of $\pm$ 3.3x $10^6 kgs^{-1}$. However, the Bering Strait outflow is balanced by the small difference between two very large terms: the Ekman and geostrophic salt fluxes across 10°N. Uncertainty in the first term is directly connected to the errors in the wind-stress climatologies. The geostrophic flux is uncertain because of the reference level problem. If we choose to force the circulation to balance any given wind-climatology, then we are more likely adding error to the flow than gaining any information. Therefore we choose to leave the total salt constraints 'weak'; i.e. they will only need to be satisfied to within the range of uncertainty of the Ekman fluxes, which is about $\pm$ 3 SV x 35psu = $1.05x10^8 kgs^{-1}$. In this way we allow the tracer conservation statements to dominate in determining the geostrophic fluxes, instead of an error-prone Ekman mass flux.

5.4.6 Weighting the Solution

Besides weighting the constraints to account for the expected uncertainty, weights are also applied to the solution vector itself to offset the scale differences its components. For instance, the cross-isopycnal velocities are expected to be of order 10^{-7} ms^{-1} and the horizontal velocity adjustments of order $10^{-3} ms^{-1}$. The solution vector in the cost function must also be normalized to account for the size difference of its various components. This is known as column weighting.

The normalizations and initial guess values used in the model are shown in Table 5.12. The cross-isopycnal terms are weighted at 10 times the canonical values. This is to ensure that the model resolves these fluxes better than the horizontal adjustment terms.

The system of constraints now becomes:

$$[WA]\, W_x x = [W\hat{T}] \qquad (21)$$

where W_x is a diagonal matrix containing the normalized inverse of the column weights.

5.4.7 Inequality Constraints

Diffusion fluxes properties down gradient and so vertical diffusivities can only be positive. This provides an additional constraint on the model, restricting the space of possible solutions in which the optimization takes place. A discussion of the implementation of the inequalities can be found in Menke (1984). The algorithm splits the set of inequalities into two groups: a slack set in which the inequality parameters are allowed to vary freely; and an exact set which are added as equality constraints to (6). In the final solution, if an inequality is found in the exact set, it means that the cost function is best minimized when that parameter is some value less than zero. Since this is not feasible, the parameter is set to zero. If an inequality is in the slack set, the cost function is best minimized when the parameter is greater that zero.

An implication of the inequality algorithm is that while iteratively optimizing the solution within the feasible space, the effective rank of the problem is changing as the inequality constraints are swapped back and forth between the slack and exact sets. The damped least-squares method is used here instead of the usual truncated minimum length solution to accommodate the technique.

5.4.8 Further Solution Restrictions

The optimization problem outlined above is still very underdetermined. To further restrict the optimization, we confine the solution space so that the circulation of LCPW at 10°N as determined by JT, is largely preserved. This is implemented by decreasing the adjustment size weight by 1/10 over the layers containing LCPW. Hence the model will adjust other parts of the solution, before the LCPW layers.

Solution component	Initial Guess	Weight
cross-isopycnal velocities (ω)	0.	$10.x10^{-7}$m/s
vertical diffusivities (**K**)	0.	$10.x10^{-4}m^2s^{-1}$
barotropic adjustments (**b**)	0.0 ms^{-1}	0.01 ms^{-1}

Table 5.12 Solution initial guesses and normalization weights used in the inverse model

5.5 A Mass and Salt Conserving Solution: M1

A solution is first found in which the cross-isopycnal terms are unconstrained, and are largely diagnosed from the initial guess flow. This circulation will only be required to obey constraints of total salt conservation and observe the topographic constrictions due to the closed basins.

Specifically the following constraints are imposed:

- mass conservation in density layers 8 through 19
- total salt conserved in the eastern box and the North Pacific
- small net inflow to the isolated deep basins west of Vanuatu
- small net inflow into the West Fiji Basin

Since the heat and salt balances in the individual layers are left unconstrained, this circulation will not conserve buoyancy. The model has a total of 56 constraints and 421 unknowns and will be referred to as model M1.

5.5.9 Choosing ε

There is no obvious way to choose the parameter ε before running the model. McIntosh and Veronis (1992) use a cross-validation technique in a model which contained several free parameters in the cost function. There is only one parameter to chose here and a simpler approach is used. The system is solved over a range of ε, and the maximum residual amplitude found (weighted by the expected error). A maximum weighted residual (MWR) greater than 1 indicates one or more constraints still has a residual larger than the expected error. The *size* of the solution is measured as the mean absolute value of the weighted solution $|\bar{x}|$. If $|\bar{x}| >> 1$, then the adjustments are much larger than the expected values.

Figure 5.6 shows the MWR and $|\bar{x}|$ for various values of ε for the solution to the mass-conserving model. A natural consequence of (11) is the tendency towards large residuals and small solution sizes as ε is increased. For the mass conserving solution, the best choice for ε is around 1.5. The effect of ε on the eigenvalue factor in (15) is shown in (Figure 5.7). The optimum choice ε=1.5 is close to being full rank, though the very smallest eigenvalues have been heavily damped.

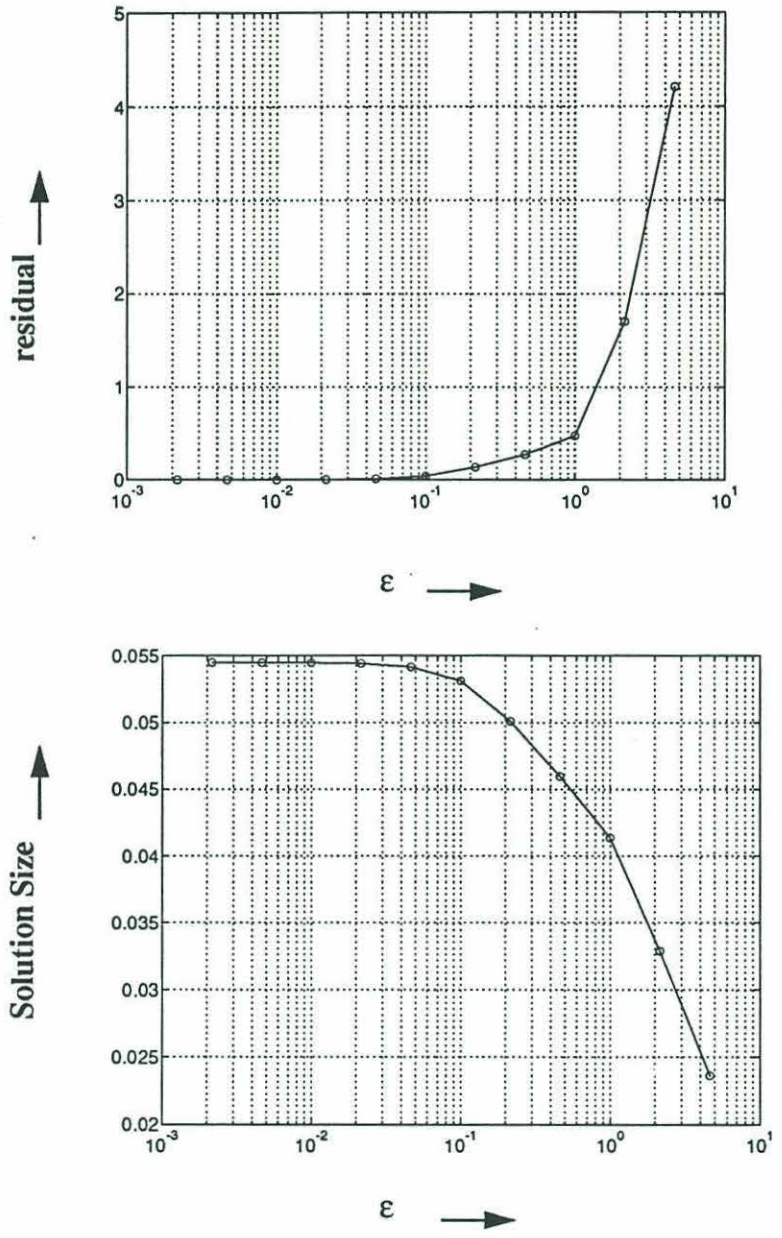

Figure 5.6 Plots used to choose ε for the mass-conserving model. (a) Maximum residual (MWR) versus ε and (b) |x|, the solution size, versus ε.

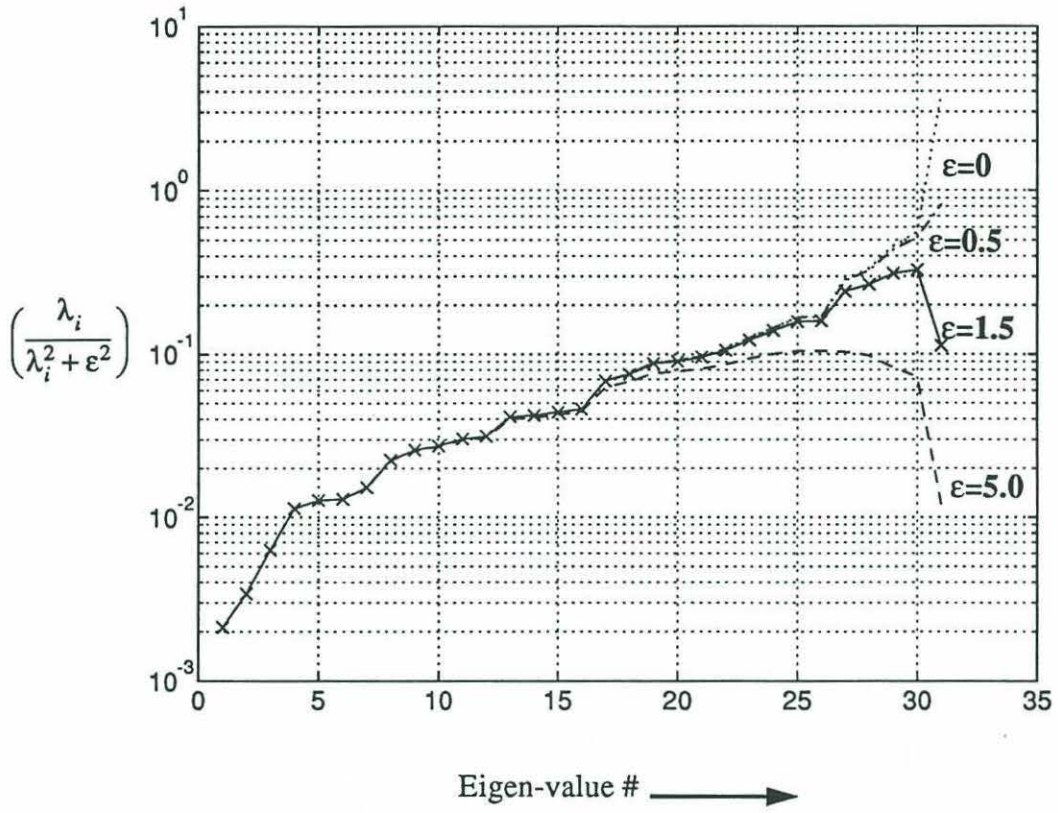

Figure 5.7 Eigen-value scale factor in the damped-least squares solution for various values of ε. The optimum value, ε = 1.5 is analogous to a rank of about 30, close to full rank.

5.5.10 Solution Analysis

In the optimum solution, $|\bar{x}| = 0.04 << 1$ meaning that the adjustments are very small compared to the expected values. This is because only a small number of strong constraints are applied to the system: no large flows into or out of the isolated basins. Continuity in layers provides only a weak constraint since the cross-isopycnal velocities are only required to be less than or comparable to their initial scaling. The station pair barotropic adjustments are very small in this model (Table 5.13) and so the model circulation is very similar to the initial guess circulation.

Ekman Corrections

In order to diagnose the solution circulations for heat and freshwater transports, it is necessary to ensure that salt is conserved in the two enclosed basins: the North Pacific and Eastern volume. Recall that the model total salt constraints allowed for the large uncertainties in the Ekman fluxes. Since the model ensures that the geostrophic flow is internally consistent, we choose to adjust the Ekman fluxes in a simple way to conserve salt. First, the salt balance in the North Pacific is used to find a correction factor for the Ekman transport across 10°N, and then the salt balance in the eastern volume gives a correction factor for the 14°S Ekman flux. Though this is a rather *ad hoc* way to conserve salt, these factors give Ekman transports within 20% of the values given by climatology, well within the errors. Once salt is conserved the heat and freshwater fluxes are simply given by the net sum of the Ekman and geostrophic fluxes. In the western box, mass is closed by assuming that the salt imbalance is due to leakage into the Indonesian Passages at the same salinity and temperature as the Mindanao Current in the upper 7 layers. The Throughflow and its impact on the heat and water budgets will be discussed later.

Cross-isopycnal Terms

The cross-isopycnal terms are diagnosed in the M1 model as a precursor to constraining them via buoyancy conservation. In the following discussion 'upwelling' will refer to cross-isopycnal fluxes, and not vertical velocity.

In the eastern box the diagnosed cross-isopycnal velocities are large only near the surface and bottom boundaries (Figure 5.8). The LCPW flowing into the box across 14°S is largely in the densest model layer, and so it must upwell into lighter layers before it can flow out

Model	Mass and salt conserving **M1**			Buoyancy conserving **B1**		
ε	1.2			0.3		
nc	33			79		
Barotropic adjustment sizes						
|b10|	0.2			0.7		
|b14|	0.8			1.8		
|b165|	1.1			5.5		
A posteriori Ekman corrections (wrt FSU winds)						
α10	0.9			0.9		
α14	0.87			1.1		
Layer mass fluxes (10^9kgs^{-1})	**10°N**	**14°S**	**165°E**	**10°N**	**14°S**	**165°E**
Ekman	39.1	-24.6	-0.9	38.6	-30.6	-0.9
TC	-37.8	27.6	13.5	-36.9	27.6	15.1
IW	-5.3	-2.3	-17.6	-5.5	0.2	-10.2
NPDW	-2.5	-13.5	0.0	-5.0	-7.0	-0.9
LCPW	7.4	15.1	-6.8	9.6	12.1	-7.0
Net	0.81	2.5	-11.8	0.80	2.3	-3.9
Heat Fluxes (PW)						
Equatorial Divergence	1.10			1.57		
10°N	0.66			0.61		
Eastern Surface (W/m^2)	21.8			30.1		
Western Surface	30.9			47.2		
Water Fluxes (P-E, 10^9kgs^{-1})						
Equatorial Divergence	-0.15			-0.1		
North Pacific Basin	+0.02			+0.0		
Eastern Surface [mm/year]	-0.1			-0.29	[-255]	
Western Surface [" "]	0.2			0.20	[+586]	

Table 5.13 Parameters and bulk fluxes for two model circulations: M1 and B1. The barotropic adjustment sizes shown are the mean absolute values for each section. The Ekman correction factors are discussed in the text. Heat fluxes are positive northward and into the ocean. Fresh water fluxes are positive northward and into the ocean.

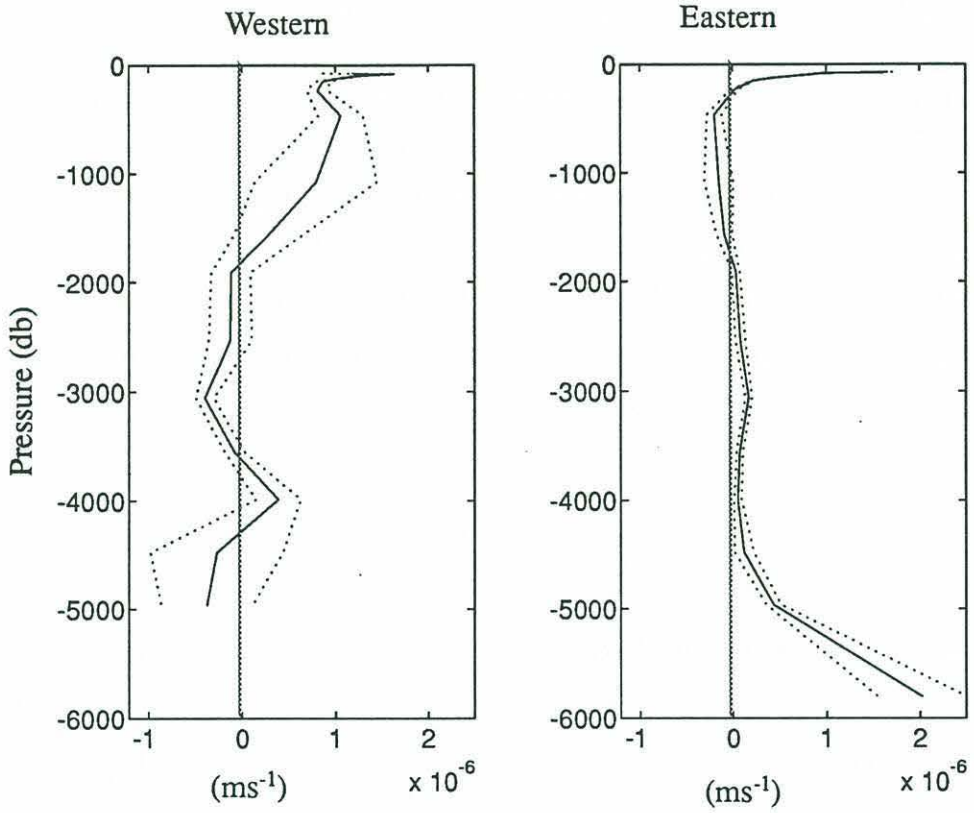

Figure 5.8 Diagnosed vertical velocities in the preliminary model M1: (a) eastern box and (b) western box. A priori error range is shown.

across 10°N and 165°E. Densification is indicated in the intermediate water below the eastern volume thermocline. This up-gradient conversion is responsible for the low heat flux values over the eastern volume in this model (Table 5.13). A large convergence of mass in the eastern Pacific thermocline layers is presumed to flow directly into the mixed layer to feed the Ekman divergence.

The western Pacific upwelling profile is dominated by the large flux of intermediate water across 165°E. This is balanced both by upwelling into the thermocline (hence the large surface heat flux required) and downwelling into the deep water layers. We will find below that the diffusivities implied by this flow are not physically possible.

The heat and salt balances (6) are used separately to diagnostically calculate the diffusivities for each box (Figure 5.9). Recall that in the M1 model, no salt or heat constraints were applied and the diffusivities are unconstrained. Though diagnosed independently, there is a similarity between the salt and heat diffusivities in each of the boxes. If heat and salt mix in the same way, $K_\theta = K_S$. As Munk (1966) and others have pointed out, mechanical mixing by turbulence results in equal diffusivities for heat and salt. If the turbulent overturning can be parameterized as a Fickian process then:

$$K\frac{\partial \rho}{\partial z}\Big|_{bottom}^{top} = \omega\rho|_{bottom}^{top} \qquad (22)$$

If $K_\theta = K_S = K$, (22) directly results from the conservation of heat and salt (since $\rho = \alpha\theta - \beta S$, where α and β are the respective expansion coefficients) only if horizontal mixing is not important and if there are no internal sources of buoyancy (for example geothermal heating). The similarity between K_θ and K_S seen in Figure 5.9 suggests that vertical mixing alone may be able to explain the water mass conversion occurring in the deep tropical Pacific.

Equally notable is the difference in character between the diffusivities in the eastern and western volume. In the eastern box the diffusivities increase towards the bottom, while the western diffusivities are smaller (generally negative), and do not indicate an increase with depth. This suggests that there may be different levels of mixing in the two boxes as well as different levels of mixing with depth. The negative diffusivities are not physically possible, and in this sense the circulation is not realistic. In particular, the negative diffusivities

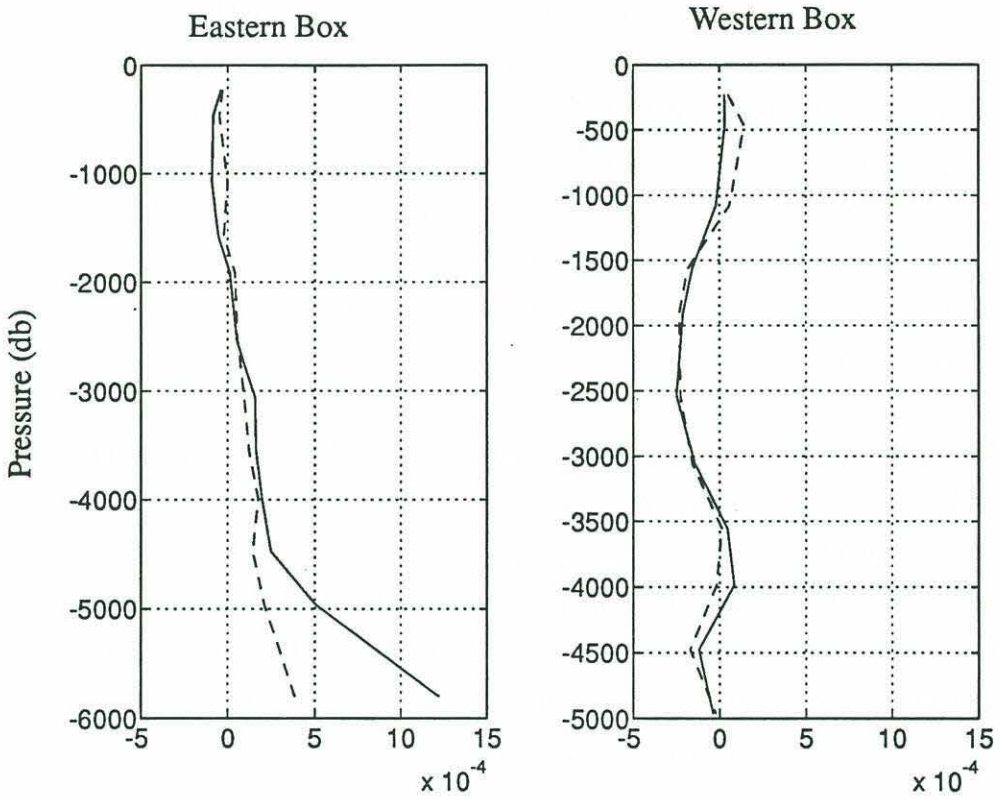

Figure 5.9 Diagnosed vertical diffusivities for (a) the eastern box and (b) the western box. The solid line is for the diffusivities implied by the heat balance; the dashed line are those implied by the salt balance.

are associated with layers where the cross-isopycnal velocity is also negative, suggesting that constraining the diffusivities to be positive will demand circulation changes.

Before proceeding, it is useful to ask whether the differences in the diffusivities for heat and salt are significant in the face of the observational errors. That is, can the buoyancy constraints really add more information to the model? Recall that the *a priori* errors in the heat and salinity equations where assumed to be the same size as the property convergence resulting from the mass flux error in each layer. Model runs for a buoyancy conserving circulation weighted with these uncertainties resulted in flows that were very different from the initial guess. The circulation was driven a long way from the initial guess in order to satisfy the constraints within the error estimates. In particular the deep western boundary current was reduced to less than half its original size at the two zonal sections, and the sense of water mass movement greatly rearranged. For these reasons, these solutions were deemed unacceptable. This in turn suggests that the *a priori* errors in the heat and salt constraints were too optimistic.

Not taken into account in the original buoyancy error estimates is the scatter in the observations of the vertical gradients of heat and salt at the layer interfaces. The distribution of the vertical gradients is fairly guassian for most layers (Figure 5.10): the gradients are not vastly different from section to section. In the bottom-most layers, however, a double peak is present which was found to be related to the spreading of the isopycnals associated with the deep-western boundary currents. The interior values, characterized by the largest peak, are similar for both sections in these deep layers.

New Buoyancy Error Estimates

The uncertainty in the diffusive fluxes due to the scatter in Figure 5.10 must first be calculated and accounted for in the model. A mean diagnostic diffusivity is defined: $K_D = 0.5(|K_\Theta| + |K_S|)$. The scatter in the diffusive property convergences for each layer were found by combining K_D with the observed scatter in the gradients. A bootstrap method was used to find the uncertainty in the model diffusive fluxes. While the uncertainty in the advective fluxes decreases with depth, the uncertainty in the diffusive fluxes increases with depth (Figure 5.11). The net error has a minima at mid-depth, meaning that these layers will be most highly weighted in the model compared to those above and below.

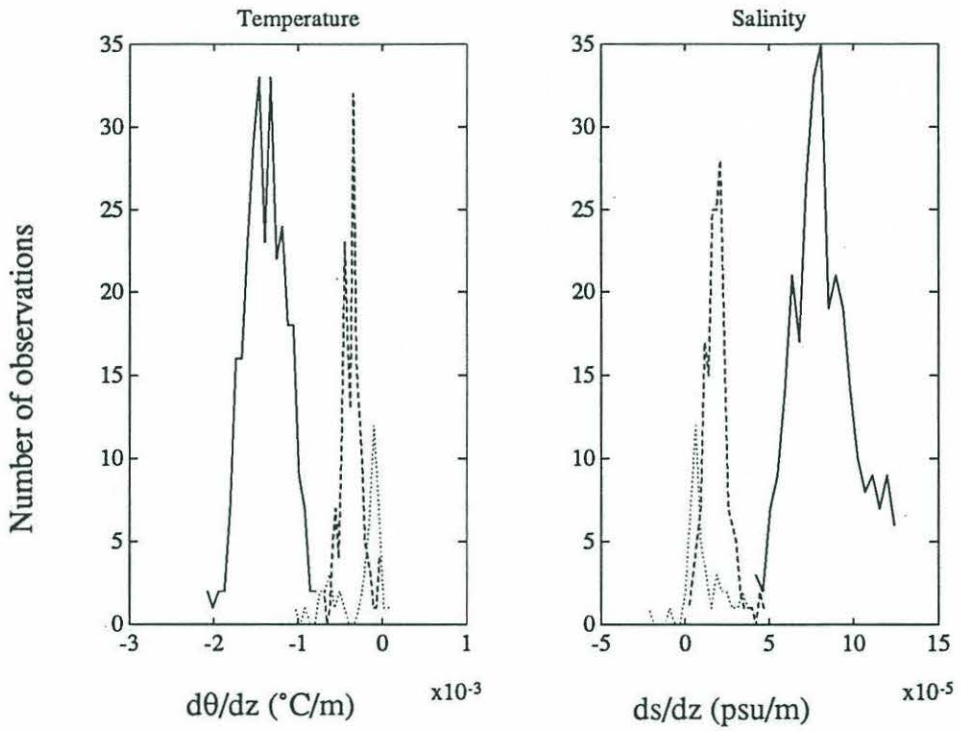

Figure 5.10 Histograms of the vertical gradients for temperature and salinity at the layer interfaces for the eastern box, shown for the 13th (solid), 16th (dashed) and 19th (dotted) surface. Each histogram consists of 20 bins.

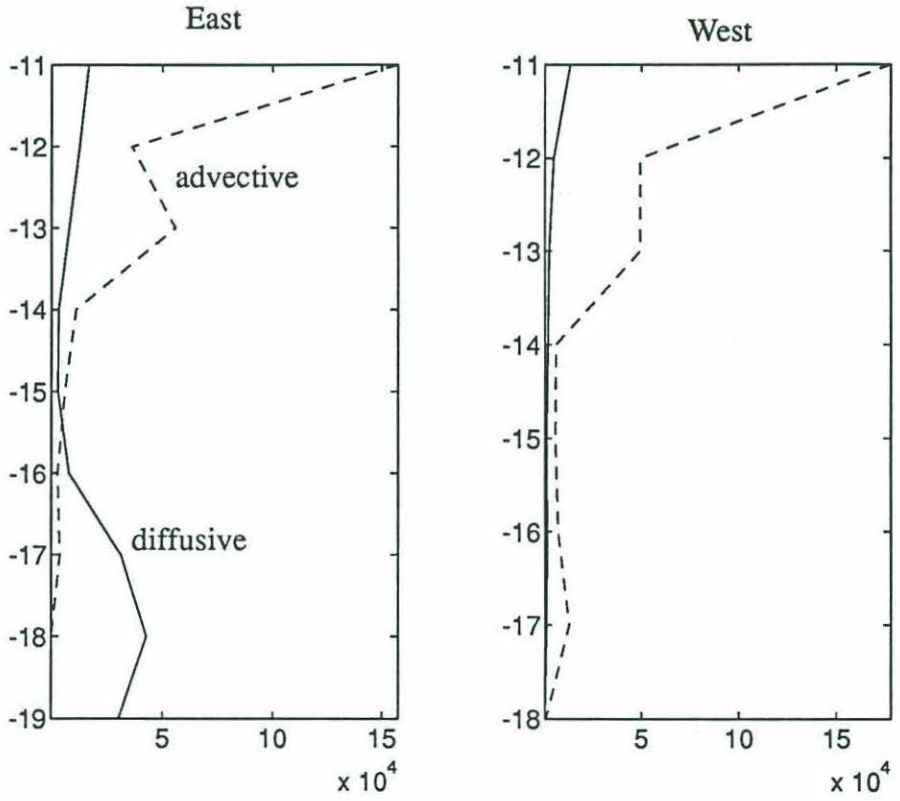

Figure 5.11 Comparison of the original (advective) and new (diffusive) errors for the salt (top) and heat (bottom) balances in layers in the eastern box. In the eastern box the new errors are substantial for the LCPW layers, while the advective error dominates everywhere else.

Finally, the contribution to the error in the buoyancy conserving equations due to scatter in the actual values of θ and S at the interfaces was found to be small, since below the intermediate waters in the tropical Pacific the change in properties along density surfaces is much smaller than the change found between density surfaces.

Are the Buoyancy Constraints Useful?

To decide whether the buoyancy constraints will add information to the model, the diagnosed diffusivities K_D are used to find the residuals in the heat and salt conserving equations (Figure 5.12). The residuals are normalized by the expected errors in the layer balances, so that where they are larger than 1, the constraint is violated. Since the diagnosed diffusivities were negative in the western box, it is not surprising that the residuals are large there. In the eastern box the residuals are smaller, though still larger than the expected errors. Thus the buoyancy constraints add information and are included in the following model.

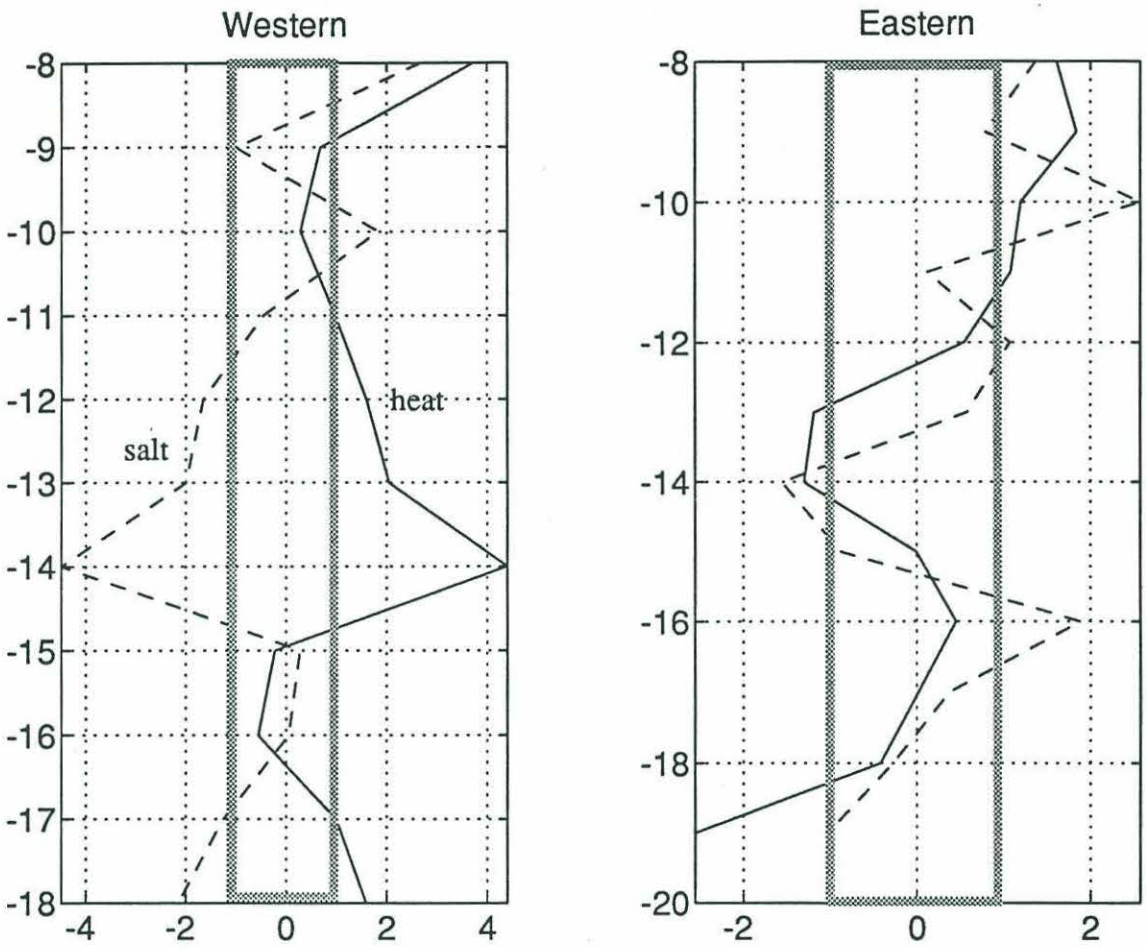

Figure 5.12 Residuals in the heat and salt conservation statements for layers in the western and eastern volumes. The residuals have been normalized by the expected errors and so are only significant if greater than 1.

5.6 Buoyancy Conserving Solution: B1

A new circulation is sought that conserves heat and salinity in isopycnal layers below 1000m. The diffusivities are allowed to vary with depth and between the two boxes. They are, however, constrained to be positive. As for M1, the Indonesian Throughflow will remain unconstrained. The total number of constraints is now 79. The optimum value of $\varepsilon = 0.3$ was found by solving over a range of ε.

The buoyancy conserving circulation, B1, has larger adjustment terms than the simpler model runs (Table 5.13), which is expected due to the larger number of constraints. The barotropic adjustment velocities are small at around 1cm/s, though they do transport considerable volumes of water (Figure 5.13). Along 10°N the anticyclonic flow in the deep and bottom water is reduced by the model, while along 14°S an anticyclonic tendency is introduced. Large quantities of water are advected across 165°E by the model adjustments, though these act to reduce the even larger flows in the initial guess field.

Some important aspects of the circulation are different from M1: the convergence of bottom water between 10°N and 14°S is reduced and the down-welling below the eastern thermocline is much weaker; and in the western volume a net deficit of mass now exists of 5SV. This does not mean that the model requires a reversal of the Throughflow since this deficit can be shown to be small in the face of the uncertainties in the flow. The result does suggest that a large Throughflow is unlikely, a point that will be explored when the warm-water circulation is considered. First we shall describe the subthermocline circulation from the bottom up, and the mixing rates associated with it.

5.7 Description of the Flow

5.7.11 Bottom Water Circulation

The net transport of LCPW across 10°N is $9.6 \times 10^9 kgs^{-1}$ exactly the same as that found by JT. Across 14°S, the net flux of LCPW is $12.1 \times 10^9 kgs^{-1}$. Of the total, 5 SV flows through the Tonga Trench and about 7SV through the Samoan Basin. These transports compare well with those of Taft *et al.* (1991) of 6.5 SV and 8.1 SV respectively for the Tonga Trench and Samoan Basin. Taft *et al.* argue that only 4.3 SV of the Tonga Trench water continues northward since the lower 2.2 SV are blocked by the Robbie Ridge. In B1 all of the water flowing into the Tonga Trench continues northward. Its flow over the Robbie Ridge may be aided by strong cross-isopycnal flow deduced in the model.

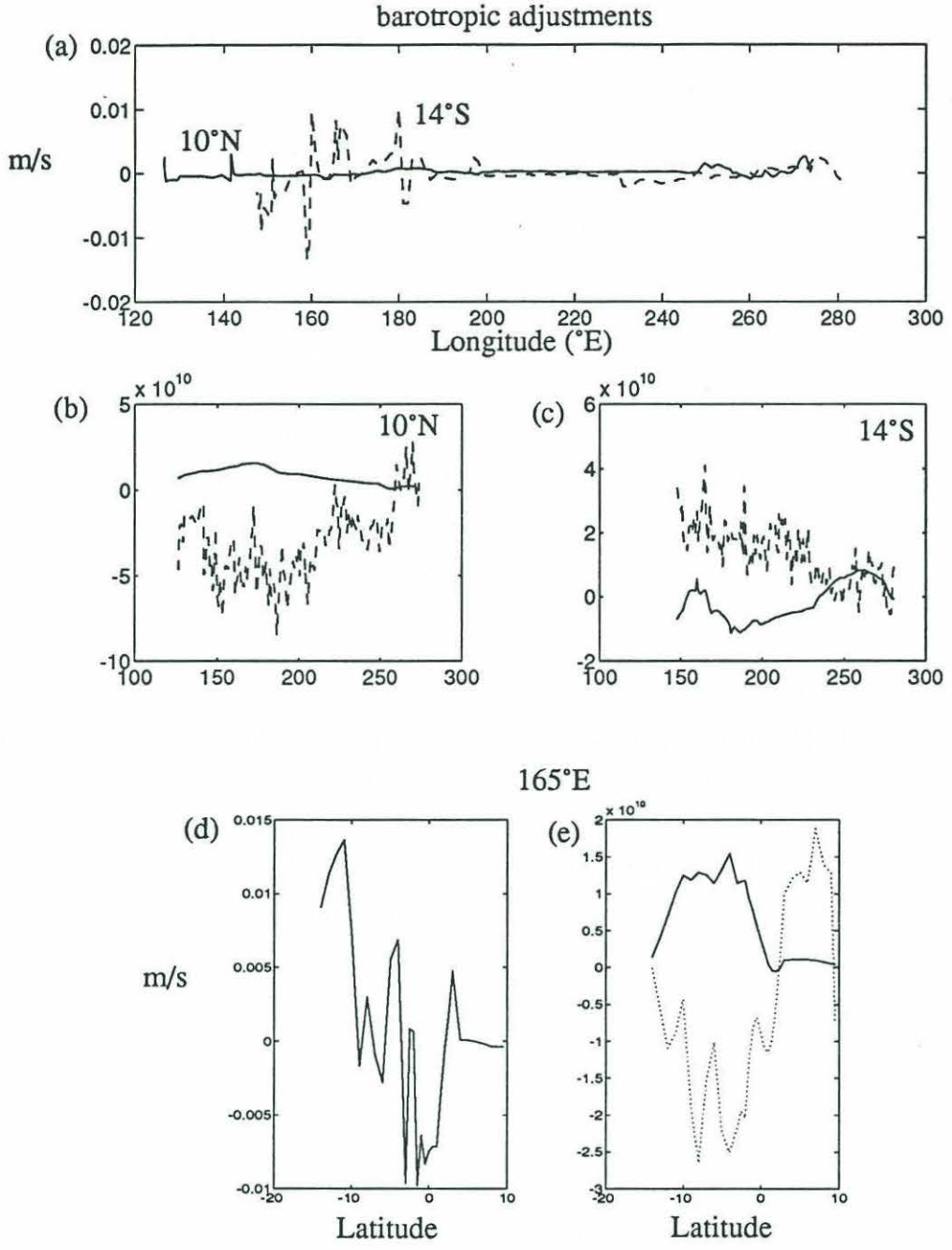

Figure 5.13 Barotropic adjustments for the model B1: zonal sections (a) and along 165°E (d). Also shown is the net transport accumulated from the east and south respectively for the zonal (b, c) and meridional sections (e) for the model adjustments (solid) and the initial guess field (dashed).

The qualitative sense of the circulation of LCPW through the equatorial volume is similar to that deduced by JT. Quantitative differences exist in that the southward recirculation of LCPW over the East Pacific Rise in B1 (10 SV) is more intense than found by JT (4.7 SV).

To best illustrate its circulation we further divide the LCPW into a dense class ($\Theta < 0.97$ °C) and a lighter class ($1.2 < \Theta < 0.97$ °C). The flow pathways of the two classes of LCPW are quite different due to the divergence in the effective western boundary at the northern end of the Tonga Rise. The bulk of the LCPW transported across 14°S is in the densest class and flows directly along the western boundary of the Central Pacific Basin to contribute to the deep western boundary current flowing along the flank of the Line Islands (Figure 5.14). Little of this water flows eastward, though a substantial part of it upwells into the lighter class above.

Though there are large outflows to the west across 165°E and along the Line Islands, the lighter LCPW layers in the eastern volume receive little direct flow across 14°S. The outflows are instead fed by a southward flux of LCPW over the flank of the East Pacific Rise, and the upwelling contribution from the densest layers below. In the eastern volume, part of transport across 165°E upwells and part flows directly northwards across 10°N as the deep western boundary current in the East Marianna Basin described by JT.

5.7.12 Deep water circulation ($1.2 < \Theta < 2.0$°C)

The deep water circulation in B1 features a cyclonic flow of NPDW along 10°N (Figure 5.15) in which about 1/3 of the southward flux over the East Pacific Rise recirculates along the equator and then northward into the western Pacific. The anticyclonic circulation in the deep water is consistent with the nutrient distributions at these depths shown by Reid (1981). Isolines of nutrients on isopycnal surfaces are tilted across the North Pacific Basin such that higher nutrients appear to spread south along eastern boundary and lower concentrations spread north along the western boundary. Along 14°S, there is a substantial flow of NPDW southwards over the western flank of the East Pacific Rise. To the east, 4SV of NPDW recirculates in and over the Bauer and Peru Basins. It is difficult to assess the deep water circulation pattern across 14°S without the nutrient data along the eastern part of the section.

Intermediate Water Circulation

The flow in the intermediate water layers is dominated by large geostrophic eddies particularly along 10°N, and it is difficult to discern the features that may be associated with the

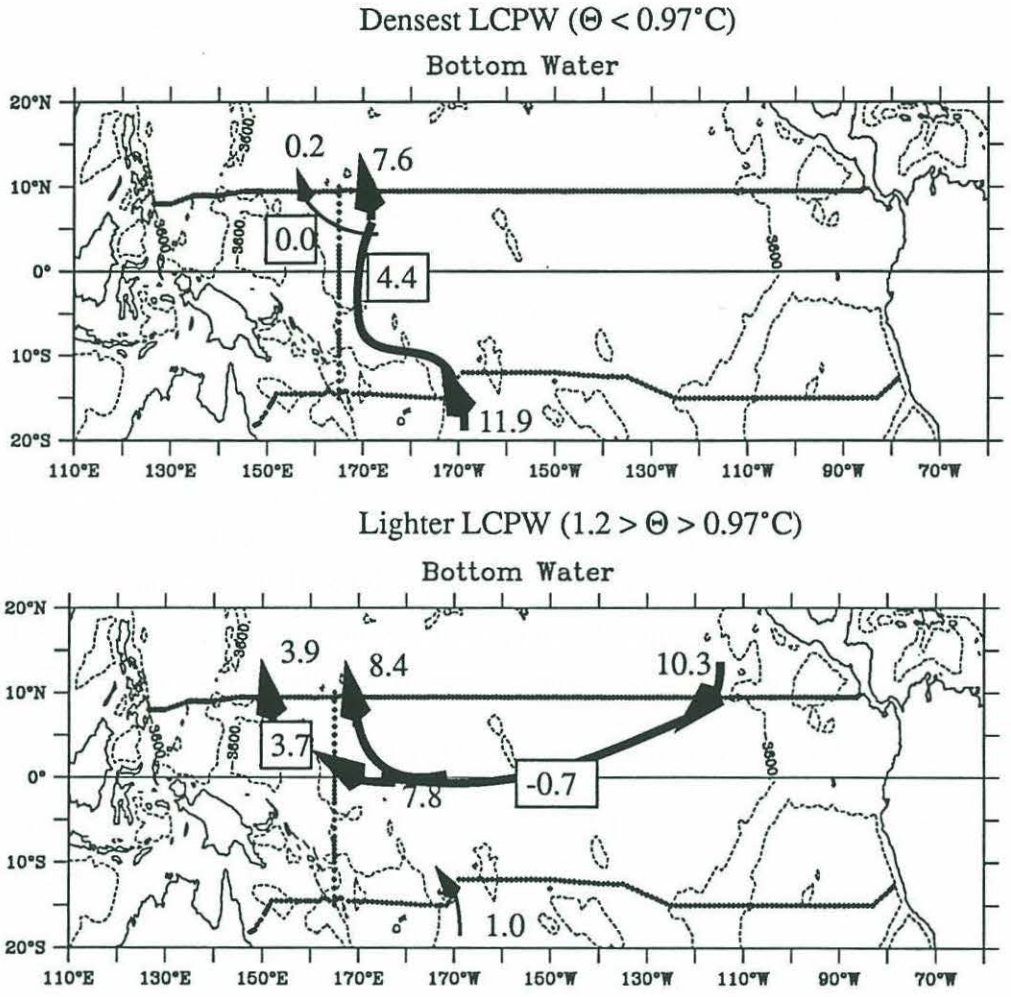

Figure 5.14 Circulation diagrams for the two classes of LCPW water. The arrows show the inflows across the section boundaries and are located where the flow is strongest. The boxed numbers are the upwelling rates (positive upwards) across the *top* of the layer under consideration. The budgets do not close exactly because of the errors allowed in the model.

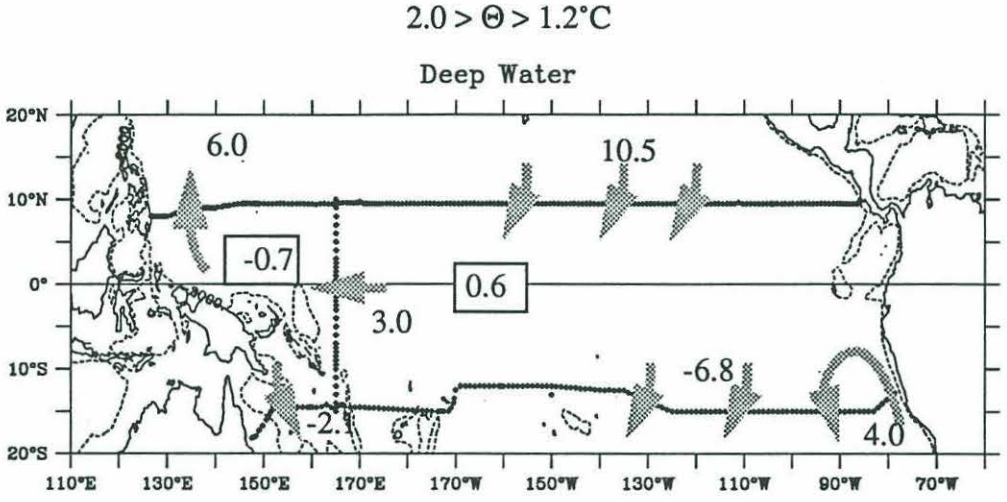

Figure 5.15 As for Figure 5.14, but for NPDW ($10^9 kgs^{-1}$)

mean flow field (Figure 5.16). At the eastern end of 10°N, there is a suggestion of poleward flow as suggested by the northward spread of equatorial influence in the nutrient fields. When compared with the large eddy fluctuations across 14°S, even the transports in the Coral Sea boundary currents are not significant.

Eastern Equatorial Water

The Eastern Equatorial Water (EEW) which is responsible for the deeper vertical salinity maxima along 10°N resides in layer 9, the lightest class of what we have broadly called intermediate water. Layer 9 is bounded by $26.7 < \sigma_\Theta < 26.9$ kgm^{-3}, which roughly corresponds to $10°C > \Theta > 8.4°C$. In contrast to the colder intermediate layers where salinity is much fresher in the south than north, the salinity in the EEW is similar along both 10°N and 14°S (Figure 5.17). Patches of low salinity intermediate water are also present in the EEW layer at various locations: very low NPIW along the coast of the Philippines; the upper part of the AAIW core near 180°W along 14°S; and the shallow South Pacific salinity minimum near 110°W along 14°S. There is little meridional flow associated with these minima, though it may be masked by the eddies. In the Coral Sea, though, there is northward transport of relatively high salinity water in this density class.

How is the EEW salinity maximum maintained against erosion by lateral mixing with the fresher waters to the north, south and from below? The flow of EEW along 165°E suggests a possible mechanism. South of the equator, the SSSCC carries salty water from the Coral Sea eastward. North of the equator, lower salinity EEW flows westward as part of the NEC. Between them, the westward EIC and the eastward NSSCC feature strong lateral salinity gradients and zonally advect mixtures of the salty southern and fresher northern waters. The northward diffusion of salt across the salinity fronts in the EIC and NSSCC can therefore occur over the breadth of the Pacific basin. It is this diffusive flux that could maintain the EEW salinity maximum north of the equator, with zonal advection acting to efficiently transport the diffused salt westward. Thus even though EEW occupies the shadow zone of the subtropical gyres (Talley, 1985; de Szoeke, 1987), it is not stagant and its properties are likely strongly affected by its recirculation in the series of intermediate currents near the equator.

Finally, as found in Chapter 2 there is no clear northward flow of AAIW along the coast of Mindanao. Though such a flow is suggested by the tracer fields, its signature appears to be lost amongst the eddies.

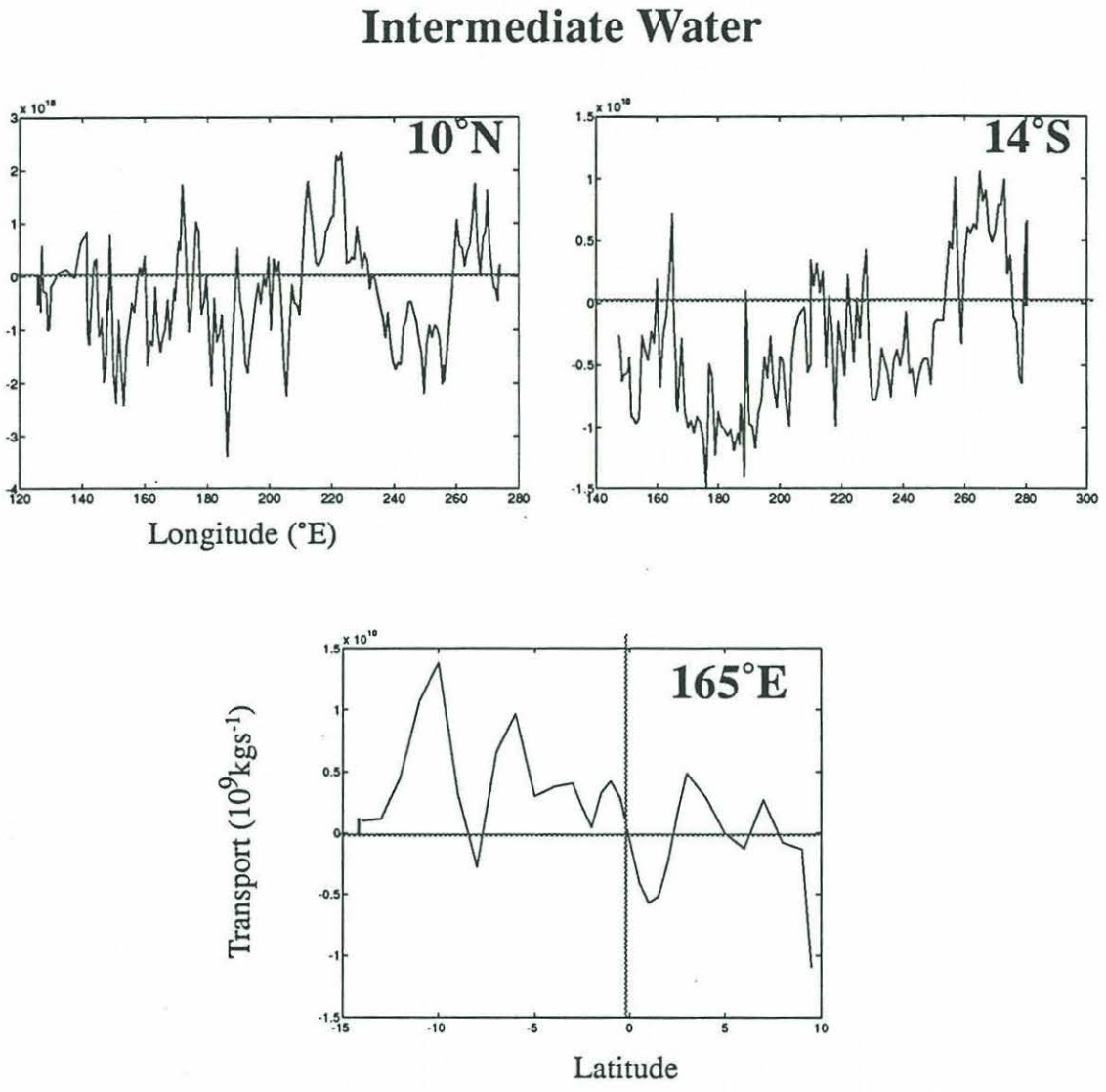

Figure 5.16 Cumulative mass transport in the intermediate water layers ($11.3 < \Theta < 2.2$°C) in the model circulation B1: (a) 10°N; (b) 14°S and (c) 165°E. The summation begins at the eastern boundary for the zonal sections and in the south for the meridional section. Positive values are for northward and eastward flow.

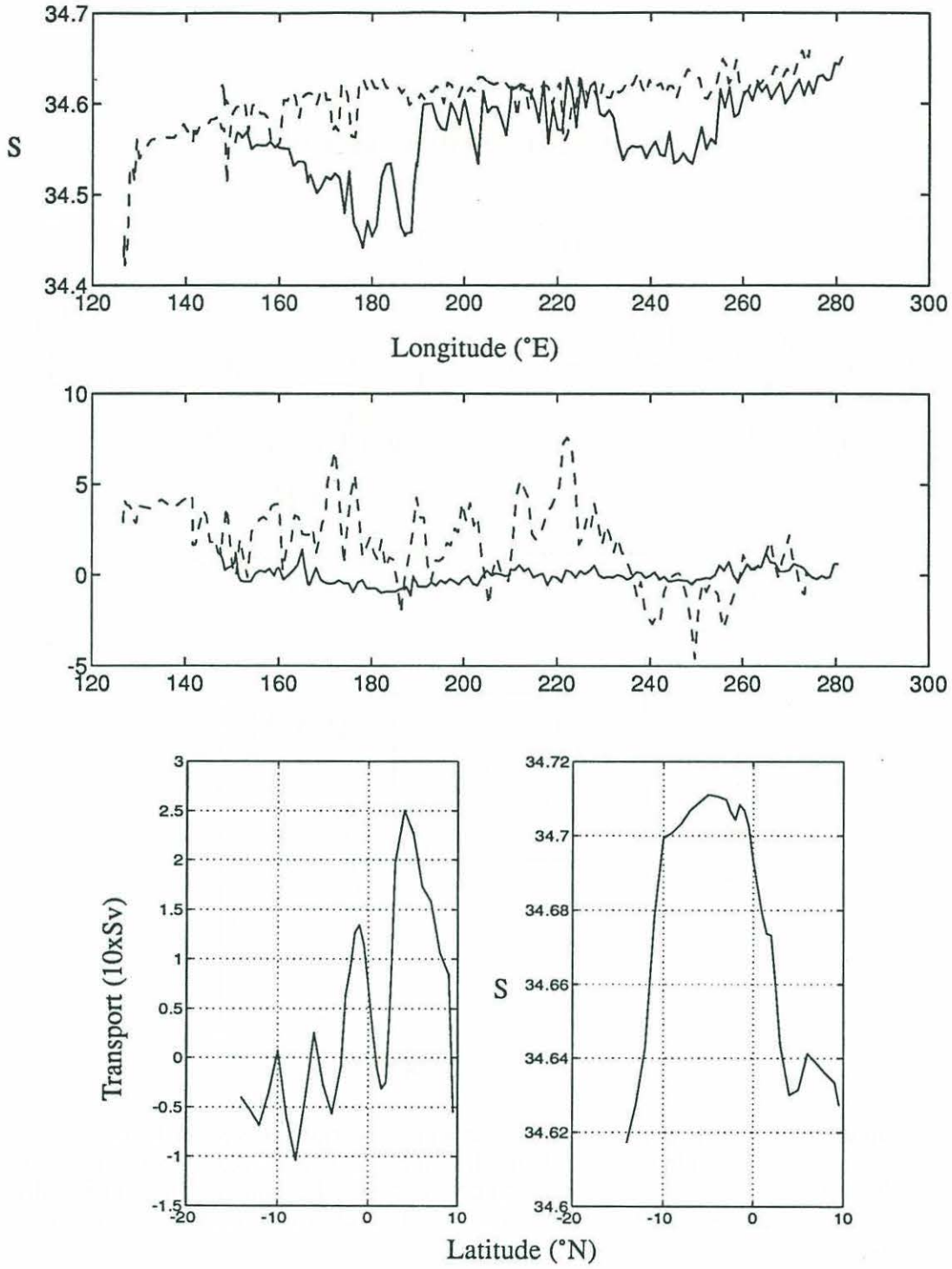

Figure 5.17 (a)Salinity (top) and cumulative transport from the east (bottom) in the EEW along the zonal sections. 10°N is dashed. (b) EEW along 165°E: layer average salinity on the (left) and accumulated transport from the south (right).

5.8 Thermocline Circulation

Contrary to the situation at the intermediate depths, the thermocline mean flows are quite energetic and are discernible in the data despite the eddy field. The data are used to construct a consistent circulation scheme for the thermocline and surface waters. This allows us to deduce how the EUC is supplied. There is an interesting asymmetry in the pathways to the EUC from the two hemispheres, and is it shown that the flow in the upper EUC is part of a strong zonal recirculation of upper thermocline water. In addition, the data reveal that the sites of greatest cross-equatorial flow are near the eastern and western boundaries of the basin, where the strong zonal flows originate and terminate, and in the wind-driven surface layer.

An additional set of data are used to further divide the eastern Pacific into two volumes: a central and far eastern box. Repeat hydrographic surveys made during the Hawaii to Tahiti Shuttle Experiment (Wyrtki and Kilonsky, 1982) were used to construct a mean section with an average longitude of 155°W between 10°N and 12°S. The averaging method and reference levels choices are described in Appendix A. The stations used to construct the mean section at 155°W only penetrate to 1000m and so do not allow the mass budget to be fully closed. Yet if we assume that the cross-isopycnal velocities at the base of the thermocline are small compared to the zonal transports, then the major flow pathways can still be studied.

Recall that we define 'thermocline water' to have $\sigma_\Theta < 26.7$, which is roughly the upper 400m of the water column over the study area. To better delineate the flow pathways, the thermocline water is divided into 4 layers: a surface layer which contains the Ekman flow across most of the Equatorial region; the upper part of the EUC in the central Pacific; the lower part of the EUC; and the 13°C Thermostad waters. At 155°W, the maximum velocity in the EUC core lies at $\sigma_\Theta = 24.5$ (Figure 5.18), defining the boundary between the upper and lower EUC (Table 5.13).

5.8.1 Circulation diagrams

The easiest way to visualize the thermocline flow is to construct circulation diagrams for each density interval. The flow across each side is found as the sum of the Ekman and geostrophic flux in a particular density interval. Along the 14°S section, partitioning the Ekman flux by density is particularly important as the mixed layer density has a large range

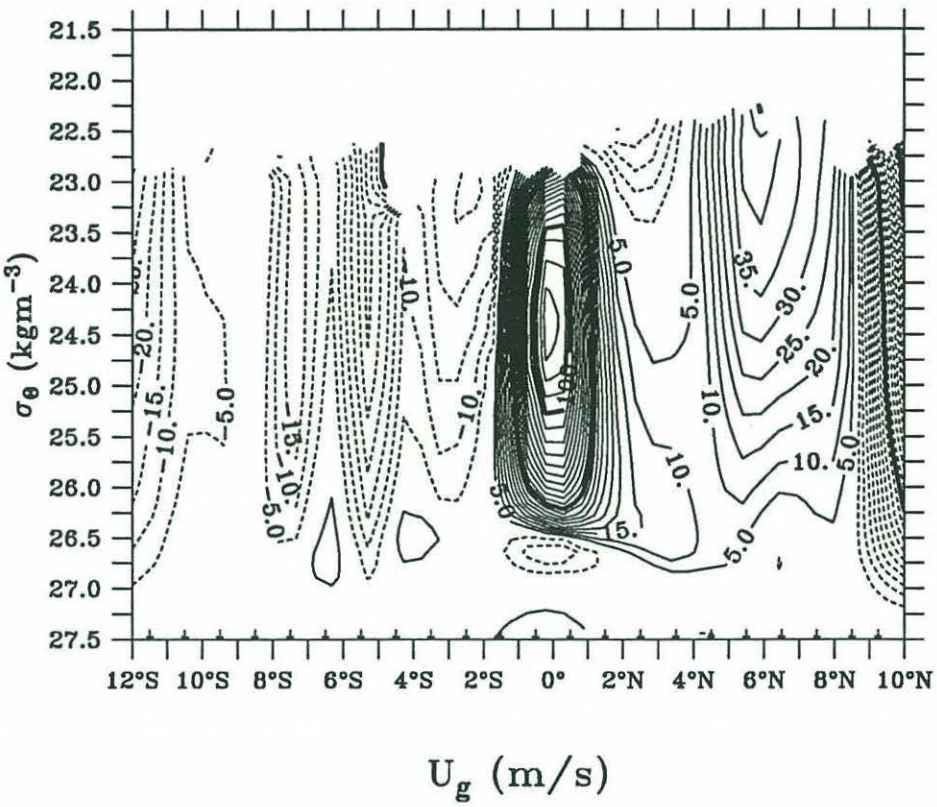

Figure 5.18 Geostrophic velocity in the central Pacific based upon a mean section from the Hawaii-Tahiti Shuttle data.

Layer	Definition	Temperature Equiv.
Surface	$\sigma_\Theta < 23.0$	$\Theta > 25.6°C$
Upper EUC	$23.0 < \sigma_\Theta < 24.5$	$25.6 > \Theta > 21.7°C$
Lower EUC	$24.5 < \sigma_\Theta < 26.2$	$21.7 > \Theta > 13.1°C$
Thermostad	$26.2 < \sigma_\Theta < 26.7$	$13.1 > \Theta > 10.0°C$

Table 5.13 Density classes used to divide up the thermocline flow. The equivalent temperature bounds are the average density interface temperature for the eastern volume. The layer descriptions loosely refer to the EUC at 155°W, where the maximum core velocity in the EUC is at 25.0 σ_Θ

($22.0 < \sigma_\Theta < 25.3$) and much of the upper thermocline outcrops along the section.

The flow across the north-south sections is further divided into 3 parts: that north of 2°N containing the NECC and southern edge of NEC; between 2°N and 2°S containing the EUC; and south of 2°S containing the SEC and SECC. The meridional flux across 2° is deduced by making an important assumption: that all the cross-isopycnal flow in the equatorial volume occurs within 2° of the equator, and that the flow is conserved in density layers elsewhere. Lastly, to prevent the diagrams from being too complex, no attempt was made to separately estimate the transports of *all* of the equatorial currents, and so the simple spacial integrations made between the ends of the sections and 2° often contain contributions from multiple currents. For instance at 155°W, the SEC that extends across the equator in the upper part of the surface layer has not been separated from the transport of the EUC between ± 2°, nor from the transport of the NECC north of 2°N. Similarly the flow south of 2°S is the sum of both the SEC and the SSSCC.

Below each circulation schematic, the distribution of meridional transport across the two zonal sections is shown, accumulated from the eastern boundary for each density interval. These plots demonstrate the broad nature of the flow in the interior and the jet-like structure in the boundary currents. They also allow one to judge the size of the flows in the schematic against the ambient eddy noise in the observations.

Total Thermocline flow ($\sigma_\Theta < 26.7$)

The net circulation in and above the thermocline reflects the combined effects of the Ekman and geostrophic components of the flow. The Ekman component dominates the *meridional* flow in the interior of the basin, while the geostrophic component dominates the western

boundary and zonal currents. Since the meridional geostrophic and Ekman fluxes oppose each other, the vertically integrated stream function may say little about the actual trajectories of water parcels in the meridional plane. However, it is useful to examine the vertically integrated thermocline flow, since it allows a direct comparison with the Sverdrup circulation predicted by the mean annual winds. Much in the observations can be accounted for by this simple theory as first found by Sverdrup (1947) in a study of this very same current system.

North of the equator, interior poleward flow across 10°N is balanced by southward flow in the Mindanao Current, resulting in only a small transport of warm water to the north (Figure 5.19a). The stream-function discontinuity at 141.5°E is due to the westward transport of the NEC flowing between 8°N and 9.5°N, where the MW893 section was joined to the mean western boundary section. Comparison with Figure 5.20 demonstrates that the Mindanao Current is the western limb of an anticlockwise Sverdrup cell that circulates 28 Sv meridionally across 8°N. The NECC makes up the southern limb of this horizontal cell, transporting about 20 Sv across 165°E and 155°W. The NEC is the northern limb transporting roughly 10 Sv westward south of 10°N, and supplying the Mindanao Current with westward flow north of 10°N. Though different wind climatologies vary on the exact strength of the cell, its location and size agree well with the direct observations.

The Sverdrup calculations also predict a clockwise cell centered at 140°W on the equator. This cell donates water to the NECC in the west and detrains water from it in the east. Also seen in the direct observations the clockwise equatorial cell explains why the NECC transport does not diminish downstream: northward detrainment to the NEC is compensated by entrainment from south.

Figure 5.19 (next page) Circulation diagrams for the thermocline flow in various density layers. Layer definitions are given rigorously in Table 5.13. Upper panel shows the integrated flow across the sections, with arrows schematically indicating the deduced flow pathways. Density surface outcrop lines are the heavy bold curves, with the potential density marked nearby. The boxed numbers show the net *convergence* (excess) of mass for each layer in each volume, which is assumed to be balanced by cross-isopycnal divergence equatorward of 2°. The large shaded arrows on the equator show the directly measured EUC transport, and the net flow across 10°N and 14°S are indicated with the large bold numbers. The lower panels show the transport stream function (zero at the eastern boundary), for the net Ekman plus geostrophic flow across the zonal sections. All fluxes are in $10^9 kgs^{-1}$. *(a)* Net thermocline flow; *(b)* Surface layer; *(c)* Upper EUC; *(d)* Lower EUC; and *(f)* Thermostad. See text for details on how the flows are deduced.

Figure 5.19a

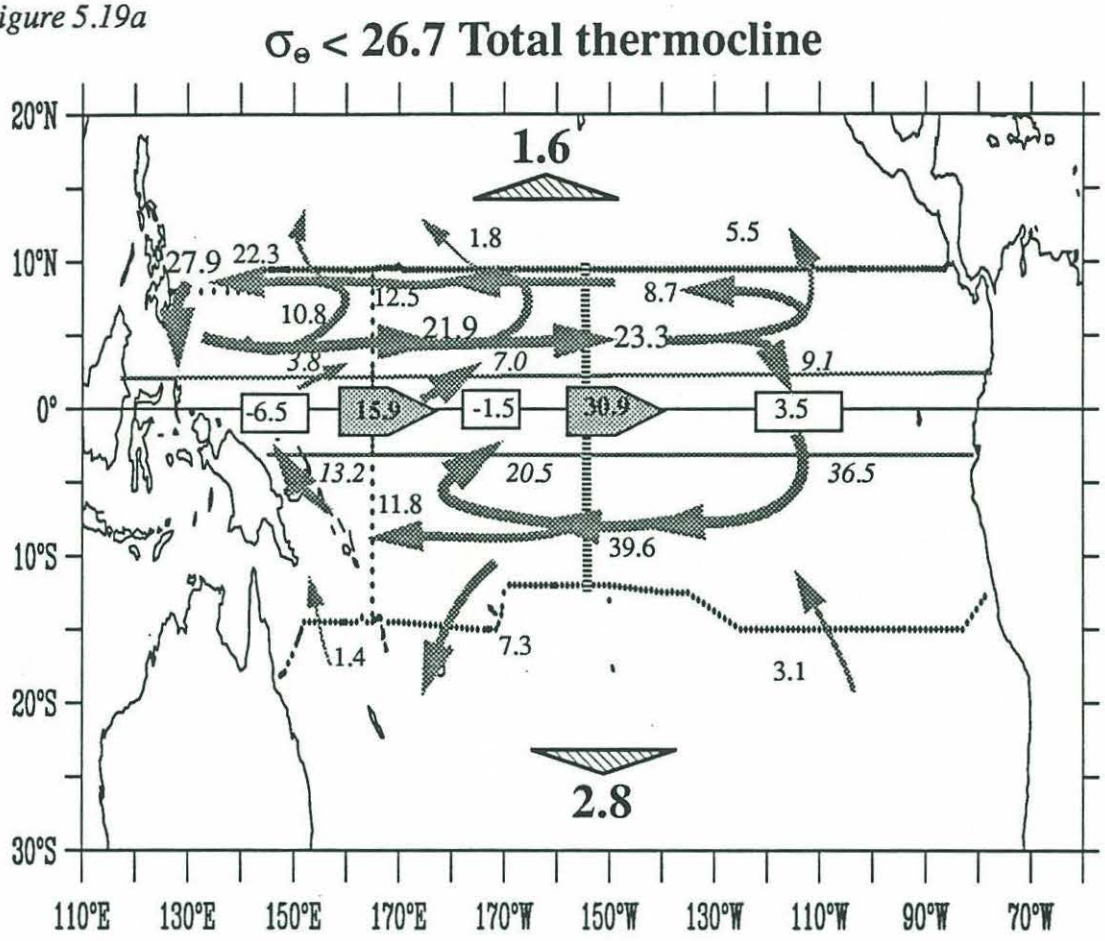
σθ < 26.7 Total thermocline
1.6
2.8
27.9
22.3
1.8
5.5
8.7
10.8
12.5
21.9
23.3
3.8
7.0
9.1
-6.5
15.9
-1.5
30.9
3.5
13.2
20.5
36.5
11.8
39.6
1.4
7.3
3.1
20°N
10°N
0°
10°S
20°S
30°S
110°E
130°E
150°E
170°E
170°W
150°W
130°W
110°W
90°W
70°W

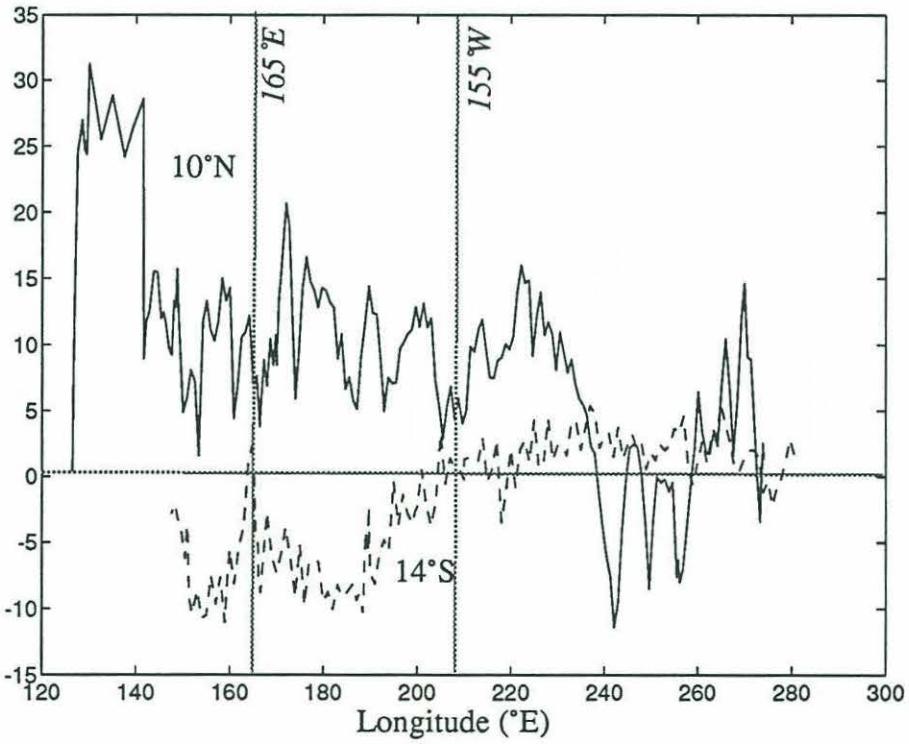
165°E
155°W
10°N
14°S
Longitude (°E)

Figure 5.19b

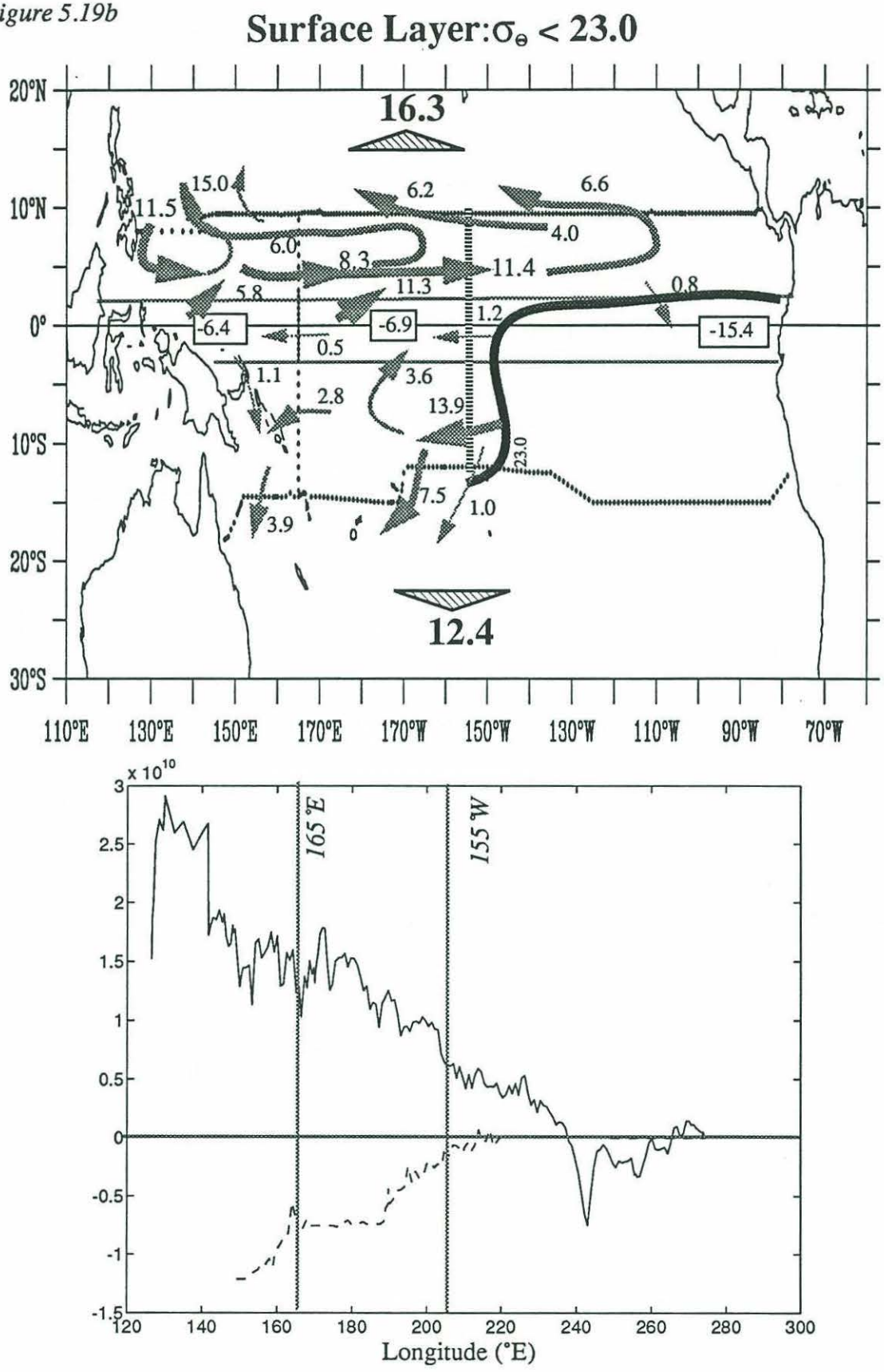
Surface Layer:σ_θ < 23.0
16.3
12.4
15.0
11.5
6.2
6.6
4.0
6.0
8.3
11.4
5.8
11.3
0.8
1.2
-6.4
-6.9
-15.4
0.5
1.1
3.6
2.8
13.9
23.0
7.5
1.0
3.9
20°N
10°N
0°
10°S
20°S
30°S
110°E
130°E
150°E
170°E
170°W
150°W
130°W
110°W
90°W
70°W
x 10^10
165°E
155°W
Longitude (°E)

Figure 5.19c **Upper EUC:23.0 < σ_Θ < 24.5**

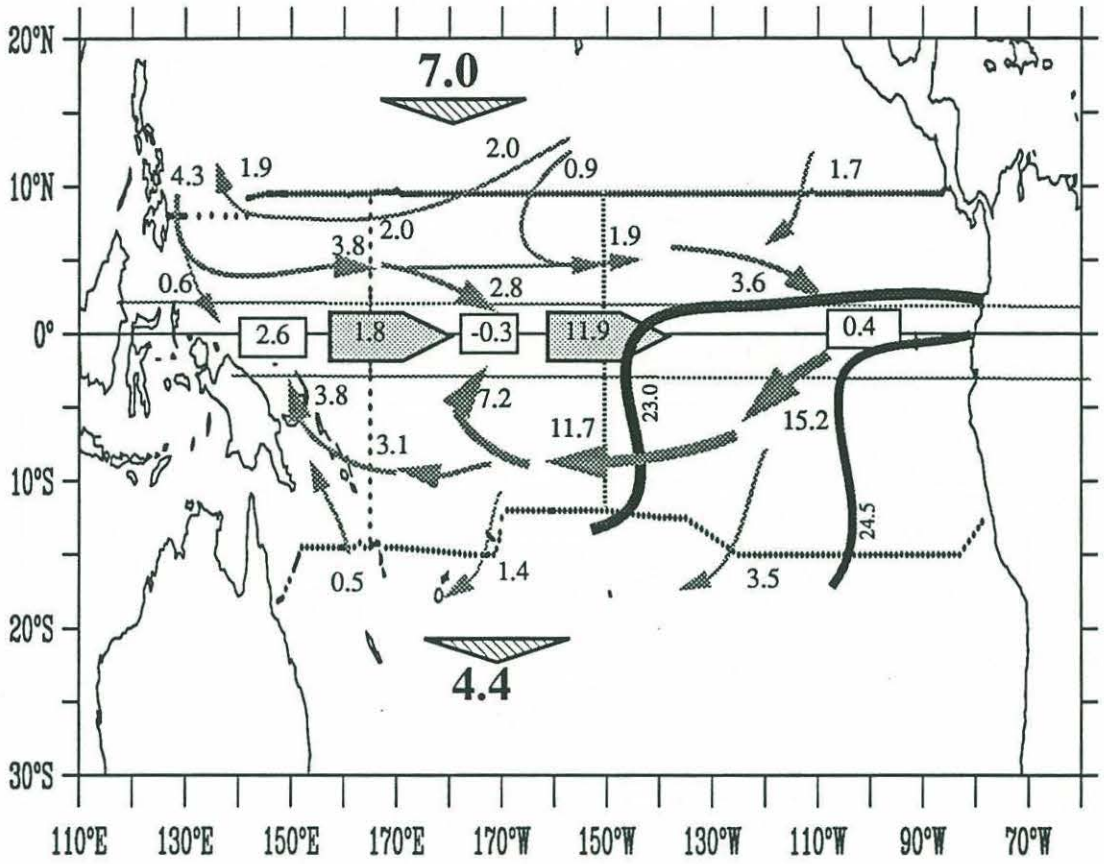

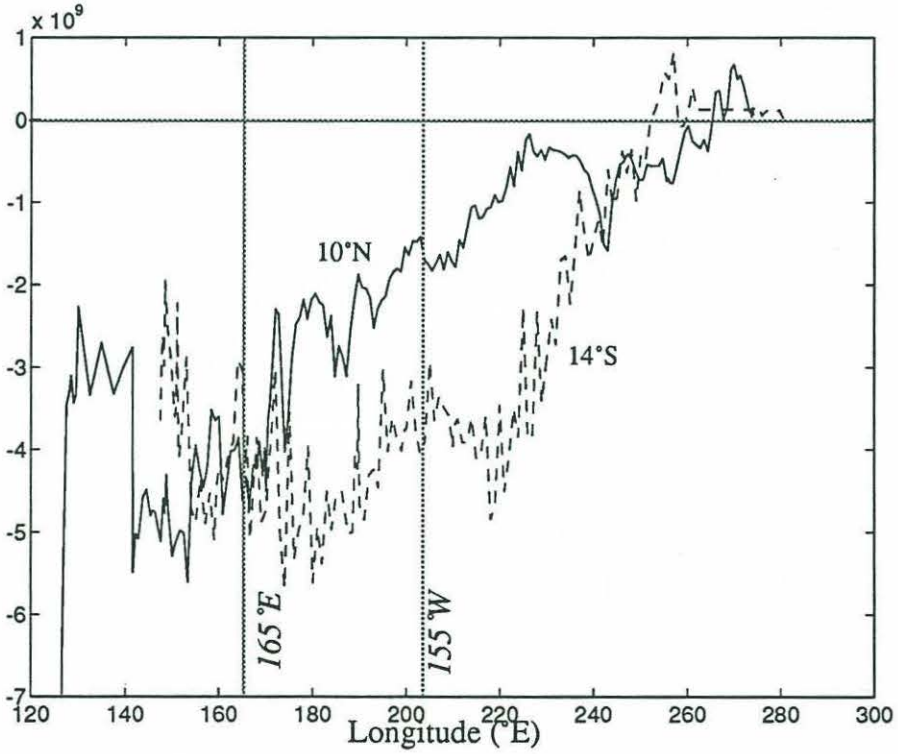

Figure 5.19d

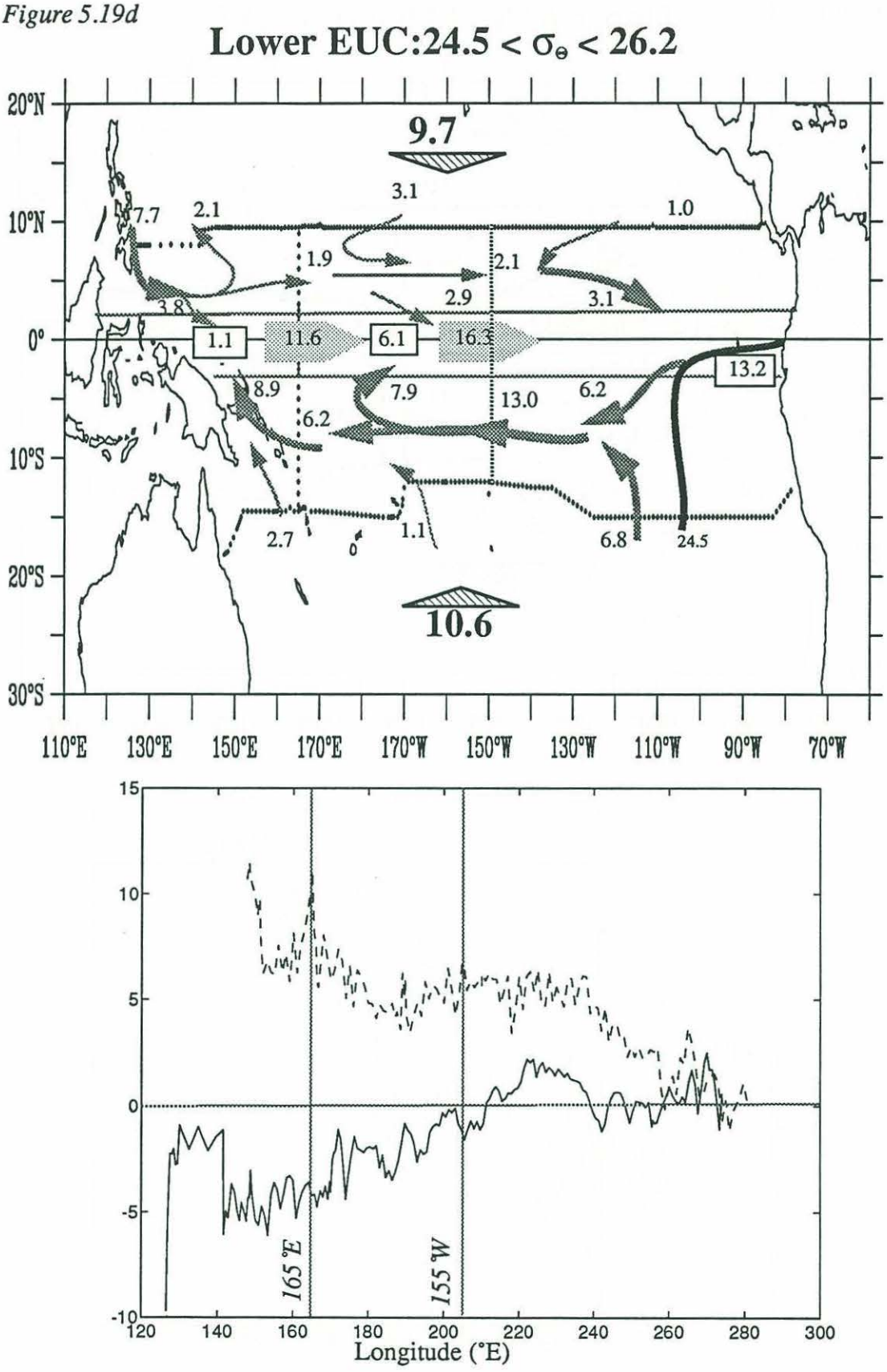
Lower EUC:24.5 < σθ < 26.2
9.7
3.1
7.7
2.1
1.0
1.9
2.1
2.9
3.1
3.8
1.1
11.6
6.1
16.3
13.2
8.9
7.9
13.0
6.2
6.2
2.7
1.1
6.8
24.5
10.6
20°N
10°N
0°
10°S
20°S
30°S
110°E
130°E
150°E
170°E
170°W
150°W
130°W
110°W
90°W
70°W
15
10
5
0
-5
-10
120
140
160
180
200
220
240
260
280
300
165°E
155°W
Longitude (°E)

Figure 5.19e

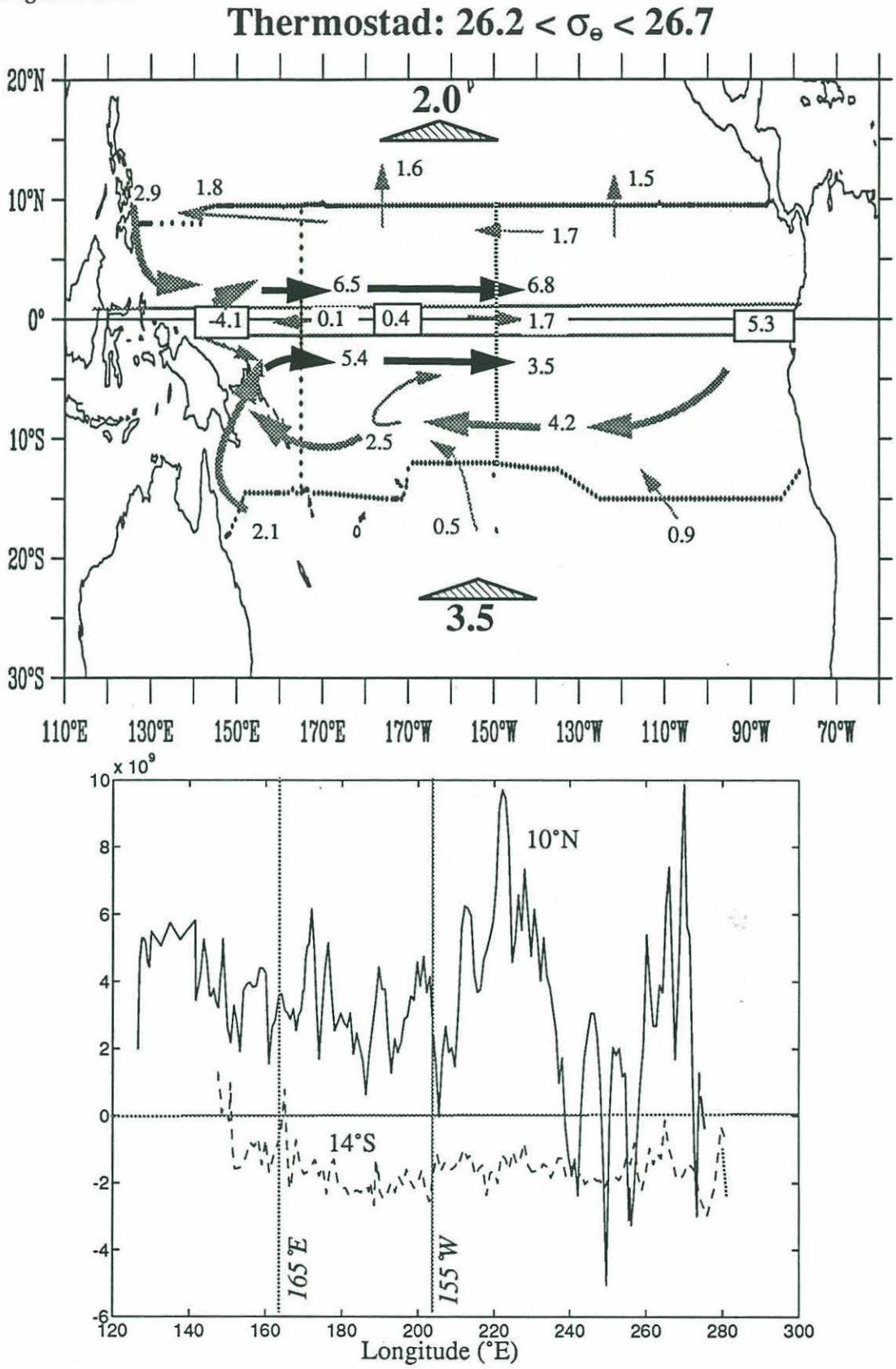
Thermostad: 26.2 < σθ < 26.7
20°N
10°N
0°
10°S
20°S
30°S
110°E
130°E
150°E
170°E
170°W
150°W
130°W
110°W
90°W
70°W
2.0
3.5
1.6
1.5
2.9
1.8
1.7
6.5
6.8
-4.1
0.1
0.4
1.7
5.3
5.4
3.5
4.2
2.5
2.1
0
0.5
0.9
x 10^9
10°N
14°S
165°E
155°W
Longitude (°E)

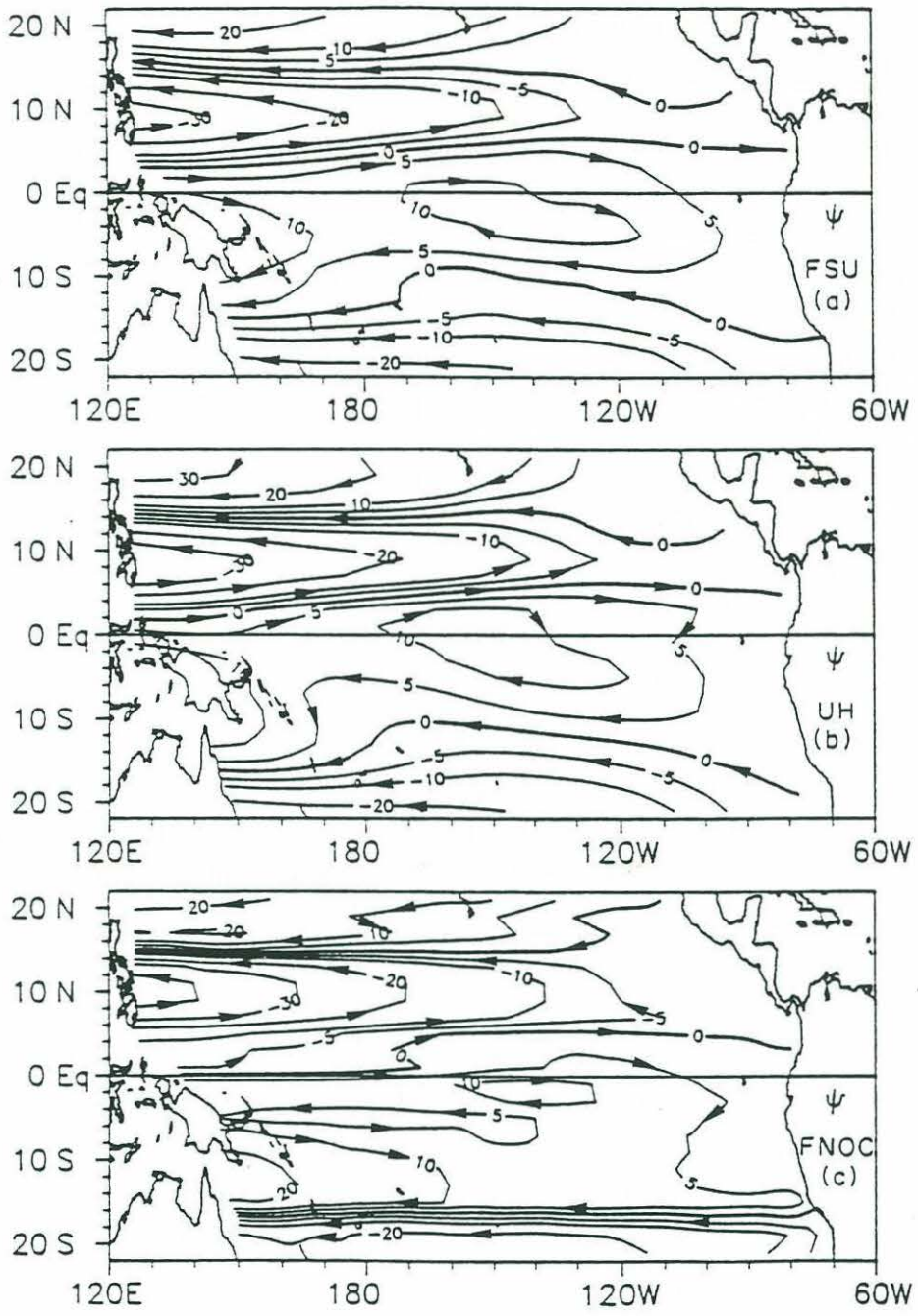

Figure 5.20 Sverdrup transport stream function ($x10^6 m^3 s^{-1}$) for three wind climatologies: (a) FSU, (b) University of Hawaii and (c) Fleet Numerical Ocean Centre. The contour interval is 10Sv, with ± 5Sv included. Taken from Landsteiner *et al.* (1990).

The size and direction of the thermocline flow across 14°S is also well accounted for in the Sverdrup calculations: weak northward flow in the east and southward flow in the central basin. The net flow of thermocline water across 14°S, is also small at only 2.8Sv to the south.

The southern hemisphere counterpart to the 30 Sv NECC/NEC Sverdrup cell is weaker (~15 Sv), consonant with the smaller boundary flow in the Coral Sea. A Throughflow would only modify the Sverdrup models by requiring an even larger poleward boundary current in the Coral Sea.

The transport of the SEC across 165°E in both the Sverdrup models and observations is around 10 Sv. In contrast, the SEC transports 40 Sv across 155°W, compared to only about 15Sv in the Sverdrup models. The large observed SEC must be fed by waters from the termination of the EUC. Much of the SEC transport returns to the EUC in the central and western basin. Though the Sverdrup calculations do show a clockwise recirculation of water associated with the cyclonic cell centered at 0°, 140°W its predicted strength is much weaker in the south than observed.

The transports of the major zonal currents estimated here agree well with those found by Kessler and Taft (1987) across a composite XBT track near 170°W. For the period between 1979-1981, in which no El Niño events occurred, they found a mean transport for the NECC of 21.1 ± 5.7 Sv (rms) relative to 450m. Between 2°S and 20°S, Kessler and Taft report an SEC transport of 35.1 Sv, which, though not directly comparable to the present observations, confirming the large transport of the SEC in the eastern Pacific.

In summary, the depth integrated thermocline flow in the Equatorial Pacific is largely explained by the Sverdrup relation. The obvious exception is the for the flow between ± 2° where Sverdrup dynamics fails to predict the EUC. The single off-equatorial element of the flow not accounted for by the wind-field, besides the western boundary currents, is the large westward transport across 155°W, which appears to be related to the recirculation of waters in the EUC. A more detailed comparison of the predicted and observed thermocline structure was made by Landsteiner, *et al.* (1990). They concluded that such comparisons are limited by the wind observations, which show more disagreement among themselves than with the oceanic observations.

The small net imbalance of water above $\sigma_\Theta < 26.7$ is indicative of the symmetry mentioned previously, where the net meridional Ekman and thermocline geostrophic flows across each zonal section are in approximate balance. Furthermore, the net divergence of thermocline water (boxed numbers in Figure 5.19a) in the 3 enclosed volumes is small except in the western box, where a substantial deficit exists. This imbalance is of the wrong sign to supply a large Throughflow, and, in the present circulation, the shortfall is supplied by upwelling intermediate water into the western thermocline. This point will be explored more thoroughly when the heat budget is discussed. For the purposes of the current discussion, it suffices to assume that the Throughflow is small.

Surface mass budget ($\sigma_\Theta < 23.0$)

The surface layer for which $\sigma_\Theta < 23.0$ encompasses the mixed layer on all the sections but 14°S, where this density surface outcrops east of 120°W, and in isolated places in the Coral Sea. The transport in this layer is strongly influenced by both the Ekman drift, which advects water poleward, and the geostrophic balance which moves water zonally and equatorward. A total of 28.7 Sv of $\sigma_\Theta < 23.0$ water is advected poleward from the equatorial volume, with the largest amount produced by upwelling in the eastern box where the EUC terminates.

Across 10°N a net of 16.3 Sv of surface water flows northward in a broad interior flow driven by the wind. This water is delivered northward by detrainment from the NECC, which in turn gains fluid from the south in the central and western Pacific. The southward flux of 12.4Sv across 14°S is supplied directly from the eastern Pacific upwelling zone east of the outcrop line. Significant divergences exist in the western and central boxes, indicating upwelling is required to balance mass in these boxes also.

Little of the water upwelled in the east flows directly to the northern hemisphere. Instead it flows westward in the SEC and across the equator in the central basin. This flow pattern is consonant with the position of a strong water mass and density front along 2°N between 130°W and the South American coast (Robinson, 1976). The front is probably maintained against mixing by zonal flow between the NECC and the part of the SEC north of the equator. A large transport across the front would have to be accompanied by huge localized surface fluxes, which are unlikely and not observed. South of the equator, the surface lateral density gradients are weaker, and are consonant with a broad westward flow that is being

gradually warmed by the sun.

The Upper EUC ($23.0 < \sigma_\theta < 24.5$)

Two water masses occupy this density interval, one from each hemisphere: NPCW from the North Pacific subtropical gyre and the upper part of the SPTW core that dominates the South Pacific thermocline. At this level we begin to see the equatorward flow that feeds the EUC and eventually upwells into the surface layer. A strong asymmetry exists in the meridional flow: across 10°N, a net of 7.0Sv flows equatorward, while 4.4Sv flows *poleward* across 14°S. This is because at 10°N this density interval is fully shielded from the wind, while along 14°S it is not, and so undergoes Ekman drift.

The North Pacific subtropical gyre delivers water to the equatorial volume in two ways: as a broad interior flux across 10°N and via the Mindanao Current. In the western box, nearly all of the flow in this density interval in the Mindanao Current is needed to supply the NECC, and little is left over to supply the EUC or a Throughflow. Following Tsuchiya, *et al.* (1989), we use the dramatic salinity difference between the northern and southern waters to partition the outflows by their hemispheric sources. For a given station pair and in each layer, the ratios of northern and southern water, R_N and R_S, are given by:

$$R_N = \frac{S - S_S}{S_N - S_S} \qquad R_S = \frac{S - S_N}{S_S - S_N} \tag{23}$$

where S is the salinity of the layer at a given station pair, S_S and S_N are the salinities in a layer of the southern and northern source waters respectively. The inflow of southern water is broad and so S_S is chosen as the average salinity around the western box south of 3°S. The northern inflow is largely in the Mindanao Current and S_N is set as the transport weighted average salinity along 8°N between the coast and 130°E. The product of these ratios and the transport gives the flux of each water type between station pair. Based on salinity, then, a separate transport stream function for the northern and southern water type is found (Figure 5.21).

Pure northern water flows into the western box in the Mindanao Current, nearly all of which flows out in the NECC. Of the inflow of southern water in the SEC, only a small amount leaves via the EUC. Hence the net convergence of mass in the box is of SEC water, not Min-

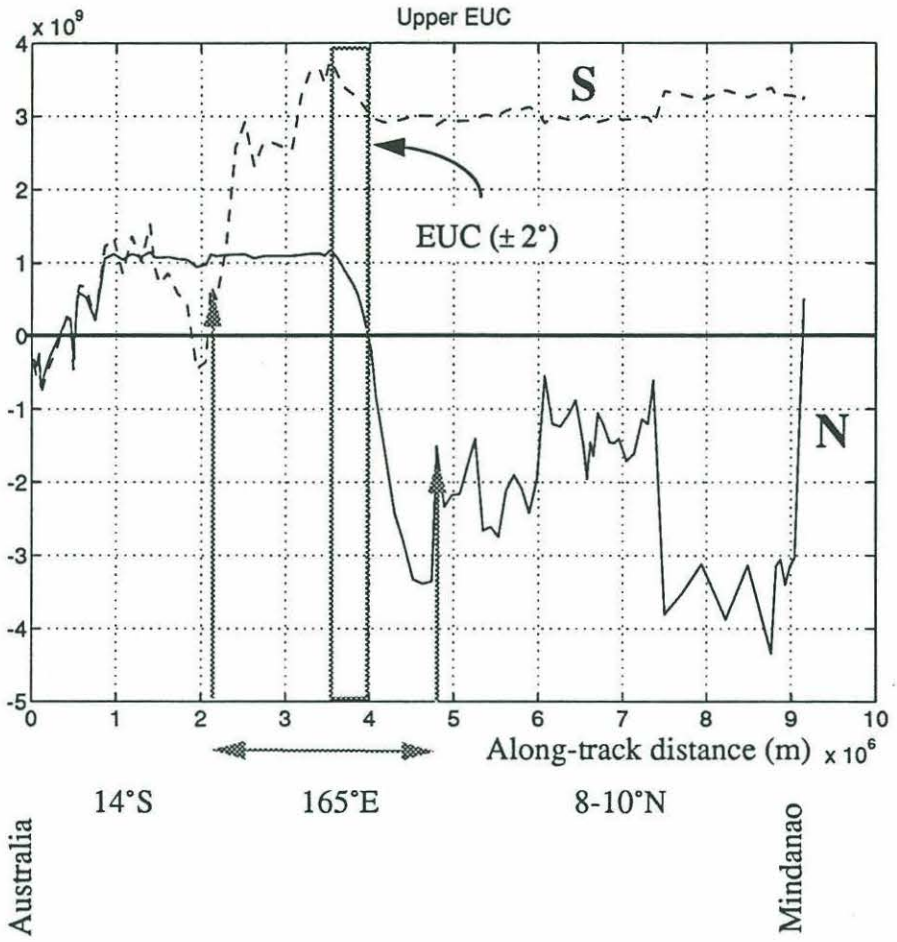

Figure 5.21 Mass transport of northern and southern waters into the western box accumulated from the coast of Australia in a counterclockwise integration for the density interval $23.0 < \sigma_\Theta < 24.5$. The box corners are shown by the upright grey arrows, and the region spanning the EUC is boxed.

danao Current water. This is an important distinction, and since the leakage through the Indonesian Passages is believed to be dominantly made up of Mindanao Current water. There is an indication of the transport of 'northern waters' in the Coral Sea, which is of course an artifact of the salinity partitioning. The $\sigma_\Theta = 23.0$ density interval outcrops in the Coral Sea, and so is probably freshened by surface rainfall and runoff and should be ignored for the present purposes.

Returning to the equator, the transport of the water of this density range in EUC across 165°E is small (Figure 5.19c). The salinity analysis indicates a slight dominance of northern over southern content (1.1 versus 0.7Sv), though the values are far too small to trust given the kind of eddy noise seen in the transport stream function (Figure 5.21).

Between 165°E to 155°W the transport of the EUC increases five fold in this layer. This transport increase is fed by meridional convergence in the central Pacific, predominantly from the SEC, which in turn is fed at the termination of the undercurrent in the eastern box.

This pattern suggests that half of the transport of the upper EUC at 155°W, is in fact water that is simply recirculating between the SEC and EUC, and that little cross-isopycnal flow is needed to close the circulation. An examination of the salinity field shows that this is impossible, and that the water must first be exposed to the surface. The SEC carries SPTW across 155°W which is the saltiest water found in the entire equatorial region. The high salinities cannot be explained by the subsurface isopycnal recirculation of the fresher water in the EUC. The high salinity SPTW in the SEC can only originate by distillation of fresher waters and their subduction below the surface layer.

Since there is only outflow to the south across 14°S in this layer, the source of the salty water must be *within* the eastern box. This density interval outcrops over a good portion of the area south of the equator in the eastern box, and maps of the freshwater flux at the surface show that the outcrop area lies under a region of high evaporation (Baumgartner and Reichel, 1975). It is plausible that lighter SPTW is formed by the evaporation and heating of denser water that has upwelled either along the equator or the off the coast of Peru, and is then subducted in the southern extent of the Cold Tongue. Some of the water formed in the eastern box at this density flows directly southward across 14°S in the Ekman layer, and may be subducted as even denser and saltier SPTW, as suggested by the outcropping of the salinity maximum along the TEW section.

The Lower EUC ($24.5 < \sigma_\Theta < 26.2$)

South of the equator, denser and saltier SPTW occupies the layer referred to here as the Lower EUC. At these densities the northern hemisphere thermocline donates the freshest thermocline waters found in the equatorial region: the shallow salinity minimum of the CCW. In comparison to the previous shallow density intervals, the lower EUC layer has the smallest outcrop window, though it includes the coastal area off Peru where large surface heat fluxes into the ocean indicate strong upwelling (Weare, *et al.*, 1981).

The northern and southern subtropical gyres donate approximately equal amounts of water to the equatorial system at these densities (Figure 5.19d). At 10°N, the bulk of the inflow is in the Mindanao Current, while the SEC delivers the southern contribution to the EUC both in the interior and along the western boundary. Note that there is also a contribution to the EUC from the south via the Coral Sea. Thus, the two types of southern hemisphere saline thermocline water in the western Pacific noted by Tsuchiya *et al.* (1989) and Tomczak and Hao (1989) can be accounted for by the deduced flow. Fresher WSPCW flows northward via the Coral Sea, while saltier and lower oxygen PEW, a mixture of SPTW and recirculated equatorial water, flows westward in the SEC close the equator.

In the west, most of the Mindanao Current transport flows directly into the EUC instead of the NECC, in contrast to the layer above. Twice as much water again, enters the EUC from the southern hemisphere. The $24.5 < \sigma_\Theta < 26.2$ layer contains the core of the EUC at 165°E, which according to the mass budget contains a ratio of 1:2 of northern to southern source waters. The salt distribution bears this out (Figure 5.22), predicting a similar partition of northern to southern waters, 4.3:7.2 Sv. Note again that there is little excess northern water left in the western box, and that the net convergence, though small, is predicted to be southern water.

Between 165°E and 155°W, the EUC in this density interval only gains another 5 Sv from the meridional convergence in the central Pacific (Figure 5.19d). Most of EUC transport in this layer is gained from the western boundary currents. Despite the large divergence caused by the EUC in the central box there is still an overall net convergence of mass. As a residual of the horizontal field, the net convergence is the most error prone part of the circulation, and its value is particularly sensitive to how the reference levels are chosen at 155°W (Appendix B). Most reasonable choices, however, imply convergence in the central

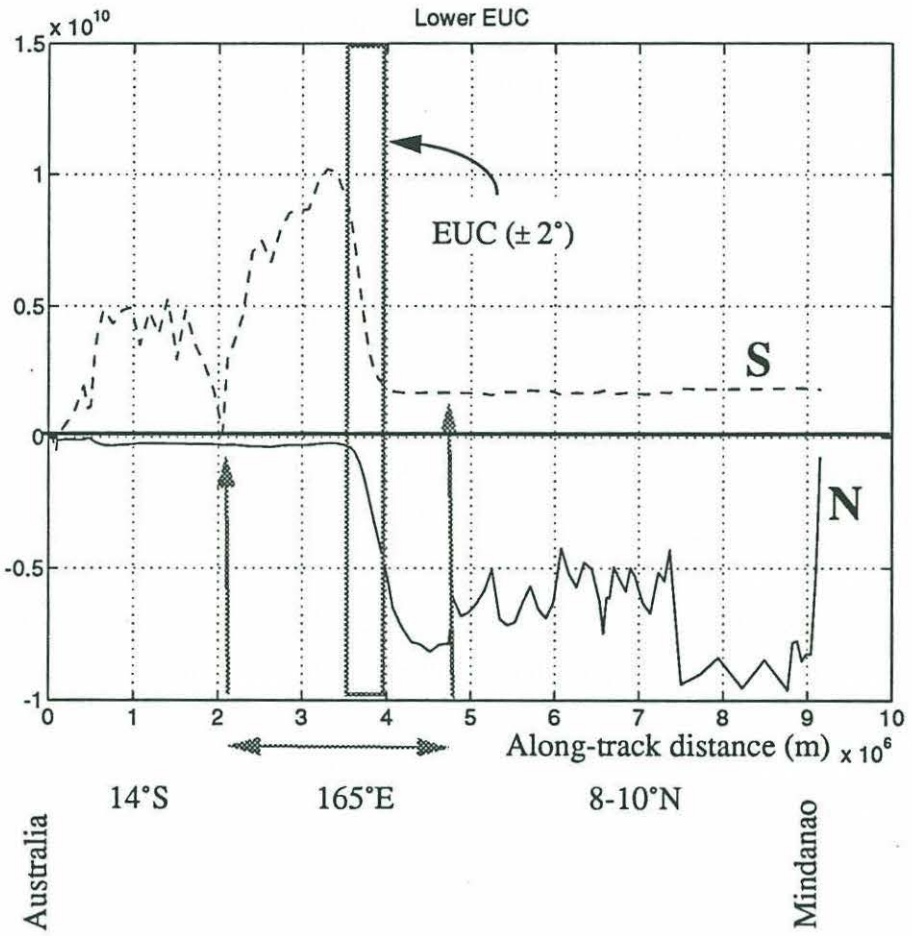

Figure 5.22 Same as Figure 5.21, except for the Lower EUC layer.

box in this layer. The convergence is needed to compensate for a divergence in the surface layer, and implies upwelling through the thermocline. That some upwelling occurs is in agreement with estimates of the heat flux in the central Pacific, to be discussed later.

As found in the shallower layers, there is a recirculation of water between the EUC and the SEC. About half of the SEC transport across 155°W is upwelled or recycled water from the EUC. The 13.2Sv of net convergence of water in the eastern box upwells to supply the SEC outflow in the layers above.

13 °C Thermostad: 26.2 < σ_Θ < 26.7

The 13°C thermostad is a layer of weak stratification observed in the lower EUC in the eastern Pacific. Tsuchiya (1981) presented an isopycnal flow path for the water occupying the Thermostad. He asserts that it is formed is the Tasman Sea by winter-time convection and is circulated equatorward in the lower part of the South Pacific subtropical gyre. Upon arriving in the western Pacific, the dense subtropical gyre water is entrained in the lower EUC and SSSCC and advected eastward to form the Thermostad. In the eastern Pacific the Thermostad water becomes depleted in oxygen, and leaves by poleward outflow as low oxygen water in the Peru-Chile Undercurrent along the coast of South America.

Toggweiler and Samuels (1992) agree with Tsuchiya that the source of the Thermostad water is the denser layers of the South Pacific subtropical gyre. However, they identify the colder Subantarctic Mode Water as the Thermostad's origin, instead of the water subducted in the Tasman Sea. Subantarctic Mode Water is formed along the northern edge of the Antarctic Circumpolar Current, and is injected into the South Pacific subtropical gyre by Ekman pumping. The basis of Toggweiler and Samuels' argument is that the observed high ΔC^{14} signature of the Thermostad water which cannot be accounted for by Tsuchiya's source. Subantarctic Mode Water, they argue is formed from Antarctic surface water, which has high ΔC^{14}.

In the present study we are interested in the Thermostad water because of its possible role in supplying water to the equatorial/coastal upwelling system in the eastern Pacific. Toggweiler and Samuels (1992) assert that the high nutrient and low ΔC^{14} levels observed in the surface SEC south of the equator imply that some of the Thermostad waters upwell along the coast of Peru.

The layer we have chosen to represent the Thermostad is defined by $26.2 < \sigma_\Theta < 26.7$. Along both 165°E and 155°W this density interval spans the upper two thirds of the SSCCs and the very upper portion of the EIC. Instead of dividing the zonal flow around the 2° lines of latitude, the SSCC transports are separated out through an *ad hoc* examination of the velocity along each section (Figure 5.19e). The transports related here for the SSCC are a little smaller than those reported by Gouriou and Toole (1993) and Wyrtki and Kilonsky (1984) because these currents extend below the Thermostad layer as defined here.

As the Thermostad lies below the EUC, the SSCC's dominate the zonal flow (Figure 5.19e). In the western box, the SSSCC is supplied from both the Coral Sea and the SEC, and its high salinity confirms this (Figure 5.23). The NSSCC, on the other hand, is too salty to be supplied solely by the fresh inflow of the Mindanao Current. This is born out remarkably well by the size of the transport along the coast of the Philippines, which is only half of the size of the NSSCC, requiring SEC water to make up the rest. There is a net shortfall of salty SEC water in the western box. In the B1 model, this deficit is supplied by upwelling water from below. The upwelled water is much fresher and colder than that flowing out in the SSCC's and so a large vertical diffusivity is needed to close the heat and mass budgets for the layer. This result is further discussed below when the cross-isopycnal terms are examined.

The SSCC's transport about 10 Sv of Thermostad water across the central basin to the eastern Pacific. Some detrainment is implied for the SSSCC though it is difficult to judge if it is real. Being a layer of low shear, the flow in the Thermostad is rather more dependent upon reference level choices than the thermocline flows, and so we have lower confidence in the transport estimates. It is clear that the SSCC's transport a significant amount of salty water to the eastern Pacific. Their high SPTW content explains the relatively high salinity of the Thermostad in the eastern Pacific. At 155°W the NSSCC forms a vertical salinity maxima, while the SSSCC is a horizontal maxima, which must be maintained by zonal advection in the face of vertical and horizontal mixing.

Of the 10 Sv of Thermostad water delivered to the eastern box, half returns to the west in the deep reaches of the SEC, and appears to recirculate in a similar manner to the cells observed in the layer above. The remaining Thermostad water is contributed to the upwelling system, with a only small outflow across 10°N. The data do not reveal a significant southward flux of Thermostad water along the coast of South America in the PCUC as

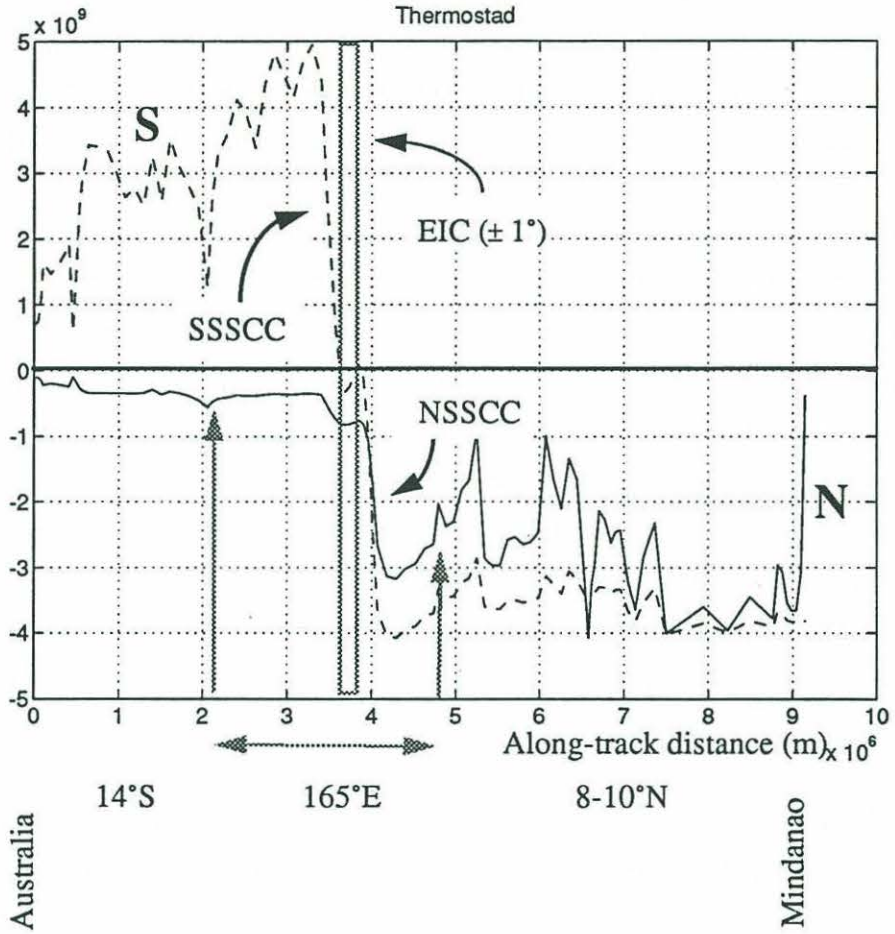

Figure 5.23 As for Figure 5.21 except for the Thermostad layer.

hypothesized by Tsuchiya (1981). Using current meter measurements at 10°S, Huyer *et al.* (1991) estimated a net transport of 1Sv for the PCUC. Such a small transport would be lost in the eddy noise in the data used here. Our study suggests that though the PCUC has a large impact on the water properties along the South American coast south of 10°S, its importance in the net mass budget of the Thermostad appears to be small.

5.8.2 Summary and Discussion of Thermocline Flow

In the thermocline, the addition of the 155°W data reveals the rich structure of the upper equatorial currents. Except at the equator and in the eastern SEC, the net thermocline flow is well accounted for by Sverdrup theory. The SEC in the southeastern equatorial Pacific is stronger than the wind-stress curl would predict, since it is fed by the termination of the EUC at the eastern boundary. The link between the EUC and the anomalously large SEC was first made by Wyrtki (1967) a few years after the EUC was discovered.

The pathways in which subtropical gyre water reaches the EUC largely reflects those seen in idealized numerical models (Liu and Philander, subm; McCreary and Lu, subm.). The densest layers in the EUC are derived from the lower parts of the subtropical gyre which can only reach the equator through the low-latitude western boundary currents. The lighter layers in the EUC flow to the equator in the interior, and contribute to the increase in the EUC transport across the basin. This difference in trajectories is a result of the beta-spiral affect which causes the subtropical gyre to shrink poleward with depth.

The idealized models differ from the ocean in that the model wind and surface conditions are symmetric about the equator. In the ocean, the pathways to the EUC not only change with depth, but also with hemisphere. The observed circulation patterns are complicated by the asymmetry in the wind field: strong wind-stress curl north of the equator drives the Sverdrup gyre containing the NECC. Surface buoyancy fluxes are also symmetric: the North Pacific subtropical gyre contains a lighter density range than its counterpart in the South Pacific, and their contributions to the EUC reflect this, with the southern waters dominating the lower EUC and the northern waters entering at shallower levels.

5.9 Sites of cross-equatorial exchange

Cross-equatorial exchange occurs throughout the water column, though the pathways vary with depth. The densest part of the LCPW flows directly across the equator by way of the

deep western boundary current which appears to simply follow the deep topography northward. Above, where the western boundary shifts westward south of the equator, the pathways are complicated by the strong zonal equatorial currents.

In the NPDW, the lack of western boundary layers removes the cross-equatorial flow pathway most favored by theory. In lieu of this pathway, we deduce that the zonal flows at the equator must be important in the modification of potential vorticity necessary to allow the 10 Sv of NPDW and intermediate water to flow across the equator. The zonal flows may act to cycle streamlines through dissipative zones such that potential vorticity can be modified, either by diffusion at side boundaries or across the equator.

The nature of the deep equatorial currents is controversial. As we lack a comprehensive observational description of these flows, theoretical explanations are difficult to test. The flow pattern is complex and includes both the deep equatorial jets (Ponte, 1988) and the off-equatorial flows first described by Firing (1989).

Kawase, *et al.* (1992) model the flow of a deep western boundary current approaching the equator using a high resolution numerical model. They find that in the long time limit, the boundary current directly crosses the equator, while in the interior steady cross-equatorial flow is not possible. The model only generated strong zonal flows on the equator during the spin-up phase, and these eventually dissipated leaving almost no flow along the equator. As a result, Kawase, *et al.*, (1992) assert that for realistic oceanic parameters (low dissipation in comparison with previous numerical studies) the zonal flows along the equator must be time dependent.

From the data in hand it is difficult to determine exactly how steady the observed deep zonal flows really are. Firing's (1989) observations at 159°W demonstrate that the near equatorial jets persisted over 16 months. They were also identified in independent observations which span 50° of longitude and were made over 12 years. The geostrophic velocity field at 165°E features similar flows. These strong equatorial zonal flows, if not steady, must have very long time and zonal scales. The role played by the deep equatorial currents in allowing fluid to cross the equator, must first wait until the nature and generating mechanism of the currents themselves is known.

In the upper ocean, the strong zonal flows of the EUC and SSCC's preclude water from pen-

etrating very far into the opposite hemisphere. The subsurface thermocline flow is convergent on the equator and is eventually entrained into the equatorial upwelling system. Poleward flow is limited to the surface layer. Near the western and eastern boundaries, direct cross-equatorial flow does occur, and is associated with the origin and termination of the EUC and SSCC's. In the west, the salinity budget clearly demonstrates that the NSSCC and deep EUC contain water from the SEC, though the southern hemisphere water does not extend past about 5°N. In the eastern Pacific, the mass budget reflects the strong asymmetry in the Cold Tongue: nearly all of the water upwelling to the surface flows southwards and then westwards in the SEC. The Ekman drift across 10°N is fed both by cross-equatorial flow and upwelling into in the surface layer in the central and western Pacific. This cross-equatorial surface flow pattern was deduced by Joyce (1988) based on a modified Sverdrup relation for flow on the equator. This demonstrates that the surface cross-equatorial flow is essentially wind-driven, and the potential vorticity constraint does not apply.

In summary, the observed horizontal circulation suggests that three pathways for cross-equatorial flow exist: in western boundary currents; the surface wind-driven layer and in the deep interior, where western boundary layers are absent. The first two pathways can be understood in terms of potential vorticity conservation, since dissipation and forcing can compensate for changes in the planetary vorticity. The third pathway is rather mysterious, since it may depend upon the deep equatorial currents which are presently poorly understood.

5.10 Mixing Rates in the Equatorial Volume

Estimating the mixing rates in the deep ocean has proven difficult, partly due to the controversy over which processes cause cross-isopycnal fluxes (Garrett, 1979). Indirect estimates based on deep budgets suffer from the difficulties in establishing the mean flow field. This is certainly true of the estimates set forth here, though it is still worth examining the deduced mixing rates in the interests of comparing them with past estimates.

In the eastern basin, the diffusivity estimates are well constrained by the model (Figure 5.24). Above 3000m the diffusivities are close to constant at around $0.2cm^2s^{-1}$ with maximum values of $0.3\ cm^2s^{-1}$. Below 3000m the diffusivities increase towards the bottom, a trend that is robust despite the increasing error size (see figure caption). The large bottom diffusivities are associated with the upwelling of 4.4 Sv of the densest bottom water to lighter density classes (Figure 5.25).

The size of the diffusivities in the western box are not as well resolved as those in the east (Figure 5.24). The smaller horizontal layer area in the west means that uncertainties in the continuity constraints have a greater impact on the buoyancy balances. Despite the large errors, the increased diffusivity in the deep water is formally significant and is associated with the cross-isopycnal flow of about 4 Sv of LCPW into the lower deep water layer (see also Figure 5.15). This upwelling is required to supply a strong eastward flow of deep water on the equator. Since we have low confidence in the deep equatorial velocity profile, we refrain from making much of this mid-depth diffusivity maximum in the west. Above the deep water, the diffusivities drop to around $0.1cm^2s^{-1}$ and then rise again just below the thermocline to $0.8cm^2s^{-1}$. The heightened subthermocline mixing rates are associated with the upwelling of 6.5 Sv intermediate water into the western Pacific thermocline, which supplies the Thermostad outflow and divergence in the layers above. An examination of the heat budget below will show that this upwelling may also not be realistic.

The large abyssal diffusivity observed in the eastern equatorial Pacific is not unusual when compared with other estimates of deep diffusivities. Where diffusivities have been deduced from abyssal heat budgets, elevated levels (compared to the canonical $1.0cm^2s^{-1}$) have been found at nearly all sites (Table 5.14). Direct microstructure measurements detect only small interior diffusivities away from topography ($\sim 0.1cm^2s^{-1}$) but suggest a rapid increase near boundaries (Polzin, 1992). Few deep microstructure profiles have been made and more data

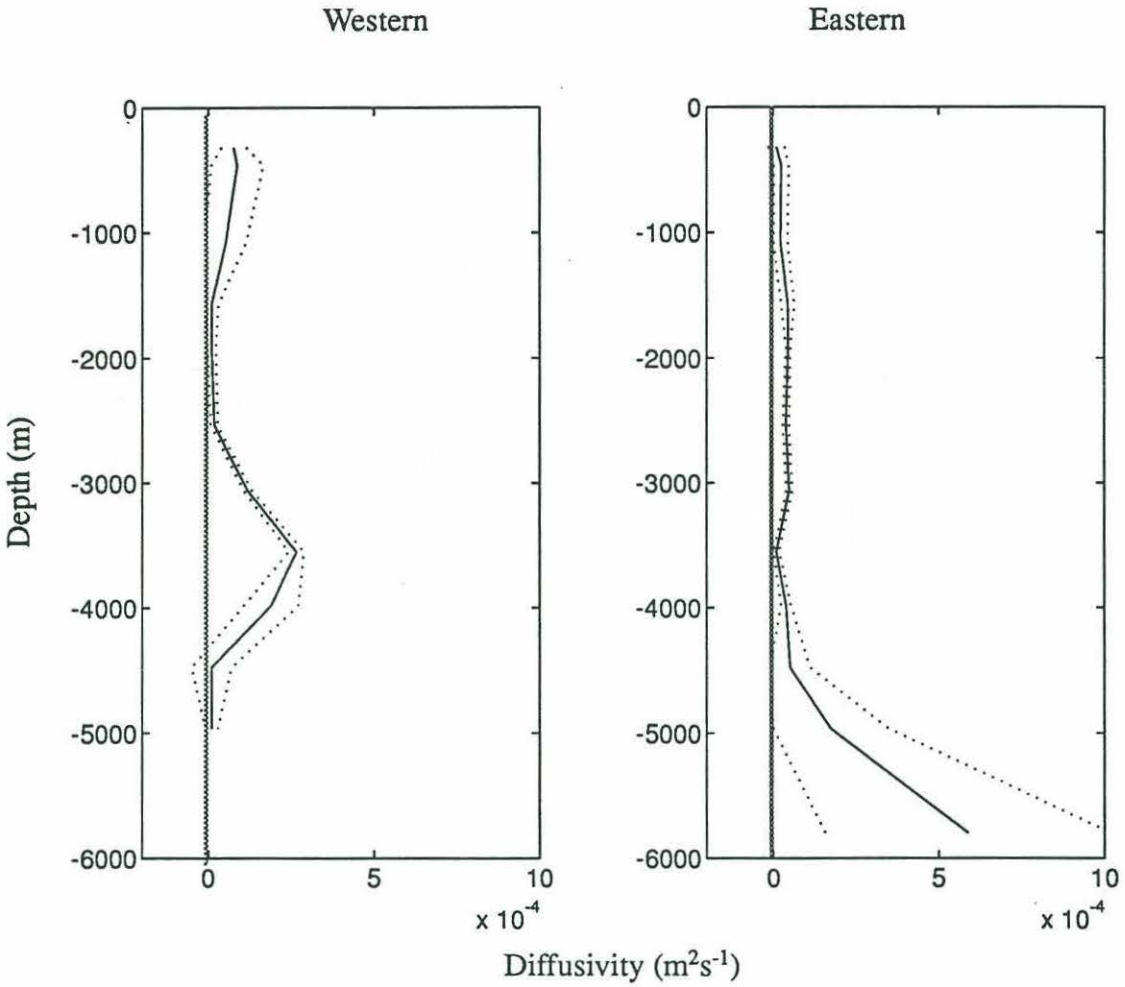

Figure 5.24 Model diffusivities and error range for the western and eastern ocean volumes. Errors are assigned to the estimates by converting the *a priori* heat and salt balance errors, σ_C, into uncertainty in the diffusivities σ_k. This is done by dividing the property error by the mean gradient and area:

$$\sigma_k = \sigma_C / \left[\frac{\partial C}{\partial x} Area\right]$$

The errors plotted are the maximum σ_k given by either the heat or salt balance. This approach gives an upper bound on the error as the actual model residuals are smaller than the *a priori* errors.

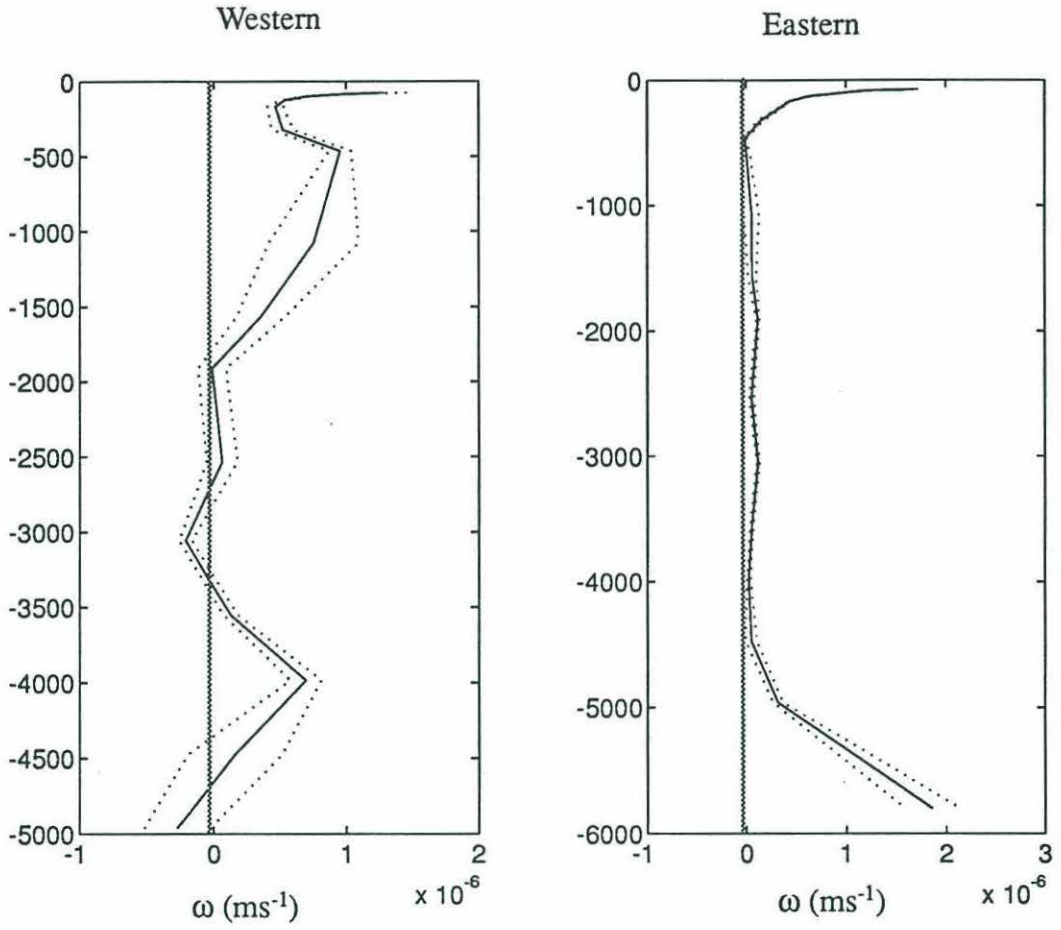

Figure 5.25 Cross isopycnal velocities in the B1 circulation, bounded by the *a priori* error estimates.

is needed before this effect can be established as universal.

The case for downward increasing diffusivities has been argued in two ways. Models of internal wave dissipation result in a inverse power law dependence of diffusivity, K on N, the buoyancy frequency: $K = a_0 N^{-q}$ (Gargett, 1984). Since N decreases in the abyss, K must therefore increase. This simple idea, however, has not stood in the light of recent micro-structure data. Polzin (1992) demonstrates that equally important in the scaling of K from internal wave dissipation, are the energy levels and frequency content of the internal wave field. Through out most of the ocean's volume these are well described by the Garrett and Munk model (Garrett and Munk, 1975), and the resulting diffusivities are small (~ $0.1 cm^2 s^{-1}$), in agreement with the values found away from the bottom in the present model. Though the Garrett and Munk internal wave model is not expected to apply at the equator, the interior diffusivities diagnosed in the equatorial circulation appear in line with those in the subtropics.

The ocean boundaries are then the next obvious location for deep ocean mixing. Armi (1979) argues that K will increase with depth due to the simple fact that the fraction of the

Source	K ($cm^2 s^{-1}$)	Method
Hogg *et al* (1992)	3.0 - 4.0	Deep heat budget for the Brazil Basin (z <= 4000m)
Saunders (1987)	1.5-4.0	Deep heat budget for the Iberian Basin
Whitehead (1989)	0.03-0.07 ~1	Salt and heat budgets for the Ceara Abyssal Plain: current meter data; geostrophic estimates.
Fieux and Swallow (1988)	1-4	Heat budget for the deep Somali Basin.
Johnson (1990)	5.3-13 1.5-6.7	Heat budget for the Somali Basin. Heat budget for equatorial Pacific (as for this study).
Polzin (1992)	0.1-0.2 > 4.0	Estimates of internal wave dissipation rates: 0-3000m away from topography; within 400m of bottom, extrapolation gives ~ 10. at the bottom.

Table 5.14 Estimates of abyssal diffusivities from the literature. All estimates are based on heat budgets in deep basins except for Polzin (1992).

area in contact with the bottom boundary layer increases with depth. If there are large mixing rates sustained near the boundary by some boundary processes (unspecified), then the averaged diffusivity is given by:

$$K = \frac{A_{int}(z)}{A(z)} K_{int} + \frac{A_{bdy}(z)}{A(z)} K_{bdy} \tag{24}$$

where the ratio of the areas over which the boundary and interior diffusivities determines their influence on the surface average diffusivity.

We can test Armi's hypothesis in the equatorial volume. The hypsometric ratios in (24) were found from a crude 1° x 1° topographic data set as follows: the average depth of each isopycnal interface was found; 1° x 1° squares where an isopycnal was within 100m of the bottom contributed to A_{bdy}; 1° x 1° squares where bottom depth was below the layer depth contributed to A_{int}.

In the eastern Pacific, Armi's model produces a reasonable fit with the model diffusivities if $K_{bdy} = 15 cm^2 s^{-1}$, though an order of magnitude less than his nominal value of 100 $cm^2 s^{-1}$ (Figure 5.26). The increase in the ratio of boundary area to total area matches the observed increase in diffusivities well. In the western Pacific, the hypsometric model does not account for the increased deep water diffusivities, though this may be due to the crude way in which the hypsometric ratios were calculated. The western Pacific has tortuously complex topography which is poorly described by the depth data base used here.

In summary, the mixing rates deduced by the circulation are consonant with previous observations of abyssal diffusivities. Above the abyss and below the thermocline, the diffusivities appear to be small ~ 0.1 $cm^2 s^{-1}$ though values up to 0.3 $cm^2 s^{-1}$ cannot be ruled out given the uncertainties. In the western basin the inferred mixing rates are less reliable, though they also tend to increase with depth. In the lower 3000 db in the eastern Pacific, diffusivities increase to values of 6 $cm^2 s^{-1}$ at the deepest interface analyses which is on average 800m above the bottom. Extrapolation with depth would result in values of around 10 $cm^2 s^{-1}$ at the bottom.

Along with previous estimates of deep diffusivities, the distribution of K in the water column suggests a that a boundary mixing process may dominate cross-isopycnal fluxes in the

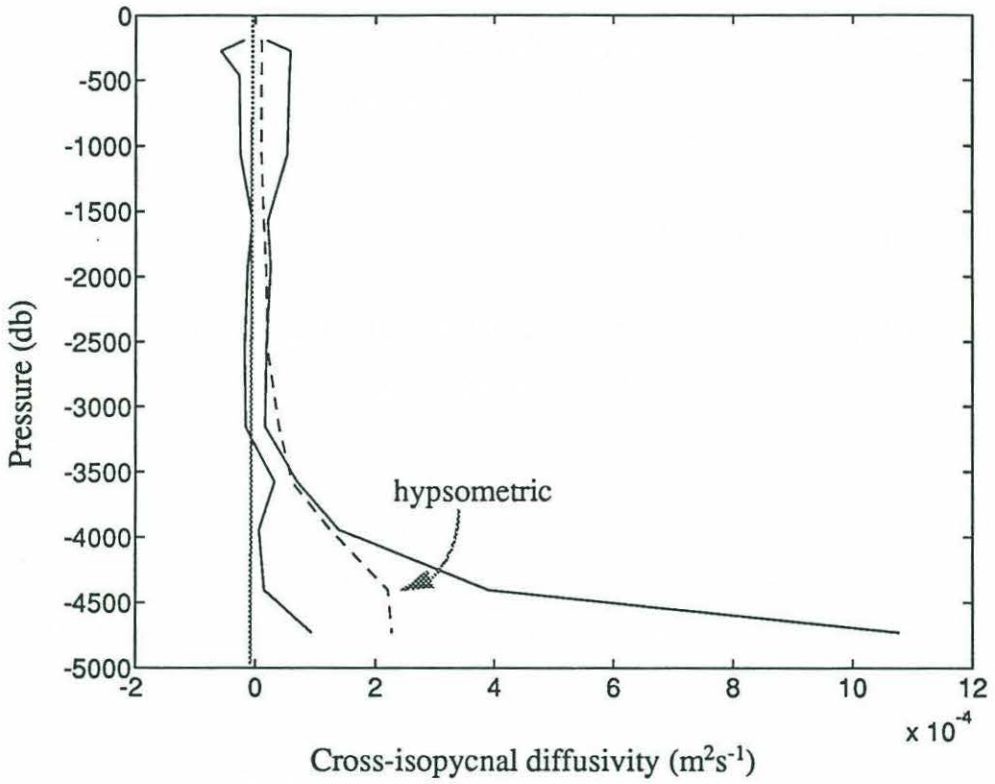

Figure 5.26 Comparison of diffusivities based on the hypsometric model (dashed) with the range deduced from the circulation in the eastern box.

deep ocean. The mixing rates found in the eastern equatorial volume are not significantly different from those found in the subtropics leading us to conclude that the mixing effect of any special equatorial processes is small when integrated over the volume between 10°N and 14°S.

In the western Pacific volume, large diffusivities are also associated with two levels of strong cross-isopycnal fluxes: in the deep water where the excess LCPW flowing into the western box upwells into the NPDW layers; and where intermediate water upwells into the thermocline. The first of these is largely determined by the deep shear profile at the equator, in which we have low confidence. The latter is also suspect, in the light of the western Pacific heat budget, discussed below.

5.11 Upwelling into the thermocline

The equatorial upwelling system is an area of intense heat absorption by the ocean and so is of primary importance in the global heat budget (Figure 5.27). We can deduce the surface heat flux from the oceanographic observations once the mass budget has been determined. Since the temperature of the waters leaving the upwelling region is known, the temperature of the water upwelled determines the amount of heat required to warm it before it exits the in the Ekman flux. In constructing the mass budget we are plagued with the uncertainty in the actual size of the Ekman divergence, which has a 10 Sv range for the volume east of 165°E.

The inverse model cannot easily change the size of the geostrophic thermocline convergence: the high shear and small horizontal area of the thermocline layers means that a large velocity adjustment is needed to alter the flow, and this in turn causes violation of constraints on the deep circulation. Uncertainty in the Ekman fluxes is, instead, propagated by the model into the cross-isopycnal velocities at the base of the thermocline. In the B1 model, the Ekman fluxes are loosely specified and their exact size is driven by the minimization of the cross-isopycnal fluxes in the constrained layers at the base of the thermocline. In a sense, this configuration minimizes the upwelling across the base of the thermocline, and indeed, all of the upwelled fluid in the eastern box originates at densities lighter than $\sigma_\Theta < 26.7$ (Figure 5.28). There is a small net downwelling at the base of the Thermostad layer at ($\sigma_\Theta = 26.7$) of -2.1 Sv, which is not significantly different from zero given the errors in the budget (compare with the eddies in Figure 5.19e for instance). Therefore,

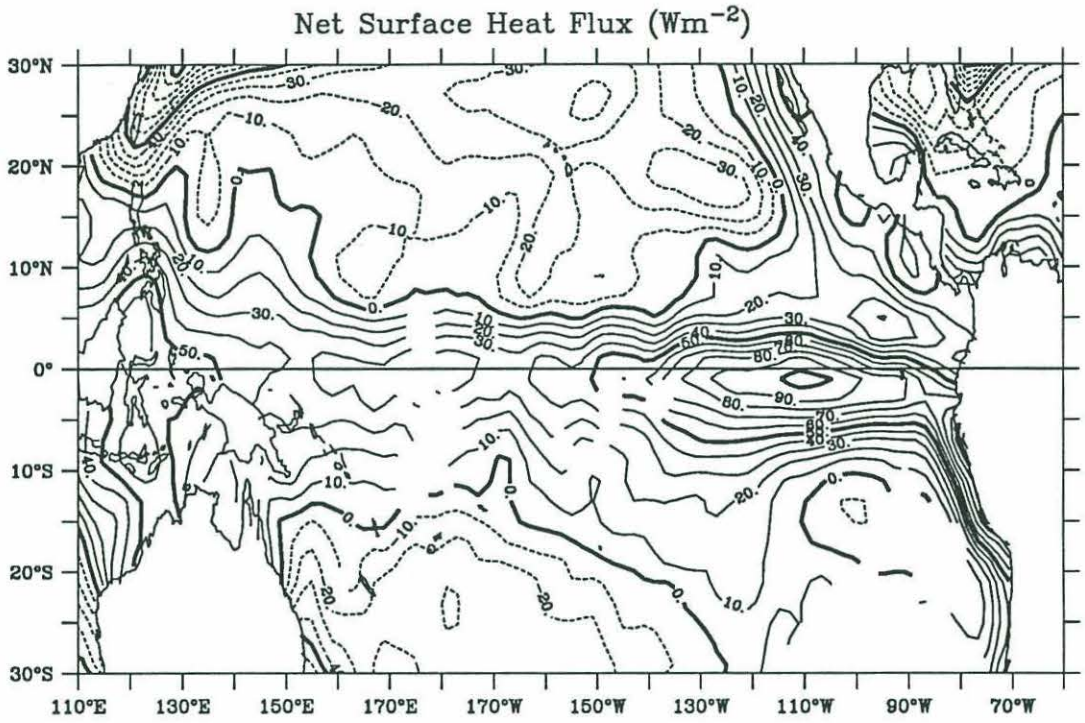

Figure 5.27 Surface heat flux (Wm^{-2}) in the equatorial Pacific from Oberhuber (1988). The contour interval is 10 Wm^{-2}, where positive values indicate heat absorption by the ocean. Regions of insufficient data are blank.

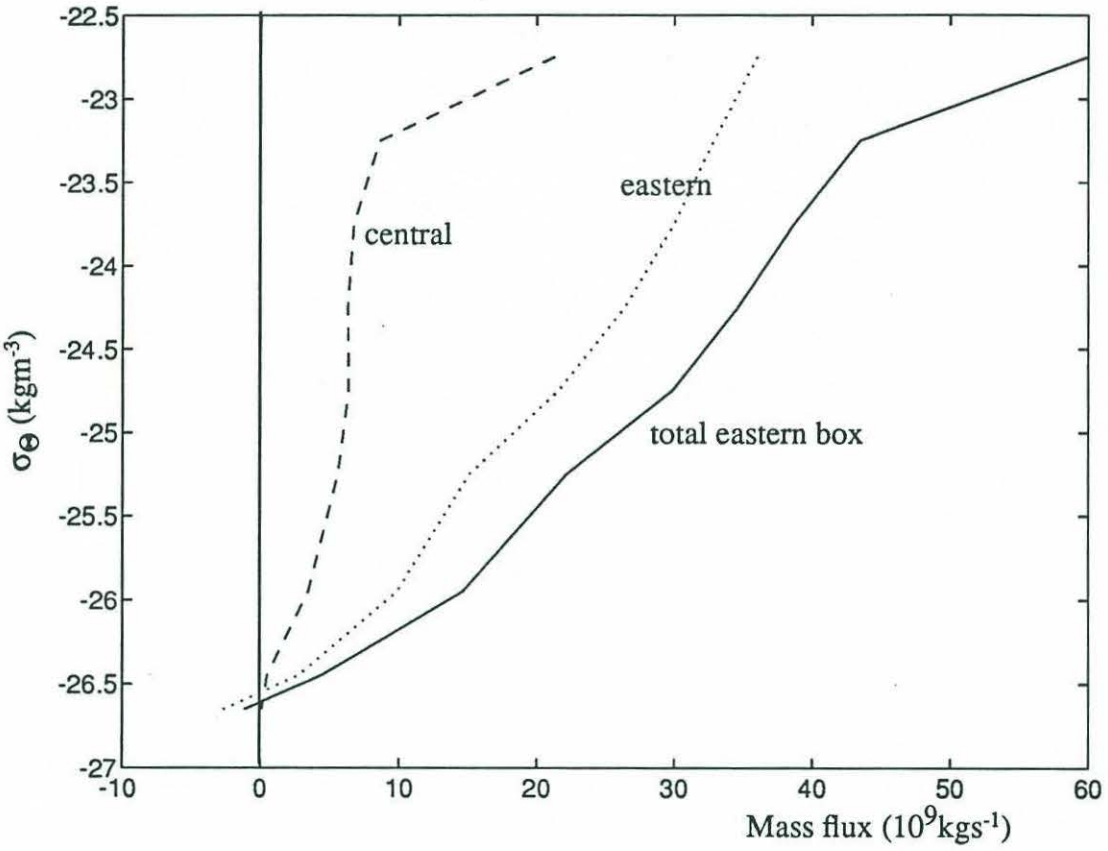

Figure 5.28 Cross-isopycnal mass flux in the upper 1000m of the water column as a function of potential density in the Pacific volume east of 165°E.

though there is a rough balance between equatorial Ekman divergence and geostrophic convergence, the small upwelling into the thermocline in the B1 circulation is due to the model's bias towards minimization of the diapycnal fluxes. We must therefore look to other studies to ascertain whether the minimum mixing approach is valid.

The data that best constrains the depth of the equatorial upwelling system are the distributions of bomb ^{14}C and tritium in the equatorial thermocline. Since the time it takes for these tracers to equilibrate with the atmosphere is long (~ 10 years for ^{14}C) and they are little affected by biological activity, the upwelled water retains a memory of its source. Waters below the thermocline are poor in these tracers since they are much less rapidly ventilated than the waters in the thermocline. The effect of upwelling is apparent as an equatorial surface minimum in the concentrations of tritium and ^{14}C. Fine, *et al.*, (1983) assert, based on the tritium distributions, that the upwelling is confined to levels above $\sigma_\Theta = 26.0$. Quay, *et al.* (1983) demonstrate via a simple model which accounts for ^{14}C, nutrient and salinity observations at 155°W, that the deepest source of upwelled waters is the $\sigma_\Theta = 26.5$ density level, which is in our Thermostad layer ($26.2 < \sigma_\Theta < 26.7$).

These studies deduce that the mixing rates and cross-isopycnal fluxes at the base of the equatorial thermocline are indeed small, and thus support the minimum mixing approach assumed in the present analysis.

5.11.3 Heat Budget of the Eastern Equatorial Pacific

Here we examine the heat budget of the upper ocean ($\sigma_\Theta < 26.7$) based on the B1 circulation. As seen previously, cold thermocline water converges in the EUC, and then upwells along the equator, predominantly in the eastern Pacific. The upwelled water is warmed by the sun in the mixed layer, requiring large heat fluxes at the ocean surface.

For the whole volume east of 165°E, the B1 circulation requires a net heat flux of 1.06 PW ($=10^{15}$W) into the ocean which corresponds to 30.1 Wm^{-2}. The bulk of this flux is due to upwelling: 22 Sv of water for which $\sigma_\Theta < 23.0$ (Figure 5.19b) leaves with an average Θ =27.8°C and is replaced by thermocline water which is 11°C cooler at 16.8°C. The temperature differences are only representative since a continuum of thermocline water participates in the cell ranging from 29.0 to 10°C. The upwelling mechanism requires 0.97 PW, while 0.07PW (2 Wm^{-2}) is diffused downwards out of the thermocline across ($\sigma_\Theta = 26.7$)

Region	Esbenson & Kushnir	Oberhuber	Model B1
Eastern Pacific (W/m2)	25.6	29.6	30.1 ± 11
Western Pacific (W/m2)	21.8	30.2	47.2
Throughflow (PW)			-0.15
Total 10°N-14°S (PW)	1.14	1.37	1.57
North Pacific (PW)	-1.22	-1.13	-0.61
Eastern sub-boxes:			
central (Wm^{-2})	17.6	16.7	19.7 ± 14
eastern	29.9	36.4	37.5 ± 10

Table 5.15 Estimates of surface heat fluxes from two climatologies and for the model circulation B1. Positive is for a net flux into the ocean

-a negligible amount.

Most of the upwelling occurs east of 155°W, along with the bulk of the heat absorption, as seen in the surface observations (Figure 5.27). Across $\sigma_\Theta = 23.0$, 15 Sv exits the box at 27.8°C and is replaced at an average Θ of 14°C, exporting heat at a rate of 0.84 PW. In the mid-Pacific box 0.21 PW are absorbed by the 7 Sv upwelling into the surface layer.

An error estimate for the heat budget is difficult since we do not know how good the assumption of no upwelling into the thermocline really is. The formal model uncertainty in the mass budget of the layer directly below the eastern thermocline is ± 2 Sv, which gives an net error of 0.15PW if this cold water that upwells into the surface layer is distributed equally between the central and far eastern sub-boxes. The uncertainty in the actual thermocline convergence as measured by the standard deviation of the transport stream function is ± 3.0 Sv and ± 3.6 Sv for the eastern and central boxes respectively. Multiplying these by the Ekman-thermocline temperature differences gives uncertainties of 0.16PW and 0.08PW. We therefore adopt error estimates of 0.23 and 0.15 PW and to include both of these affects, for the eastern and central subboxes respectively. The total heat divergence estimate for the equatorial volume east of 165°E is therefore 1.06 ± 0.38PW.

In Table 5.15 the B1 model heat fluxes are compared with two surface climatologies: Esbenson and Kushnir (1981) and Oberhuber (1988). These were integrated over the box

surface areas so that direct comparisons with the circulation-based could be made. For the eastern volume and its sub-boxes, the B1 fluxes agree very well with those from the two climatologies, and especially well with those of Oberhuber (1988). A more comprehensive comparison with surface based flux estimates is made below, after exploring the heat budget of the western box.

5.11.4 The heat budget in the Western Equatorial Pacific

Though the Throughflow is small in the B1 model (1.6 Sv) it has a large associated temperature flux (0.14PW) due to its warm temperature: 23.4°C. The net Ekman divergence for the western box is 11.8 Sv with a temperature 28.3°C. The net thermocline convergence is only 4.5Sv, and consists of a 9.3Sv convergence above $\sigma_\Theta < 25.5$ at a Θ of 25.6 °C and a divergence in the lower thermocline ($25.5 < \sigma_\Theta < 26.7$) of -4.8Sv at 12.9°C. The B1 model upwells 8.7Sv of intermediate water at 9.8°C to supply the lower thermocline divergence (4.7), the excess Ekman outflow (11.8-9.3) and the Throughflow (1.5). Though only 2.5Sv of the intermediate water is used to balance the excess Ekman divergence, a large heat flux is needed to do this: 0.19PW. The net surface heat flux into the western box is 0.51PW ($47.2 Wm^{-2}$), and almost half is associated with the conversion of intermediate water to surface water.

The B1 model heat flux for the western box is somewhat higher than the climatologies in Table 5.15. For comparison, Hsiung's (1985) maps suggest a mean for the western box of between 20 - 40 Wm^{-2}, Weare, *et al.*, (1981) find higher values of around 40-60Wm^{-2}, and Hastenrath (1980) has values < 50Wm^{-2}. Due to this large range, the B1 circulation is well within the spectrum of climatological estimates, though on the high side.

However, Godfrey and Lindstrom (1989) argue that the presence of a shallow fresh mixed layer in the western Pacific dampens the downward mixing of heat into the deep isothermal layer beneath, and thus the thermocline. Due to this 'barrier' layer effect, they concluded that the maximum heat flux into the warm pool in the western Pacific can be at most 20Wm^{-2}, and suggest that bulk formulae used to construct climatologies consistently overestimates the downward heat flux. Direct measurements (though only at low wind speeds) have confirmed this (Godfrey *et al*, 1991).

The larger surface heat flux required by the B1 model conflicts with Godfrey and Lind-

strom's arguments. The required heat flux would be much reduced if the net convergence in the thermocline were larger, negating the need to upwell water from below. To explore this possibility we assess errors in the warm water mass budget in the Western Box.

5.11.5 The Warm-water Budget in the Western Equatorial Pacific

Of the three sections bounding the western box, the southern section is most likely to be aliased by transients since it is based on a single occupation. However, the comparison made with Ridgway and Godfrey's (1993) analysis demonstrated good agreement with historical data. It is unlikely that the Coral Sea can supply large quantities of thermocline water to the western box. Hence, we adopt Ridgway and Godfreys' (1993) error bar on the warm-water mass transport across 170°E of ± 2 Sv.

The Mindanao Current transport is the next least reliable component of the flow being based on only 7 surveys. The standard error for the transport based on the US/PRC-TOGA surveys at 8°N is 4Sv for $\sigma_\Theta < 27.0$.

The large number of surveys used to construct the mean 165°E section make this component of the flow the least likely to be in error. The small differences between averages over different time periods seen in Table 4.2 suggest that an uncertainty of about 5Sv is reasonable. Lastly, the Ekman divergence is uncertain at the 30% level, which translates to an upper layer transport error of ± 4Sv.

In total then, the combined uncertainty in the warm water budget is ± 15 Sv which provides some flexibility in the circulation. Based on the small surface heat fluxes of Godfrey *et al.* (1991), upwelling into the thermocline must be negligible. Such a scenario is within the errors, as only 7.1 Sv is required to balance the budget with no Throughflow. The remaining uncertainty, therefore, allows a maximum value for the Throughflow of 7.9 Sv.

5.11.6 Implications for the Throughflow

The heat budget and the error analysis above imply that the maximum Throughflow that can be plausibly supplied by the circulation is about 8 Sv. Though the errors in the data allow for a fairly sizeable Throughflow, the analysis suggests a small value, since we find no evidence for excess of warm water being delivered to the Indonesian Passages by the Pacific circulation.

The Throughflow is largely confined to the upper 200m (Wyrtki, 1987) and appears to be of Mindanao Current water (Lukas, *et al.*, 1991; Ffield and Gordon, 1992). Thus, the simplest way to modify the present circulation to supply a Throughflow is to increase the flow of the Mindanao Current. This has minimal effects on the heat and salt budget since we assume it exits south of Mindanao at much the same temperature and salinity as when it flows across 8°N.

Recent estimates of the geostrophic mass flux between Australia and Indonesia based on long term repeat XBT survey presently provide the best available estimate of the mean Throughflow (Meyers, Bailey and Worby, subm.). A total of 56 XBT occupations over a period of 4 years gives a mean transport of 5Sv with respect to 400db. This is within the range deduced from the present study. The large Throughflow values deduced in the past, now seem unlikely (Table 5.16).

Table 5.16 Estimates of the Throughflow from previous studies, adapted from Gordon (1986)

Source	Throughflow (Sv)	Method
Wyrtki (1961)	1.7	dynamic method
Cox (1975)	18.0	numerical general circulation model
Godfrey and Golding (1981)	10.0	mass transport in the eastern Indian Ocean
Piola and Gordon (1984)	14.0	freshwater budget for the Pacific and Indian Oceans
Fine (1985)	5.1	tritium budget for the Indian Ocean
Fu (1989)	6.6	mass budget for the Indian Ocean
Godfrey (1989)	16±4	global Sverdrup model
Kindle, *et al.* (1989)	7.0±4	single layer reduced gravity wind-driven numerical model
Toole, Zou and Millard (1988)	1.0	mass and salt budget for the western tropical Pacific Ocean
Semtner and Chervin (1992)	10	global general circulation model.
Meyers, *et al.* (1993)	5.0	long-term average XBT transect
This study	0-7	

5.12 The meridional overturning of the North Pacific

The zonally averaged (on pressure surfaces) geostrophic transport at 10°N and 14°S reveal the characteristic overturning mode of the deep North Pacific. Northward transport of LCPW into the North Pacific Basin occurs below 3500m at both 10°N and 14°S (Figure 5.29). Southward return flow occupies the water column between 3500m and 1000m. Above 1000m the equatorward convergence of thermocline water is apparent.

The net flow of LCPW across 14°S is 12.1Sv, nearly all of which is in the densest model layer (Figure 5.30). Across 10°N, there is net southward transport in the shallowest layer included in the LCPW definition (model layers 16-19). Excluding this southward transport, the total northward transport of bottom water across 10°N is 10.6 Sv. All of the northward flowing LCPW returns below the thermocline across both zonal sections in the B1 circulation, with little upwelling of abyssal water into the North Pacific thermocline.

This cell compares well with other direct circulation studies both north and south of the equator. In an inverse study of the South Pacific, Wunsch, *et al.* (1983) found a deep overturning cell of 12Sv with all of the LCPW returning below 1000m. In the North Pacific, Roemmich and McCallister (1989) deduced a similar cell, with 9.6Sv flowing north across 24°N and 8.2Sv of deep water returning southwards. Bryden, *et al.* (1990) find a slightly different flow with southward transport of NPDW across 24°N of 8.4Sv supplied by 4.9Sv of LCPW and 4.3Sv of intermediate water. Again, none of these direct calculations of the circulation feature a significant upwelling of abyssal water in the North Pacific thermocline.

The depth (and temperature) at which the LCPW flows out of the North Pacific has implications for both the heat budget of the North Pacific, and the global thermohaline circulation. It is therefore worth examining more carefully. As discussed above, the largest source of uncertainty in the equatorial mass budget are the size of the Ekman fluxes across the zonal sections. In B1 these are controlled by the minimization of the cross-isopycnal flux terms. The result is an equatorial Ekman divergence of similar magnitude to the thermocline geostrophic convergence. The quantity that impacts the North Pacific overturning is the imbalance between the thermocline and Ekman fluxes across 10°N.

To explore this issue, model solutions were found where a strict salt balance was required in the North Pacific with the Ekman flux across 10°N set at different values ranging between 30 and 45Sv. All of the solutions feature a northward flux of LCPW of around 10 Sv across

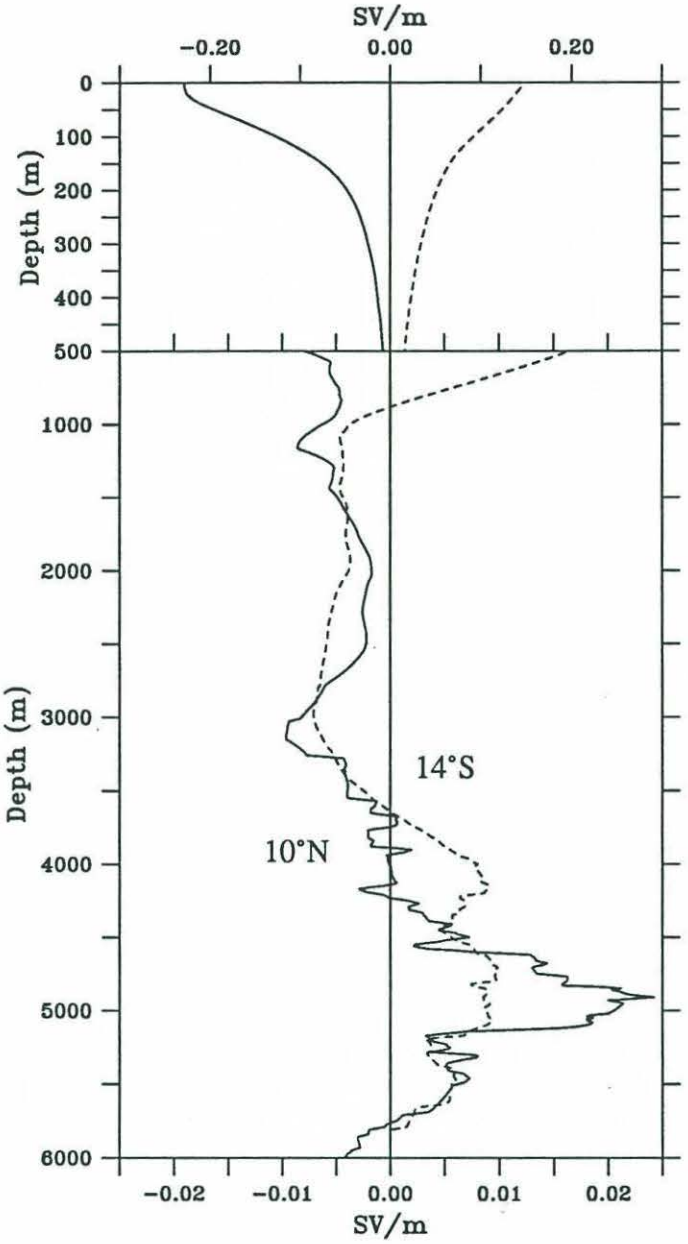

Figure 5.29 Geostrophic transport per unit depth across 10°N (solid) and 14°S (dashed) for the model circulation B1. Note the large scale change for the upper 1000m.

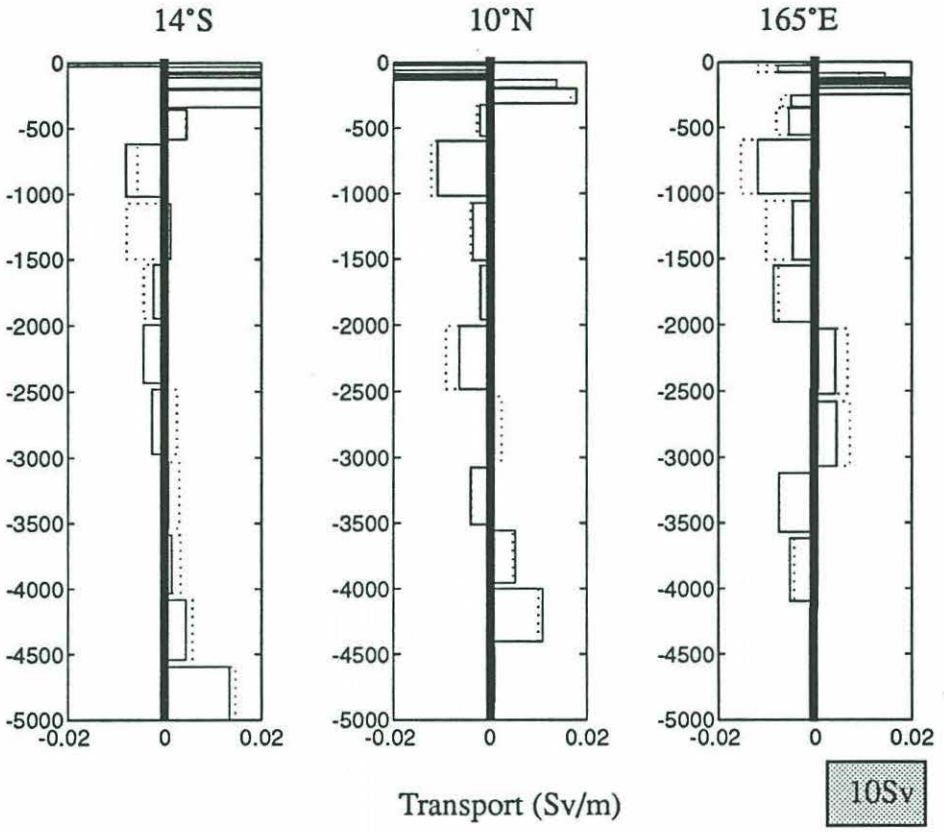

Figure 5.30 Transport in density classes across the 3 principle sections. Solid lines are for the B1 solution and dotted are for the initial guess. The units are in Sverdrups/m and for reference the plot area corresponding to 10Sv is shown below the 165°E plot. The direction is positive northwards and eastwards.

both zonal sections, independent of the Ekman flux. The transports at mid-depth, on the other hand, show a strong dependency on the Ekman transport across 10°N. This can be easily explained: the deep and intermediate water layers have the largest area and they can be used to adjust the net section mass flux without large penalties in the cost function. The increase in transport of NPDW across 10°N is reflected in a similar increase across 14°S, requiring little change in the amount of cross-isopycnal advection in the equatorial volume.

A way to distinguish these solutions is to examine the implied upwelling profile in the North Pacific Basin. Imbalance between the southward flow of thermocline water and northward Ekman flux across 10°N must be compensated by either upwelling or downwelling across the base of the thermocline in the North Pacific. "Downwelling" implies production of denser water from lighter water as could be caused by air-sea interaction. All of the curves in Figure 5.31 clearly show the production of waters in the thermocline density classes consonant with ventilation of the North Pacific subtropical gyre. At depth, upwelling associated with the robust deep cell is associated with the conversion of LCPW to NPDW. In the intermediate and upper deep waters the solution curves diverge. For small 10°N Ekman flux, abyssal waters upwell into the thermocline; when the 10°N Ekman flux is large, the model shows that thermocline waters downwell and exit the basin as intermediate and upper deep water. The issue at the heart of the Ekman transport uncertainty is thus the depth of ventilation in the North Pacific basin.

Density surfaces below $\sigma_\Theta = 26.8$ are not observed to outcrop in the open North Pacific basin, and so are not directly ventilated by large-scale air-sea interaction. Reid (1965) asserts that below $\sigma_\Theta = 26.8$ mixing becomes the dominant modifier of properties. More recently, Talley (1991) suggested that the low salinity water mass that forms the NPIW minimum is due to leakage of very fresh water from the Okhotsk Sea north of Japan. There, the combination of brine rejection due to sea-ice formation and surface cooling produce waters dense enough to spread into the open ocean at intermediate depths. The affected density range is between $26.8 < \sigma_\Theta < 27.6$ and includes the intermediate water layers 9 through 11 in our study. Downwelling or production of water at these densities is therefore consistent with Talley's (1991) observations. She estimates that roughly 5 Sv of water cycling through the Okhotsk Sea can account for the low salinity of the NPIW layers.

Downwelling across this density range is present in the B1 model and is associated with an interesting cusp in the upwelling curves just at the base of the thermocline. This cusp

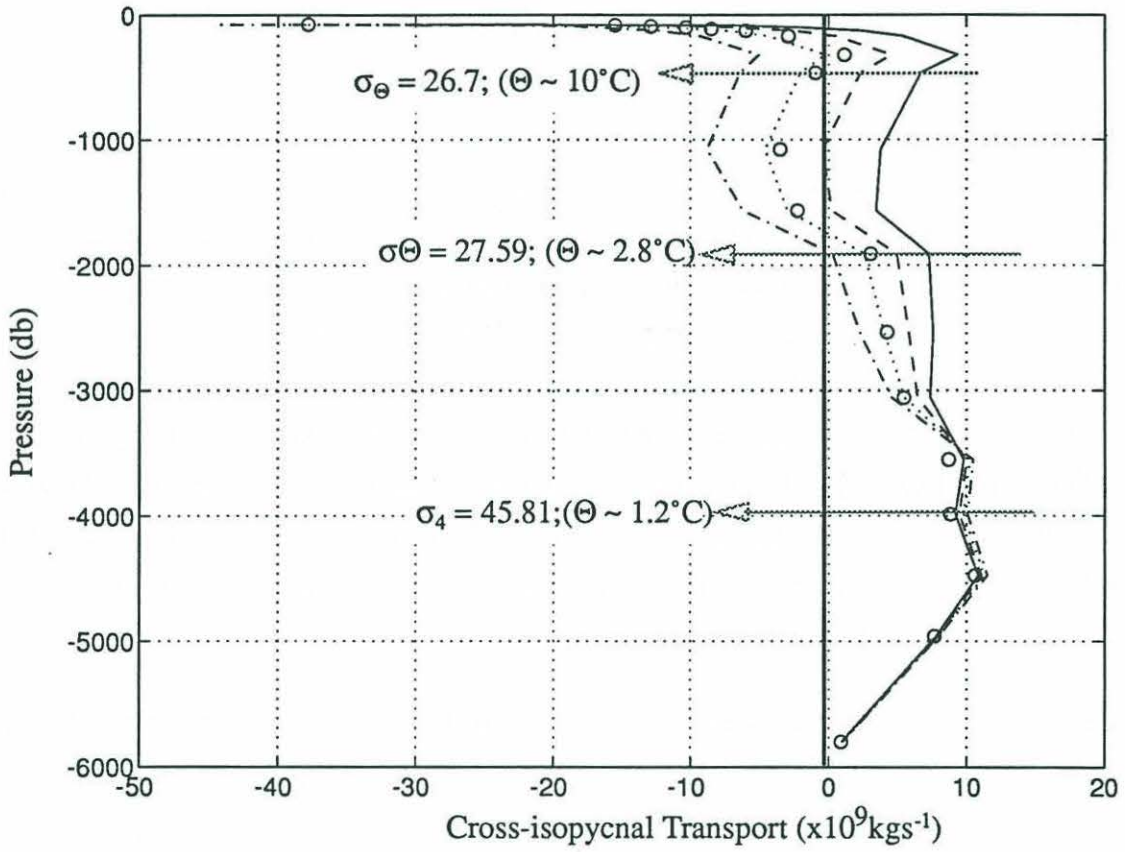

Figure 5.31 Mass flux across isopycnals in the North Pacific north of 10°N deduced from the flux in density layers across 10°N. Several model solutions are shown: B1 (circles); 10°N Ekman flux held at 30, 35, 40 and 45Sv for the solid, dashed, dotted and chain-dashed lines respectively. Densities at some selected layer interfaces are shown. The interface depths used in the plot are the average along 10°N, and are therefore not representative of the average depth in the North Pacific.

implies a triple cell structure in the overturning north of 10°N. Besides the abyssal and thermocline meridional cells, there is a third cell associated with the *northward* flow of lower thermocline and upper intermediate water across 10°N, which returns as denser intermediate water. Bryden, *et al.*, (1991) observed a similar feature across 24°N and identified the water northward flowing water as AAIW. In the B1 solution, however the waters that supply the production of intermediate water have temperatures of $13.1 < \Theta < 8.4$ °C, too warm to be AAIW. Presently we do not know what drives this cell, though the entrainment of overlying warmer waters in the Okhotsk Sea outflow may be a good candidate.

Help in constraining the circulation was also sought through the heat budget of the North Pacific Basin. The bulk of the heat transport across 10°N is achieved by the wind-driven cell: the northward transport of warm surfaces waters in the Ekman layer and their return as slightly cooler water in the thermocline. The heat transport across 10°N is directly proportional to the Ekman transport and formally ranges from -0.2 PW up to 1.6PW given the uncertainty in the Ekman flux (Table 5.17).

Independent estimates based on surface observations were assembled in the hope that they may further constrain the heat flux and so the circulation. However the range deduced from surface climatologies is almost as great as that for the model. Integrating the surfaces fluxes over the smaller area between 24°N and 10°N reduces the effect of bias uncertainty in the fluxes, and the net can be added to Bryden *et al.*'s (1991) heat transport across 24°N to get a revised transport at 10°N. Unfortunately the range of revised fluxes is still too large to effectively constrain the flow (Table 5.17).

We are left to fall back on consistency checks with previous studies of the North Pacific circulation. The studies of Wunsch *et al.* (1983) and Roemmich and McCallister (1989) agree with the B1 solution which does not upwell large amounts of abyssal water into the thermocline. Talley's (1991) conclusion that ventilation occurs down to densities of about 27.6 σ_Θ leads us to expect the zero crossing curve in the upwelling profile should lie near this surface. We will argue the B1 model is consistent with these studies, as well as the constraints set on the depth of the equatorial upwelling discussed previously.

5.13 South Pacific Heat Budget

Talley (1984) drew attention to the confusion over the size of the meridional heat flux in

Source	24°N	10°N	14°S	10°N*	14°S*	10°N-14°S
Wyrtki (1965)	0.1	-0.6	-2.5	0.1	-1.8	-1.9
Emig (1967)	0.5	0.0	-1.6	0.3	-1.3	-1.6
Hastenrath (1980)	1.2	0.5	-1.7	0.1	-1.4	-2.2
Weare, *et al* (1981)	0.1	0.3	-2.0	1.0	-1.3	-2.3
Esbenson and Kushnir (1981)	0.8	0.8	-0.5	0.8	-0.5	-1.2
Hsuing (1985)	0.8	1.0	-0.1	1.0	-0.1	-1.1
Oberhuber (1988)	0.9	1.3	-0.1	1.0	-0.1	-1.3
Bryden, Roemmich and Church (1991)	0.8					
Model						
B1		0.61	-0.81		-1.5	
$M_{EK}^{10°N} = 30.$ Sv		-0.1	-1.2		-1.1	
$M_{EK}^{10°N} = 35.$		0.3	-1.0		-1.3	
$M_{EK}^{10°N} = 40.$		0.7	-0.7		-1.5	
$M_{EK}^{10°N} = 45.$		1.2	-0.4		-1.6	

Table 5.17 Annual mean meridional heat transport in the Pacific Ocean across 24°N, 10°N and 15°S. The third and fourth columns (10°N*, 14°S*) contains estimated of the heat transports based on a southward integration of the indirect estimates starting with the Bryden, Roemmich and Church (1991) direct transport estimate at 24°N. The heat flux divergence between 10°N and 14°S is also shown. All of the indirect estimates, except for Hsiung and Oberhuber, were taken from the figures of Talley (1984), and so are only approximate.

the South Pacific Ocean. Estimates based on surface observations require an integration point in order to deduce the net basin flux across latitude lines. In the Pacific, the northern land boundary is used where a zero flux condition can safely be assumed. The disadvantage of this method is that bias uncertainty in the fluxes accumulate away from the integration point, making estimates in the South Pacific extremely uncertain, so much so that the sign of the heat flux there is unknown. Wunsch, *et al.* (1982) calculated the ocean heat transport across 28°S and found it to be small and southwards: -0.2 ± 0.2 PW. McDonald (1993) repeated the calculation with the same result. These results assume a zero Throughflow, which is consonant with our findings.

The B1 circulation produces a rather large temperature transport across 14°S: -0.81 PW, including the Throughflow temperature flux of 0.15PW. To obtain a flux divergence estimate, the Throughflow temperature flux is removed to give -0.96 PW which is directly comparable with the estimates at 28°S. The mechanism producing this heat flux is the same as that across 10°N. The 30 Sv Ekman flux at 26.9°C is replaced by thermocline water at 20.1°C producing a southward heat flux of 0.82PW which accounts for the majority of the 14°S heat flux. This mechanism is robust, though subject errors in the Ekman flux. A 5 Sv error in the cell gives an uncertainty of 0.15 PW if the flow distribution with respect to temperature classes remains constant.

Estimates based on the surface climatologies show a large range: -1.8 to -0.1PW, though the more modern results tend to predict a small heat flux across 14°S. Together with the direct estimates at 28°S, the model result requires that there be a heat loss to the atmosphere of 0.76PW between 14°S and 28°S. This corresponds to roughly a $30 Wm^{-2}$ average flux to the atmosphere between the sections. According to the maps of Oberhuber (1988) and Weare, *et al.* (1981), heat loss is found in the Tasman Sea and north of New Zealand, while west of roughly 150°W, the heat flux is into the ocean intensifying over the upwelling region along the coast of South America. These areas of opposite heat flux tend to cancel resulting in a flat meridional ocean heat transport curve between 14°S and 28°S. An examination of the curves presented by Talley (1984) show that this is true of most surface climatologies. Hence, we conclude that the large southward heat flux deduced across 14°S is at odds with the surface heat flux observations in the South Pacific. This issue deserves further study.

Chapter 6

Summary and Conclusions

6.1 Summary of Thesis

The primary aim of this thesis has been to identify and measure the important pathways for cross-equatorial exchange in the Pacific Ocean. To realize this aim it was first necessary determine the mean circulation in the equatorial region. This is a challenging task, due both to the size of the equatorial Pacific and the strong interannual variability of the flow there.

Much of the thesis is devoted to this first step: building the tools and elements needed to construct a full mass budget for the equatorial Pacific. Chapters 2 and 3 focus on the flow across two transpacific sections, at 10°N and 14°S, paying particular attention to the western boundary currents which have been poorly observed in the past. Chapter 4 presents the flow across the 165°E meridian.

The issue of interannual variability was addressed by using repeat survey data where possible: at 8°N, 7 surveys were available across the Mindanao Current, the low-latitude western boundary current in the North Pacific; and along 165°E 23 surveys crossed the highly variable equatorial currents. To ensure that the interior parts of the one time sections were not badly aliased by variability, an end-point comparison was made with historical XBT and CTD data. This comparison showed that despite the presence of large interannual fluctuations, the onetime sections used in this analysis were fortuitously representative of the mean conditions. The flow along the South Pacific western boundary (the Coral Sea) was measured using a onetime section only, though the circulation compared favorably with a new study in the same region based on extensive historical observations.

In Chapter 5, the mass budget for the equatorial Pacific is assembled via an inverse calculation. Pains were taken to ensure that the cross-isopycnal fluxes are dealt with in a physically consistent manner: diapycnal diffusion and advection are explicitly included in the model, with the added constraint that the diapycnal diffusivity be positive. A major uncertainty in the circulation is the size of the Ekman fluxes across the zonal sections, which are an important part of the flow. The approach taken here was to allow the inverse model to vary the Ekman fluxes within the range suggested by the various wind-climatologies, in order to satisfy mass conservation in the enclosed volumes. This is in essence a minimum

mixing approach. The circulation that resulted agrees well with previous studies of the Pacific circulation.

6.2 Major Results

6.2.1 Overview of the Circulation: Pathways of Cross-equatorial Flow

Subthermocline Flow

Below 1000m, the zonally averaged flow across both 10°N and 14°S is dominated by a closed cell circulating roughly 10 Sv northwards near the bottom and returning it at mid-depth. Previous studies of the flow in the North (Roemmich and McCallister, 1989) and South Pacific (Wunsch, *et al.*, 1983) have also observed this cell, which transports Lower Circumpolar Water (LCPW) northward and North Pacific Deep Water (NPDW) southwards. When viewed in the zonally averaged sense, the flow in the abyssal cell appears little affected by the dynamical barrier at the equator.

An examination of the flow pathways in density layers suggest that two different mechanisms may be allowing fluid to cross the equator below the thermocline. The bulk of the LCPW that crosses the equator, does so in the lower part of the deep western boundary current that appears to follow topography directly across the equator. We expect that the dissipation occurring in the boundary current can modify the potential vorticity of the fluid, allowing it to cross the strong potential vorticity gradient at the equator. This part of the LCPW features large diapycnal diffusivities, though the analysis cannot distinguish whether the mixing is occurring in the boundary current or is due to a hypsometric affect when mixing is enhanced near all boundaries.

In the upper part of the LCPW and in the overlying NPDW layers, strong zonal near-equatorial currents are observed at 165°E which recirculate much of the fluid flowing across 10°N and 14°S. Comparison of the geostrophic current structure along 165°E with an average field based on direct velocity measurements at 159°W, reveal a similar structure, suggesting that the deep zonal flows are fairly steady and have long zonal length scales. In the LCPW, a strong westward jet at the equator feeds the upper part of the two deep western boundary currents flowing northward across 10°N. The westward jet is supplied by recirculated LCPW from the north and by upwelling of denser LCPW from below. Strong mixing in the NPDW is inferred in the western Pacific, though we would like to obtain better

measurements of the velocity profile at the equator before concluding that this mixing is real.

The deep water layers are devoid of the shear or property signatures of western boundary currents, and instead feature a broad southward flux of NPDW across both 10°N and 14°S. We postulate that in these layers, zonal recirculation in the near-equatorial flows allows sufficient time for fluid parcels to laterally diffuse their potential vorticity, and so be able to cross the equator. Exploration of this issue requires a better understanding of the nature and origin of the deep equatorial flow field.

Between the base of the thermocline at $\sigma_\Theta = 26.7$ and the top of the deep water at $\Theta = 2.0°C$, is the layer we have loosely termed intermediate water. The property fields indicate that subpolar waters from both the northern and southern hemisphere flow equatorward, mainly in the western half of the basin. The tracer fields also suggest a poleward return flow of oxygen depleted and relatively salty intermediate water along the eastern boundary. The equatorial intermediate water is presumably formed by both vertical and lateral mixing along the equator, associated with the set of strong zonal intermediate currents. In the western Pacific, the property signature of Antarctic Intermediate Water spreads northwards along the western boundary, suggestive of cross-equatorial flow. However, in the present analysis, attempts to delineate the movement of the intermediate waters is confounded by the presence of large geostrophic eddies along the zonal sections. These eddies dominate the transport stream function and mask the mean features of the flow.

Thermocline and Above

In the upper waters where $\sigma_\Theta < 26.7$, the zonally averaged flow is dominated by the equatorial upwelling system: thermocline waters from both hemispheres converge on the equator below the mixed layer, are upwelled along the equator and flow poleward in the Ekman drifts. The data show a robust balance between the Ekman divergence and thermocline geostrophic convergence, implying little upwelling of subthermocline waters along the equator. This conclusion is subject to the large errors in the Ekman divergence, though independent studies of tracer budgets and distributions in the equatorial Pacific support the fact that the subthermocline contribution to the upwelling system is small.

In addition to the equatorial Ekman divergence being balanced by thermocline conver-

gence, a symmetry exists in that across each zonal section the Ekman flux is equal and opposite to the thermocline flux. This has two implications: that their is little direct exchange between the North and South subtropical gyres; and that there is little conversion of abyssal to thermocline water in the North Pacific. The latter conclusion is also implied by the fact that all of the LCPW flowing across 10°N returns below the thermocline as NPDW.

The symmetry of the wind-driven gyres about the Pacific equator, contrasts with the situation in the Atlantic as presented by Roemmich (1983). There, a strong asymmetry exists in which the northward geostrophic thermocline transport across 8°S is about 10 Sv larger than the southward Ekman flux. This excess northward transport of thermocline water is converted into surface water via equatorial upwelling, and exported across 8°N as an excess of Ekman over geostrophic transport.

Despite the apparent symmetry indicated by the zonally averaged picture, the equatorward pathways taken by the thermocline waters differ substantially between hemispheres. This is due to the asymmetry about the equator of the Sverdrup flow, which accounts for all of the major currents except for the Equatorial Under Current (EUC) and the large transport of the South Equatorial Current (SEC) in the eastern Pacific. The discrepancy in the SEC transport is explained by the fact that nearly all of the waters upwelled at the termination of the EUC in the eastern Pacific are absorbed by the SEC.

Cross-equatorial flow does occur in the thermocline: in the western Pacific southern hemisphere lower-thermocline water penetrates to about 4°N to feed the Northern Subsurface Counter Current. However, no thermocline water reaches past 4° in the opposite hemisphere before it is entrained into the eastward flowing currents that feed the upwelling system. Once upwelled along the equator, the newly formed surface water is deduced to flow northwards in the western Pacific and southward in the eastern Pacific. This clockwise surface flow pattern was deduced by Joyce (1988) based on a modified Sverdrup theory for flow on the equator. In addition, the southward flow of the upwelled waters is consistent with the asymmetry of the surface temperature distribution in the Cold Tongue in the eastern Pacific. There, a strong temperature front is situated at 2°N, while south of the equator the surface isotherms are broadly spread, with increasing values to the south and west, in the direction of the deduced flow.

The Throughflow

The leakage of water from the Pacific to the Indian Ocean is deduced here to be essentially zero, though an error analysis of the flow components gives a range of 0-7 Sv. This result relies, in part, on the assertion of Godfrey *et al.* (1989; 1991) that the heat flux into the western equatorial Pacific is small (~10Wm^{-2}), which in turn precludes upwelling intermediate water into the western Pacific thermocline to supply the Throughflow.

Though past estimates of the Throughflow range between 0 and 18 Sv, the best direct estimates indicate a mean transport of 5 Sv (Meyers, *et al.*, 1993), which is within the error range deduced by the present analysis. Since the Throughflow exits the Pacific north of the equator, it requires cross-equatorial flow and must be ultimately supplied by southern hemisphere water. Direct flow of SEC water across the equator and into the passages is not likely given the fact that the thermocline in the Indonesian Seas is occupied by predominantly North Pacific water. The pathway for cross-equatorial flow that can account for the North Pacific properties of the Throughflow and which is consistent with the present analysis is presented in Figure 6.1, and described below.

South Pacific thermocline water flows towards the equator in the SEC, and is entrained into the EUC, either at the western boundary as shown in Figure 6.1, or in the interior. This water is eventually deposited close to the surface by the EUC in the eastern Pacific, warmed and advected southwards to supply the upper part of the SEC. Upon reaching the western Pacific once again, it crosses the equator in a northward surface. Once entrained in the surface North Equatorial Counter Current, the water is advected eastwards and then northwards in the Ekman drift into the North Pacific subtropical gyre. At this stage the southern hemisphere characteristics of the flow have been obliterated by contact with the atmosphere. From the subtropical mixed layer the fluid is subducted into the North Pacific thermocline, and is advected southwestward to eventually join the Mindanao Current, and then leaves the Pacific south of Mindanao in the Throughflow. The salient feature of this rather complex pathway is that the cross-equatorial flow occurs in the surface layer where potential vorticity constraint may be broken by the constant buoyancy and momentum forcing of the atmosphere.

6.2.2 Global Thermohaline Circulation

The impression that emerges from this study is that the 'global conveyor belt' described by

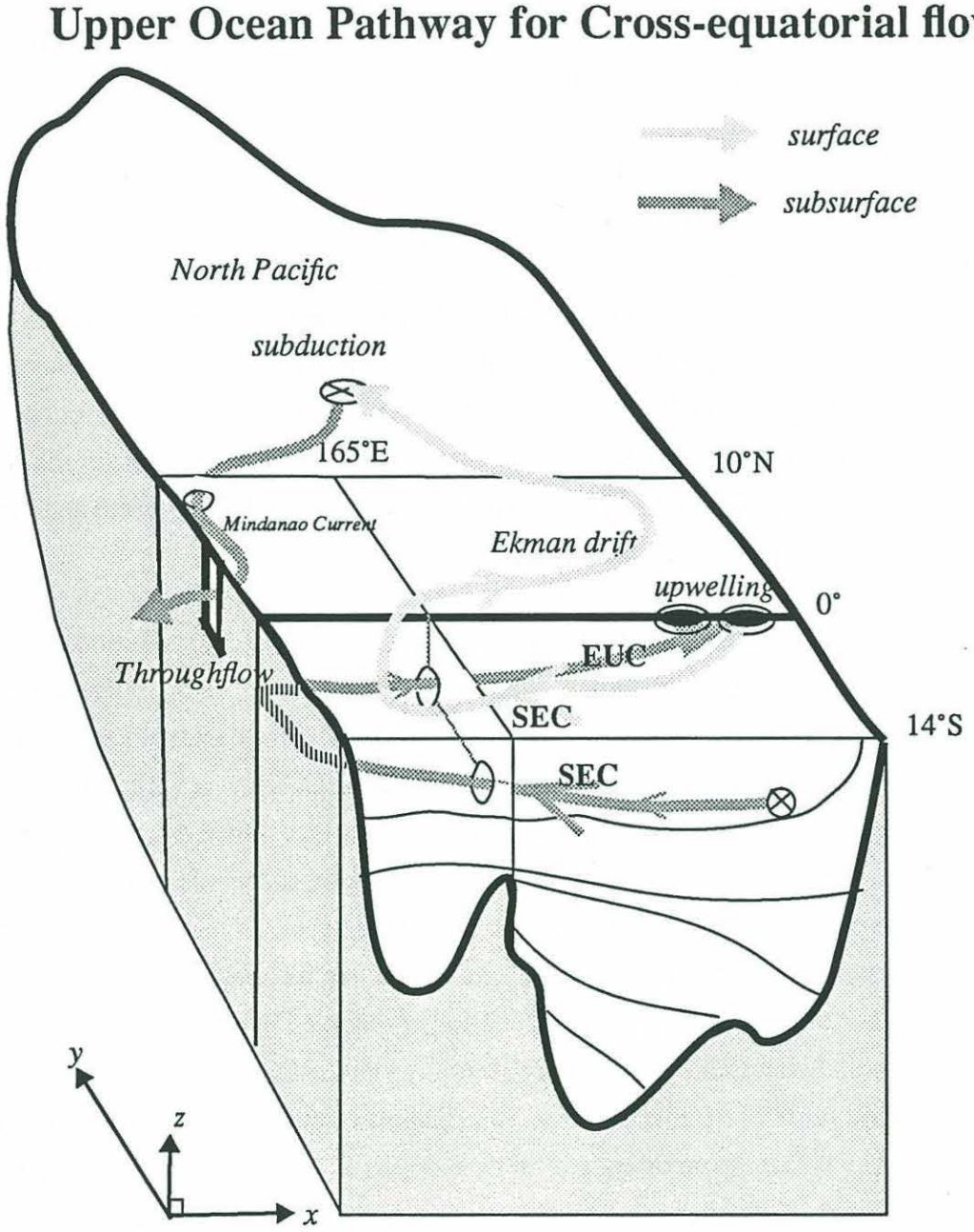

Figure 6.1 Schematic for the upper ocean pathway for cross-equatorial flow and supply of the Throughflow

Broecker (1991), based on Gordon's (1986) preferred warm-water pathway, is much weaker than first hypothesized. The role of the Pacific in Gordon's scenario is to convert large amounts of the bottom water that was formed in the Atlantic, into Pacific thermocline water. The thermocline water in this scheme could then flow out of the Pacific, through the Indonesian Passages into the Indian, and eventually reach the Atlantic Ocean and be able to supply the surface water consumed in the production of the North Atlantic Deep Water.

When combined with the results of Roemmich and McCallister (1989) and Wunsch, *et al.*, (1983), the analysis presented here reveals a much different scenario. Firstly, Gordon's large outflow of warm-fresh water to the Indian Ocean is missing in the present study. Rather, a modest Indonesian throughflow of about 5Sv or less is supplied by southern hemisphere thermocline water through a complex flow path involving the equatorial upwelling system and the tropical mixed layer. The Pacific basin would thus appear to play a more important role in that part of the global thermohaline circulation involving the recycling of Antarctic Bottom Water from the Southern Ocean.

References

Anderson, D. L. T., 1976: The low-level jet as a western boundary current, *Monthly Weather Review*, **104**, 907-921.

Anderson, D. L. T. and D. W. Moore, 1979: Cross-equatorial inertial jets with special relevance to very remote forcing of the Somali Current, *Deep-Sea Research*, **26**, 1-22.

Andrews, J. C. and S. Clegg, 1989: Coral Sea circulation and transport deduced from modal information models. *Deep-Sea Research*, **36**, 957-974.

Armi, L., 1979: Effects of variations in eddy diffusivity on property distributions in the oceans. *Journal of Marine Research*, **37**, 515-530.

Bahr, F., E. Firing and J. Songnian,1989: Acoustic Doppler Current Profiling in the Western Pacific during the US-PRC TOGA Cruises 2, 3 and 4. *Joint Institute for Marine and Atmospheric Research UH-NOAA Data Report* **005**.

Baumgartner, A. and E. Reichel, 1975: *The World Water Balance*. Elseiver, 179 pp.

Bingham, F. M. and R. Lukas, 1993: The southward intrusion of North Pacific Intermediate Water along the Mindanao Coast, subm. to *Journal of Physical Oceanography*.

Broecker, W. S., 1991: The Great Ocean Conveyor, *Oceanography*, **4**, 79-89.

Bryden, H. L. and E. C. Brady, 1985: Diagnostic model of the three-dimensional circulation in the upper equatorial Pacific Ocean, *Journal of Physical Oceanography*, **15**, 1255-1273.

Bryden, H. L., D. Roemmich and J. Church, 1991: Ocean heat transport across 24°N in the Pacific. *Deep-Sea Research*, 38, 297-324.

Chereskin, T. K. and D. Roemmich, 1991: A comparison of measured and wind-derived Ekman transport at 11°N in the Atlantic Ocean, *Journal of Physical Oceanography*, **21**, 869-878.

Church, J. A. and F. M. Boland, 1983: A permanent undercurrent adjacent to the Great Barrier Reef. *Journal of Physical Oceanography*, **13**, 1747-1749.

Church, J. A., 1987: East Australian Current adjacent to the Great Barrier Reef. *Aust. J. mar. Freshwat. Res.*, **38**, 671-683.

Coachman, L. K. and K. Aagaard, 1988: Transports through Bering Strait: Annual and interannual variability, *Journal of Geophysical Research*, **93**, 15 535-15 539.

Cook, M., L. Magnum, R. Millard, G. LaMontagne, S. Pu, J. Toole, Z. Wang, K. Yang and L. Zhao, 1990: Hydrographic observations from the US/PRC Cooperative Program in the western equatorial Pacific Ocean: Cruises 1-4. *Tech. Rep.* **WHOI-90-07**, Woods Hole Oceanographic Institution, 378 pp.

Craig, H., W. S. Broeker and D. Spencer, 1981: *GEOSECS Pacific Expedition, Volume 4, Sections and Profiles*. Sponsored by International Decade of Ocean Exploration, National Science Foundation, U. S. Government Printing Office, Washington D. C., 251 pp.

Delcroix, T., G. Eldin and C. Hénin, 1987: Upper ocean water masses and transports in the western tropical Pacific (165°E), *Journal of Physical Oceanography*, **17**, 2248-2262.

Delcroix, T. , G. Eldin, M. Radenac, J. Toole and E. Firing, 1992: Variation of the western equatorial Pacific Ocean, 1986-1988. *Journal of Geophysical Research*, **97**, 5423-5445.

EPIC Voyageurs, 1991: Hydrographic data from the 10°N transpacific cruise: RV *Moana Wave* Cruise #89-3,4,6. WHOI Technical Report # **WHOI-91-32.**

Efron, B. and G. Gong, 1983: A leisurely look at the bootstrap, the jackknife, and cross-validation. *American Statistician*, **37**, 36-48.

Eriksen, C. C., 1982: Geostrophic equatorial deep jets. *Journal of Marine Research*, **40** (supl.), 143-157.

Esbensen, S. K. and Y. Kushnir, 1981: The heat budget of the Global Ocean: an atlas based on estimates from marine surface observations. Climatic Research Institution, **Report 29**, Oregon State Univ., Corvallis, 27pp, 188 fig.

Ffield, A. and A. L. Gordon, 1992: Verticle mixing in the Indonesian thermocline, *Journal of Physical Oceanography*, 22, 184-195.

Fiadeiro, M. E. and G. Veronis, 1982: On the determination of absolute velocities in the ocean. *Journal of Geophysical Res. (Supl.)*, **40,** 159-182.

Fine, R. A., 1985: Direct evidence using tritium data for the through flow from the Pacific into the indian Ocean, *Nature*, **315,** 478-480.

Fine, R. A., W. H. Peterson, C. G. H. Rooth, and H. G. Ostlund, 1983: Cross-equatorial tracer tranportin the upper waters of the Pacific Ocean, *Journal of Geophysical Res.*, **88**, 763-769.

Fine, R. A., W. H. Peterson and H. G. Ostlund, 1987: The penetration of tritium into the Tropical Pacific, *Journal of Physical Oceanography,* **17,** 553-564.

Firing E., 1987: Deep zonal currents in the central equatorial Pacific. *Journal of Marine Research,* **45**, 791-812.

Firing, E., 1989: Mean zonal currents below 1500m near the equator, 159°W. *Journal of Geophysical Res.*, **94**, 2023-2028.

Firing, E. and J. M. Toole, 1991: Variability of low-latitude western pacific boundary currents, 1986-1991, Abs # 011A-3, *Eos Transactions*,**72.**

Gargett, A. E., 1984: Vertical eddy diffusivity in the ocean interior, *Journal of Marine Research,* **42**,359-393.

Garrett, C., 1979: Mixing in the ocean interior, *Dynamics of Atmospheres and Oceans*, **3**,239-265.

Garrett, C. J. R., and W. H. Munk, 1975: Space-time scales of intenal waves: a progress report. *Journal of Geophysical Research*, **80**, 291-297.

Godfrey, J.S., 1989: A Sverdrup model of the depth-integrated flow for the World Ocean allowing for island circulations. *Geophys. Astrophys. Fluid Dynamics*, **45,** 89-112.

Godfrey, J. S. and E. J. Lindstrom, 1989: The heat budget of the western equatorial Pacific surface mixed layer, *Journal of Geophysical Research*, **94**, 8007-8017.

Godfrey, J. S., M. Nunex, E. F. Bradley, P. A. Coppin, and E. J. Lindstrom, 1991: On the net surface heat flux into the western equatorial Pacific, *Journal of Geophysical Research*, **96** (suppl.),

3391-3400.

Goldenberg, S. B., and J. J. O'Brien, 1981: Time and space variability of tropical Pacific wind stress, *Monthly Weather Review*, **109**, 1190-1207.

Gordon, A. L., 1986: Interocean exchange of thermocline water, *Journal of Geophysical Research*, **91**, 5037-5046.

Gouriou, Y. and J. M. Toole, 1993: The mean circulation of the upper ocean in the western equatorial Pacific, *Journal of Geosphysical Research*, in press.

Harrison, D. E., 1989: On climatological monthly mean wind stress and wind stress curl fields over the world ocean, *Journal of Clim*ate, **2**, 57-70.

Hastenrath, S., 1980: Heat budget of the tropical ocean and atmosphere, *Journal of Physical Oceanography*, **10**, 159-170.

Hayes, S. P., 1982: A comparison of geostrophic nad measured velocities in the equatorial undercurrent. *Journal of Marine Research*, **40**, suppl. 219-229.

Hellerman, S. and M. Rosenstein, 1983: Normal monthly wind stress over the world ocean with error estimates, *Journal of Physical Oceanography*, **13**, 1093-1104.

Hsiung, J. 1985: Estimate of global ocean meridional heat transport, *Journal of Physical Oceanography*, **15**, 1405-1413.

Hogg, N., 1987: A least-squares fit of the advective-diffusive equations to Levitus Atlas data, *Journal of Marine Research*, **45**, 347-375.

Hogg, N., P. Biscaye, W. Gardner and W. J. Schmitz, Jr., 1982: On the transport and modification of Antarctic Bottom Water in the Vema Channel, *Journal of Physical Oceanography*, **40** (supl.), 231-263.

Huyer, A., M. Knoll, T. Paluszkiewicz and R L. Smith, 1991: The Peru Undercurrent: a study in variability, *Deep-Sea Research*, **38** (supl.), 247-271.

Johnson, G. C., 1990: Near-equatorial deep circulation in the Indian and Pacific Oceans. Ph.D. The-

sis. MIT/WHOI, WHOI-90-50.

Johnson, G. C and J. M. Toole, 1993: Flow of Deep and Bottom Waters in the Pacific at 10°N, *Deep-Sea Research*, **40**, No. 2, 371-394.

Joyce, T. M., 1988: Wind-driven cross-equatorial flow in the Pacific Ocean, *Journal of Physical Oceanography*, **19**, 19-24.

Kawase, M., 1987: Estalishment of deep ocean circulation driven by deep-water production, *Journal of Physical Oceanography*, **17**, 2294-2317.

Kawase, M., L. M. Rothstein, and S. R. Springer, 1992: Encounter of a deep western boundary current with the equator: a numerical spin-up experiment, *Journal of Geophysical Research*, **97**, 5447-5463.

Kessler, W. S., 1986: Observations of long Rossby waves in the northern tropical Pacific, *NOAA Technical Memorandum*, ERL PMEL-86, 169 pp.

Kessler, W. S. and B. A. Taft, 1987: Dynamic heights and zonal geostrphic transports in the central tropical Pacific during 1979-84, *Journal of Physical Oceanography*, **17**, 97-122.

Killworth, P. D., 1991: Cross-equatorial geostrophic adjustment, *Journal of Physical Oceanography*, **21**, 1581-1601.

Kubota, M. and K. Ono, 1992: Abyssal circulation model of the Philippine Sea, *Deep-Sea Research*, **29**, 1439-1452.

Lake, B., K. Yang, Z. Luizhi, R. Millard, S. Pu, J. Toole, Z. Wang and L. Mangum, 1991: Hydrographic observation from the US/PRC Cooperative Program in the western equatorial Pacific Ocean: Cruises 5-8. WHOI Technical Report # **WHOI-91-19**.

Landsteiner, M. C., M. J. McPhaden and J. Picaut, 1990: On the sensitivity of Sverdrup transport estimates to the specification of wind stress forcing in the tropical Pacific, *Journal of Geophysical Res.*, **95**, 1681-1691.

Levitus, S., 1982: Climatological atlas of the world ocean, *National Oceanic And Atmospheric Administration professional paper*, **13**.

Lindstrom, E., R. Lukas, R. Fine, E. Firing, S. Godfrey, G. Meyers and M. Tsuchiya., 1987: The Western Equatorial Pacific Ocean Circulation Study., *Nature*, **330,** 533-537.

Lukas, R. and E. Firing, 1984: The geostrophic balance of the Pacific Equatorial Undercurrent, *Deep-Sea Research*, **31**, 61-66.

Lukas, R., 1986: The termination of the Equatorial Undercurrent in the Eastern Pacific, *Prog. Oceanog.*, **16**, 63-90.

Lukas, R., 1988: Interannual fluctuations of the Mindanao Current inferred from sea level. *Journal of Geophysical Res.*, **93**, 6744-6748.

Lukas, R., E. Firing, P. Hacker, P. L. Richardson, C. A. Collins, R. Fine and R. Gammon, 1991: Observation of the Mindanao Current During the Western Equarorial Pacific Ocean Circulation Study, *Journal of Geophysical Res.*, **96**, 7089-7104.

Luyten, J. R. and J. C. Swallow, 1976: Equatorial undercurrents, *Deep-Sea Research*, **23**, 999-1001.

MacDonald, A. M. 1993: Property fluxes at 30°S and their implications for the Pacific-Indian throughflow and the global heat budget, *Journal of Geophysical Res.*, **98**, 6851-6868.

McCartney, M. S., 1982: The subtropical recirculation of Mode Waters, *Journal of Marine Research*, **40** (supl.), 427-464.

McCarty, M. E. and M. J. McPhaden, 1993: Mean seasonal cycles and interannual variations at 0°, 165°E during 1986-1992, NOAA Technical Memorandum ERL **PMEL-98**.

McDougall, T. J., 1984: The relative roles of diapycnal and isopycnal mixing on subsurface water mass conversion, *Journal of Physical Oceanography*, **14**, 1577-1589.

McDougall, T. J., 1991: Parameterizing mixing in inverse models, *Dynamics of Oceanic Internal Gravity Waves*, edited by P. Muller and D. Henderson, Proceedings of the sixth 'Aha Huliko'a Hawaiian Winter Workshop, University of Hawaii at Manao, 355-386.

McIntosh, P. C. and G. Veronis, 1992: Solving underdetermined tracer inverse problems by spatial smoothing and cross-validation, subm. *Journal of Physical Oceanography*

Magnum, L., J. Lynch, K. McTaggart, L. Stratton, and S. Hayes, 1991: CTD/02 data measuremetns collected on TEW (Transport of Equatorial Waters) cruise, June-August 1987, NOAA Data Report ERL PMEL-33.

Masumoto, Y. and T. Yamagata, 1991: Response of the western tropical Pacific to the asian winter monsoon: the generation of the Mindanao Dome, *Journal of Physical Oceanography*, **21**,1386-1398.

Menke, W., 1984: *Geophysical Data Analysis: Discrete Inverse Theory.* Academic Press, Florida, 260 pp.

Meyers, G., R. J. Bailey and A. P. Worby, 1993: Volume transport of the Indonesian Throughflow relative to 400db, submitted to *Nature*.

Muench, J., E. Kunze and E. Firing, 1993: The potential vorticity structure of the equatorial deep jets, subm. *Journal of Physical Oceanography.*

Munk, W. H., 1966: Abyssal recipes. *Deep Sea Research*, **13**, 707-730.

Nitani, H., 1972: Beginning of the Kuroshio. In: *Kuroshio, physical aspects of the Japan current*, H. Stommel and K. Yoshida, editors, University of Washington Press, pp. 129-163.

Nof, D., 1990: Why are some boundary currents blocked by the equator? *Deep Sea Research*, **37**, 853-874.

Oberhuber, J. M., 1988: An atlas based on the 'COADS' dat set: the budgets of heat, buoyancy and turbulent kinetic energy at the surface of the Global Ocean, **Report 15**, Max-Planck-Institute for Meteorology, Hamburg.

Pickard, G. L., J. R. Donguy, C. Henin, F. Rougerie, 1977: A review of the physical oceanography of the Great Barrier Reef and western Coral Sea. *Australian Institute of Marine Science Monograph Series #2.*

Piola, A. R. and A. L. Gordon, 1983: Pacific and Indian Ocean upper-layer salinity budget, *Journal of Physical Oceanography*, **14**, 747-753.

Polzin, K. L, 1992: Observation of turbulence, internal waves and background flows: an inquiry into

the relations between scales of motion, Ph. D. Thesis. MIT/WHOI, **WHOI-92-39.**

Polzin, K. L, J. Toole and R. Schmitt, 1993: Finescale parameterizations of turbulent dissipation, subm. *Journal of Physical Oceanography.*

Ponte, R V. , 1988: Observations and modelling of deep equatorial currents in the Central Pacific, Ph. D. Thesis. MIT/WHOI, **WHOI-88-9**

Quay, P. D., M. Stuiver and W. S. Broecker, 1983: Upwelling rates for the equatorial Pacific Ocean derived from the bomb ^{14}C distribution, *Journal of Marine Research*, **41**, 769-792.

Qui, B. and T. M. Joyce, 1992: Interannual variability in the mid- and low-latitude wesern North Pacific, *Journal of Physical Oceanography*, **22,** 1062-1079.

Rasmusson E. M. and T. H. Carpenter, 1982: Variations in tropical sea surface temperature and surface wind fields associated with the Southern Oscillation/El Niño, *Monthly Weather Review,* **110**, 354-384.

Reid, J. L., 1965: *Intermediate Waters of the Pacific Ocean*, The Johns Hopkins Oceanographic Studies, No. 2, The Johns Hopkins Press, Baltimore, 85 pp.

Reid, J. L., 1973: The shallow salinity minima of the Pacific Ocean, *Deep Sea Research*, **20**, 51-68.

Reid, J. L., 1981: On the mid-depth circulation of the World Ocean. In: *Evolution of Physical Oceanography-Scientific Surveys in Honor of Henry Stommel,* B. A. Warren and C. Wunsch, Eds., MIT Presss, 623 pp.

Reid, J. L., 1986: On the total geostrophic circulation of the South Pacific Ocean: flow patterns, tracers and transports. *Prog. Oceanog.*, **16**, 1-61.

Reid, J. L and A. W. Mantyla, 1978: On the mid-depth circulation of the North Pacific Ocean, *Journal of Physical Oceanography*, **8**, 946-951.

Ridgway, K. R and J. S. Godfrey, 1993: Mass and heat budgets in the East Australian Current: a direct approach, submitted to *Journal of Geophysical Research.*

Rintoul, S. R.,1991: South Atlantic interbasin exchange, *Journal of Geophysical Research*, **96,**

2675-2692.

Robinson, M. K., 1976: *Atlas of North Pacific Ocean Monthly Mean Temperatures and Mean salinities of the surface layer*, Naval Oceanogr. Office, Ref. Pub. 2, 173 figs.

Rochford, D. J., 1968: Origin and circulation of water types on the 26.00 sigma-t surface of the south-west Pacific. *Aust. J. mar. Freshwat. Res.*, **19**, 107-127.

Roemmich, D., 1980: The application of inverse methods to problems in ocean circulation, Ph. D. thesis, 287pp, MIT-WHOI Joint Program, Cambridge, Mass.,

Roemmich, D., 1983: The balance of geostrophic and Ekman transports in the tropical Atlantic Ocean, *Journal of Physical Oceanography*, **13**, 1534-1539.

Roemmich, D., and C. Wunsch, 1985: Two transatlantic sections: meridional circulation and heat flux in the subtropical North Atlantic Ocean. *Deep-Sea Research*, **32**, 619-664.

Roemmich, D. and T. McCallister, 1989: Large scale circulation of the North Pacific Ocean, *Progress in Oceanography*, **22**, 171-204.

Saunders, P. M., 1987: Flow through Discovery Gap, *Journal of Physical Oceanography*, **17**, 631-643.

Scully-Power, P. D.,1973: Coral Sea flow budgets in winter. *Aust. J. mar. Freshwat. Res.*, **24**, 203-215.

Semtner, A. J. and R. M. Chervin, 1992: Ocean general circulation from a global eddy-resolving model, *Journal of Geophysical Research*, **97**, 5493-5550.

Stommel, H. and A. B. Arons, 1960: On the abyssal circulation of the world ocean II. An idealized model of the circulation pattern and amplitude in oceanic basins. *Deep-Sea Research*, **6**, 217-233.

Sverdrup, H. U., 1947: Wind-driven currents in a baroclinic ocean; with application to the equatorial currents of the eastern Pacific. *Proceedings of the National Academy of Science on the U.S.A.*, **33**, 318-326.

Szoeke, de, R. A., 1987: On the wind-driven circulation of the South Pacific ocean, *Journal of Physical Oceanography*, **17**, 613-630.

Taft, B. A., S. P. Hayes, G. E. Frederich and L. A. Codispoti,1991: Flow of Abyssal Water into the Samoa Passage. *Deep Sea Research*, **38**, suppl., 103-128.

Talley, L. D., 1984: Meridional heat transport in the Pacific Ocean, *Journal of Physical Oceanography*, **18**, 89-106.

Talley, L. D., 1985: Ventilation of the subtropical North Pacific: the shallow salinity minimum, *Journal of Physical Oceanography*, **15**, 633-649.

Talley, L. D., 1991, An Okhotsk sea water anomaly: implications for ventilation in the North Pacific, *Deep Sea Research*, **38**, suppl., 171-190.

Tomczak, M. and D. Hao, 1989: Water masses in the thermocline of the Coral Sea, *Deep-Sea Research*, **36**, 1503-1514.

Toggweiler J.R. and B. Samuels, 1992: New Radio Carbon Constraints on the Upwelling of Abyssal Water to the Ocean's Surface. In: *The Global Carbon Cycle*, M. Heimann, ed. NATO ASI Series, Springer-Verlag, Berlin.

Toole, J. M., E. Zou and R. C. Millard, 1988: On the circulation of the upper waters in the western equatorial Pacific Ocean, *Deep Sea Research*, **35**, 1451-1482.

Toole, J. M., R. C. Millard, Z. Wang, and S. Pu, 1990: Observationsof the Pacific North Equatorial Current Bifurcation at the Philippine Coast, *Journal of Physical Oceanography*, **20**, 307-318.

Tsuchiya, M., 1968, Upper waters of the intertropical Pacific Oceans, The Johns Hopkins Oceanographic Studies, No. 4, The Johns Hopkins Press, Baltimore, 50 pp.

Tsuchiya, M., 1981: The origin of the Pacific Equatorial 13°C Water, *Journal of Physical Oceanography*, **11**, 794-812.

Tsuchiya, M., 1991: Flow path of the Antarctic Intermediate Water in the western equatorial South Pacific, *Deep Sea Research*, **38**, suppl., 273-280.

Tsuchiya, M., R. Lucas, R. Fine, E. Firing, and E. Lindstrom, 1989: Source Waters of the Pacific Equatorial Undercurrent. *Progress in Oceanography*, **23**, 101-147.

Uehara, K. and K. Taira, 1990: Deep hydrographic structure along 12°N and 13°N in the Philippine Sea. *Journal of the Oceanographical Society of Japan*, **46**, 167-176.

Warren, B. A., 1973: Transpacific hydrographic sections at Lats. 43°S and 28°S: The SCORPIO Expedition-II. Deep water. *Deep Sea Research*, **20**, 9-38.

Warren, B. A., 1981: Deep Circulation of the World Ocean. *Evolution of Physical Oceanography-Scientific Surveys in Honor of Henry Stommel*, B. A. Warren and C. Wunsch, Eds., MIT Presss, 623 pp.

Warren, B. A., 1983: Why is no deep water formed in the North Pacific?, *Journal of Marine Research*, **41**, 327-347.

Weare, B. C. and P. T. Strub and M. D. Samuel, 1981: Annual mean surface heat fluxes in the tropical Pacific Ocean, *Journal of Physical Oceanography*, **11**, 705-717.

Whitehead, J., 1989: Surges of Antarctic Bottom Water into the North Atlantic,*Journal of Physical Oceanography*, **19**, 853-861.

Wijffels, S. E., R. W. Schmitt, H. L. Bryden and A. Stigebrandt, 1992: Transport of freshwater by the oceans, *Journal of Physical Oceanography*, **22**, 155-162.

Worthington, L. V., 1981: The water masses of the world ocean: some results of a find-scale census. *In: Evolution of Physical Oceanography-Scientific Surveys in Honor of Henry Stommel*, B. A. Warren and C. Wunsch, Eds., MIT Presss, 623 pp.

Wunsch, C., 1978: The general circulation of the North Atlantic west of 50°W determined from inverse methods, *Reviews in Geophysics and Space Physics*, **16**, 583-620.

Wunsch, C., D. Hu, and B. Grant, 1983: Mass,heat and nutrient fluxes in the South Pacific Ocean, *Journal of Physical Oceanography*, **13**, 725-753.

Wyrtki, K, 1960: *Surface circulation in the Coral and Tasman Seas*. CSIRO Aust. Div. Fish. and Oceanogr. Tech. Pap. 8.

Wyrtki, K., 1961: Physical oceanography of the southeast Asian waters. *Naga Rep.*, **2**, 195pp.

Wyrtki, K., 1962: The subsurface water masses in the western South Pacific Ocean. *Aust. J. mar. Freshw. Res.*, **13**, 18-47.

Wyrtki, K., 1967: Circulation and water masses in the eastern equatorial Pacific Ocean. *International Journal of Oceanology and Liminology*, **1**, 117-147.

Wyrtki, K., 1987: Indonesian through flow and the associated pressure gradient,*Journal of Geophysical Research*, **92**, 12 941-12 946.

Wyrtki, K. and Kilonsky, 1982: Transequatorial water structure during the Hawaii to Tahaiti Shuttle Experiment, Univ. Hawaii, **HIG-77-1**, 65p.

Wyrtki, K. and B. Kilonsky, 1984: Mean water and current structure during the Hawaii-to-Tahiti shuttle experiment. *Journal of Physical Oceanography*, **14**, 242-254.

Appendix A

Intercalibration of Cruise Data

The data from the various cruises were compared for calibration consistancy. Differences in techniques, salinometer types and standards used on each cruise can result in salinity offsets between cruise data sets. In this study the MW893 data at 10°N was used as the standard against which the other cruises are calibrated.

In calibrating the 165°E cruise data, stations between 8 and 10°N were compared to the MW893 data near 165°E. The deep equatorial Pacific is very homogeneous and salinity offsets that are independent of temperature can only be due to a calibration problem. The data were visually inspected in Θ-S space for temperatures below 2°C, which brought the worst cases to our attention. In general, the Θ-S curves for different cruises would have the same slope, and differ by a constant offset. To quantify the offset, salinity differences were found on Θ surfaces colder than 2°C and a mean and standard deviation calculated. Typically, the standard deviation of the difference was 0.001 psu or less. If the mean offset was greater than 0.001, it was considered significant and an adjustment made to the cruise data, or cast (Table A.1).

There was no significant salinity offset at the join between the eastern and western legs of the TEW section. However, there was a significant offset between TEW3 and the MW893 data at 165°: 0.0067 psu. Since all the TEW data appeared internally consistant: i.e. TEW2 (both legs) and TEW3 have the same calibration, a salinity adjustment of 0.0067 was applied to the entire TEW data set. The effect of the adjustment was checked in the central Pacific by comparing the deep Θ-S curves in the deep western boundary current stations. The correction appears to increase the overlap between the MW893 data and TEW in the deep water (2°C - 1°C), which is desireable since this is known to be a well mixed water mass (Figure A.1).

Cruise	Stations	Offset	Notes
US/PRC 5	10°N	-0.003	This cruise had to be calibrated station by station, starting with adjustments towards the MW893 data in the north, and doing intercomparisons going south.
	8°N	-0.004	
	7°N	-0.004	
	6°N	-0.004	
	5°N	-0.004	
	0.5°N	+0.004	
	0.5°S	-0.002	
	1°S	-0.002	
	1.5°S	-0.002	
USPRC 6	10°N (1)	+0.014	first of two stations at 10°N
	8°S	-0.005	
	8.5°S	-0.005	
SURTROPAC 8	all	-0.018	same as was found Gouirou and Toole (subm)
PROPAC 1	all	-0.018	"
PROPAC 3	all	-0.034	entire TEW 14°S section adjusted
TEW	all	-0.007	

Table A.1 Salinity offsets (psu) applied to the cruise data to make it consistent with the MW893 cruise data. Offsets are *added* to the cruise data to correct the calibration differences.

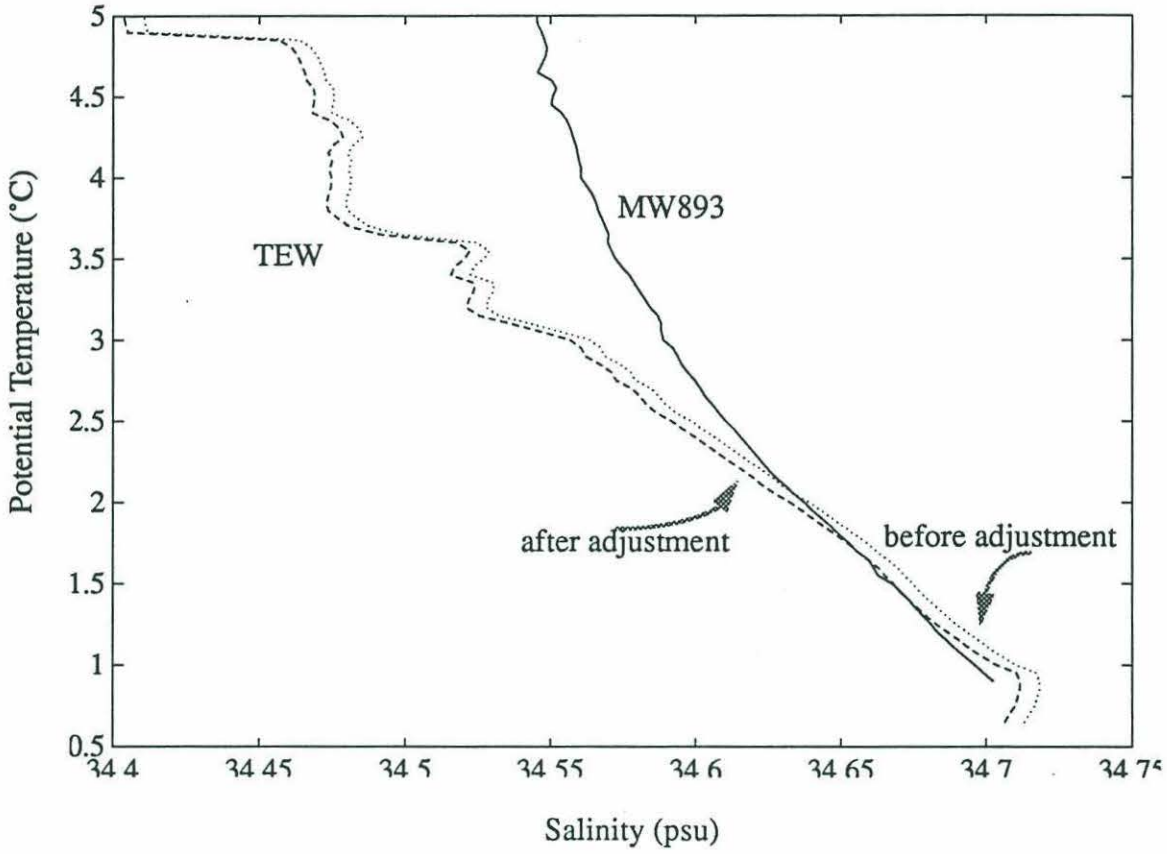

Figure A.1 Θ-S plots of casts in the deep western boundary currents along 10°N(MW893) and 14°S (TEW) The salinity adjustment made to the TEW data decreases the salinity difference between the sections in the deep water.

Appendix B

Repeat Surveys at 155°W: the Hawaii to Tahiti Shuttle

The repeat surveys made during the Hawaii to Tahiti Shuttle (HT) experiment allow the eastern box to be broken up into two smaller boxes around 155°W. Though the HT data only penetrate to 1000m, the mass budget can be closed by extending one of the results of the inverse model: that the vertical velocities in the eastern Pacific are small around 1000m. As shall be seen, the data themselves independently support this assumption.

The Hawaii to Tahiti Shuttle experiment was part of the NORPAX program and sampled the meridional section near 155°W almost continuously between January 1979 to June 1980. The data have been utilized in numerous studies of the equatorial circulation; for a detailed description of the data see Wytki and Kilonsky (1983). The ship sampled 0 to 10°N three times per transect, resulting in around 60 total station occupations for that latitude band (Wyrtki and Kilonsky, 1983). South of 4°S the number of station occupations drops to the number of cruises, which was 15. A mean section of 1° resolution between 9°N and 13°S was found by averaging on density surfaces as was done at 165°E. Cruises ranged in longitude between 150° and 158°W and were averaged together to form a section at roughly 155°W. Propeties in the upper 600m are shown in Figure B.1.

B.1 Reference Level Choice

Initially geostrophic velocities were found relative to 980 db, the common depth of sampling for most stations. Following the experience gained at 165°E, a shallower reference level of 500db was used between ± 5° for best representation of the EIC and SSCC's. In order to be able to include this section in an analysis of the thermocline mass budget, further adjustments were necessary.

Using the initial reference levels at 155°W, budgets for the middle thermocline box revealed large imbalances in the net thermocline mass budget, as well as in those layers most affected by the reference level issue: the low shear layers below the thermocline. Adjustments to the reference velocity at 155°W were found through a simple damped-least squares inverse. The constraints applied to the middle box were:

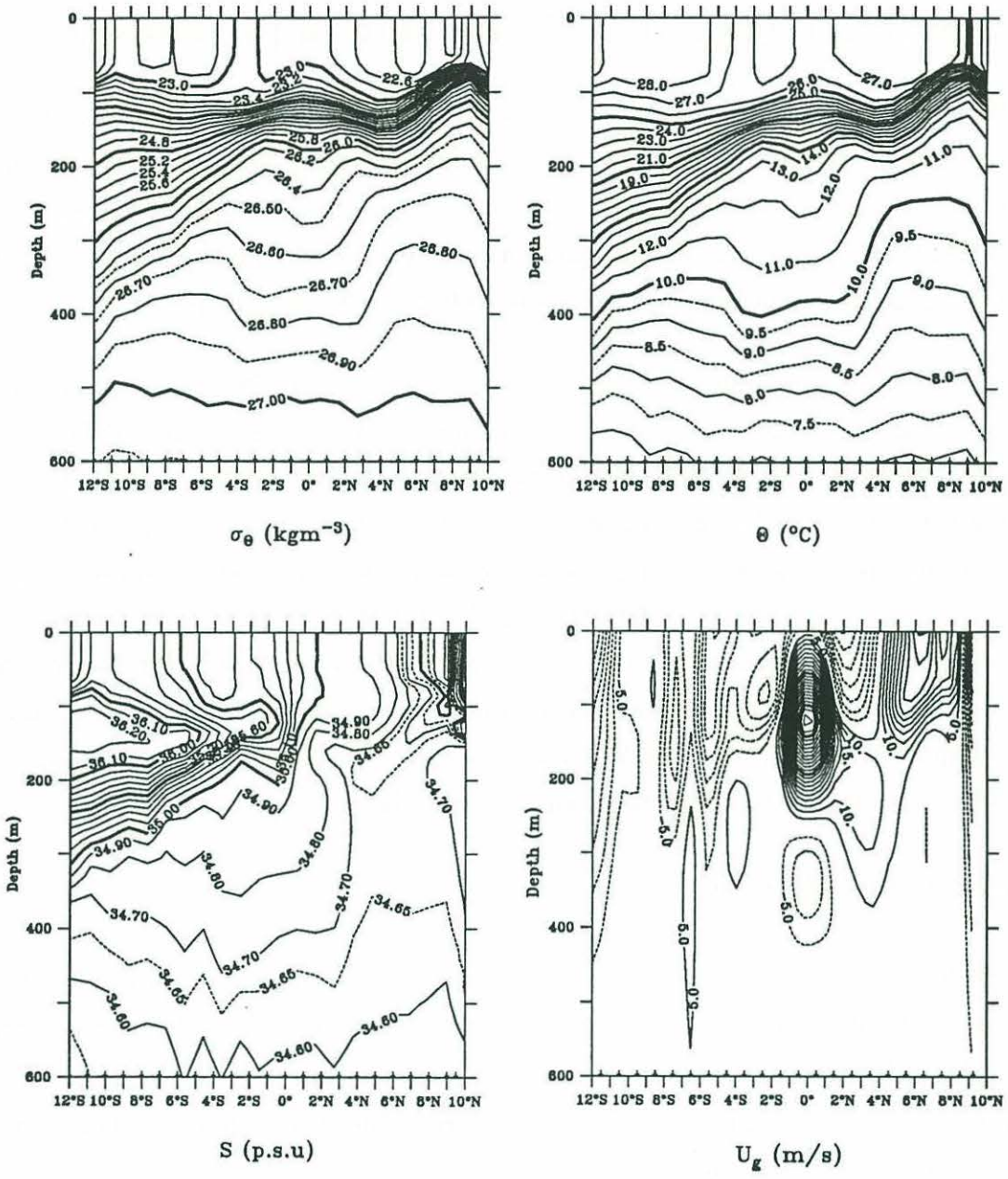

Figure B.1 Properities along a mean section at 155°W.

- total salt must be conserved above $\sigma_\Theta = 26.9$ (the first layer resolved by the 155°W data)
- total mass conserved in the two subthermocline layers defined by the surfaces $\sigma_\Theta = 26.2, 26.9$

These constraints implicitly assume that the net upwelling from below $\sigma\Theta = 26.9$ into the thermocline in the central Pacific is small, and that the subthermocline flow is nearly ideal. The assumptions are supported by tritium measurements in the equatorial Pacific which show that the dilution effect of equatorial upwelling is not seen for surfaces below $\sigma\Theta = 26.2$ (Fine, et al., 1993). Along these deep isopycnals tritium is fairly constant suggestive of a dominance of horizontal and not vertical exchange. In addition, the buoyancy-conserving model B1 diagnoses low mixing rates in the subthermocline layers over the large eastern volume, and one expects this to be true for its subvolumes.

The velocity adjustements at 1000db (except for ±2°) derived from the simple inverse for the middle box are reasonable being of order ~2cms^{-1} (Figure B.2), and have greatest impact on the transport in the subthermocline layers.

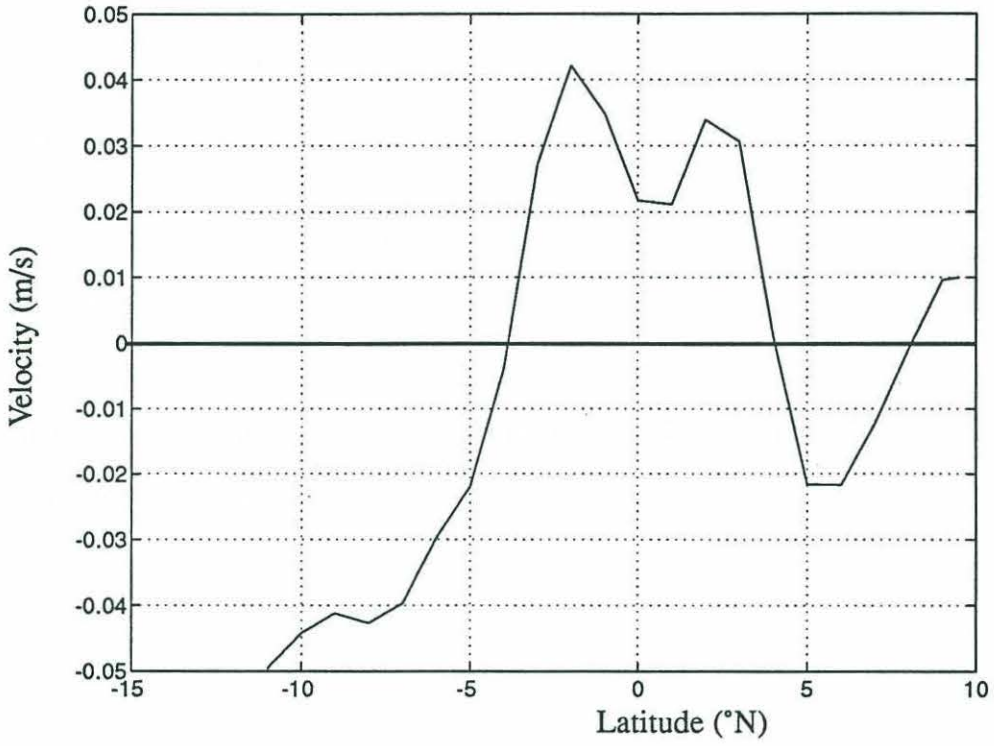

Figure B.2 Reference level velocity adjustments applied to the section at 155°W

Appendix C

Direct Observations of the Ekman Balance at 10°N in the Pacific

DIRECT OBSERVATIONS OF THE EKMAN BALANCE AT 10°N IN THE PACIFIC

Susan Wijffels
MIT-WHOI Joint Program in Oceanography
Woods Hole Oceanographic Institution
Woods Hole, Massachusetts 02543

Eric Firing
Department of Oceanography
University of Hawaii
Honolulu, Hawaii 96822W

Harry Bryden
Department of Physical Oceanography
Woods Hole Oceanographic Institution
Woods Hole, Massachusetts 02543

Submitted to the Journal of Physical Oceanography

Woods Hole Oceanographic Contribution Number:

ABSTRACT

The wind-driven Ekman transport and velocity structure are estimated from direct current measurements and geostrophic shears along a transpacific section at 10°N. The velocity field is dominated by the North Equatorial Current and its eddies, but near-inertial oscillations and an Ekman spiral are robust features of the shear. The ageostrophic component of shear averaged across the section can be approximated as a slab layer with a velocity of $5cms^{-1}$ in the top 30-40m, overlying a shear layer in which the velocity goes to zero below 80m. The zonally-integrated mass transport of this Ekman layer is 62 ($\pm$10) $x10^9 kgs^{-1}$ to the north, similar to the estimate of 52 ($\pm$10) $x10^9 kgs^{-1}$ based on winds measured from the ship. Climatological winds also yield similar transports. The zonally-averaged velocity relative to the velocity at the top of the thermocline forms a clockwise spiral, decaying with depth. As has been found at higher latitudes, this mean Ekman spiral results from diurnal cycling of the mixed layer.

INTRODUCTION

Ekman (1905) hypothesized a momentum balance for the flow in the surface layer of the ocean that is directly driven by the wind. If wind-stress is transported down into a barotopic water column to some finite depth by mixing processes and turbulence, then in a steady-state linear ocean, the boundary layer stress is balanced by the Coriolis acceleration in such a way that:

$$\int_{-\delta}^{0} \rho u dz = \frac{\tau}{f} \tag{25}$$

where τ is the wind-stress, ρ the water density, f the Coriolis parameter, **u** velocity to the right of the wind and δ the penetration depth of the wind-stress. This is the Ekman balance, and it is independent of the details of the mixing processes that maintain the boundary layer. If the turbulent stresses can be modeled as a diffusive process and the coefficient of eddy-viscosity is vertically uniform, the current structure associated with this balance is a smooth clockwise spiral with depth, with the surface velocity 45° to the right of the wind.

Though used routinely in models of the wind-driven ocean circulation, the Ekman balance has not been easily observed in the ocean. Those studies that have successfully confirmed the Ekman balance, such as Price, Weller and Pinkel (1986) and Price, Weller and Schudlich (1987), have relied upon data from long-term upper ocean moorings that were specially designed to measure the wind-driven shear. It was found that only by averaging such data over a few months could the Ekman balance be observed. The upper ocean often contains energetic near-inertial waves and eddies that can mask the shear associated with the local wind-driving.

Recently, Chereskin and Roemmich (1991) demonstrated the Ekman balance via direct measurements of the wind and near-surface currents along a transatlantic section at 11°N. Here, the methods of Chereskin and Roemmich (1991, hereafter CR) are applied to a transpacific hydrographic section also at 10°N. Besides testing the Ekman balance, we examine the structure of the wind-driven shear along the section and its relation to the stratification in the upper ocean.

THE DATA

A transpacific zonal hydrographic section near 10°N was taken from February 9 through May 10, 1989 on the RV MOANA WAVE. The section begins off the coast of Mindanao in the Philippines and ends in Costa Rica (Figure 1). Three data types are used in this study: ship winds, ship-mounted acoustic Doppler current profiles and CTD profiles.

1. Hydrographic Data

Hydrographic profiles are spaced along the section roughly every 90 km, though with closer spacing over continental margins and shallow topography. Eliminating test and calibration stations the 10°N section includes a total number of 213 stations. The data and their processing are described in EPIC Voyageurs (1991).

2. Wind Data

Ship-relative wind speed and direction were measured at 1 minute intervals throughout the cruise by the ship's anemometer mounted on the mast approximately 18m above sea-level. Heading from the ship's gyro compass was also recorded at 1 minute intervals. Wind speed and heading were low-pass filtered using a half power at 30 minutes, and then decimated to 15 minute samples. The anemometer measured wind direction relative to the ship's heading, and so the relative wind direction from north was found by adding the heading to the anemometer wind direction. Wind speed and direction over the ground were obtained by vector addition of the ship velocity as determined from the Doppler data reduction procedure described below.

Our first estimate of wind velocity over the ground was coherent with the ship's velocity at the 8 hour period of station work. The coherence was due to an angle offset between the coordinate frame in which the relative winds were measured and that in which the ship's motion was measured. By comparing the relative wind just before and after the ship accelerated and decelerated coming on and off station, the offset angle could be estimated for each leg, and the relative wind series rotated to account for the offset. For legs 1, 2 and 3, the angle offset was 16.5°, 8.1° and 16.6° respectively.

Leg Number	Leg Name	Start Date	End Date	# Days	CTD Stations
1	MW8903	02/06/89	03/05/89	19	1-83
2	MW8904	03/09/89	03/24/89	15	84-119
3	MW8906	04/02/89	05/10/89	34	120-221

Table 1

Details of the 3 legs of the 10°N transpacific hydrographic section. The "number of days" column refers to the subset of data used in the analysis i.e. excluding the transit time to and from the first and last hydrographic station for each leg.

The calibration procedure also indicated that the wind amplitude is not biased and that wind-speed is accurate to within 5%. The corrected time series of wind over the ground was not coherent with the ship's motion, indicating that the angle bias had been successfully removed. The source of the angle offsets is not known, nor the reason for the change in the bias angle for the middle leg.

Excepting the first and last few days, the winds are consistently blowing from the north-east at about $8ms^{-1}$ over the 3 months of the cruise (Figure 2). Wind-stress was calculated using the bulk formulae of Large and Pond (1981) assuming neutral stability in the atmospheric boundary layer. A comparison with climatologies shows that the ship winds are typical of average conditions for the months of the cruise (Figure 3).

3. Acoustic Doppler Current Profiler Data

Currents were measured with a shipboard acoustic Doppler current profiler (ADCP) made by RD Instruments, operating at 153.6 kHz (Model VM-150). The transmitted pulse sampled 16 m in the vertical and the returns were processed in time ranges corresponding nominally to 8 m in the vertical; each depth bin thus sampled a 24 m depth range, with uniform weight given to the middle 8 m. Successive bins are correlated by 40%, every other bin by only 5%. The center of the first bin was at 20 m. The sampling rate was slightly less than once per second, and the individual profiles were vector-averaged in 5-minute ensembles. The ship's gyrocompass was used to rotate each profile into earth coordinates before averaging; pitch and roll were not measured and hence were approximated as zero.

One of the four ADCP transducer beams failed two thirds of the way through leg 1, causing a 30-hour gap. For the remainder of leg 1 and all of leg 2, currents were measured using only the 3 operative beams. After leg 2 the transducer was replaced, so all 4 beams were used throughout leg 3. We found no indications of significant error from using 3 beams instead of 4.

The ADCP measurements were processed as described by Bahr *et al* (1989) and Firing (1991); a brief outline follows. Satellite fixes were provided at irregular intervals, typically 1-2 hours, by a dual-channel Transit receiver, with the ADCP serving as a speed log. GPS fixes were recorded at the end of each 5-minute ADCP averaging interval when available, varying from 5 to 10 hours per day. After editing, both the Transit and the GPS fixes were used to calculate the velocity of the ship. This was added to the ADCP measurement of the water velocity relative to the ship averaged over a reference layer to give a raw estimate of the absolute velocity of the reference layer. This reference layer velocity was then low-pass filtered (half power at 2.5 hours period) before being used for a final estimate of the ship's velocity, and hence of the absolute water velocity profiles.

The transducer was calibrated for angular offset and scale factor on each leg using the procedure

just described for the wind measurements (Joyce, 1989; Pollard and Read, 1989). Only the station arrivals and departures with GPS coverage could be used. For legs 1 and 2 the ADCP velocities were scaled by 1.01 and rotated by a constant angle. For leg 3, with a different transducer and orientation, the scale factors (0.995) and the angular offset were calculated independently. All of the analysis in this paper is based on velocities relative to some reference level, which are much less sensitive to calibration than are absolute velocity estimates.

Like the wind measurements, the ADCP velocity profiles were low-pass filtered in time (half power at 30 minutes period) and sub-sampled at 15-minute intervals. Nominal depths were corrected using sound speed profiles calculated from nearby CTD profiles, and the velocities were then interpolated to integral multiples of 10 m. Data from the region of strong currents near the western boundary, from the Philippine coast at 126°E to 130°E, were excluded from the analysis.

Much of the velocity variance along the section is uniform through the upper 100 m or so; currents at 20 m and 100 m are very similar, with slightly decreased amplitude at 100 m (Figure 4). The shear between 20 and 100 m is dominated by a near-inertial peak in the clockwise rotary spectrum (Figure 5). Between 20 and 30 m there is no inertial peak but there is a strong diurnal peak, primarily in the zonal component. This diurnal energy decreases rapidly with depth and is not significant below about 60 m.

The prominence of the inertial and diurnal peaks in these spectra indicates that their associated phenomena must have large zonal scales. The average ship speed was 2.5 ms^{-1}, so the near-inertial motions, with a period of 72.5 hours at 9.5°N, must have zonal wave-numbers much smaller than $2\pi/650$ km. If the inertial oscillations are excited by changes in the wind-stress, then the zonal wavenumber of the oscillations should roughly match that of the wind variability on a time scale of hours to days. We will argue that the diurnal variability in the shear is phase-locked to the sun, so its zonal wave-number is $2\pi/6300$ km.

THE EKMAN TRANSPORT

To test the Ekman balance, we want to compare a directly measured estimate of the net cross-track wind-driven mass flux with that predicted by the winds. A cross-track ageostrophic velocity was calculated as the difference between the ADCP velocity and the geostrophic estimate. The ADCP profiles were averaged during each transit between adjacent stations, neglecting on-station profiles. Above 20 m, the center of the shallowest ADCP bin, the velocity was assumed constant. Cross-track geostrophic velocity was also calculated between adjacent stations, and then referenced to the corresponding ADCP velocity at 150 m. Averaged across the section, the geostrophic velocity is about 1.8 cms^{-1} southward in the upper 35 m, decreasing roughly linearly to less than 0.5 cms^{-1} at 200 m (Figure 6). The averaged ADCP velocity decreases from about 3.2 cms^{-1} northward in the upper 40

m to zero at 100 m. The section-averaged ageostrophic velocity, presumed to be primarily Ekman flow, is therefore about 5 cms^{-1} to the north near the surface, and drops rapidly between 40 and 90 m.

Comparing the ageostrophic velocity profile at 10°N in the Pacific with that determined by CR for 11°N in the Atlantic: the depth of penetration of the ageostrophic shear is the same, roughly 100m; the magnitude of the near surface Ekman velocity is also similar (5 cms^{-1} at 20m, compared with 4 cms^{-1} in the Atlantic); most significant, though is the difference in the character of the section mean ageostrophic shear near the surface. The mean profile in the Pacific features a slab between 20 and 40m (3 ADCP bins), while the Atlantic profile has linear shear to the shallowest depth bin. There was little mean shear below the first ADCP depth bin in the Pacific, so linearly extrapolating the ADCP data to the surface gave results similar to the assumption of constant velocity.

1. Direct Estimate of the Ekman Transport

A direct estimate of the net ageostrophic mass flux across the section is calculated by integrating each profile of ageostrophic velocity (V_E) vertically and then zonally:

$$M_{EK} = \int_{86°W}^{130°E} \int_{-\delta}^{0} \rho V_E dz dx. \tag{26}$$

The depth of penetration of the wind-driven flow, δ is chosen as 80m, the shallowest depth at which the section average ageostrophic velocity becomes less than its standard error. This yields our best estimate of the Ekman transport, 61.8 x $10^9 kgs^{-1}$. Integrating down to 100m or to the reference level (150m) yields alternative estimates of 66.4 and 71.1 x$10^9 kgs^{-1}$, respectively.

2. Wind-based Estimate

From the Ekman balance (1) the predicted net Ekman flux across the section was calculated from the observed winds. Ship winds were binned and averaged every 2° of longitude and the net Ekman transport integrated across the section. The western boundary region, missing from the direct estimate is included in the wind estimate, but contributes relatively little to the section total. The net Ekman mass transport across the section predicted by ship winds is 52.5 ± 10 x $10^9 kgs^{-1}$. Estimates based upon the climatological winds were also found (Table 2).

There is good agreement between the directly-measured and wind-based estimates of the total Ekman mass flux across the section. In addition, the direct and wind-based estimates have a similar horizontal structure (Figure 7). Stronger zonal winds in mid-basin cause an increase in the rate of accumulation of the Ekman flux as one sums the station ageostrophic transports across the section. This structure is typical of the Trade Wind regime, and was also seen in the Atlantic by CR. Steeper slopes in Figure 7 indicate stronger winds in the wind-based estimates, and deeper integration

depths in the direct estimates.

3. Errors

In calculating the random error in the direct estimate, we follow the method of CR. The independent length scale is assumed to be 600km: the time the ship travels in one inertial period. The section is divided into 14 pieces 600km long and estimates of the ageostrophic mass flux are made for each piece. Since the winds are fairly steady we expect the variability in the estimates to predominately reflect near-inertial motions. The standard deviation of the estimates is 2.5 x $10^9 kgs^{-1}$ and so the standard error for the total section, which is 14 times longer, is 10 x $10^9 kgs^{-1}$. From Figure 7, however, it appears that the random errors may be smaller. The 'wiggles' in the accumulated directly measured flux are probably also a good indicator of the size of the random error, and these have amplitudes of about 5 x $10^9 kgs^{-1}$. More serious than the random error are the questions of how deep to integrate the ageostrophic shear in order to capture all of the wind-driven mass flux, and at which level the geostrophic and ADCP velocities are set equal. To find a range of transports, reference levels were varied between 120m and 180m, and integration depths between 80m and the reference depth. The resulting extrema of the cross track ageostrophic flux are 51.9 and 70.2 x $10^9 kgs^{-1}$ (120m reference level integrated to 80m; and an 180m reference level and integration depth, respectively). Reference levels above 120m have a rapidly decreasing total, as do integration depths above 80m, indicating that these choices are too shallow to capture all of the wind-driven shear. Our best estimate of 61.8± 10 x $10^9 kgs^{-1}$ encompasses all reasonable values for the directly measured wind-driven mass flux across the section.

The error in the ship wind measurements depends upon the calibration of the ship's anemometer and how well the absolute winds are determined by removing the ship's motion. We found that the angle correction described earlier has the largest impact on the wind-stress calculated from the ship winds. The standard error of the angle adjustment was about 1.5^o in all 3 legs. Based upon a mean wind direction of 225^o True, this angle error translates into an error in the east component of wind-stress of 0.01 Pa. Since such an error would appear as a bias, applying this to the section length results in an error of ± 10 x $10^9 kgs^{-1}$.

It is difficult to decide upon a reasonable error estimate for the wind climatologies, given the complexities of differing data sets, treatments and stress algorithms. Harrison (1989) states that the Hellerman-Rosenstein climatology over-estimates wind-stress by 30%. Böning, *et al* (1991) compare the Hellerman-Rosenstein and the more recent Isemer-Hasse climatologies over the Atlantic and conclude that the Hellerman-Rosenstein climatology may be significantly *under-estimating* the wind-stress in the Trade Wind regions (by 50%!). Here we have simply assumed a random error of 30% for the wind climatologies.

Direct Estimates:	Σ 80m	**61.8**± 10
	Σ 100m	66.4
	Σ 150m (ref. level)	71.1
	MLD	35.6
	TTC	50.8
Wind-based Estimates:	Ship winds	**52.5** ± 10
	HR (cruise months)	67.8 ± 20
	FSU (cruise months)	61.2 ± 18
	FSU (annual mean)	37.4 ± 11

Table 2

Estimates of the net Ekman mass flux across the section and associated standard errors. Errors for the direct and *in situ* wind based estimates are explained in the text. A 30% error was assumed for the wind-climatologies. Units are in $10^9 kgs^{-1}$. The estimates considered 'best' are in bold-face.

THE VERTICAL STRUCTURE OF THE WIND-DRIVEN FLOW

The good agreement between the directly-measured and wind-based prediction of the Ekman mass flux suggests that the wind-driven shear has been successfully isolated by combining the ADCP and hydrographic data. We now examine the vertical structure of the wind-driven shear in the data.

Ekman used a constant eddy diffusivity of momentum to model the downward mixing of the surface wind-stress. This produced a velocity profile that smoothly decays with depth. However, observations from both moorings and laboratory experiments suggest that turbulent overturning driven by the wind and surface wave field homogenizes momentum and density in the upper ocean, forming a mixed layer. In the mixed layer velocity is expected to be constant; the layer acts as a slab, with a region of high shear at its base.

CR investigated the vertical penetration of the Ekman velocity relative to the mixed-layer depth in the Atlantic. They defined the bottom of the mixed layer as the depth at which the temperature differed from that at 6db by 1.0°C. An ageostrophic transport was then found for each increment of 1/10th of a mixed layer depth, and the result integrated across the section. In contrast to a slab response in which no shear is expected between the surface and one mixed layer depth, CR's profile features strong shear between 0.5 and 1.2 mixed layer depths. They repeated the calculation using a temperature difference of 0.1°C, and found a similar result. CR then concluded that a slab model for velocity in the mixed layer was not appropriate along 11°N in the Atlantic, and that significant shear exists in the mixed layer.

Using the transpacific data, we have repeated the calculations done by CR and similar profiles result, which appeared to confirm their findings. However, the lack of a slab layer seemed at odds with other observations of upper ocean shear (Price, *et al*, 1986), and the notion of turbulent overturning in the mixed layer. Furthermore, we had noticed that individual profiles of the ADCP data along the transpacific section often contained a layer of very weak shear near the surface, with strong shear below, suggesting the existence of a slab layer (Figure 8).

Did the definition of the mixed layer used by CR really capture the depth at which the active wind-driven turbulence ceased? Price *et al* (1986) found that a temperature difference of 0.1°C (which corresponds to a density change of $0.023 kgm^{-3}$) can have a profound effect on the structure of the wind-driven flow. We therefore tried a more stringent definition of the mixed layer depth (MLD), and used the depth at which the density differs from that at the surface by $0.01\ kgm^{-3}$. This criterion was determined by Schneider and Müller (1990) as the best MLD indicator in a study of the mixed layer variability in the Hawaii to Tahiti Shuttle data near 150°W. A second depth, which we call the top of the thermocline (TTC) is the shallowest depth at which the density *gradient* is greater than or equal to $0.01\ kgm^{-4}$. The hydrographic data allowed us to estimate the MLD and TTC approximately every 8 hours (Figure 9). Across the section, the MLD (open circles) falls randomly between the surface and the TTC; both shoal in the eastern part of the section. Note that the TTC is less variable from station to station than the MLD. The definitions of mixed layer depth used by CR fall closer to the TTC than to the MLD along our section.

To test for the existence of a slab layer above our new mixed layer depth, the ageostrophic velocity profile between each pair of hydrographic stations was normalized in depth by the average MLD at the two stations, and then averaged over the section (Figure 10). A low shear layer, a slab, is indeed found in the top 0.9 MLD of the profile. Repeating the calculation with the TTC in place of the MLD gave a slab above 0.4TTC and a high shear region from there to 1.2TTC. These profiles were not significantly altered by the assumption of linear shear in the upper 20m, nor by halving or doubling the critical mixed layer gradient or density values. In particular, the TTC is extremely well defined

along the section.

Instead of there being of a thin layer of high shear at the base of the mixed layer, our observations show shear penetrating downwards at least another MLD. At 30°N, Price *et al*, (1986, hereafter PWP) observed a thick layer of shear below the slab layer; they named it the transition layer. To model the transition layer PWP invoked gradient Richardson Number mixing. They concluded that in the slab layer turbulence is strong, homogenizing both density and velocity, while in the transition layer, shear instability further mixes the wind's momentum into the stratified water column. Along the transpacific section, integration of the ageostrophic shear to the MLD only captures about two thirds of the wind-driven mass transport (Table 2), indicating that the stress at the base of the mixed layer is about one third of the wind-stress. The transition layer carries a large part of the Ekman mass flux, and absorbs much of the winds momentum.

THE DIURNAL CYCLE

The profound effect of stratification on the structure of the wind-driven shear was demonstrated by PWP through observations of the diurnal heating cycle. Due to the buoyancy input by solar insolation, the mixed layer was found to cycle daily, from deepest at sunrise to shallowest in mid-afternoon after the maximum heating had taken place. The velocity slab-layer was also observed to follow this cycle.

Along the transpacific section, we averaged mixed layer depth in 2 hour bins of local time of day to produce a section mean diurnal cycle (Figure 11). Each bin has about 20 profiles in it, and the standard error is about 6m for each bin. The mean mixed layer depth is 37m. A well defined diurnal cycle is apparent with a peak to trough excursion of 30m, shoaling to a minimum of 20m around midday and deepening to 50m at night. Schneider and Müller (1990) found a mean mixed layer depth at 10°N, 150°W of 40m with a diurnal peak to trough variation of 30m, consonant with our results. The ubiquity of diurnal cycling is apparent. Schneider and Müller (1990) observed it at all latitudes between Hawaii and Tahiti near 150°W, and we observe it at 10°N across the entire Pacific basin.

Further evidence for diurnal cycling along the 10°N section is the 24 hour peak found in the 20-30m shear spectra (Figure 5). This peak is present on all three legs. When the mixed layer shoals during the morning due to solar heating, the wind's momentum becomes trapped in a thin surface layer and the currents are accelerated downwind as a jet (Price *et al*, 1986). Along the transpacific section most of the 24 hour energy is in the east-west component of velocity which is dominantly in the downwind direction. In addition, the diurnal peak disappears below 60m consonant with the diurnal cycle depth in Figure 11. We believe that this surface trapped diurnal energy is an expression of the 'diurnal jet'. As a further check, the depth at which the ageostrophic velocity differed from that at

20m by 5cms^{-1} was found at each station pair. From station to station, this depth is highly correlated with the MLD (correlation coefficient of 0.88) and also displays a diurnal cycle (Figure 11).

DIURNAL-CYCLE SPIRAL

A fascinating result of the work of PWP and Price, Weller and Schudlich (1987) was that despite the presence of a slab-like velocity layer in the upper ocean at any given moment, the averaged current structure turned out to be a smooth spiral qualitatively similar to that predicted by Ekman. PWP named this spiral the 'diurnal-cycle spiral' since its existence depends upon the cycling of slab-layer thickness.

To determine a mean Ekman spiral in our ADCP data, we first subtracted the velocity at a reference depth. This removed most of the geostrophic current, which is relatively independent of depth above our chosen reference level. The relative velocity profiles, together with the wind vectors, were then averaged over successive inertial periods to suppress the energetic near-inertial oscillations. Following Price, Weller and Schudlich (1987), the ocean velocities were rotated into a crosswind-downwind coordinate system. The resulting wind-relative velocity profiles were then averaged over each cruise leg. Since no ADCP data are available above the shallowest Doppler depth bin (20m), a constant velocity slab layer was assumed in the upper 20m. The crosswind and downwind transports relative to the reference layer were found by integrating the profiles vertically.

Before discussing the results, we first point out that choosing the reference depth is of considerable importance in this calculation. Along 10°N, the thermocline is shallow (200m in the west rising to 50m in the east), and it supports the strong westward shear of the North Equatorial Current (NEC). Unlike the shear due to near-inertial waves, the shear of the NEC does not average out over large spatial scales. To exclude the NEC shear, a reference level must be chosen above the thermocline. Further guidance for picking a reference level came from comparing the resulting downwind and crosswind transports for each reference level choice. We used the depth at which the downwind transport was a minimum, resulting in reference levels of 90m, 70m and 70m for legs 1, 2 and 3 respectively. These depths coincide roughly with the top of the thermocline calculated from the CTD data and so must exclude most of the NEC shear.

For each leg the wind-relative currents rotate clockwise with depth with a smoothly decreasing amplitude (Figure 12). As found by Price, Weller and Schudlich (1987), the spirals appear 'flat': compared to Ekman's spirals they decay faster in amplitude than they rotate with depth. The agreement between the predicted and observed Ekman transports is fair (Table 3). Crosswind transports agree within 25% and downwind transports are less than the standard error in all but the last leg (MW8906) where the MLD and TTC were very shallow. Here the calculation was severely hampered by the lack of data in the upper 20m.

DISCUSSION AND CONCLUSIONS

Directly measured currents along the 10°N transpacific section include several distinct phenomena in the upper 250 m. The depth-averaged flow is dominated by the North Equatorial Current and its geostrophic eddies. The shear, on the other hand, is largely ageostrophic, composed of strong near-inertial oscillations superimposed upon a persistent Ekman flow. Averaging the ageostrophic northward velocity component along the section removes most of the near-inertial signal, permitting a direct calculation of the Ekman mass flux. Our best estimate, $62\pm10 \times 10^9 kgs^{-1}$, is in good agreement with the estimate of $52\pm10 \times 10^9 kgs^{-1}$ based on winds measured from the ship. Estimates from climatological winds are similar as well.

The vertical structure of the Ekman layer at 10°N in the Pacific is similar to that found at 11°N in the Atlantic by CR and at 30°N by PWP. A surface slab layer overlies a sheared transition layer of similar thickness. The diurnal cycle of buoyancy flux leads to a diurnal cycle in the depth of the mixed layer and of the surface current. The average over many such cycles yields a "flat" Ekman spiral, with a shorter depth scale for amplitude decay than for rotation (Price, Weller, and Schudlich, 1987). The diurnal cycle can be seen only with a stringent definition of MLD, such as that proposed by Schneider and Müller (1990). The definition of MLD also determines whether one interprets the transition layer shear as occurring in or below the mixed layer. The conclusion reached by CR, that the slab model is inappropriate at 11°N in the Atlantic, appears to rest on their less stringent definition of MLD. Their MLD is more similar to our TTC; and we find almost all of the ageostrophic velocity, transition layer and slab layer alike, above this TTC.

Our findings differ from CR's in one important respect. They found the average temperature of the

Table 3

Time mean estimates of directly observed cross-wind and down-wind transport in the current spirals of Figure 11, and the corresponding wind-based estimate. Errors shown are the standard errors. Degrees of freedom (dof) are defined as the number of inertial periods in the record for each leg, and the error at the 95% level (based upon at Student's-t distribution) is obtained by multiplying the standard error by 1.89, 1.94 and 0.57 for a903, a904 and a906 respectively.

Ekman Transport: (m^2s^{-1})	Observed M_e^x	e_x	Wind-based M_e^y	e_y	M_e^τ	e_τ
a903 (6 dof)	**3.46**	± 1.12	0.36	± 0.38	**4.83**	± 0.88
a904 (5 dof)	**2.67**	0.33	-0.13	0.25	**3.80**	0.26
a906 (10 dof)	**3.22**	1.35	1.24	0.60	**2.97**	0.41

Ekman transport in the Atlantic to be 1°C colder than the surface temperature; we find 80% of the transport at temperatures within 0.1C of the surface temperature, and all of it within 0.2C of the surface. In our data set, therefore, approximating the temperature of the Ekman transport as the sea surface temperature causes negligible error in the heat flux. We cannot explain this discrepancy between our results and CR's, and are reluctant to attribute it to differences between physical processes in the two oceans. Perhaps statistical uncertainty is a significant factor. Because the transpacific section is four times longer than the transatlantic section, we expect averages of the former to provide more reliable estimates.

Acknowledgments

The transpacific hydrographic section was supported in its entirety by the National Science Foundation (NSF). The CTD and ADCP measurements used in this work were supported under NSF Grant OCE87-6910. We are especially appreciative of Esther Brady's help in organizing the cruise and in supervising the ADCP data acquisition at sea. We would like to thank: Frank Bahr and Willa Zhu for processing the ADCP data; John Toole and Rebecca Schudlich for their comments and helpful discussion; and Laura Praderio for help in editing the manuscript. SW was supported by a NASA Graduate Student Fellowship in Global Change and HLB was supported by the National Science Foundation under Grants OCE87-16910 and OCE91-04211.

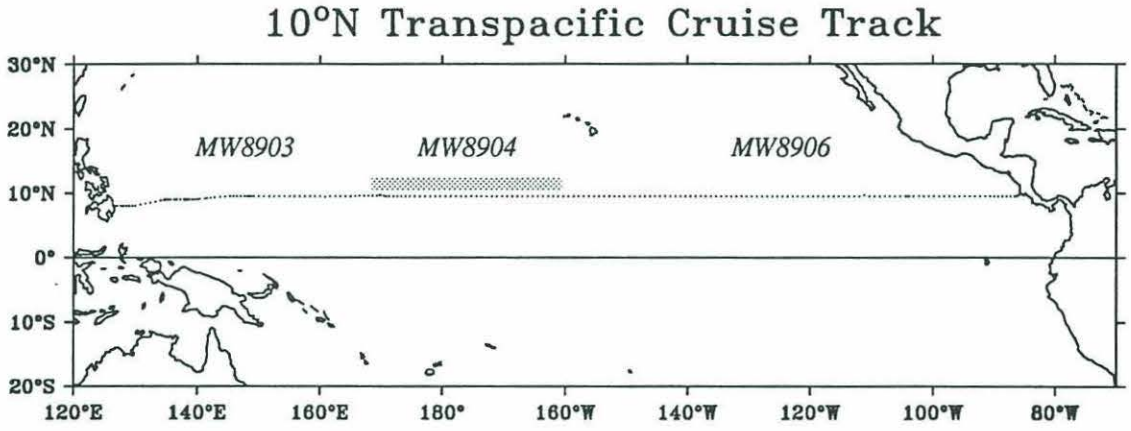

Figure 1

Positions of the hydrographic stations along the 10°N transpacific section. The section was taken in 3 legs from west to east. The middle leg goes from 171°E to 158°W, and is shaded in the figure.

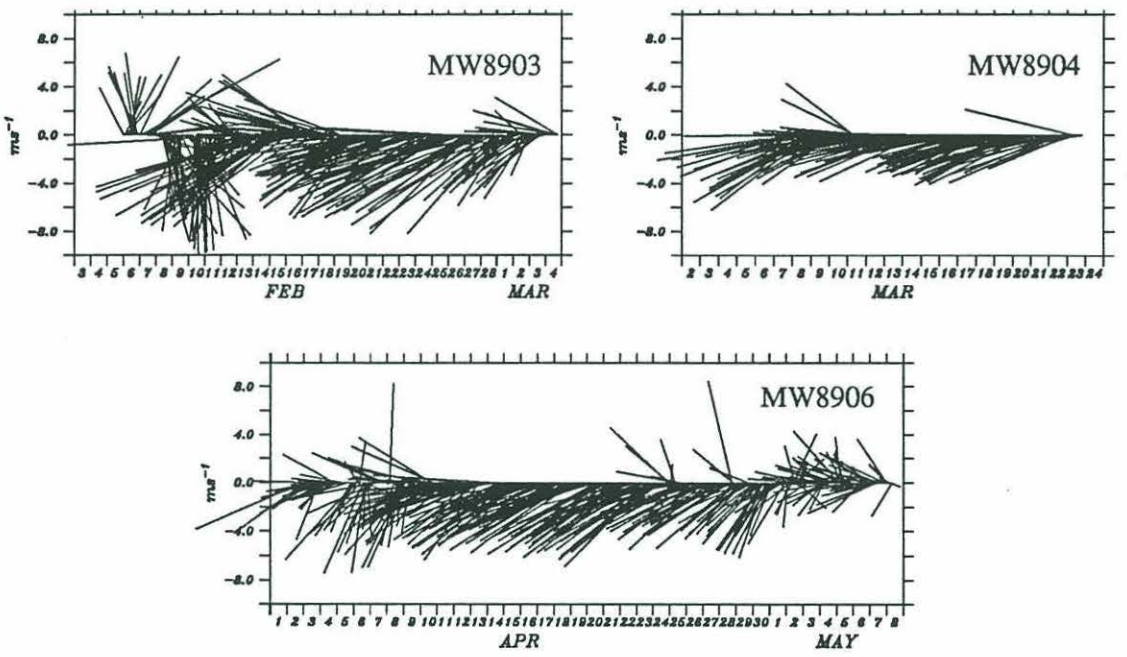

Figure 2

Vector wind plots for the three legs of the cruise: MW8903, MW8904 and MW8906. The original 15 minute time series had been subsampled every 2 hours before plotting.

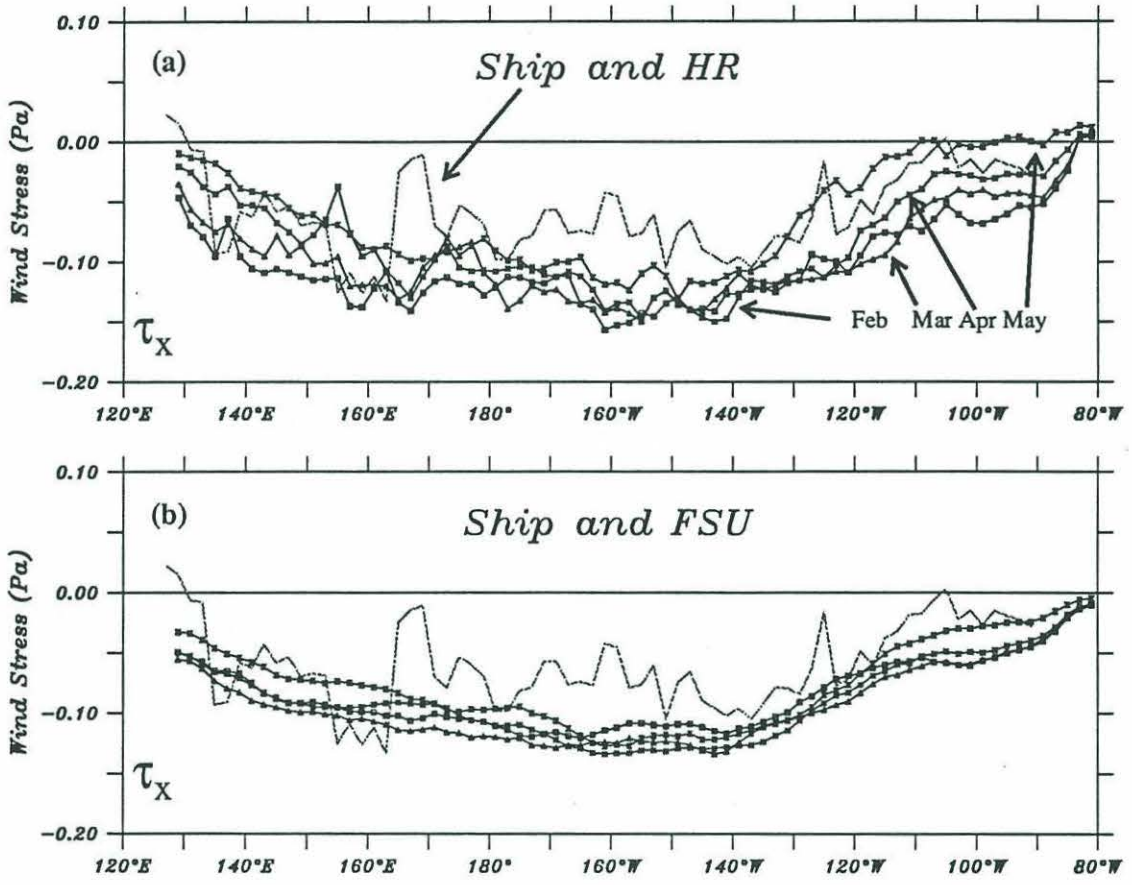

Figure 3

The zonal component of wind-stress based upon the in situ winds binned every 2° for comparison with the cruise months winds from the climatologies of (a) Hellerman and Rosenstein(1983); (b) 18 years of the FSU winds (Goldenberg and O'Brien, 1981).

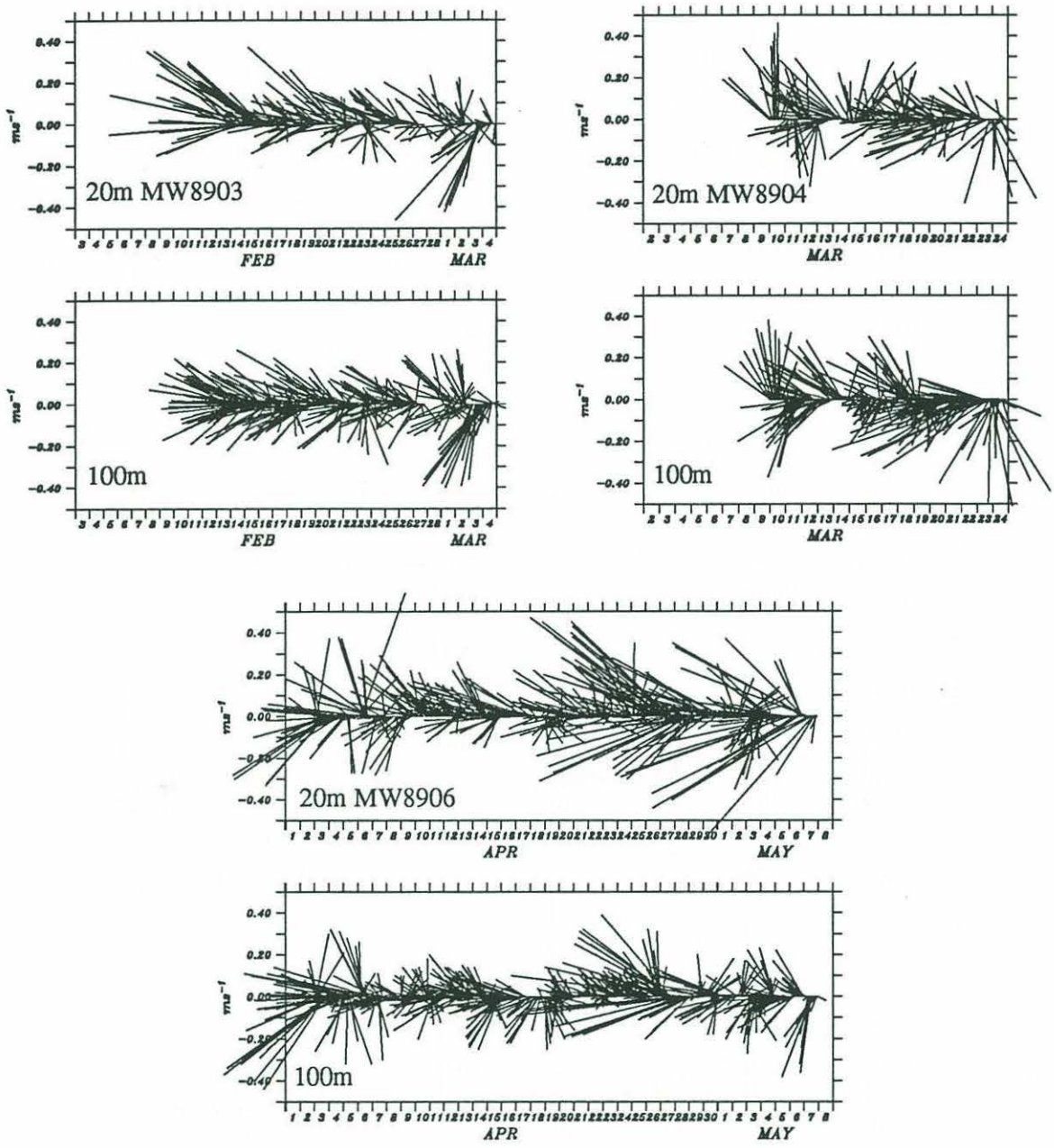

Figure 4

Time series vector stick plots of the ADCP velocities at depths of 20m and 100m for the 3 legs of the cruise. The data have been subsampled every 2 hours for plot clarity. Notice that the majority of velocity variance is common to both depths, though with a slightly reduced amplitude at 100m. The ratio of the variance in the difference velocity to the mean velocity for these depth levels is about 0.5 for all 3 legs. Comparison of the cross-track geostrophic and ADCP data indicate that geostrophic eddies are responsible for most of the velocity variance common to 20m and 100m.

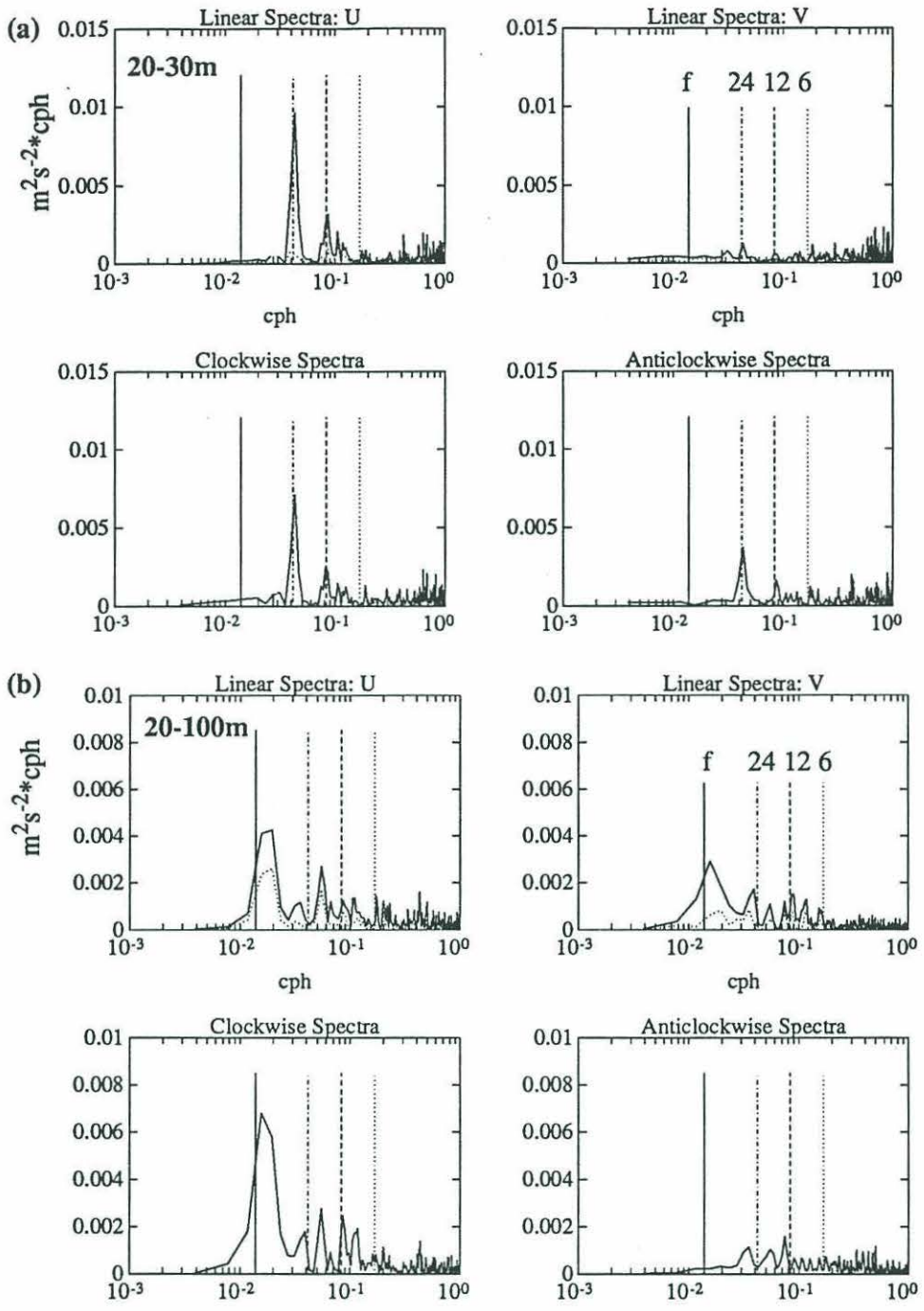

Figure 5

Energy preserving spectra of: (a) shear between 20 and 30m; (b) shear between 20m and 100m. The ordinate shows the variance in m^2s^{-2} times the frequency in cycles per hour. The peak in the clockwise energy in the 20m-100m shear corresponds to an amplitude of 8 cms^{-1}. The line frequencies indicated are for the inertial period (72.5 hours) and for 24, 12 and 6 hours. Spectra are shown for the middle leg (MW8904) only, but are qualitatively similar for the other two legs.

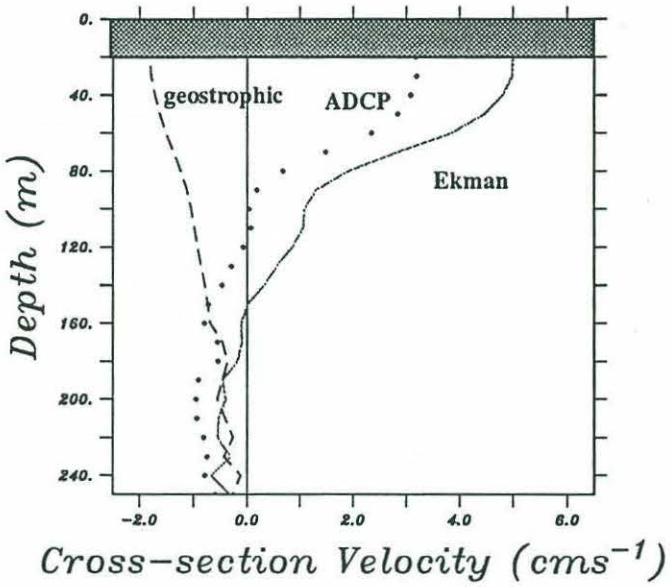

Figure 6

Section averaged cross-track velocity profiles. The geostrophic and ADCP velocities are set equal at 150m. The area above 20m where no ADCP data exists has been blanked out.

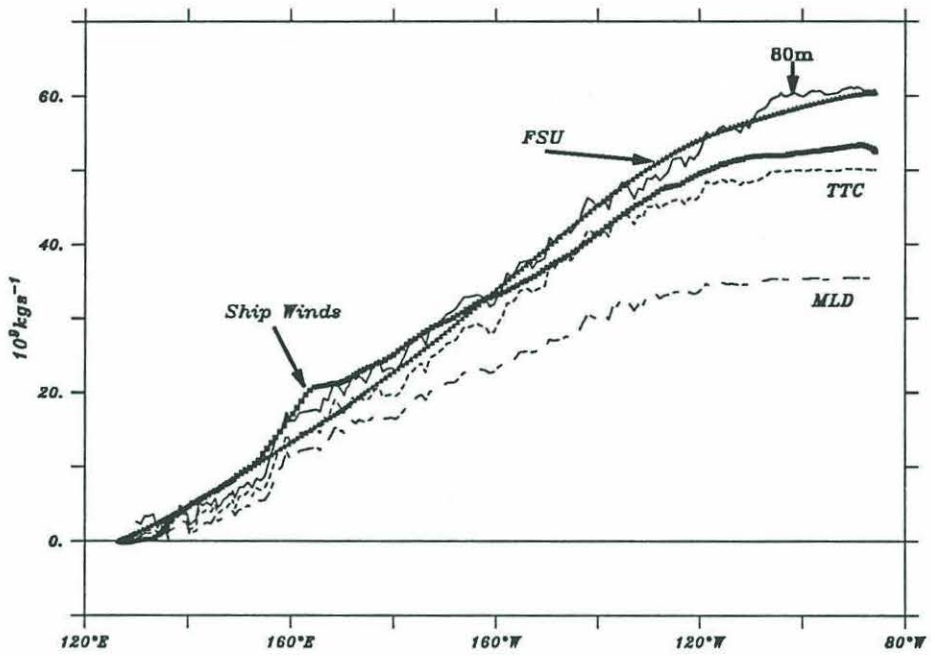

Cummulative Ekman Mass Flux: 10°N

Figure 7

Accumulated Ekman mass transport across the section. Direct estimates are integrated to various depths as explained in the text, and are plotted as thin lines. The wind-based estimates are the thick lines and are from the *in situ* ship winds and a climatology based upon 18 years of Florida State Uni-

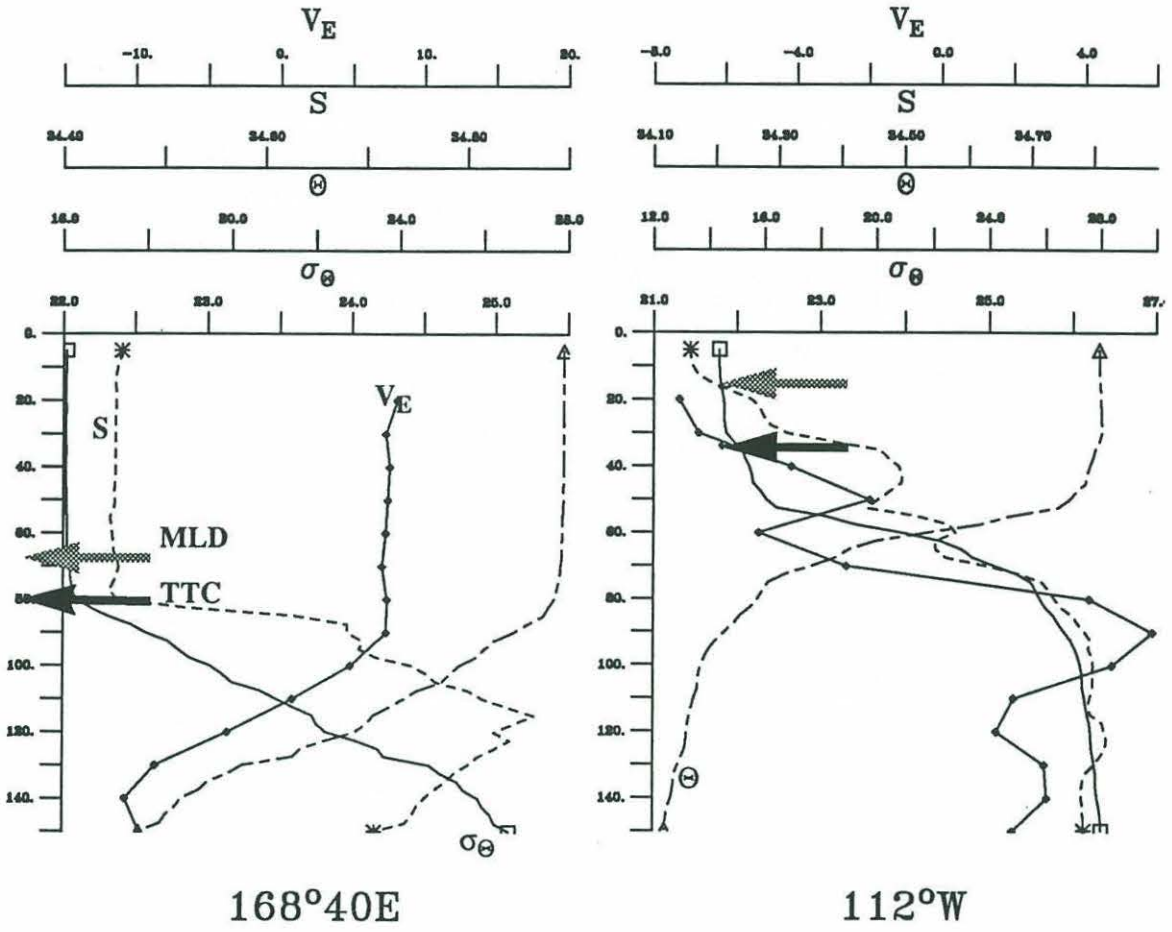

Figure 8

Vertical profiles of potential density, salinity and potential temperature for two CTD stations from the transpacific section. Also shown is the ageostrophic shear between the station and its neighbor to the east. The depth of the MLD and TTC are shown with the arrows against the potential density profiles.

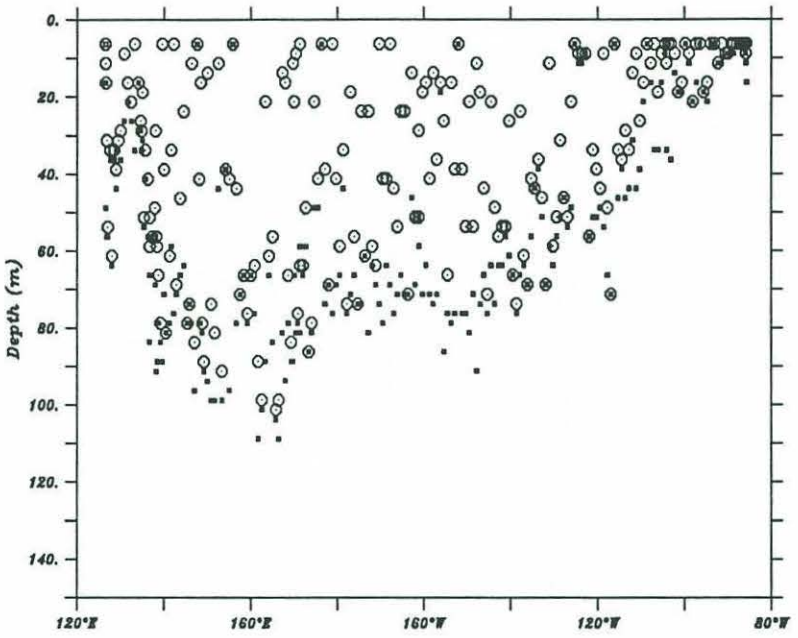

Figure 9

Mixed layer depth (open circles) and the top of the thermocline (black squares) across the section. The mixed layer depth is where the density differs from that at 2.5db by 0.01kgm^{-3}, while the top of the thermocline is the shallowest depth at which $\partial\rho/\partial z > 0.01\text{kgm}^{-4}$.

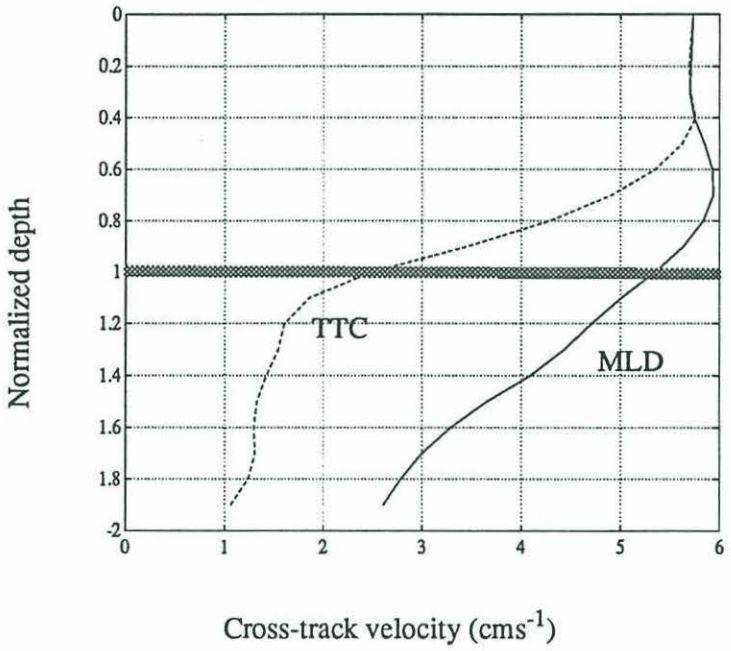

Figure 10

Section mean profile of across-track ageostrophic velocity, normalized by the mixed layer depth (MLD) and the top of the thermocline (TTC).

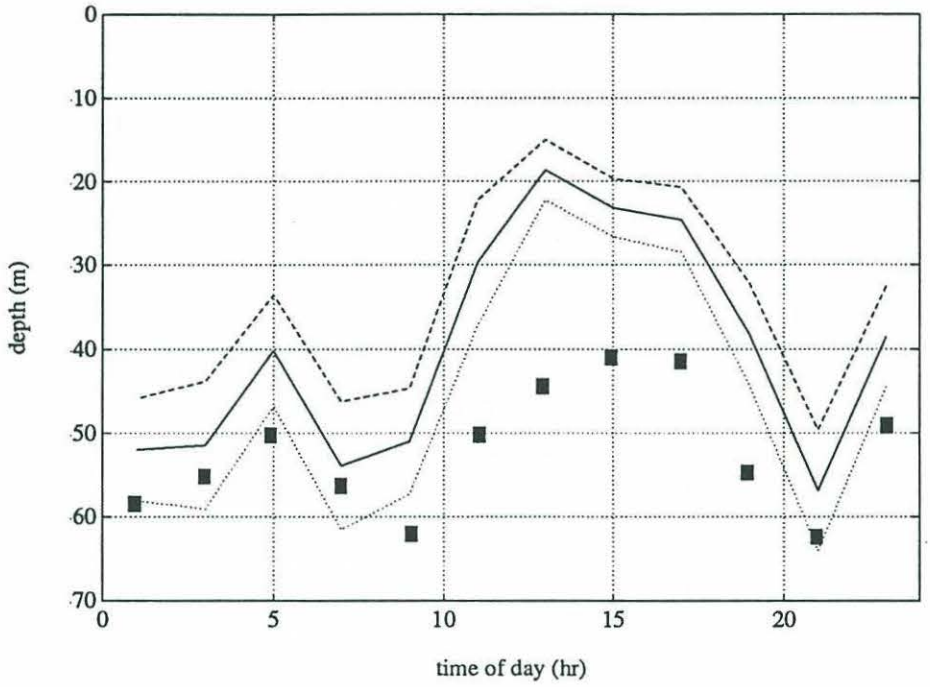

Figure 11

Diurnal cycle of the mixed layer depth. Mixed layer depth was binned in 2 hour bins of local time of day across the section. The most western 500km were excluded from the calculation. The dashed lines are the envelope of one standard error about the mean. The black squares show the diurnal cycle for the depth where velocity differs from that at 20m by $5cms^{-1}$.

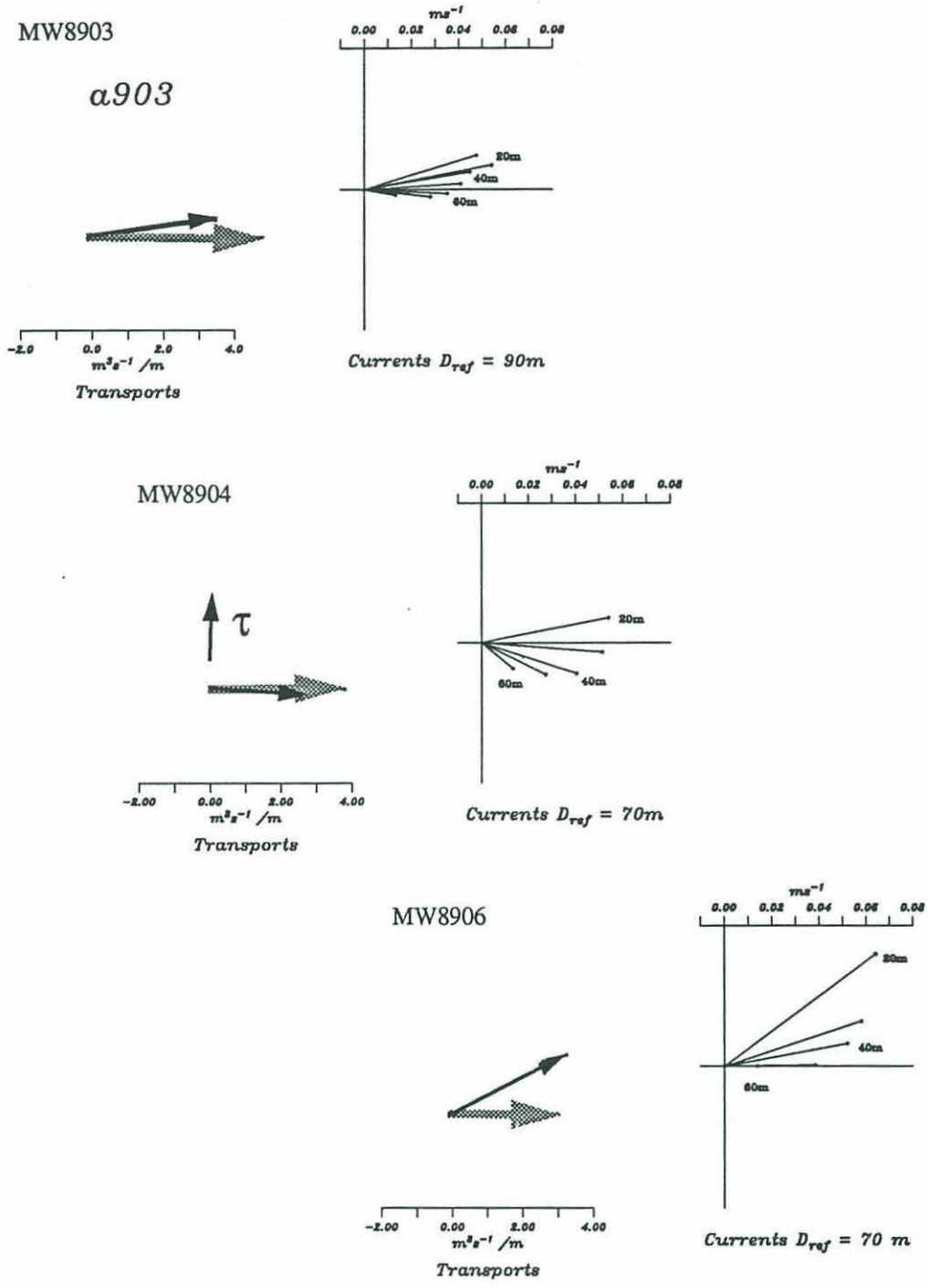

Figure 12

Wind-relative current spirals and transports for the 3 legs of the cruise. The wind direction is to the top of the page and the Ekman transport predicted by the winds is plotted as a grey arrow for comparison with the ADCP measured transports (black arrow).